LAYERED DOUBLE HYDROXIDES: SYNTHESIS AND APPLICATION IN GENE DELIVERY TO MAMMALIAN CELLS IN CULTURE

by

BLAKE BALCOMB

Submitted in fulfillment of the academic requirements for the degree

MASTER OF SCIENCE

in the School of Chemistry
Faculty of Science and Agriculture
University of KwaZulu-Natal
Westville

As the candidate's supervisor, I have approved this dissertation for submission.

Supervisor: Dr S. Singh Signed_____ Date_____

Co-supervisor: Dr M. Singh

2010

PREFACE

The experimental work described in this thesis was carried out at the School of Chemistry and the Department of Biochemistry, Faculty of Science and Agriculture, University of KwaZulu-Natal, Westville, from January 2010 to November 2010, under the supervision of Dr S. Singh and Dr M. Singh.

These studies represent original work by the author and have not otherwise been submitted in any form for any degree or diploma to any tertiary institution. Where use has been made of the work of others, it is duly acknowledged in the text.

DECLARATION – PLAGIARISM

I, Blake Balcomb, declare that

1. The research reported in this thesis, except where otherwise indicated, is my original research.

2. This thesis has not been submitted for any degree or examination at any other university.

3. This thesis does not contain other persons' data, images, graphs or other information, unless specifically acknowledged as being sourced from other persons.

4. This thesis does not contain other persons' writing, unless specifically acknowledged as being sourced from other researchers. Where other written sources have been quoted, then:
   a. Their words have been re-written but the general information attributed to them has been referenced
   b. Where their exact words have been used, then their writing has been placed in italics and inside quotation marks, and referenced.

5. This thesis does not contain text, images or tables copied and pasted from the Internet, unless specifically acknowledged, and the source being detailed in the thesis and in the References sections.

ACKNOWLEDGEMENTS

- I would like to thank my God, Jesus Christ for His grace, mercy, wisdom, love and kindness at all times. “Trust in the Lord with all your heart and lean not on your own understanding; in all your ways acknowledge him, and he will make your paths straight” (Proverbs 3:5-6).

I would like to express my sincere thanks to the following people:

- Dr S. Singh for his supervision, guidance and wealth of scientific knowledge.

- Dr M. Singh, Department of Biochemistry, University of KwaZulu-Natal (UKZN) (Westville) for her invaluable guidance and advice throughout this study.

- Professor M. Ariatti, Department of Biochemistry, UKZN (Westville) for his unwavering support and advice throughout this study.

- Dr J. Wesley-Smith and the staff of the Electron Microscopy (EM) Unit, UKZN (Westville) for their invaluable assistance in obtaining electron microscopy images.

- Mr V. Dasireddy for his assistance in obtaining powder X-ray diffraction data.

- Members of the Catalysis Research Group, UKZN (Westville).

- Members of the Gene Delivery Research Group, UKZN (Westville).

- The technical staff of the School of Chemistry (Westville) and the Department of Biochemistry (Westville) UKZN.

- The National Research Foundation (NRF) Scarce Skills Masters Scholarship for financial assistance.

- Finally, to my family and friends for their encouragement during my years of study.

ABSTRACT

Layered double hydroxides (LDHs) or hydrotalcite-like compounds (HTLcs) are classified as anionic clays in which their structure is based upon brucite and are represented by the following general chemical formula:

$$[M^{II}_{1-x}M^{III}_{x}(OH)_2]^{x+}(A^{n-})_{x/y}.yH_2O$$

where M^{II} and M^{III} represent various possible divalent cations, e.g., Mg^{2+}, Zn^{2+}, Ni^{2+}, Co^{2+} and Fe^{2+} and trivalent cations, e.g., Al^{3+}, Fe^{3+} and Cr^{3+} respectively. The value *x* is equal to the stoichiometric ratio of $M^{III}/(M^{II}+M^{III})$ and A^{n-} represents exchangeable anions such as CO_3^{2-}, Cl^- and SO_4^{2-}. It is these exchangeable interlayer anions, which make layered double hydroxide compounds excellent carriers of negatively charged or anionic containing biomolecules, such as DNA and hence can be exploited in their use in gene therapy.

In this study, a variety of Mg-Al hydrotalcites (HTs), Zn-Al, Zn-Fe and Mg-Fe LDHs were synthesized using co-precipitation. The synthesized compounds were characterized by X-ray diffraction (XRD), Fourier transform infrared spectroscopy (FTIR), Raman spectroscopy, Inductively coupled plasma-optical emission spectroscopy (ICP-OES), Transmission electron microscopy (TEM), Scanning electron microscopy (SEM) and Scanning electron microscopy-energy dispersive X-ray spectroscopy (SEM-EDX). XRD patterns for the synthesized HTs and LDHs exhibited characteristic features indicative of an ordered layered material. Elemental analysis of the compounds revealed a measured value of *x* in the range of 0.25-0.33 for Mg-Al HTs and Zn-Fe LDHs, 0.11-0.16 for Zn-Al LDHs and 0.55-0.58 for Mg-Fe LDHs. FTIR and Raman spectroscopy confirmed the presence of characteristic functional groups and interlayer anions. From electron microscopy, the compounds exhibited classical morphologies typical of HT and LDH compounds and had a lateral size range of 200-300 nm.

These compounds were studied in their ability to bind DNA with the use of a gel retardation or band shift assay. This assay confirmed that these compounds are indeed able to bind DNA. The binding mechanism of DNA to the HT and LDH compounds was evaluated and plausible mechanisms were proposed. Furthermore, nuclease digestion assays were carried out in order to evaluate the potential protecting ability that these compounds afford towards the bound DNA in the presence of serum. It was observed that

all compounds protected most of the bound DNA. The cytotoxicity of the compounds was evaluated in the HEK293, HepG2 and HeLa mammalian cell lines using the MTS (3-(4,5-dimethylthiazol-2yl)-5(3-carboxymethoxyphenyl)-2-(4-sulfophenyl)-2H-tetrazolium, inner salts) assay with a concentration range of 20-100 μg of respective HT/LDH compound. For most of the compounds, cell viability was observed in excess of 80 %. Finally, transfection studies were carried out utilizing green fluorescent protein (GFP) analysis and luciferase gene expression using the same mammalian cells in culture. It was noted that all HTs and LDHs were able to release DNA in a controlled prolonged manner over a period of three days. Green fluorescent protein gene expression commenced after 27 hours and reached a maximum at 72 hours. Efficient luciferase gene expression was observed with luciferase activities for DNA: HTs ranging from 0.05×10^6 - 2.0×10^6 RLU / mg protein and DNA: LDHs ranging from 0.05×10^6 - 16.7×10^6 RLU / mg protein. Highest luciferase activity was recorded as 16.7×10^6 RLU / mg protein.

CONTENTS

Page No.

DEFINITIONS AND CALCULATIONS

1. **Scherrer's Equation:** To calculate crystallite size

$$\text{Crystallite Size} = \frac{(K)(\lambda)}{(B)(\cos\theta_B)}$$

where K = *XRD instrument standard constant*

λ = *X-ray wavelength*

B = *Full width at half maximum (FWHM) of peak corresponding to 100 % intensity*

θ_B = *Bragg angle or 2-theta angle of peak corresponding to 100% intensity*

2. **Value of x:**

$$x = \frac{M^{III}}{(M^{II} + M^{III})}$$

where M^{II} = Divalent cation

M^{III} = Trivalent cation

ABBREVIAITIONS

DNA	:	Deoxyribonucleic acid
EDX	:	Energy dispersive X-ray spectrometry
FCS	:	Fetal calf serum
FITC	:	Flourescein-5-isothiocyanate
FTIR	:	Fourier transform infrared spectroscopy
GFP	:	Green fluorescent protein
HEK293	:	Human embryonic kidney cell line 293
HT	:	Hydrotalcite
HTLc	:	Hydrotalcite-like compounds
ICP-OES	:	Inductively coupled plasma-optical emission spectroscopy
IR	:	Infrared spectroscopy
LDH	:	Layered double hydroxide
pCMV	:	Plasmid containing cytomegalovirus promotor
RLU	:	Relative light units
SEM	:	Scanning electron microscopy
SEM-EDX	:	Scanning electron microscopy-energy dispersive X-ray spectrometry
TEM	:	Transmission electron microscopy
XRD	:	X-ray diffraction

LIST OF FIGURES

Page No.

Page No.

Page No.

Page No.

LIST OF TABLES

Page No.

CHAPTER ONE
INTRODUCTION

1.1 Historical background

Since the discovery of naturally forming hydrotalcite (HT) in Sweden in the early 1940s, hydrotalcite-like (HTLc) or layered double hydroxides (LDHs) have been studied in their use as catalysts and precursors to various other catalysts as early as 1970 [1, 2]. The application of HTs (Mg-Al) in gene delivery studies was first published in 2000 by Choy et al. [3]. Since then, researchers have continued to use Mg-Al HTs in gene delivery studies specifically focusing on the optimization of synthesis conditions, particle size and the elucidation of mechanisms of deoxyribonucleic acid (DNA) binding and cellular uptake.

Shortly after the discovery of naturally forming HT, a German scientist, W. Feitknecht, synthesized a variety of HTLc compounds which he named “doppelschichtstrukturen” or double sheet structure [1]. Feitknecht described these structures as having a layer of hydroxide of one cation followed by a hydroxide layer of the second cation.

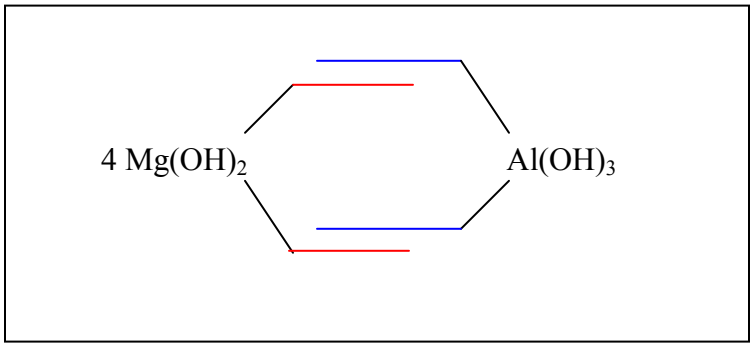

Figure 1.1 Figure depicting “doppelschichtstrukturen”, coloured lines indicate layered structure (Adapted from [1]).

Feitknecht’s theory was later disproved and corrected by the pioneering work of Allman and Taylor in which their single crystal X-ray diffraction studies carried out on mineral samples revealed the main structural entities of LDHs [4]. These studies showed that the two cations were in fact located in a single layer and the interlayers were composed of

water and carbonate ions. Although the main entities of LDHs have been elucidated, Evans and Slade [4] have suggested that several intrinsic details still remain to be fully understood. These include the possible stoichiometric range and composition, the position and arrangement of metals within each cationic layer. In addition, the extent at which these layers associate with the interlayer and its various range of possible anions. Previous to the study by Evans and Slade, Miyata [5, 6] and Miyata and Okada [7] described many structural features of HTs and LDHs containing different guest anions. From their findings, these authors were able to describe the relation of synthetic HTs and LDHs to that of brucite and $Cd(OH)_2$-like structures. Layered double hydroxides are classified as clays. According to Annabi-Bergaya [8], although clay science has been investigated for a long time, breakthroughs in this area have only occured in the last decade. Annabi-Bergaya has forecasted that clays will be important materials of the future and their understanding will constantly evolve as more data becomes available.

1.2 Clay minerals

Clays are found in abundance in nature and are usually formed from the weathering and decomposition of silicate and igneous materials at the surface of the earth [9, 10]. Clays are layered materials and are classified within the phyllosilicates. The layers are based on a two-dimensional stack of inorganic layers. Each layer is composed of either tetrahedral sheets of SiO_2, octahedral sheets of metal oxide and hydroxide (LDHs) or both [10]. Hydrogen bonding and van der waals interactions between cations, interlayer anions and water molecules ensure that the layered organization is maintained between subsequent sheets. Clays are classified into two broad groups, viz., cationic clays, widespread in nature and the less common, anionic clays. The application of clays include the preparation of ceramics and building materials, paper coatings and fillings, drilling muds, foundry moulds, cat litters, pharmaceuticals, adsorbents, catalysts or catalyst supports, ion exchangers, decolorizing agents, environmental remediation, polymers, electronics and fuel cells [9-12].

Cationic clays

Clay minerals are based upon hydrous layer silicates of the phyllosilicate family, which are built upon tetrahedral Si(-O,-OH) and octahedral $M(-O,-OH)_6$ sheets. Different combinations of these sheets give rise to different forms of cationic clays. When one tetrahedral sheet joins an octahedral sheet, a 1:1 clay mineral is formed, e.g., kaolinite. Furthermore, when an octahedral sheet is wedged between two tetrahedral sheets, a 2:1 clay mineral is formed, e.g., pyrophyllite and montmorillonite. It is possible for Si substitution or replacement by various other cations such as Al, Mg and Fe resulting in a negative charge balance within the sheets. This charge is balanced by various other inorganic cations provided by the soil and hence resulting in an overall positive charge, hence the term cationic clay minerals [10-12].

Anionic clays

Although anionic clays are classified as phyllosilicate clay materials, their structure is based on brucite ($Mg(OH)_2$) instead of silicate. Each Mg cation is octahedrally surrounded by hydroxyl groups forming an infinite sheet or layer (Figure 1.2).

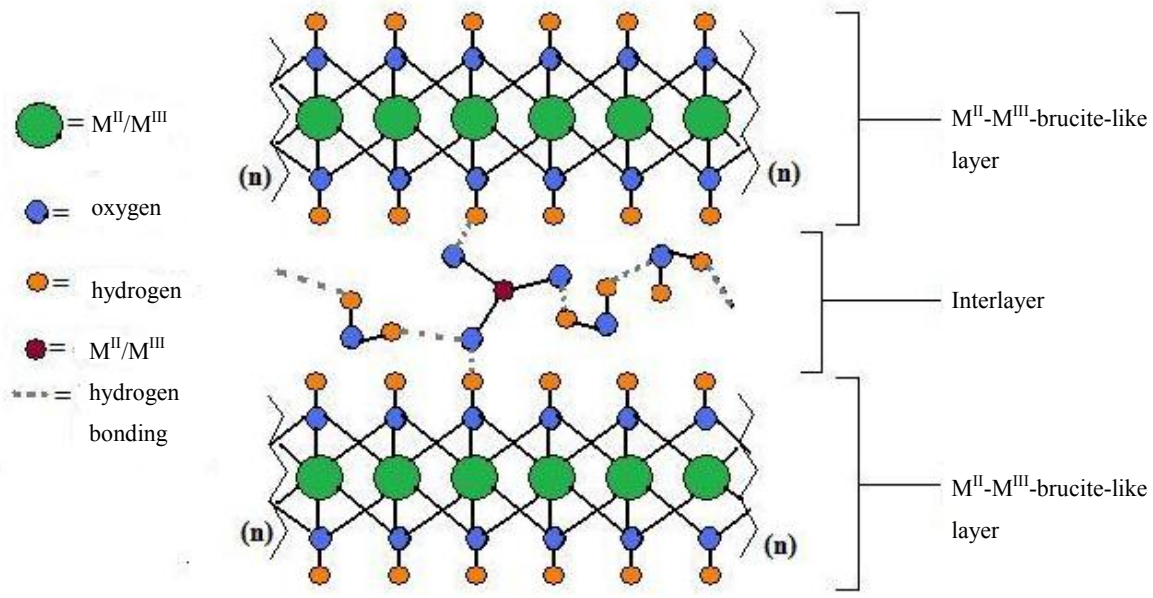

Figure 1.2 Figure depicting the structure of hydrotalcite-like compounds (Redrawn and adapted from [13,14]).

Anionic clays are also termed hydrotalcite-like compounds (HTLcs) or layered double hydroxides (LDHs). As with cationic clays, cation substitution or replacement is also possible giving rise to a wide variety of isomorphous materials. When cations are replaced by cations with a higher valency than those within the brucite-like sheet, the brucite-like sheets bear an overall positive charge, in which counter balance is provided by extra-framework interlayer anions [10-15].

Currently, there is considerable interest in the ion exchange of various anionic pharmaceutically important molecules into the interlayer region of LDHs. In addition, they have higher anion exchange capacities than other anionic exchange resins and have the added advantage of being readily synthesized in the laboratory from a variety of desired precursors. The chemical composition and structure of LDHs plays an important role in the ion exchange capacity of these anionic clays [15-17].

1.3 LDH structure and composition

LDHs are chemically classified as anionic clays in which their structure (Figure 1.3) is based on brucite layers ($Mg(OH)_2$) [18].

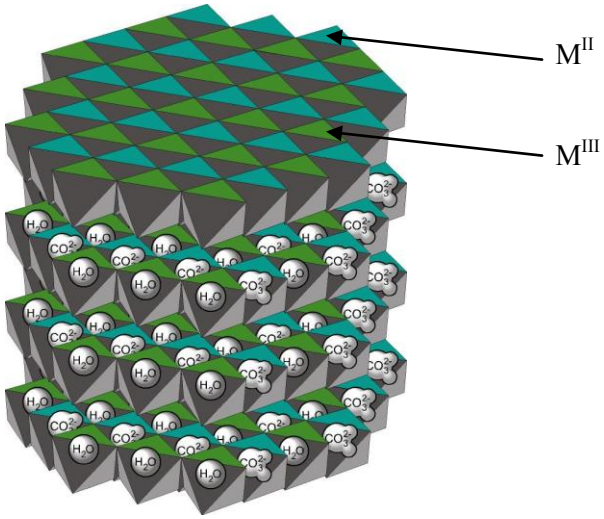

Figure 1.3 Diagrammatic representation of LDH compound (Redrawn from [11] using Macromedia Freehand MX Software, 2004). (M^{II} = Mg^{2+}, Zn^{2+}, Ni^{2+}, Co^{2+} and Fe^{2+}; M^{III} = Al^{3+}, Fe^{3+} and Cr^{3+}).

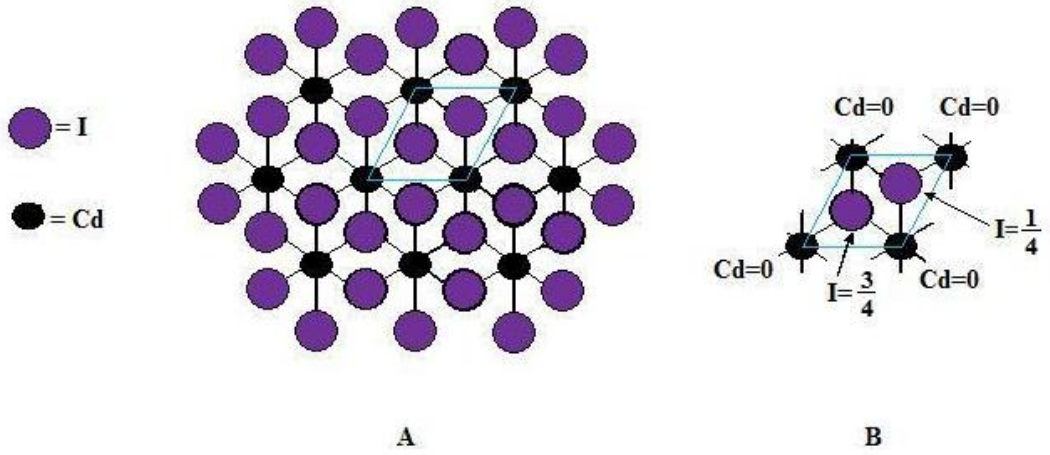

Figure 1.4 Figure depicting, (A) a single layer of the structure of Cd atoms coordinated to halogen atoms, and (B) hexagonal unit cell found within layers of (A) (Redrawn and adapted from [19, 20]).

Each Mg^{2+} ion is coordinated octahedrally towards OH^- ions (Figure 1.2) and exhibits a close-packing structure based on the AX_2 structure, similar to that observed in cadmium iodide (CdI_2) (Figure 1.4). Furthermore, each octahedral unit shares edges between subsequent octahedral units and hence forms an infinite sheet. These sheets stack on top of one another and are held together by hydrogen bonds with the OH^- ion positioned perpendicular to each sheet [4]. When Mg^{2+} is replaced by a trivalent cation similar in radius, an overall positive charge results in the hydroxyl sheets and counter balance is provided by carbonate ions which are positioned within the hydroxyl interlayer. In addition to carbonate ions, water molecules are found in the interlayer gallery. The nature of the interlayer anion and the extent of hydration often determine the layer spacing between each brucite-like sheet [21].Within the two-dimensional hydroxyl sheets it has been speculated that there is further ordering of the trivalent and divalent cations. Furthermore, it has been postulated that the trivalent cations are unlikely to position themselves, side on, neighboring each other in cation sites [22]. As a result of the trivalent cations occupying non-neighboring sites, the ratio of trivalent to divalent cation should result in an entirely ordered superlattice with unit-cell parameters in the brucite-like sheets of $\sqrt{3}a$ (where a represents the average cation-cation distance) and the hexagonal lattice rotated by 30^o from that of brucite [22]. The brucite-like sheets may

occur in two different symmetries, namely rhombohedral and hexagonal. In nature, the rhombohedral symmetry is wide spread. However, in mineral samples, the hexagonal symmetry is seen to favour the interior of the crystallite samples, while the rhombohedral symmetry is found on the exterior. This is a result of cooling during crystallite transformation, in which the exterior surface of the crystallite cools much quicker than the interior and hence the interior hexagonal form cannot transform due to a higher energy transformation barrier at lower temperatures. From these observations, it has been deduced that the hexagonal symmetry is favored by high temperatures [1,5]. Naturally occurring minerals that exhibit a LDH structure include manasseite, pyroaurite, sjogrenite, barbetonite, takovite, reevesite, desautelsite and stichtite. They differ from one another in the stacking arrangement of the octahedral layers [1, 23].

LDHs are represented by the following general chemical formula:

$$[M^{II}_{1-x}M^{III}_{x}(OH)_2]^{x+}(A^{n-})_{x/y}.yH_2O$$

where M^{II} and M^{III} represent various possible divalent cations, e.g., Mg^{2+}, Zn^{2+}, Ni^{2+}, Co^{2+} and Fe^{2+} and trivalent cations, e.g., Al^{3+}, Fe^{3+} and Cr^{3+} respectively and A^{n-} represents exchangeable anions, e.g., CO_3^{2-}, Cl^- and SO_4^{2-}. Stoichiometric ratios, *x* and *y* may be altered to give varying types of LDH iso-structural materials [13, 18, 24-28]. The value *x* is equal to the stoichiometric ratio of $M^{III}/(M^{II}+M^{III})$. Thus, the typical LDH structure can be simplistically viewed as alternating layers of cations upon counter anions within hydroxyl sheets.

1.4 Possible range of M^{II} and M^{III} ions

Any divalent or trivalent ion that is capable of being positioned in the close packed configuration of the hydroxyl groups of the brucite-like layers can form a hydrotalcite-like structure. Most of the divalent metal ions (Be^{2+}, Mg^{2+}, Cu^{2+}, Ni^{2+}, Co^{2+}, Zn^{2+}, Fe^{2+}, Mn^{2+}, Cd^{2+} and Ca^{2+}) form LDHs, with the exception of Cu^{2+} which forms a LDH structure only when another divalent cation is present. However, with this additional divalent cation present, the ratio between the Cu^{2+} ion and the additional ion should be equal to or lower than one. A ratio above one, results in the Jahn-Teller effect which is due to the gain in energy derived from a distorted octahedral coordination structure. The

Cu^{2+} ions are positioned in close proximity of one another in near-lying octahedra and hence the formation of a distorted octahedral structure is energetically favourable than that of a LDH [1]. LDH compounds containing Cu^{2+} ions have been prepared and characterized although copper containing materials show a corrugation of the sheets associated with the Jahn-Teller distortion [4, 29]. Trivalent ions, with the exception of Ti^{3+} and V^{3+}, with atomic radii ranging from 0.50-0.8 Å form LDH structures. More recently, Islam and Patel [17] have synthesized LDHs containing thorium (IV), while others have synthesized LDHs containing Zr^{4+}, Sn^{4+}, Ti^{4+} and Si^{4+} [30, 31]. However, much doubt has been cast on these tetravalent containing LDHs [32]. According to Evans and Slade [4], it has been clearly shown by X-ray absorption spectroscopy and Mössbauer spectroscopy, that tetravalent cations separate from the LDH structure and form tetravalent oxide-like compounds. Layered double hydroxides containing monovalent lithium have been successfully prepared and characterized [33].

1.5 Possible values of *x*

Pure phases of LDH compounds are produced when x falls in the range of $0.2 \leq x \leq 0.33$. However, HT and LDH compounds with x ranging from 0.1-0.5 have been synthesized. There is doubt as to whether these compounds are indeed pure phases since $Mg(OH)_2$ and $Al(OH)_3$, in most cases are not detectable by X-ray measurements [1, 4, 5, 11, 33-36]. López-Salinas et al. [37] reported the synthesis of Mg-Ga-CO_3 LDHs for a value of x as low as 0.07. Also, values of x in the range of 0.17-0.18 have been reported for Mg-Al-CO_3 and Mg-Ga-CO_3 LDHs [38]. In addition, LDHs with values of x as high as 0.4 - 1.0 have been synthesized [6, 39-41] including Fe^{II}-Fe^{III} with a value of 0.5 [42]. According to Brindley and Kikkawa [34], in compounds where the value of x is lower than 0.33, the Al octahedra are non-neighbouring. However, when the value of x is greater than 0.33, the chances of neighbouring Al octahedral increases, favouring the formation of $Al(OH)_3$.

1.6 LDH interlayer

The interlayers of LDHs contain both anions and water molecules [1, 4, 5, 11, 21, 43-45]. Within these interlayers there exists a network of electrostatic and hydrogen bonding between the hydroxyl groups, anions and water molecules. It is the number, size, orientation, and strength of the bonds between the anions and the hydroxyl groups that determine the thickness of the interlayer. The oxygen atoms of both carbonate and water anions are positioned in sites very close to the symmetry axes of hydroxyl groups located perpendicularly to adjacent brucite-like layers. This is due to the close proximity of the oxygen atoms in each group, only one site is occupied, therefore, three adjacent sets of sites are filled by the oxygen atoms for each carbonate group. According to Cavani et al. [1], water molecules form a tetrahedral configuration through hydrogen bonding between nearby oxygen atoms or hydroxyl groups, whereas Evans and Slade [4] state that the hydroxyl groups bonded to trivalent cations are strongly polarized and interact with the interlayer anions. Thus, every anion is required to satisfy the excess positive charge of both adjacent octahedral layers which are electrically balanced by two neighbouring interlayers. It has been suggested that charge compensation in LDHs has features characteristic of resonance effects. The interlayer arrangement described, is found in the hydroxide, carbonate, nitrate and chloride LDHs. Cavani and co-workers [1] also observed that sulphate $(SO_4)^{2-}$ and chlorate $(ClO_4)^{-}$ containing LDHs exhibit a different interlayer arrangement to those containing nitrate or carbonate. This observation is attributed to the difference in geometries that sulphate and chlorate anions exhibit. The amount of water (y) in the interlayer of LDHs may be calculated from thermogravimetric measurements of weight loss. Alternatively, the amount of water may be calculated from the total number of sites occupied by oxygen subtracting the sites occupied by the anions [11]. According to Miyata [6], the amount of water may be calculated by assuming a close packed configuration using the equation, $y = 1\text{-}Nx/n$, where N = the number of sites occupied by the anion, $x = M^{III}/(M^{II}+M^{III})$, and n = charge of the anion. For $(CO_3)^{2-}$, $y = 1\text{-}3x/2$. However, it has been argued by Evans and Slade [4] that when calculating the amount of water in the interlayers, the extrinsic water that can be adsorbed onto the external surface of the LDH should be taken into consideration. A wide variety of anions

have been incorporated into the interlayer region of LDHs that have resulted in their application in catalysis [1, 46-56], industry and agriculture [1, 18, 57-59], ion exchangers [1, 58, 60], conductors [61], insulators [1], pharmaceutics [1, 13, 16, 26, 27, 62-74], corrosion inhibitors [1] and magnetic materials [18] (Table 1.1). The incorporation of these anions into the interlayer region is due to the ion exchange nature that HTs and LDHs exibit [11, 12]. It is these exchangeable interlayer anions in the LDH structure, which make these compounds excellent carriers of negatively charged or anionic containing biomolecules, such as DNA and hence can be exploited in their use in gene therapy.

Table 1.1 Interlayer anions of various synthesized HTs and LDHs

Interlayer anion		Reference
Inorganic anions:	Cl^-, $(CrO_4)^{2-}$, $(NO_3)^-$, $(SO_4)^{2-}$, $(CO_3)^{2-}$	[44]
	Br^-, F^-, I^-, Cl^-,$(NO_3)^-$,$(CO_3)^{2-}$	[7]
	$[Co(CN)_6]^{3-}$	[44]
	OH^-	[75]
	$(ClO_4)^-$	[34]
	$(HPO_4)^{2-}$	[76]
	$(ClO_4)^-$	[6]
	$(V_{10}O_{28})^{6-}$	[77]
	$[Fe(CN)_6]^{3-}$, $[Fe(CN)_6]^{4-}$	[40]
	$[SiO_3]^{2-}$, $(Mo_7O_{24})^{6-}$, $(Cr_2O_7)^{2-}$	[43]
	$[Rh^0]$	[46]
	$HRh(CO)(TPPTS)_3$ (TPPTS = tris(3-sodium sulfonatophenyl) phosphine)	[78]
Organic molecules:	Acetate, terephthalate and benzoate	[79]
	Benzenedicarboxylates and napthalenesulfonates	[80]
	2,4-dichlorophenoxyacetate	[81]
	Oxalic acid, adipic acid, succinic acid, tartric acid	[82]
	Phosphonic Acid	[83]
	Acetate	[62]
	Terephthalate, biphenyl-4,4'-dicarboxylate	[84]

Table 1.1 Continued

Layered compounds:	Mineral chlorite, $(Mg_2Al(OH)_6)^+.[Mg_3(OH)_2/Si_3AlO_{10}]^-$	[1]
Surfactants:	Alkyl-sulphates, alkanesulphonates	[85]
	Octylsulphonate, octanebenzenesulphonate, dodecylbenzenesulphonate, octadecanesulphonate	[86]
Pharmaceuticals:	Gramicidin, amphotericin B, ampicillin, nalidixic acid	[16]
	Phenylphosphonic acid	[87]
	Gliclazide	[63]
	Fenbufen	[13]
	Heparin	[64]
	L-ascorbic acid	[65]
	Mefenamic and meclofenamic acid	[66]
	Podophyllotoxin	[67]
Biomolecules:	Amino acids, oligopeptides	[68, 69]
	Monotriphosphates, Flourescein-5-isothiocyanate (FITC), c-myc antisense oligonucleotide	[71]
	Small interfering ribonucleic acid (siRNA)	[88, 89]
	Deoxyribonucleic Acid (DNA)	[26, 27, 73]

1.7 Gene therapy

The idea of correcting an inherited or acquired genetic error has been in existence since the early 1930s when the term „genetic engineering' was first described [90]. However, it was only until a decade later that Avery et al. [91] described the notion of the inducible delivery of deoxyribonucleic acid (DNA) into bacterial cells and hence illustrating DNA transfection in *pneumococcal* strains. Avery's findings, coupled with the discovery of the structure of DNA and its genetic implications sparked the beginning of the gene therapy era. The idea of the delivery of exogenous or foreign DNA into cells encouraged

researchers to investigate whether this strategy could be exploited in the delivery of a therapeutic gene into diseased human cells. From the early 1950s till the late 1980s the field of gene therapy was largely dominated by the use of modified viruses in the delivery of a therapeutic gene to diseased mammalian cells due to the high efficiency that these modified viruses afforded. Among the first non-viral gene therapy methods used during this time included the use of DEAE dextran [92] and calcium phosphate co-precipitation [93]. A major development in gene therapy was the first human gene therapy *ex vivo* experiment carried out on patients in the 1990's by the National Institute of Health (NIH) USA, in which a four-year old patient whom suffered from severe combined immunodeficiency (SCID) underwent gene therapy. The goal was to insert a therapeutic gene (*ADA* gene, coding for adenosine deaminase) into healthy lymphocytes and reintroduce these modified lymphocytes into the patient. A new drug therapy that had been developed in treating SCID was simultaneously administered to the patient. To date, this patient is still receiving the drug treatment, however, the NIH remains unsure as to whether the gene therapy initially administered, was a dominant factor in this patient's healthy recovery [94]. During this time Rosenberg et al. [95] reported an *ex vivo* gene transfer trial in patients suffering from melanoma using modified lymphocytes containing an inserted therapeutic gene by retroviral gene transduction. A number of other such experiments done in the late 1990s, including *in vivo* studies, resulted in the deaths of many patients due to the body's response towards the vector used in the gene therapy strategy, most of which have been viral vectors. Although gene therapy using modified viruses appears very efficient, the adverse activation of the immune response towards these introduced modified viruses greatly impaired the development of viral gene therapy research. Thus, for many years, gene therapy researchers have been striving to develop an ideal non-viral or improved viral vector for the delivery of a therapeutic gene into diseased mammalian cells. According to research, an „ideal' gene therapy vector should have the following properties: ability to deliver a therapeutic gene safely into a cell, have a high loading capacity, exhibit little or no toxicity, non-immunogenic, biodegradable, include a wide availability, stable during storage and after administration, have the ability to target specific cells and afford relatively efficient gene expression [27, 96]. Of the many vectors that have been developed, a select few can satisfy all of the above

requirements. The wide variety of viral vectors that have been utilized in gene delivery include the Retrovirus, Adenovirus, Adeno-Associated virus and Herpes simplex virus. Although viral vectors are amongst the most efficient in gene delivery vectors, a majority of the viral vectors have numerous disadvantages such as the inability to produce high titers of the modified virus, elevated cytotoxicity and activation of the immune response resulting from replication competent viral particles.

Non-viral vectors on the other hand, such as the direct gene gun method, liposomes, lipid based molecules, polymers, organic and inorganic nanoparticles, as well as other biomaterials exhibit properties such as lower immunogenic effects, simplicity and feasibility to large scale production. Although many of these non-viral vectors exhibit properties rendering them as attractive alternatives to the use of viral vectors, the drawbacks of many non-viral vectors include adverse cytotoxic and biological effects, low gene delivery efficiency and transient gene expression. Despite these drawbacks, researchers have pressed on in the search, design and synthesis of more favorable non-viral vectors. A fairly recent non-viral vector that is receiving much attention due its favorable „ideal' properties is that of LDHs [71]. A LDH compound posseses versatile properties that make them appropriate for gene therapy such as good biocompatibility, low cytotoxicity, diverse functionality, controllable particle sizes, wide availability, high loading capacities, protection of biomolecules in the interlayers and the potential capability of targeted delivery and controlled release of carried genes [25-28, 71]. Of the various studies utilizing these compounds in gene therapy, many have been conducted on Mg-Al HTs since their structural and chemical nature have been extensively studied. Cytotoxicity studies on Mg-Al HT compounds have been carried out and have been found to cause minimal cell death [25-28, 71]. To date, HT compounds have been utilized as carriers of DNA, monotriphosphates, flourescien-5-isothiocyanate (FITC), c-myc antisense oligonucleotide (As-myc), small interfering ribonucleic acid (siRNA) and pharmaceutical drugs [13, 25-28, 71].

1.8 Motivation and objectives of study

Mg-Al HTs have shown immense potential as an alternative non-viral vector in gene therapy as they exhibit properties rendering them as an „ideal' vector [25-28, 71]. Although the use of Mg-Al HTs in gene therapy has attracted much attention, no work has been published on the application of LDHs of varying cationic compositions in gene therapy strategies. Thus considering the properties exhibited by HTs, the need to further investigate LDHs of varying compositions in gene delivery strategies would provide insight into the effects of varying cationic compositions and their effectiveness in relation to Mg-Al HTs. These findings would thus have a direct impact in developing HTs and LDHs into *in vivo* models and eventually the use in treating a patient suffering from perhaps a debilitating genetic disease. Literature has suggested that the mechanism of HT-DNA complex formation occurs via ion-exchange, whether this mechanism indeed occurs in LDH-DNA complexes will be explored [25-28]. Furthermore, the potential application of these compounds in gene delivery to mammalian cells in culture will be investigated. These insights will provide a greater understanding of the use of LDHs in gene therapy and will pave a way forward in order to improve current non-viral gene therapy strategies using these compounds as well as to ascertain their future in gene delivery strategies.

The objective of this study was to synthesize different combination of compounds with the formula:

$$[M^{II}_{1-x}M^{III}_{x}(OH)_2]^{x+}(A^{n-})_{x/y}.yH_2O$$

where M^{II}=Mg^{2+}, Zn^{2+} and M^{III}=Al^{3+}, Fe^{3+} and to investigate their potential application in gene delivery to mammalian cells in culture. These compounds were characterized using X-ray diffraction (XRD), Fourier transform infrared spectroscopy (FTIR), Raman spectroscopy, Inductively coupled plasma-optical emission spectroscopy (ICP-OES), Transmission electron microscopy (TEM), Scanning electron microscopy (SEM) and Scanning electron microscopy-energy dispersive x-ray spectroscopy (SEM-EDX). Thereafter their DNA binding abilities, cytotoxicities as well as transfection activities were examined *in vitro* using the HepG2, HEK293 and HeLa mammalian cell lines.

CHAPTER TWO
SYNTHESIS AND CHARACTERIZATION OF HYDROTALCITES (HTs) AND LAYERED DOUBLE HYDROXIDES (LDHs)

2.1 Experimental

Layered double hydroxides have been synthesized by various techniques. Some of the most popular and extensively used techniques include co-precipitation, hydrothermal methods and ion exchange [1, 4, 5, 7, 11].

2.1.1 Methods of LDH synthesis

2.1.1.1 Co-precipitation

Co-precipitation remains the most commonly used technique for the synthesis of LDHs. This technique involves the addition of aqueous solutions of M^{II}, M^{III} and the anion that is to be incorporated into the LDH structure. The direct addition of prepared precursors allow for a variety of cations and anions to be incorporated into the formulation of various LDHs. Co-precipitation is also the method commonly used in the formulation of organic anion LDHs which are difficult to obtain by other methods [4]. For the co-precipitation of two or more cations, it is essential to maintain the reaction mixture in a state of supersaturation. Supersaturation is achieved physically by evaporation or chemically by controlling pH [1]. It has been observed that in order for co-precipitation to progress, the pH should be maintained at a value equal to or higher than the one at which the more soluble hydroxide precipitates [1, 4, 11].

The optimum pH for precipitation of the hydroxides of some common metals used in LDH preparation is shown in Table 2.1.

Table 2.1 Optimum pH of precipitation for some common divalent and trivalent ions [1]

Cation	pH ([0.01] M)	pH ([0.0001] M)	pH (hydroxide re-dissolves)
Mn^{2+}	8.5	10.0	
Co^{2+}	7.5	9.5	
Fe^{2+}	7.5	6.5	
Ni^{2+}	7.0	8.0	
Zn^{2+}	6.5	8.5	14.0
Cu^{2+}	5.0	9.0	
Cr^{3+}	5.0	9.0	12.5
Al^{3+}	3.9	10.0	9.0-12.0

Subsequent to the co-precipitation reaction, thermal treatment is typically employed in order to increase product yield and/or the crystallinity of the product [4]. There are three methods of co-preciptation that have been employed in the synthesis of LDHs, viz., titration, precipitation at low supersaturation and precipitation at high supersaturation [1].

Titration method

The titration method involves the sequential addition of alkali to the reaction vessel containing the various precursors, yielding a gradual precipitation curve. From the precipitation curve, the optimum precipitation range is determined. However, due to a sequential precipitation of ions it is not possible to obtain pure LDHs. This method was first used by Feitknecht where LDHs were prepared by titration of dilute solutions of Mg^{2+} and Al^{3+} with a dilute sodium hydroxide solution up to a pH of 10. The resulting flocculated precipitate was placed in a dialysis bag and immersed in water at 333 K for one month. During this time, sodium and chlorine ions were removed and carbon dioxide was provided from the atmosphere. The precipitate was then crystallized [1].

Co-precipitation at low supersaturation

Precipitation at low supersaturation is achieved by the slow addition of a mixed solution of divalent (M^{II}) and trivalent (M^{III}) metal salts into a reaction vessel containing an aqueous solution of the desired interlayer anion. During the addition of the mixed metal salt solution, an alkali solution is added simultaneously to maintain a constant pH within the reaction solution. According to Evans and Slade [4], the anion that is to be incorporated into the LDH should have a high affinity for the LDH interlayer and should be in excess, otherwise counter-anions of the metal salts may be incorporated by competing for vacancies in the interlayers. Thus, metal chloride and metal nitrate salts are preferred due to the low selectivity that LDHs afford towards these anions. Low supersaturation gives rise to precipitates which are highly crystalline. In addition to a high degree of crystallininty, a large number of particles are obtained and are usually small in size [1].

Co-precipitation at high supersaturation

Precipitation at high supersaturation is achieved by the addition of a mixed metal salt solution containing divalent and trivalent metal ions to an alkali solution of the desired interlayer anion [4]. This method usually gives rise to particles with a lower degree of crystallinity due to the high number of crystallization nuclei. Also, when using this method, it has been observed that high levels of impurites such as $M(OH)_2$ or $M(OH)_3$ phases and LDHs with undesired M^{II}/M^{III} ratios are obtained [4].

2.1.1.2 Hydrothermal techniques

Hydrothermal preparation methods have been employed in order to control the particle size and distribution when soluble magnesium and aluminium salts were used together with alkali solutions to prepare Mg-Al-carbonate LDHs and to transform amorphous precipitates into crystalline LDHs [1, 4]. There are two routes to hydrothermal treatment. In the first case, materials are treated at temperatures more than 373 K in a pressured autoclave. Here, the LDHs may be synthesized from precursors such as MgO and Al_2O_3 or from mixtures obtained from the decomposition of the nitrate forms of these precursors [1, 78, 97]. More specifically, the precursors are placed in an autoclave set at

temperatures above 596 K and pressures between 10-130 MPa for a fixed time period. In the other case, LDHs are synthesized at low temperatures and undergo a process of aging. Aging involves refluxing the precipitate at a set temperature for 18 hours.

2.1.1.3 Ion exchange

This technique involves the exchange of the interlayer anions with anionic guest molecules, i.e., molecules one wishes to introduce into the LDH structure in order to produce the desired LDH-guest molecule compound as shown in the figure below.

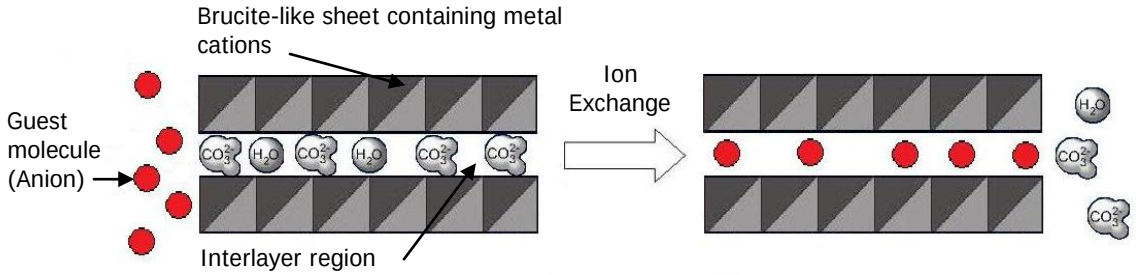

Figure 2.1 Figure depicting ion exchange (Adapted from [15]).

Ion exchange may occur in one of two ways, the first involves an anionic precursor containing weak anions such as NO_3^-, Cl^- and ClO_4^-, which exhibit weak electrostatic interactions with the brucite-like sheets. The introduction of a guest molecule into the reaction vessel would favour the release of the weak interacting anions and allow the incorporation of guest anions within the LDH interlayer regions. The second method involves anion precursors such as carboxylates, carbonates and terephthalate which are susceptible to acidic attack. Synthesis of LDHs using ion exchange methods have been carried out by a number of researchers [6, 21, 31, 44, 72, 77, 84]. Drezdzon [77] synthesized Mg-Al-OH-tetraphthalate dianion (TA) using traditional co-precipitation methods. This compound was added to a solution containing a desired anion, $Mo_7O_{24}^{6-}$, provided by $Na_2MoO_4.2H_2O$ followed by slow addition of 4 N HNO_3 to the mixture in order to partially digest the HT-like-TA. The digestion together with vigorous stirring at room temperature allowed for exchange of TA for the molybdate ion $Mo_7O_{24}^{6-}$. Suzuki et al. [44] synthesized a variety of LDH minerals of the formula Mg-AI-X where X = NO_3^- , CI^-, SO_4^{2-}, or CrO_4^{2-}. These materials were intercalated with $Co(CN)_6^{3-}$ by an anion

exchange method to produce Mg-Al-CN HTs. According to He et al. [15], there are several factors which determine the extent of ion exchange. These include:

The affinity for the incoming guest anion

The exchange ability of incoming guest anions increases with increasing negative charge and decreasing ionic radii. For inorganic anions the following trend is observed:

divalent anions, $CO_3^{2-} > HPO_4^{2-} > SO_4^{2-}$

monovalent anions,$OH^- > F^- > Cl^- > Br^- > NO_3^- > I^-$.

Nitrate ions are considered to have one of the weakest affinities for the LDH layers, hence its frequent use in the preparation of HT and LDH compounds.

The medium in which the exchange occurs

The medium in which the ion exchange reaction occurs can expand the interlayer favouring ion exchange [15]. An aqueous medium favours the exchange by inorganic anions, whilst an organic medium favours the exchange by organic ions.

The pH

A low pH value favours the release of the original anion as the conjugate acid and the incorporation of a less basic anion from the solution. However, the pH should not be below 4, as the basic LDH layers will begin to dissociate [15].

The chemical composition of the LDH brucite-like layers

The interlayer spacing of the LDH may be contracted or expanded depending on the interlayer anion. A number of interlayer spacing values have been reported, in which some anions and their respective values are shown overleaf in Table 2.2 [1].

Table 2.2 Interlayer spacing values of some common interlayer anions [1]

Anion	Interlayer spacing (Å)
$(ClO_4)^-$	9.20
$(SO_4)^{2-}$	8.58
$(NO_3)^-$	8.79
I^-	8.16
Br^-	7.95
Cl^-	7.86
F^-	7.66
$(CO_3)^{2-}$	7.65
OH^-	7.55

According to Meyn et al. [100], the interlayer arrangement of organic anions depends strongly on the area available to them. Studies were carried out on the available area and the degree in which alkyl chain compounds positioned themselves within the LDH interlayers. It was found that a small available area resulted in the alkyl chain compounds positioning themselves by pointing away from the interlayer surface to form monolayer films of high regularity. In the case of secondary alkane-sulphonate compounds, a similar observation was made with the formation of bilayer films within the interlayers. Crepaldi et al. [101] utilized an unconventional ion exchange method in which they relied on the interaction of cationic and anionic surfactants. The LDHs were synthesized containing an intercalated anionic surfactant, e.g., dodecylsulphate or dodecylbenzenesulphonate. Thereafter, a cationic surfactant, e.g., N-cetyl-N,N,N-trimethylammonium bromide is added together with a solution containing the desired anion that is to be incorporated into the LDH interlayer. The strong interaction between cationic and anionic surfactant favours the release of the anionic surfactant into solution and binds to the cationic surfactant. The vacancies left in the LDH from the released anionic surfactant is filled by the desired interlayer anion.

2.1.2 Preparation of HTs and LDHs

The HTs and LDHs were prepared using the co-precipitation technique at low supersaturation. In a typical experimental preparation, calculated amounts of nitrate precursors of magnesium, $Mg(NO_3)_2.6H_2O$ *(Saar Chem, Krugersdorp, R. S. A.)* and aluminium, $Al(NO_3)_2.9H_2O$ *(Reidel-De Haën AG Seelze-Hanover)* were dissolved in 200 ml of double distilled water. The metal salt solution was added dropwise to a solution of sodium carbonate *(Merck Chemicals, Gauteng, R.S.A.)* with vigorous stirring. Sodium hydroxide (1 M) was added intermittently to maintain a pH of 11. A white gelatinous precipitate was obtained after the complete addition of the metal solution. The suspension was placed in a round bottom flask and heated under reflux at 80 ^oC for 18 hours. The precipitate was then filtered and washed thoroughly with distilled water until the filtrate reached a neutral pH. The precipitate was dried in an oven for 12 hours at 110 ^oC. Other materials were prepared using a similar method. Relevant calculations and the calculated amounts of precursors can be found in the appendix (Table A1). The prepared HTs and LDHs samples were named according to Table 2.3.

Table 2.3 Prepared HT and LDH samples with corresponding abbreviation

Compound	Stoichiometry (x)	Abbreviation
Mg-Al HT	0.25	MgAl.25
	0.30	MgAl.30
	0.33	MgAl.33
Zn-Al LDH	0.11	ZnAl.11
	0.14	ZnAl.14
	0.16	ZnAl.16
Zn-Fe LDH	0.25	ZnFe.25
	0.30	ZnFe.30
	0.33	ZnFe.33
Mg-Fe LDH	0.55	MgFe.55
	0.58	MgFe.58
	0.62	MgFe.62

2.1.3 Characterization of HTs and LDHs

In the present study, Inductively coupled plasma-optical emission spectroscopy (ICP-OES), X-ray diffraction (XRD), Fourier transform infrared spectroscopy (FTIR), Raman spectroscopy, Transmission electron microscopy (TEM), Scanning electron microscopy (SEM) and scanning electron microscopy-energy dispersive X-ray spectroscopy (SEM-EDX) were utilized in the characterization of all HT and LDH samples.

2.1.3.1 Inductively coupled plasma-optical emission spectroscopy (ICP-OES)

Inductively coupled plasma-optical emission spectroscopy (ICP-OES) is classified as optical atomic emission spectroscopy. In atomic emission spectroscopy, atoms of a sample are excited by an external energy source, supplied by plasma, in the form of heat or electrical energy. Once subjected to a form of external energy, molecules are promoted to higher electronic states termed as an excited state. The excited atoms last for a few nanoseconds in this state and quickly return to the ground state, simultaneously releasing their gained energy in the form of photons of visible or ultraviolet radiation. A spectrometer is often incorporated into the ICP-OES instrument and hence the characteristic wavelength of released visible or ultraviolet radiation is isolated, transduced (photomultiplied) and computed into a signal characteristic of that specific element. The typical source of heat energy used in ICP-OES is an argon torch which consists of three concentric quartz tubes through which argon gas tangentially flows. Magnetic induction results in a magnetic field which causes the ions and electrons to flow in a closed annular path. The resistance of the ions and electrons to this flow of charge causes ohmic heating of the plasma. Temperatures of 8000 K are reached within the argon plasma core. After heating of the plasma, the sample is introduced in the form of a fine mist or aerosol. The conversion of the liquid sample into a suspension of finely divided liquid or solid particles in a gas (aerosol) is carried out with the use of a nebulizer. Thus, the excitation of the sample atoms is achieved and a characteristic emission signal is detected [101].

The analysis of each sample was carried out on a *Perkin Elmer Optima 5300 DV Spectrometer*. Calibration of the instrument was conducted using a mixed metal standard solution. A mixed metal stock solution was prepared using nitrate metal precursors of magnesium, aluminum, zinc and iron. Zinc and iron salts were purchased from *Merck*

Chemicals, Gauteng, R.S.A. The stock solution was made up in 1 litre of double distilled water to a final concentration of 100 ppm. A series of mixed metal standard solutions with concentrations of 0.25 ppm, 0.5 ppm, 1.5 ppm, 3 ppm and 5 ppm were prepared using the stock solution for calibration. For sample analysis, approximately 0.01 g of finely ground, dry product was placed in a 25 ml volumetric flask. To this flask, approximately 10 ml of 0.1 M HNO_3 was added in order to digest the powdered product. The flasks were heated in some cases to aid digestion. The digested solution was made up to the mark with double distilled water. Approximately 10 ml of this solution was then transferred to a 15 ml centrifuge tube and set aside for ICP-OES analysis. Each standard and sample solution was done in triplicate.

2.1.3.2 Powder X-ray diffraction (XRD)

Powder XRD remains an essential tool in the characterization of many materials. Although single crystal analysis remains the technique of choice for the analysis of crystal structures, the size and quality of single crystals of a material often prevent this analysis from being utilized. XRD proves to be an excellent alternative in the above case, in which the crystal structure, lattice parameters, micro and macro strain, crystalline and amorphous phases as well as crystal sizes can be elucidated [103]. XRD was first described by Bragg and Bragg in 1913, where they developed a relationship to explain the reflection of X-ray beams on the faces of crystals at certain angles of incidence. This relationship is expressed as the Bragg equation, $n\lambda=2d\sin\theta$, where n is an integer, λ is the wavelength of the incident X-ray beam, d is the distance between atomic layers in a crystal and θ is the diffraction angle. The reflection of the incident beam of X-rays by the atomic planes of a crystal is due to the constructive interference of the X-rays entering the material which results in the observed diffraction pattern (Figure 2.2). This phenomenon is termed X-ray diffraction.

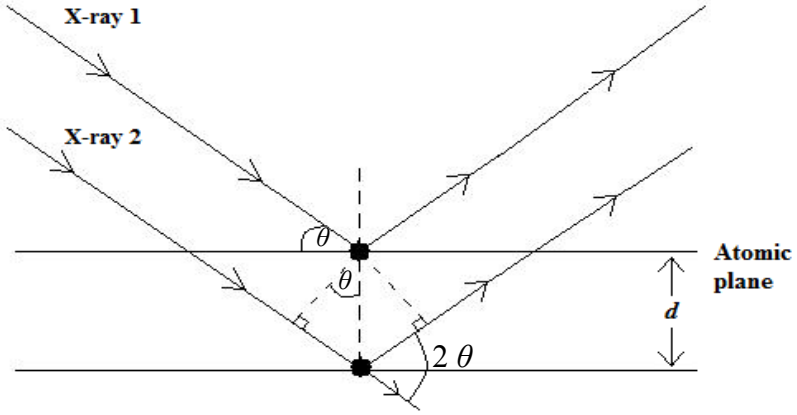

Figure 2.2 Diffraction of incident X-rays according to Bragg (Redrawn and adapted from [103]).

The Bragg analysis depicts X-rays like visible light being reflected by the surface of a mirror, with X-rays being reflected at lattice planes. Lattice planes are crystallographic planes, portrayed by Miller indices (hkl). Parallel planes also present in the crystal structure, have identical indices and are separated by the distance $d_{(hkl)}$. X-rays penetrate through the material resulting in reflections due to crystal faces as well as additional reflections due to numerous other parallel planes. Thus, as the diffracted X-rays travel in the same direction with respect to the atomic plane, superposition of the scattered rays occurs. Bragg's equation is only satisfied for constructive interference of X-rays 1 and 2. In reality, the X-rays are not reflected and are infact scattered by electrons bound to the atoms as indicated as solid black circles on Figure 2.2. Both the Bragg equation and expressions of the Bragg equation can be derived from calculations based upon the geometry of the scattering taking place at the position of atoms in consecutive planes as well as the energy associated with the X-rays [103]. Analysis software accompanying XRD instrumentation computes diffraction patterns in relation to intensity of the diffracted X-rays.

All samples were analyzed directly on a *Bruker D8 Advance XRD* (CuKα radiation), using *Bruker* analysis software. A mass of approximately 0.5 g was used in each case. The scan-speed was set to 0.5 seconds for all samples, with a total analysis time of 40-50 minutes per sample.

2.1.3.3 Fourier transform infrared (FTIR) spectroscopy

The basic modes of motion namely, translation, vibration and rotation of a molecule indicate the ways in which a molecule may store energy. The transitions between different energy states can be observed spectroscopically [104]. Fourier transform infrared (FTIR) spectroscopy is based upon the measurement of the wavelength and intensity of the absorption of infrared light by a molecule. Due to this absorption, molecules within a sample may undergo vibrational, bending or rotational modes. Thus, each type of chemical bond exhibits a specific IR absorption band at a characteristic wavelength. Spectroscopic methods such as ultra-violet (UV) or visible spectroscopy rely on the use of a monochromator or filter to isolate the desired wavelength band so that only the band of interest is detected and measured [102]. FTIR spectroscopy is unique in that it contains an interferometer in place of a monochromator that produces interference patterns which contain the infrared spectral data. In addition, FTIR detectors are able to detect all wavelengths continuously. Thus, based upon the characteristic modes of motion of bonds at characteristic wavelengths, FTIR is able to compute the radiant power produced as a function of wavelength, as the source signal is modulated by the interferometer to produce an absorption spectrum of the sample. Most interferometers compute absorption spectra of molecules in relation to interference patterns from a background (solvent, ambient water and CO_2) spectrum [102]. In this study, attenuated total reflection-fourier transform infrared spectroscopy (ATR-FTIR) was employed. ATR-FTIR operates by measuring the changes that occur in a totally internally reflected infrared beam when the beam comes in contact with a sample. An infrared is first passed through a dense crystal with a high refractive index. The beam undergoes internal reflectance within the crystal and creates an evanescent wave that extends beyond the surface of the crystal and penetrates the sample. Where the sample absorbs energy, the evanescent wave will be attenuated or altered. The attenuated or altered energy from each evanescent wave re-enters into the infrared beam which exits the opposite end of the crystal and enters into a detector. The ATR-FTIR system then produces an infrared spectrum [105].

All samples were analyzed directly on a *Perkin Elmer Spectrum Universal ATR 100 FT-IR Spectrometer*. Prior to sample analysis, the crystal area was cleaned and the background collected. Approximately 0.4 g of each product (dry, finely ground) was

placed over the surface of the crystal and the pressure arm locked into place. The spectra were then collected.

2.1.3.4 Raman spectroscopy

Raman spectroscopy is based upon the observations of a change in frequency when light is scattered by molecules [106]. The scattering of light was first observed in 1982 by Raman and Kishnan. Since then, the measurement of light scattering has been referred to Raman spectroscopy [107]. The change of frequency of light which can be related to an equivalent energy change. This change in frequency is the result of the difference between incident light with a frequency, v_0 and scattered light with a frequency v_s. Raman spectroscopy is often used in conjunction with FTIR spectroscopy since both these techniques give a better analysis of the vibrational structure of a molecule.

For analysis, each sample was placed in a clear shell vial (*VWR International*, West Chester, PA), approximately 5 mm from the base of the vial. The shell vial was then sealed and gently tapped at an angle, causing the sample to lie at an angle sloping upwards. The shell vial was then placed into the sample holder on a *DeltaNu Advantage 532* Raman Spectrometer. Raman analysis was performed on each sample and spectra captured using *NuSpec*^{TM} software and spectra analysis using *GRAMS/AI* spectroscopy software suite 9.00 R2.

2.1.3.5 Transmission electron microscopy (TEM)

Electron microscopy is routinely used in the characterization of various compounds, including HTs and LDHs. Electron microscopy utilizes electrons in a very similar way to that of light in microscopes and makes use of a source of illumination (electron gun), condenser lenses (electromagnetic lenses) and an imaging system. In order to produce high resolution images of the sample, a focused beam of electrons produced by an electron gun is directed onto the sample. The electron gun consists of a tungsten filament surrounded by a cone-shaped Wehnelt cylinder shield except for the tip which is exposed to an anode. Upon heating of the tungsten filament to high temperatures (>2700^{o}C), electrons are ejected from the tip of tungsten filament, forming a diverging beam. Thereafter, a high negative voltage is applied to the Wehnelt cylinder creating a large

potential difference between this highly negatively charged Wehnelt cylinder and the positive anode. This potential difference forces the attraction of the electrons from the tip of the tungsten filament towards the anode. With the presence of electromagnetic lenses, this stream of electrons is focused into a beam, which is further directed towards the sample.

Transmission electron microscopy (TEM) is utilized in order to study the interior and exterior surfaces of a sample. Samples are thinly sliced or placed directly into a copper grid sample holder and subjected to the striking of the sample by the electron beam resulting in the formation of an image. Images formed in TEM result in changes in direction of electrons penetrating the sample creating a contrasting image, i.e., electrons that strike a denser area of the sample will not pass through the sample and will thus be scattered, depicted as a darker area on the TEM image. However, electrons that strike a translucent or less dense area of the sample will pass through the sample, thus appearing as a light area on the image. Thus images of varying brightness are formed.

All samples were viewed using a *JEOL 1010 Megaview 3 Soft Imaging TEM System*, employing *iTEM* software. For TEM analysis, approximately 0.001 g of finely ground, dry HT or LDH material was suspended in approximately 5 ml of absolute alcohol *(Merck Chemicals, Gauteng, R.S.A.)* and sonicated for 20 minutes. Thereafter, 1 µl of each sample was placed onto a copper grid. The copper grids were then air-dried and viewed.

2.1.3.6 Scanning electron microscopy (SEM) and scanning electron microscopy-energy dispersive X-ray spectrometry (SEM-EDX)

Scanning electron microscopy (SEM) is utilized in order to study the surface areas of the sample and makes use of a focused spot of electrons (probe) that scans the surface of the sample. The formation of an image using SEM relates to the interactions that these electrons have on the surface of the sample. These electrons will deflect at different angles according to the angles forming at the surface of the actual sample. These deflected electrons which are referred to as secondary electrons are analyzed by a detector. The electrons that strike the surface of the sample which are deflected straight into the detector will appear as bright areas on the SEM image and those electrons that

deflect away from the detector will therefore appear as dark areas of the image. Thus, the SEM image formed is a representation of the different deflection patterns of electrons.

In addition to obtaining images, the chemical or elemental analysis of the surface of a sample can be determined. This type of spectroscopy is related to the fact that every element has a distinct atomic structure and X-ray pattern when irradiated with charged particles such as electrons. Atoms at rest contain ground state electrons which upon irradiation with charged electrons results in the promotion of some of these ground state electrons to higher energy level orbitals. Therefore, an orbital vacancy now exists resulting in electrons from higher energy level orbitals to fill these vacancies. This change in energy levels of electrons causes an emittance of characteristic X-rays. The number of X-rays, as well as the energy associated with these X-rays is detected by an energy dispersive spectrometer (EDS/X). The exact elemental surface composition of that sample is obtained.

For sample analysis, a strip of double sided carbon tape (*Nisshin EM, CO. LTD*) was placed onto a SEM stud. Thereafter, each sample was placed onto this stud and carbon coated using a *JEOL JEE-4C Vacuum Evaporator*. The stud was placed in a *LEO 1450 SEM*, using *SmartSEM* software version 5.03.05. For SEM-EDX, a *JEOL JSM-6100 Scanning Microscope* was used equipped with *Bruker Espirit* software, version 1.9.

2.2 Results and discussion

2.2.1 HT and LDH physical properties

The synthesized HTs (Mg-Al) were white powders and LDHs, Zn-Al, Zn-Fe and Mg-Fe were white, cream-orange and orange-rust powders respectively. All the samples were pliable but not elastic and smooth in texture. Varying degrees of solubilities were observed for all the samples (Appendix, Table A2, Figures A2 and A3).

2.2.2 Characterization

2.2.2.1 ICP-OES

The results of elemental analysis are shown in Table 2.4. The measured M^{II}:M^{III} values were similar to that of the calculated values for Mg-Al HTs and Zn-Fe LDHs only.

Table 2.4 ICP-OES data for Mg-Al HTs, Zn-Al, Zn-Fe and Mg-Fe LDHs

Compound	Stoichiometry (x)	M^{II} : M^{III}	
		Calculated	Measured
Mg-Al HT	0.25	3 :1	2.9 :1
	0.30	2.3 :1	2.2 :1
	0.33	2 :1	1.9 :1
Zn-Al LDH	0.11	3 :1	8.0 :1
	0.14	2.3 :1	6.3 : 1
	0.16	2:1	5.4 :1
Zn-Fe LDH	0.25	3 :1	3.1 :1
	0.30	2.3 :1	2.3 :1
	0.33	2 :1	2.1 :1
Mg-Fe LDH	0.55	3 :1	0.8 :1
	0.58	2.3 :1	0.7 :1
	0.62	2 :1	0.6 :1

The Mg:Fe values showed a range of 0.6-0.8:1 (Mg:Fe). There is a fairly equal distribution of both cations within the brucite-like layers and this could be attributed to the fact that these cations have very similar ionic radii (Mg^{2+}= 0.65 Å, Fe^{3+}= 0.64 Å). Hence, it is possible that the two cations would position themselves fairly evenly throughout metal positions within the brucite-like layer. Zn-Al LDH samples, on the other hand, showed a greater amount of Zn with *x* being lower than calculated. According to Rojas Delgado et al. [108], Zn-Al LDHs can be obtained with M^{II}:M^{III} values ranging from 1-5 (i.e. 1:1-5:1 M^{II}:M^{III}). They observe that higher values are due to electrostatic repulsion between trivalent metals. However, too high M^{II}:M^{III} values result in a collapse of the interlayer region as they are less populated by charge compensation anions. Here, an increase in the value of *x* is due to greater substitution of Zn^{2+} by Al^{3+} within the brucite-like layer, which increases the electrostatic attraction between the brucite-like layers and the interlayer anions. This attraction results in a compression of the LDH structure. In addition, the increasing amounts of Al^{3+} within the brucite-layer results in greater repulsion of neighbouring Al^{3+} ions [41]. The samples prepared in this study showed greater amounts of zinc. This could be the result of the repulsion of trivalent Al, leaving vacant positions within the brucite-like layer for Zn^{2+} to fill.

2.2.2.2 Powder XRD

In general, XRD diffractograms for hydrotalcite show sharp, symmetric and intense lines at low 2θ values and less intense and generally asymmetric lines at higher 2θ values [37]. The sharp intense lines are indicative of a well ordered crystalline material. Also distinctive of an XRD diffractogram for hydrotalcite is a doublet peak at a 2θ value of 60^{o} which is indicative of an ordered layered material. Figure 2.3 displays the diffractograms of the synthesized HT materials with different *x* values. All HT samples showed d-spacing values and peaks (★) at corresponding 2θ values almost identical to that indicated JCPDS file No. 14-191. Both Zn-Fe and Mg-Fe XRD patterns exhibit a prominent, heightened non-smooth baseline and hence the minor peaks are not that apparent. Most of the LDH samples exhibited XRD patterns similar to that of hydrotalcite with the exception of XRD patterns for Zn-Fe LDH samples. In addition, all Mg-Al, Zn-

Al and Mg-Fe XRD data and patterns are consistent with literature findings [1, 6, 38, 111]. The d-spacing values for all HT and LDH samples are shown in the appendix (Table A3).

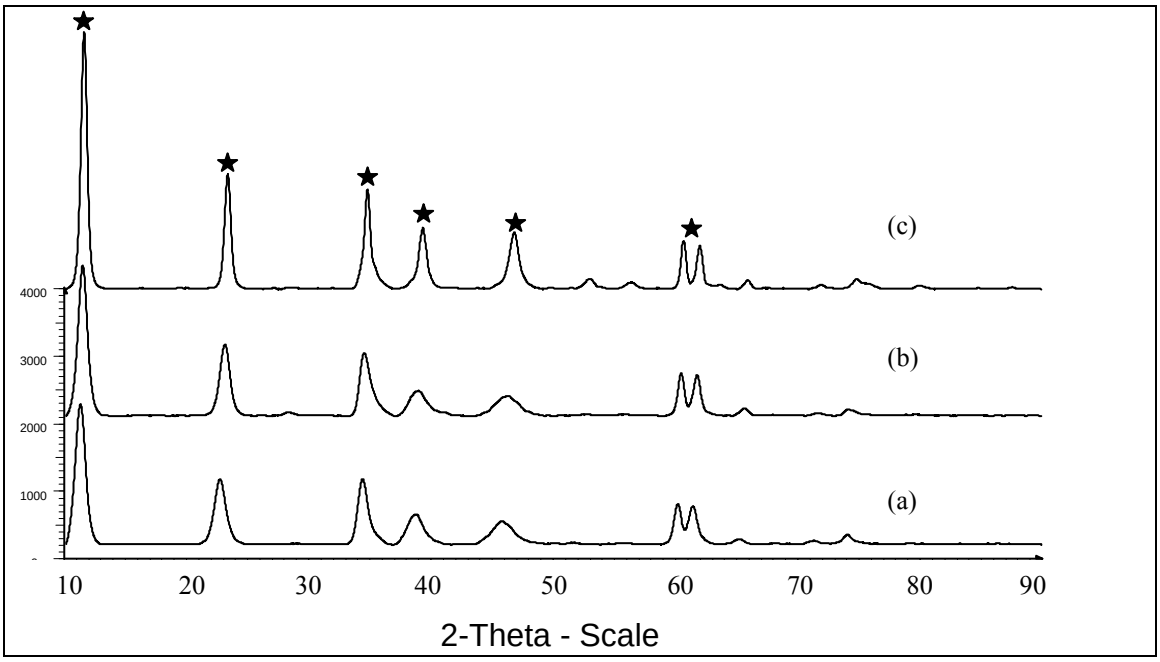

Figure 2.3 Powder X-ray diffraction patterns of (a) MgAl.26, (b) MgAl.31, and (c) MgAl.34.

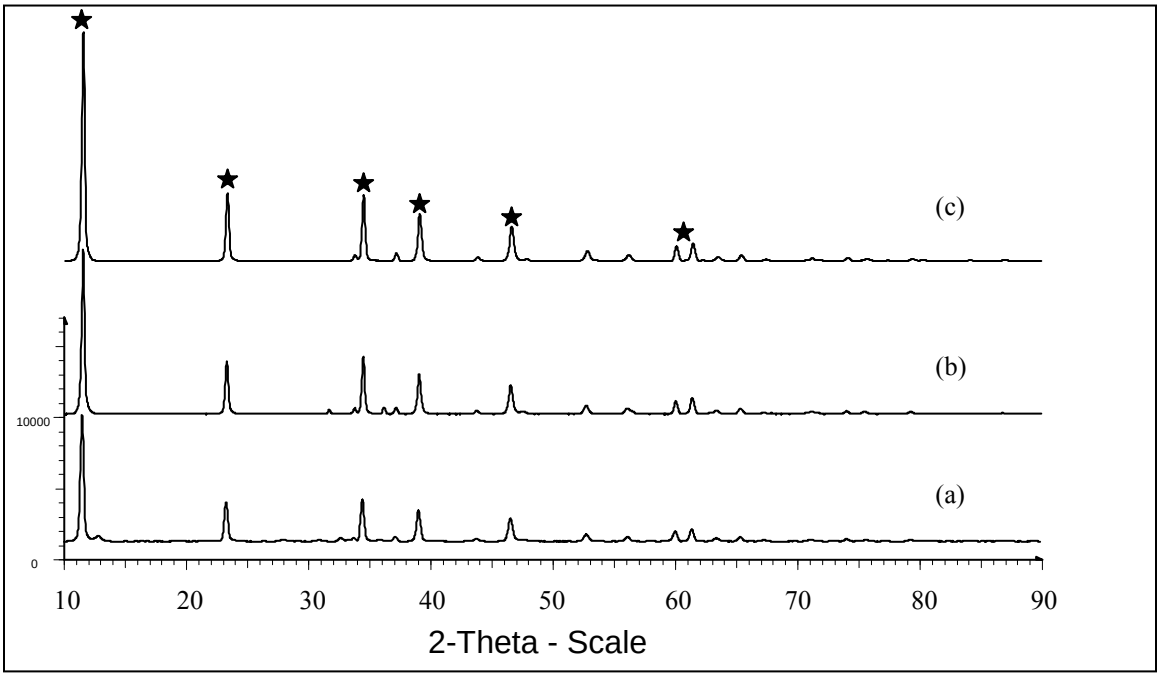

Figure 2.4 Powder X-ray diffraction patterns of (a) ZnAl.11, (b) ZnAl.14, and (c) ZnAl.16.

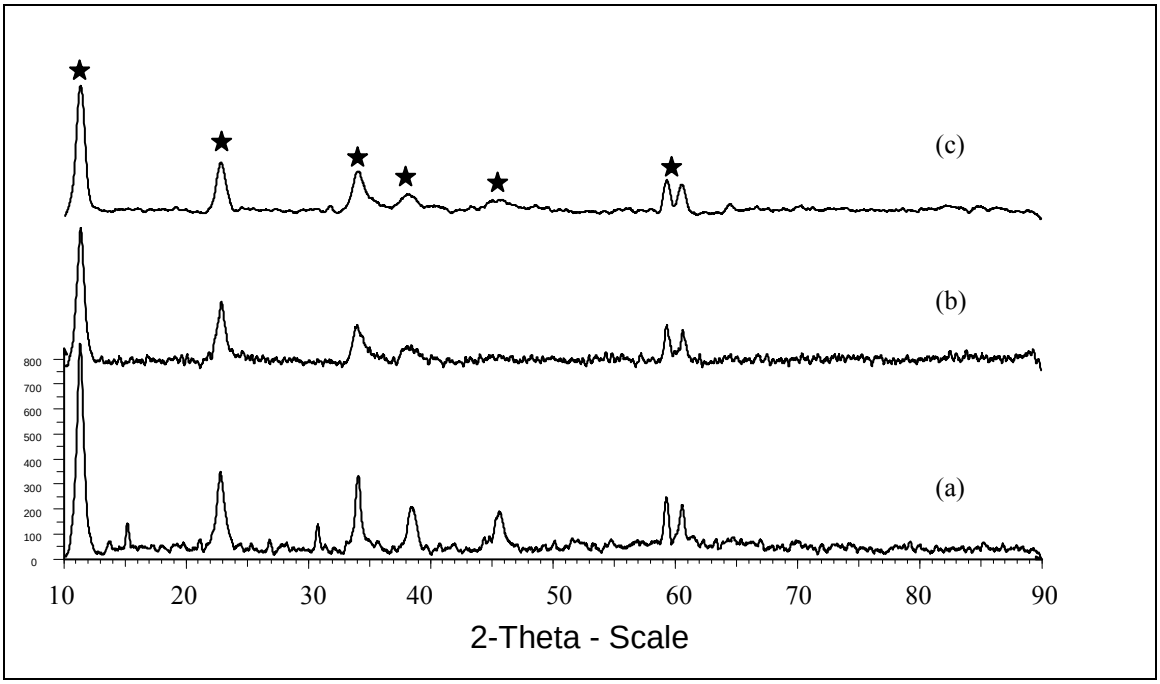

Figure 2.5 Powder X-ray diffraction patterns of (a) MgFe.55, (b) MgFe.58, and (c) MgFe.62.

The XRD patterns for synthesized Zn-Fe LDHs (Figure 2.6) exhibit a very similar pattern to the experimental results of Zhang et al. [109]. Also, the XRD pattern suggests that the materials are slightly amorphous with extremely small crystallites. Crystallite sizes for Zn-Al LDHs are the largest of the prepared samples, followed by Mg-Fe LDHs and Mg-Al LDHs. There appears to be no specific trend in relation to increasing or decreasing values of x. The crystallite sizes of each HT and LDH synthesized in this study are shown in Table 2.5.

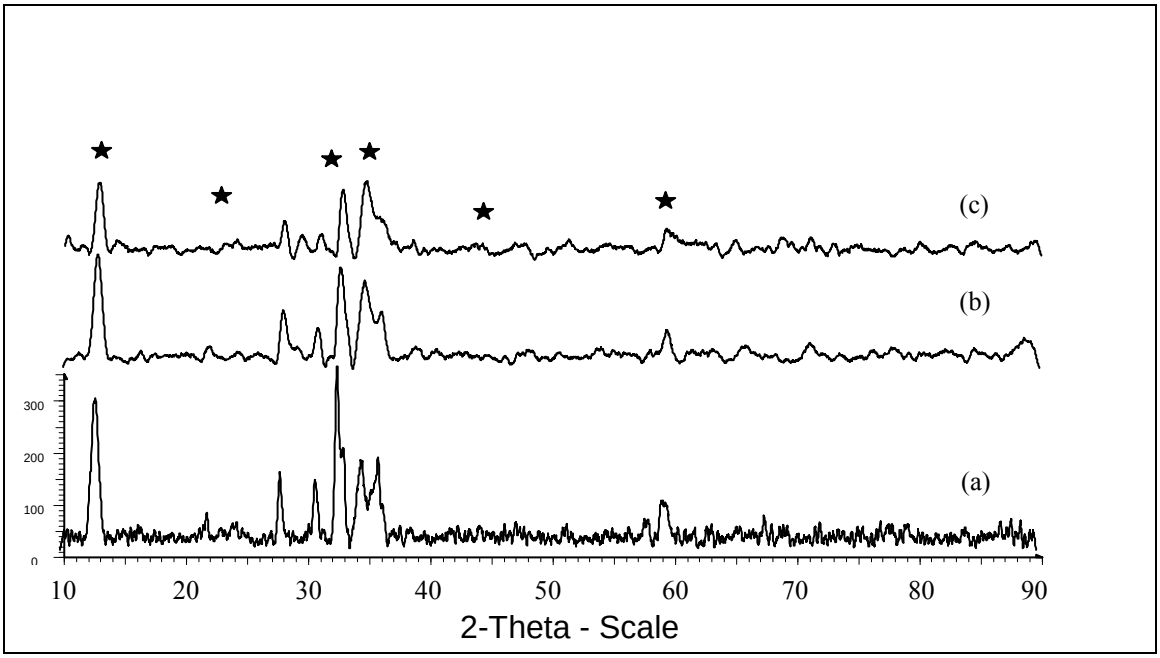

Figure 2.6 Powder X-ray diffraction patterns of (a) ZnFe.24, (b) ZnFe.30, and (c) ZnFe.32.

2.5 Crystallite sizes of HTs and LDHs.

Compound	Stoichiometry (x)	Crystallite size[a] / nm
MgAl.25	0.25	1.64
MgAl.30	0.30	1.65
MgAl.33	0.33	2.51
ZnAl.11	0.11	5.38
ZnAl.14	0.14	5.16
ZnAl.16	0.16	5.27
ZnFe.25	0.25	1.69
ZnFe.30	0.30	1.66
ZnFe.33	0.33	1.66
MgFe.55	0.55	2.19
MgFe.58	0.58	1.78
MgFe.62	0.62	2.04

[a]Calculated using the Scherrer's equation, FWHM values shown in Table A4, Appendix.

2.2.2.3 FTIR.

The FTIR spectrum of Mg-Al HT samples are shown in Figure 2.7. The spectra for all Mg-Al HT samples exhibit a band at around 410-415 cm^{-1} and 440-456 cm^{-1} which can be ascribed to Mg-OH translation modes [35, 110]. A single band observed in the 380-390 cm^{-1} region is due to O-Al-O vibrational modes. Bands found at 640-650 cm^{-1} and around 730 cm^{-1} are due to Mg-Al-O stretching modes [33].

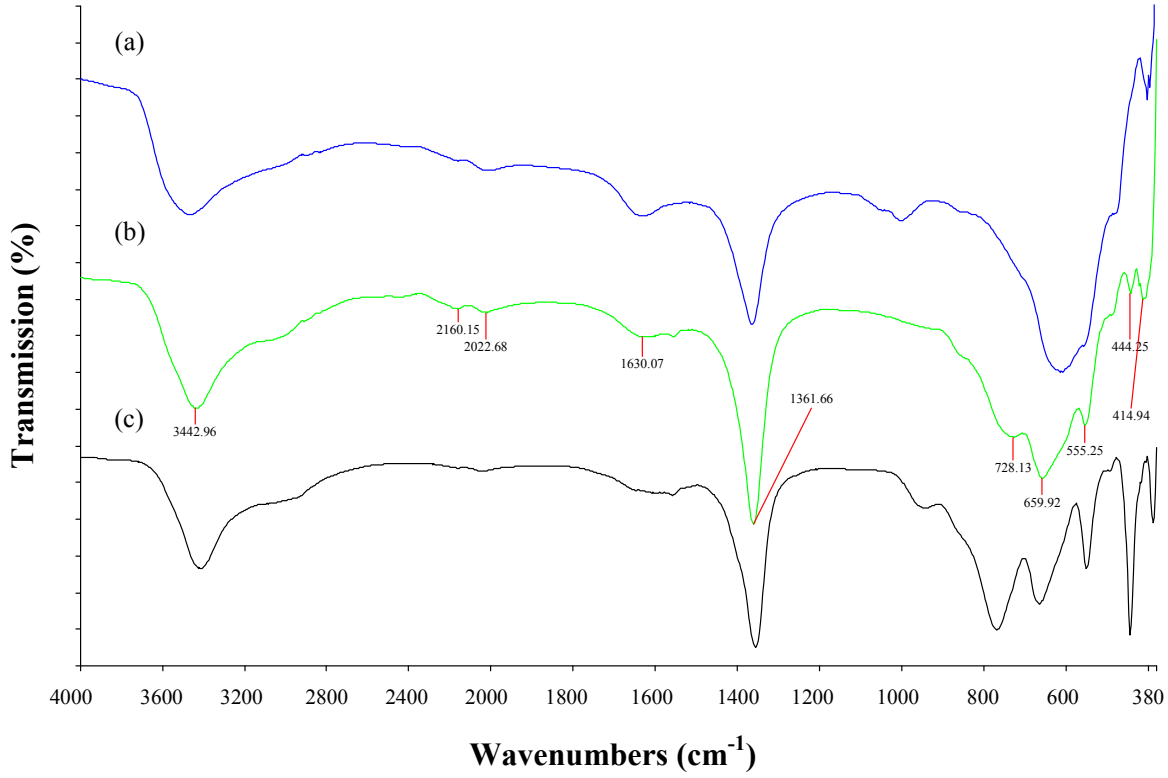

Figure 2.7 FTIR patterns of (a) MgAl.26, (b) MgAl.31, and (c) MgAl.34.

According to Panda et al. [110], the bands at 550 and 660 cm^{-1} have a tendency to overlap and hence the appearance as a broader single peak (Figure 2.7(c)). In addition to Mg-Al-O modes at around 730 cm^{-1}, an overlap of the anti-symmetric v_4 vibration of CO_3^{2-} is also expected [110, 111]. A very weak broad band is observed at around 850 cm^{-1} (Figure 2.7, (a) and (c)) which is assigned vibrational modes v_2 of CO_3^{2-} [111]. For Figure 2.7(b), this band appears at 920 cm^{-1}. The weak band observed at 1002-1050 cm^{-1} is due to the v_1

mode of CO_3^{2-} [1]. The appearance of the v_1 mode of CO_3^{2-} is due to a lowering of symmetry of the anion and according to Miyata [6] this is due to the coordination of the carbonate anion within the interlayer. The carbonate anion can exist as a monodentate or bidentate complex [1, 42]. The strong band at around 1360 cm^{-1} is associated with anti-symmetric v_3 vibration of CO_3^{2-} [1, 110, 111]. The weak broad band at 1560-1630 cm^{-1} is due to the bending mode of interlayer water molecules. According to Xie et al. [112] the weak bands observed at 2020-2050 cm^{-1} can be ascribed to adsorbed CO_2. A broad band at about 3410-3460 cm^{-1} is due to the stretching of the O-H group of the interlayer water molecules [110], the twisting vibrations of physisorbed water, vibrations of hydroxyl groups within the brucite-like layer, characteristic valency vibrations of OH···OH, and/or characteristic stretching vibrations of metal-OH [35]. A weaker shoulder on this peak is observed at around 2900-3000 cm^{-1} which is ascribed as water-carbonate hydrogen bonding within the interlayer region, also describes as the bridging mode of water and carbonate [35, 110, 111]. As observed from the spectra the broad band at about 3410-3460 cm^{-1} shift towards lower frequencies from spectrum (a) to (c) in Figure 2.7. According to Panda et al. [110], upon increasing the Mg ion concentration, this band shifts towards higher frequencies which indicates a reduction in the covalency of the metal-O interaction. This is due to the electronegativity of the Mg ion being less than that of the Al ions which increases the mean metal-O distance, hence decreasing the hybridization of the oxygen atoms which polarizes the O-H.

The FTIR spectrum of Zn-Al LDH, Zn-Fe and Mg-Fe samples are displayed in Figure 2.8-2.10.

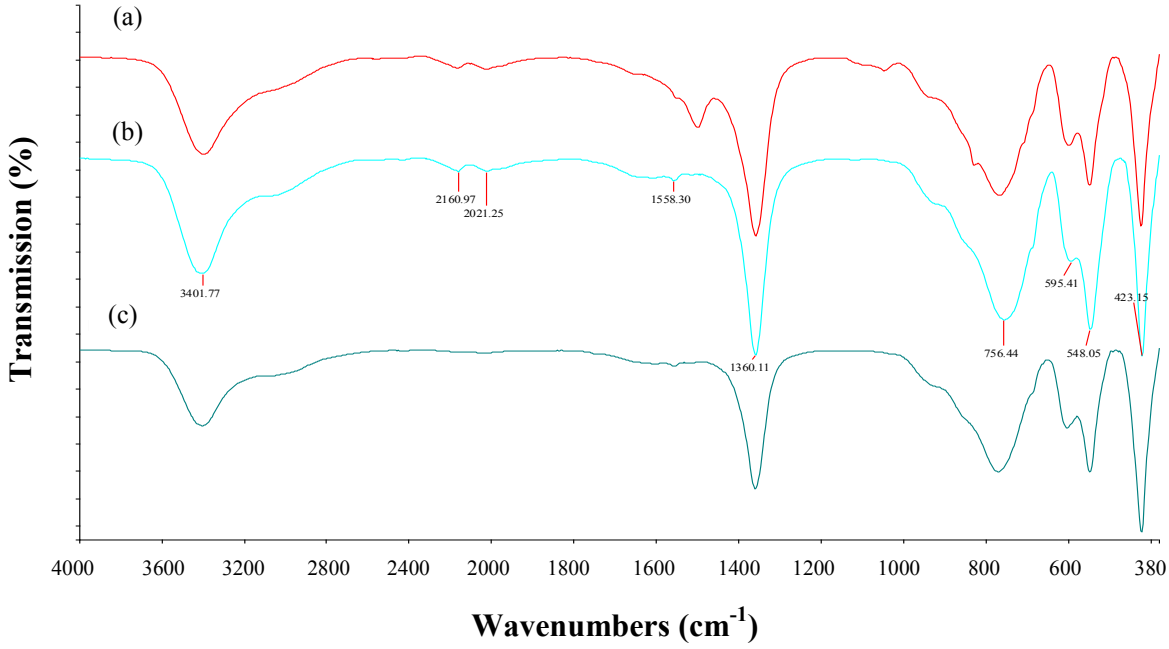

Figure 2.8 FTIR patterns of (a) ZnAl.11, (b) ZnAl.14, and (c) ZnAl.16.

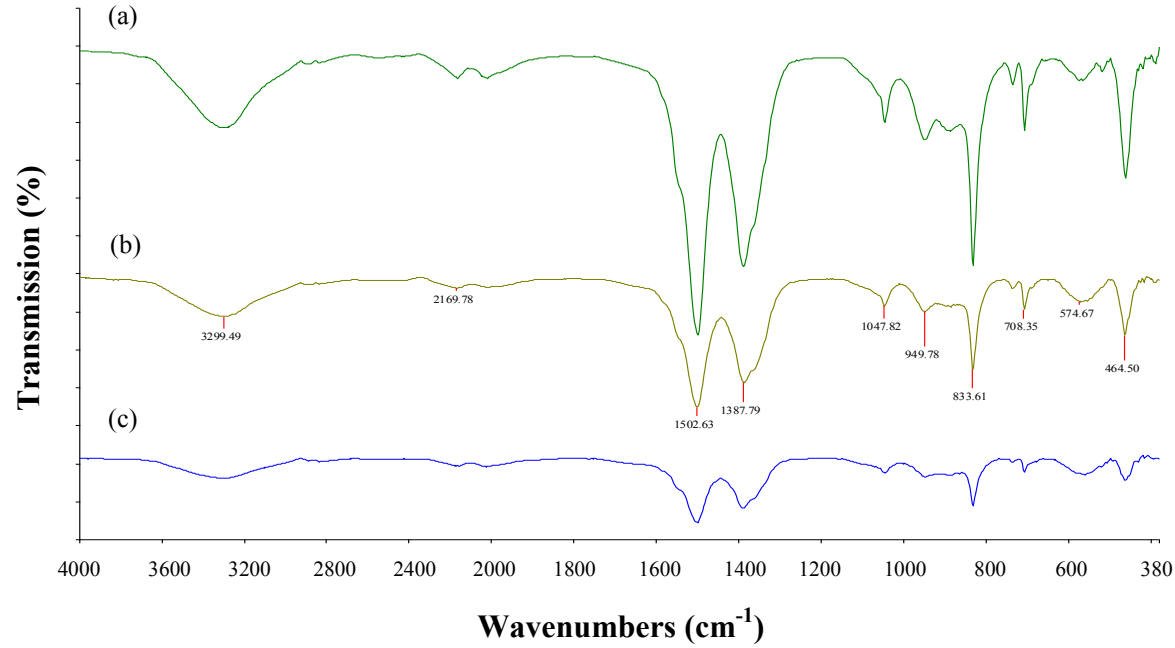

Figure 2.9 FTIR patterns of (a) ZnFe.24, (b) ZnFe.30, and (c) ZnFe.32.

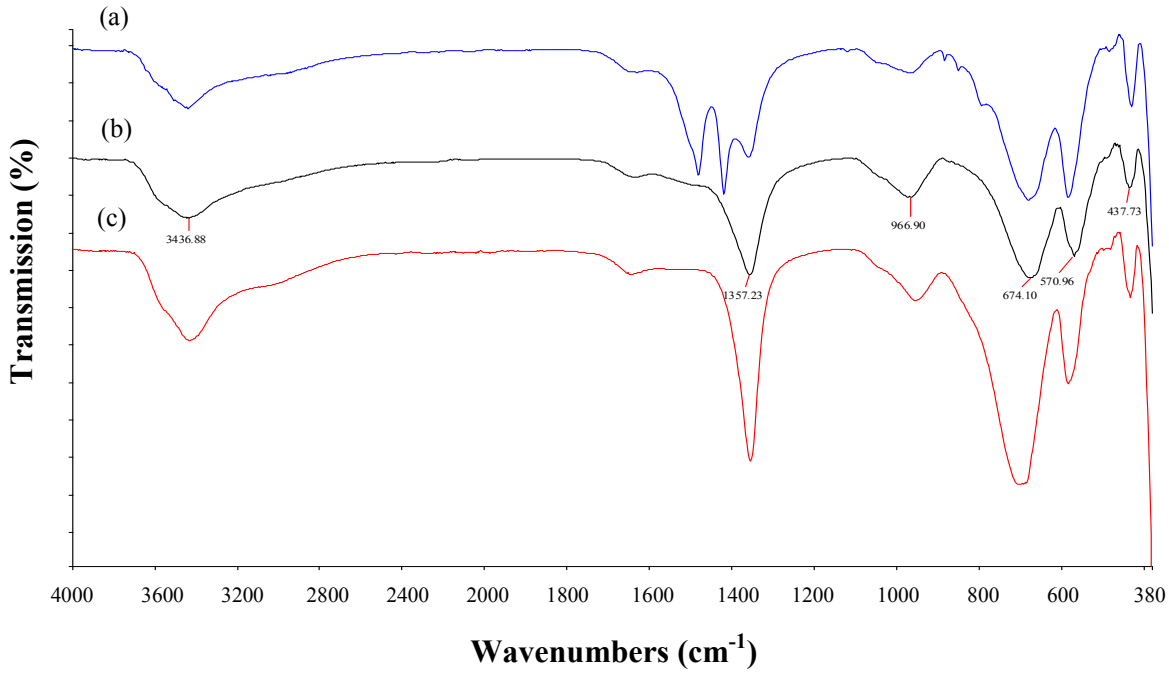

Figure 2.10 FTIR patterns of (a) MgFe.55, (b) MgFe.58, and (c) MgFe.62.

The spectra for all Zn-Al, Zn-Fe and Mg-Fe LDH samples exhibit similar patterns to that of Mg-Al HT samples. Bands below 800 cm^{-1} are assigned to metal-OH translation modes. The strong band at around 1360 cm^{-1} is associated with anti-symmetric v_3 vibration of CO_3^{2-}. This band is seen as a doublet in Figures 2.8(a), 2.9(a, b and c) and 2.10(a) at around 1500-1502 cm^{-1} and 1387-1389 cm^{-1} respectively. This doublet is attributed to a lowering of the symmetry of the carbonate (v_3 anti-symmetric vibration modes) as well as an indication of the disordered nature of the interlayer [1]. Perhaps the disordered nature of the interlayer may cause a destabilization in the layered structure. The weak bands observed at 2020-2050 cm^{-1} can be ascribed to adsorbed or trapped CO_2 within the interlayer region [113]. These bands are not evident in Figure 2.10. A broad band seen at 3401-3405 cm^{-1} is due to the stretching of the O-H groups which are hydrogen bonded to the interlayer water molecules [110, 111]. A weaker shoulder on this peak is observed at around 2900-3000 cm^{-1} which is ascribed as the bridging mode of water and carbonate [35, 110].

2.2.2.4 Raman spectroscopy.

Figure 2.11 displays the Raman spectra for MgAl.26 HT. The other spectra for Mg-Al HTs are shown in the appendix. The spectra for Mg-Al HT samples exhibit a strong broad bands at around 400-480 cm^{-1} which are associated with linkage oxygen bonds of brucite-like layer, metal-O-metal as well as metal-OH_2 coordinated water [110].

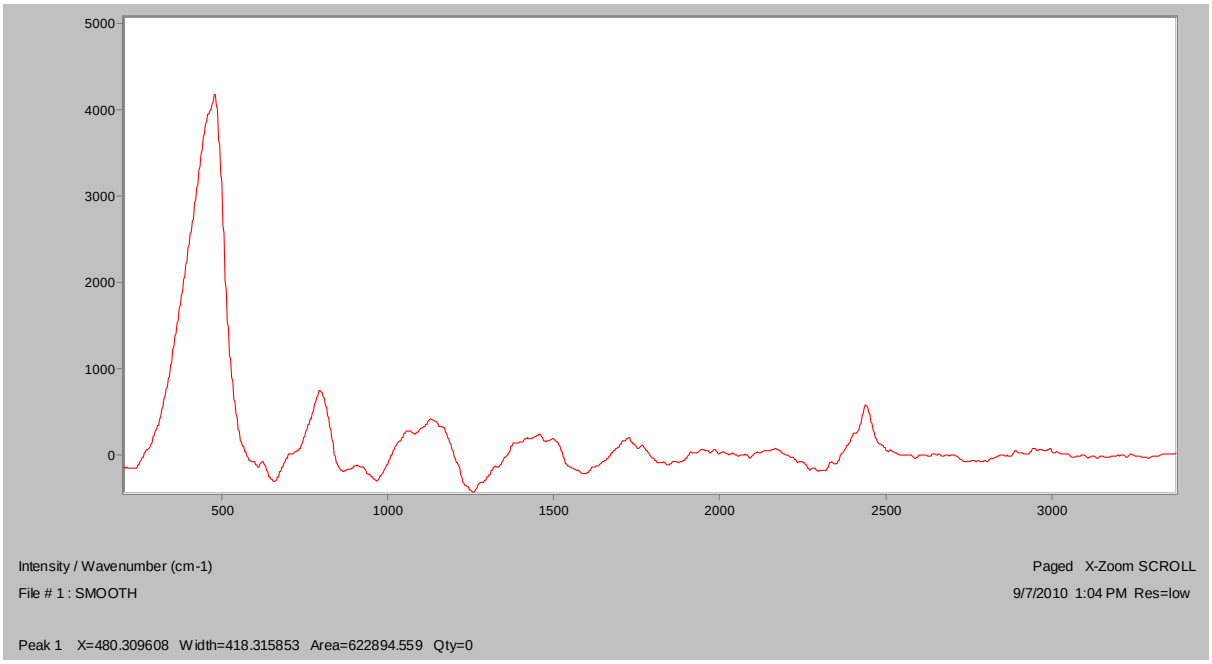

Figure 2.11 Raman spectrum of MgAl.26.

A weak band appears at 800-830 cm^{-1} is due to the v_1 vibrational mode of CO_3^{2-} interacting with the hydroxyl groups of the brucite-like layer. A weaker band at around 1050 cm^{-1} could be attributed to the v_1 vibrational mode of CO_3^{2-}. A slightly stronger band is observed in the 2400 cm^{-1} due to weak v_1 vibrational modes of adsorbed CO_2 interacting weakly with the interlayer region. For Mg-Al HT samples it appears that upon the increase of x, more Mg^{2+} is substituted by Al^{3+} which increases the electrostatic attraction between the brucite-like layer and interlayer anions [41]. This electrostatic compression of the LDH structure would thus result in stronger bonding of the adsorbed CO_2 and CO_3^{2-} anions and hence the intensity of the Raman bands thus increases from MgAl.26 to MgAl.34. With the increase in bonding, there appears to be a slight decrease

in the $d_{(003)}$-spacing value. In addition, the band assigned as the anti-symmetric v_3 vibration of CO_3^{2-} (1360 cm^{-1}) increases in the sharpness with an increase in the value of x. This further compliments stronger bonding between the adsorbed CO_2 and CO_3^{2-} anions. The Raman spectrum for MgAl.31 (Appendix, Figure A3) shows similar features to that of MgAl.26. Additional bands for MgAl.31 are observed between 1050-1060 cm^{-1} which may be assigned to the v_1 vibrational mode of CO_3^{2-}. Further bands for MgAl.34 are seen between 1490-1530 cm^{-1} and these are due to the bending of water and carbonate bridges. A peak at around 1700 cm^{-1} could be due to water deformation modes [111].

The Raman spectra for ZnAl.11, ZnFe.24 and MgFe.55 are shown in Figures 2.12-2.14. All other Raman spectra for Zn-Al, Zn-Fe and Mg-Fe LDHs are shown in the appendix. From Figures 2.12-2.14, it can be observed that all the materials exibit similar spectra to that of Mg-Al HTs. A strong band exists between 420-500 cm^{-1} which may be associated with linkage oxygen bonds of brucite-like layer, metal-O-metal as well as metal-OH_2 coordinated water.

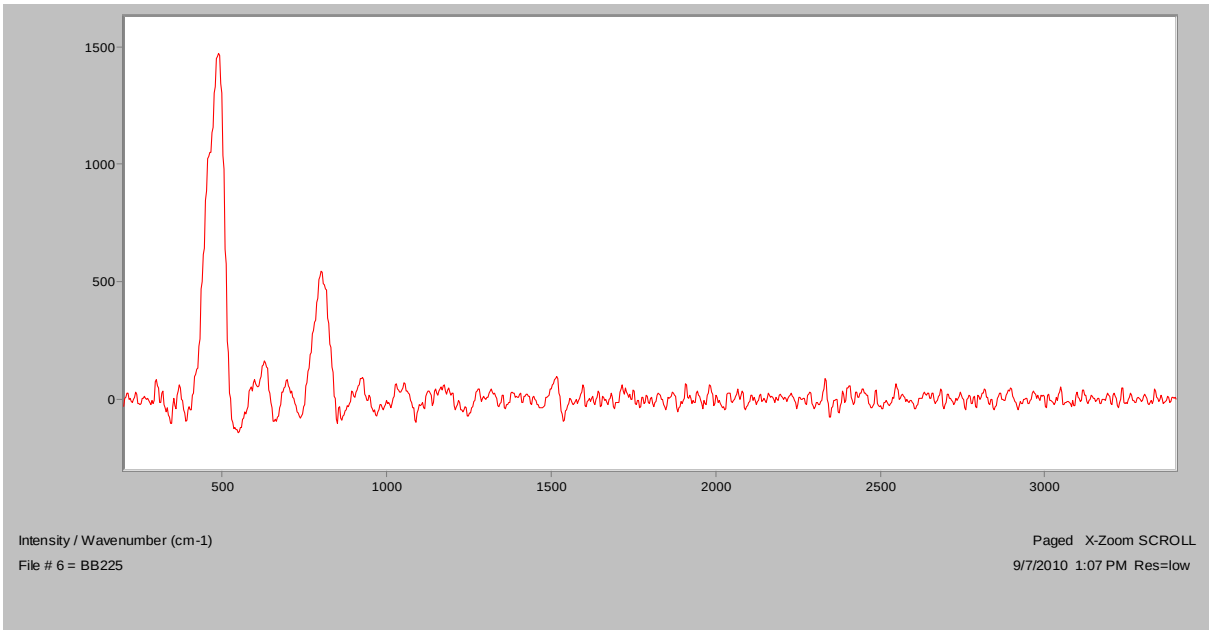

Figure 2.12 Raman spectrum of ZnAl.11.

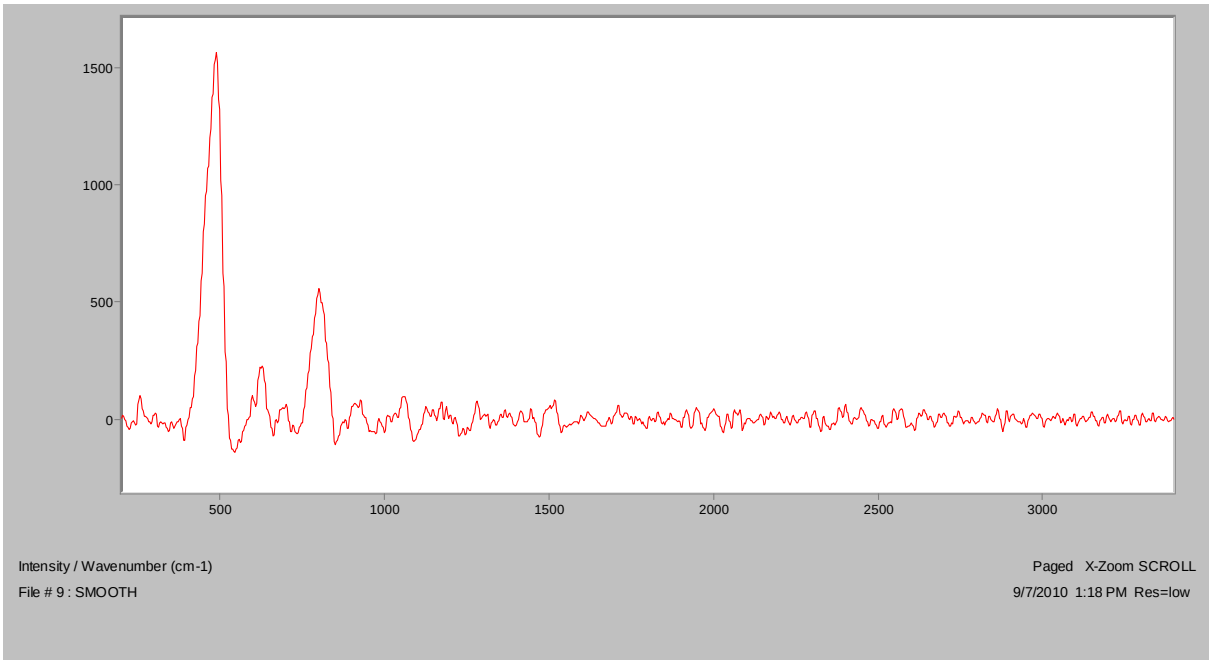

Figure 2.13 Raman spectrum of ZnFe.24.

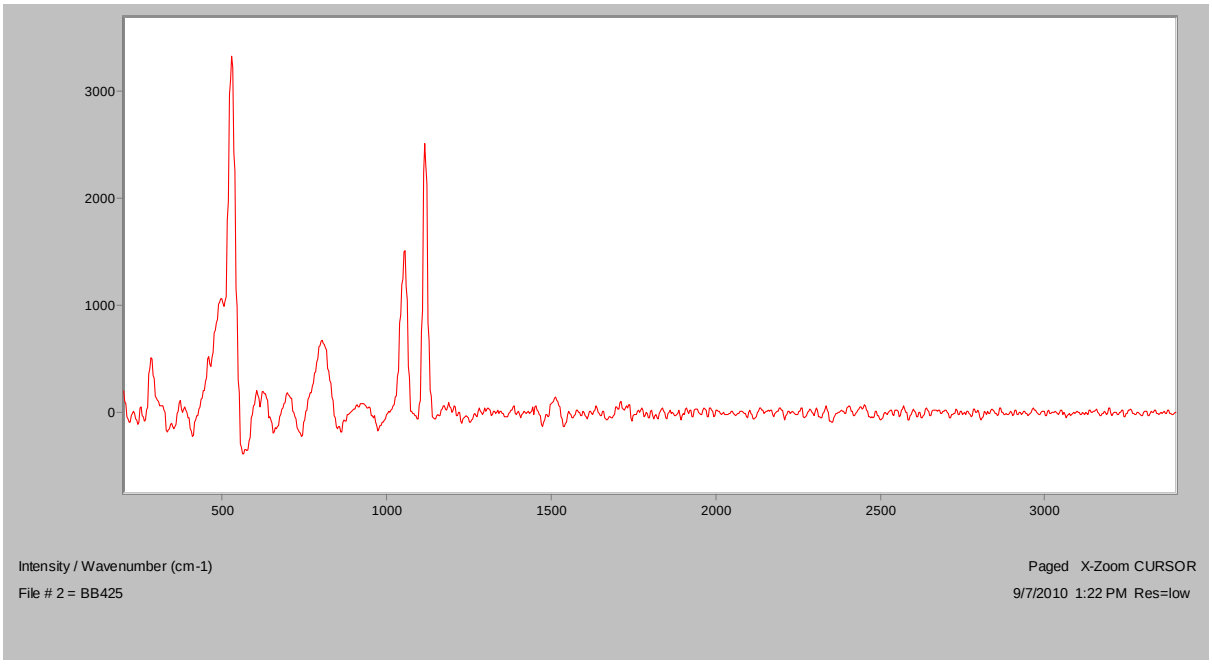

Figure 2.14 Raman spectrum of MgFe.55.

The band between 750-800 cm^{-1} is assigned to the v_1 vibrational modes of CO_3^{2-} interactions with hydroxyl groups from the brucite-like layer.

In some spectra (Figures A4, A6, and A9, Appendix) there is a strong band at band at 1050 cm^{-1} which is assigned as ν_1 vibrational modes of CO_3^{2-}. For MgFe.55 (Figure 2.14), two appear at 1050 cm^{-1} and 1110 cm^{-1}. The first band is due to symmetric stretching of CO_3^{2-} which is either bonded to external water molecules or the hydroxyl groups of the brucite-like external surface and the second band is due to CO_3^{2-} that is interlayer bound [114]. A band at 2400 cm^{-1} due to adsorbed CO_2 increases intensity for some samples (Figures A3, A4, A6, A9 and A10, Appendix). This increase in intensity results in a decrease in the $d_{(003)}$-spacing value. This band at 2400 cm^{-1} is not evident in the remaining samples.

2.2.2.5 TEM

Figure 2.15 shows the TEM images of all Mg-Al HT samples. The Mg-Al HT samples were noted to be fairly translucent in nature. The particle morphology ranged from round to hexagonal to irregular and was consistent with literature findings [25-28].

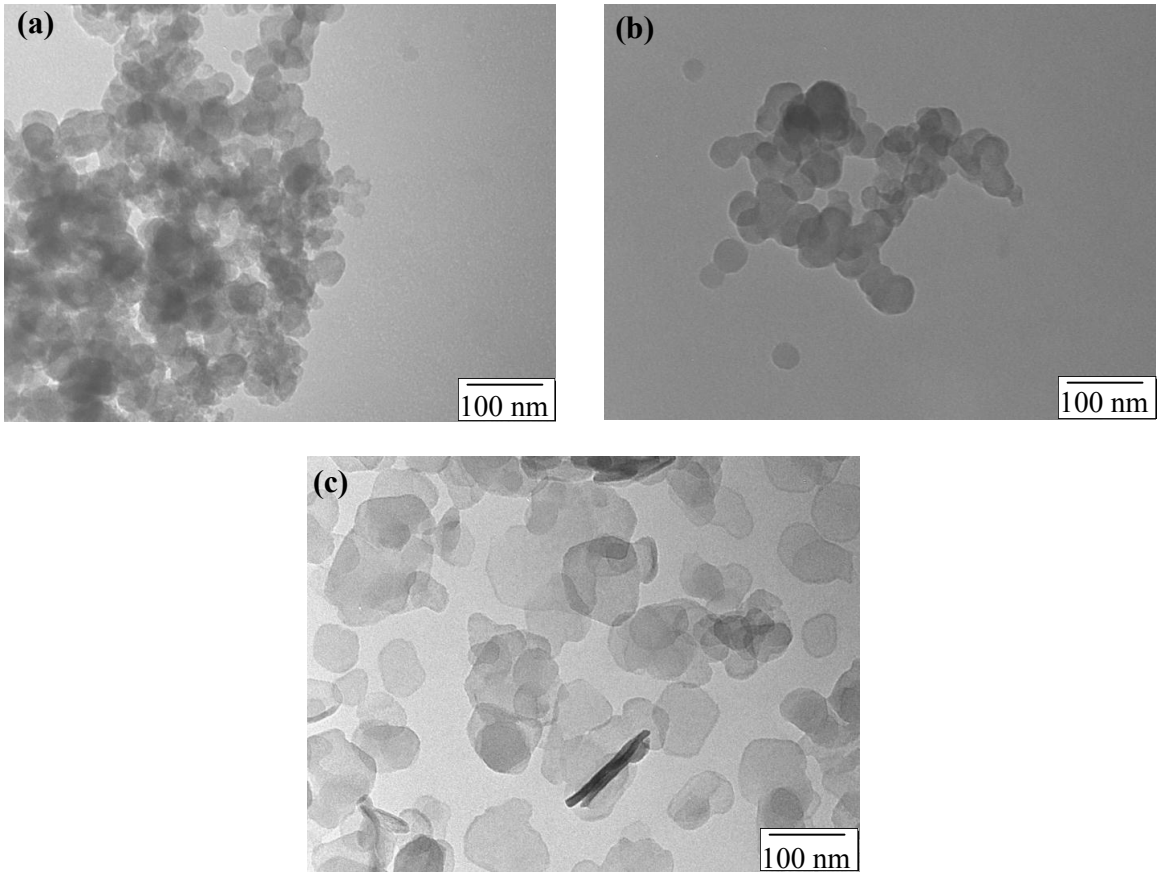

Figure 2.15 TEM images of (a) MgAl.26 (x200k), (b) MgAl.31 (x200k), and (c) MgAl.34 (x200k).

Short darker rod-like particles are seen overlapping one another and these are attributed to the LDHs residing in the side on position opposite to the direct plane of view. Using *iTem* software particle width and lateral size may be measured. The particle width of rod-like particles ranged from 5-15 nm. The particle lateral size range for Mg-Al HT samples was 50-250 nm with a mean size of 100 nm, SD ± 30 nm (n = 3).

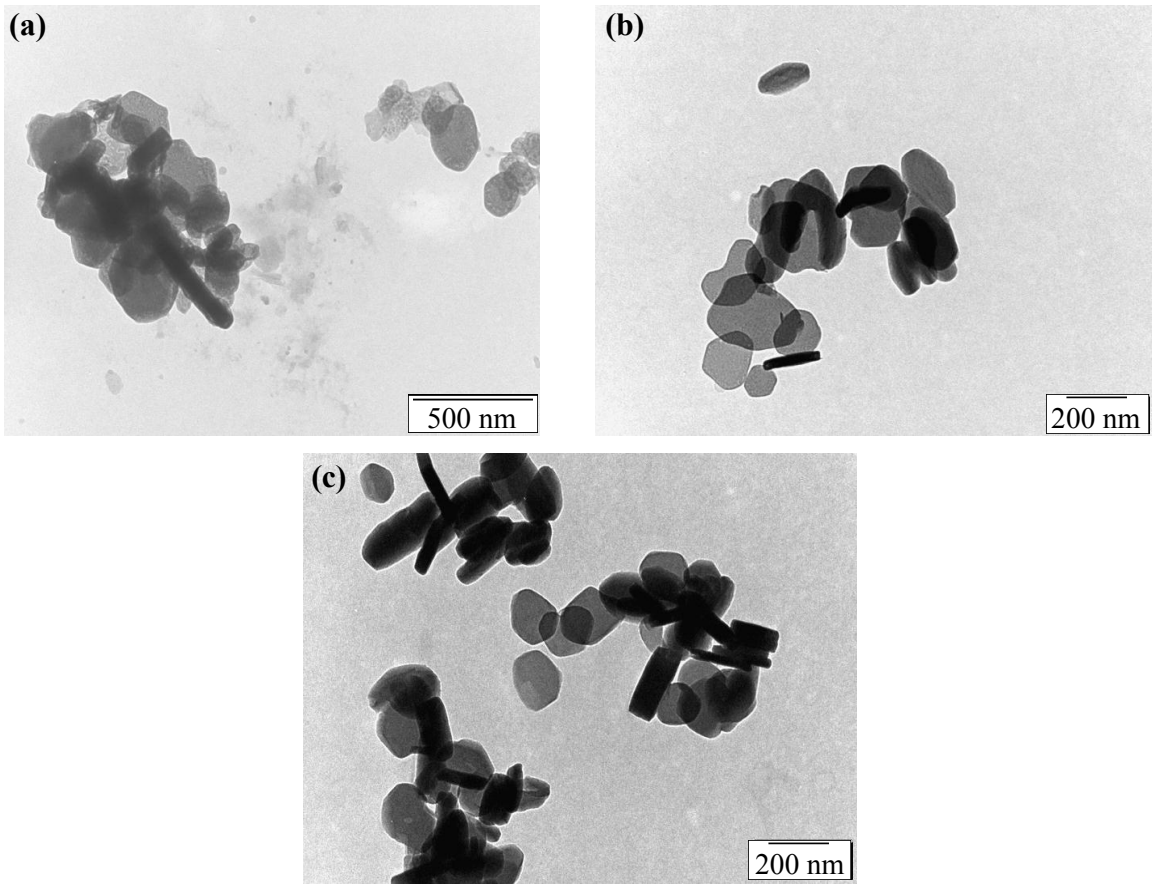

Figure 2.16 TEM images of (a) ZnAl.11 (x60k), (b) ZnAl.14 (x75k), and (c) ZnAl.16 (x75k).

The particle morphology of the Zn-Al LDH samples ranged from irregular to hexagonal with these particles appearing much denser than Mg-Al HT samples, although they appeared slightly translucent (Figure 2.16). The particles lying on their side were much wider than Mg-Al HT samples, with widths ranging from 50-70 nm. The particle size range was 80-320 nm with a mean size of 220 nm, SD ± 13 nm (n = 3).

Figure 2.17 shows the TEM images of all Mg-Fe LDH samples. The particle morphology ranged from round to irregular and resembled those of Mg-Al HT samples. The particles lying on their side had a width ranging from 5-15 nm. The particle size range was 20-400 nm with a mean size range of 100 nm, SD ± 23 nm (n = 3). These Mg-Fe LDH samples were also translucent in nature.

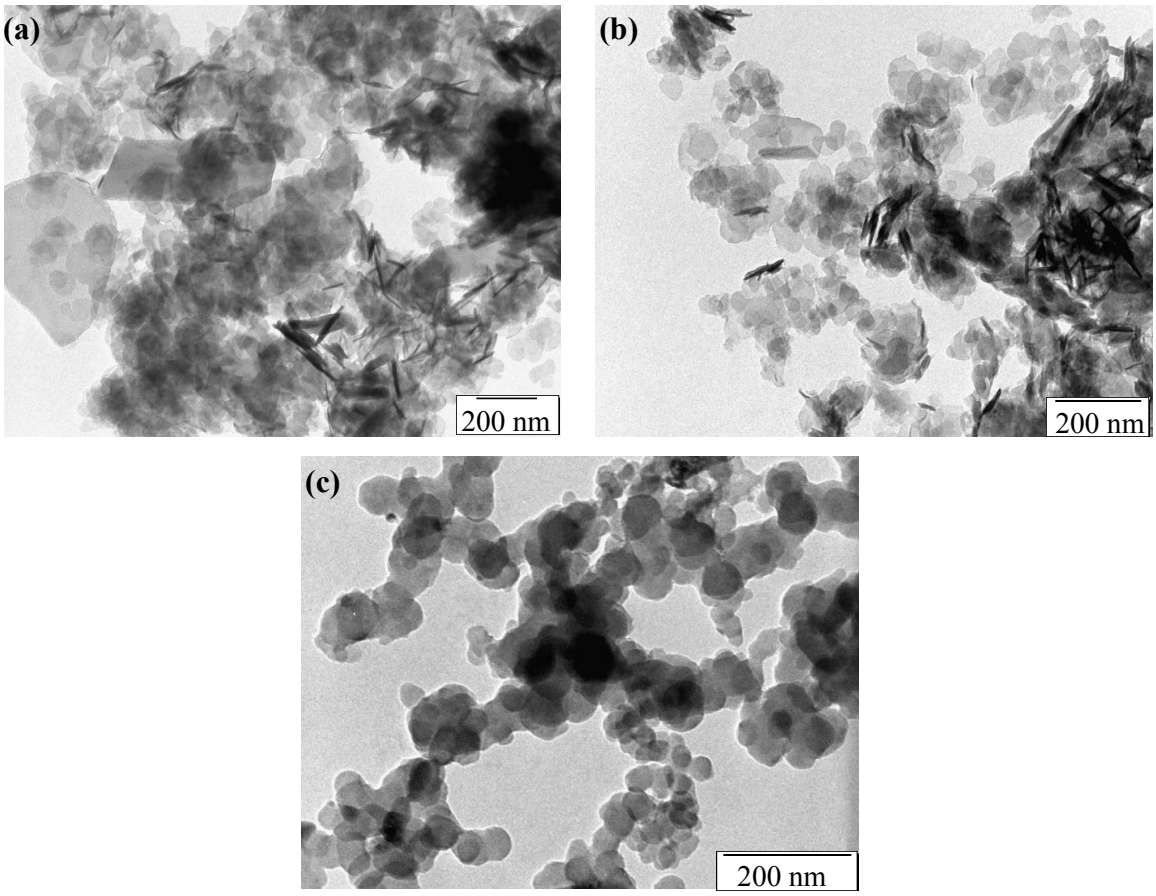

Figure 2.17 TEM images of (a) MgFe.55 (x100k), (b) MgFe.58 (x120k), and (c) MgFe.62 (x200k).

The particle morphology for Zn-Fe LDHs was quite different to that of all the other HT and LDH samples (Figure 2.18). From the images, two types of particles existed. The small dark circular particles with a size of 5 nm were in abundance. These particles aggregated to form larger clumps. The second type of particle was larger in size and irregular in shape. The size range of these larger particles was 50 nm-100 nm. Only the larger particles appeared translucent. The mean size for the larger particles was 100 nm, SD ± 21 nm (n = 3). Additional TEM images of all HT and LDHs are shown in the appendix.

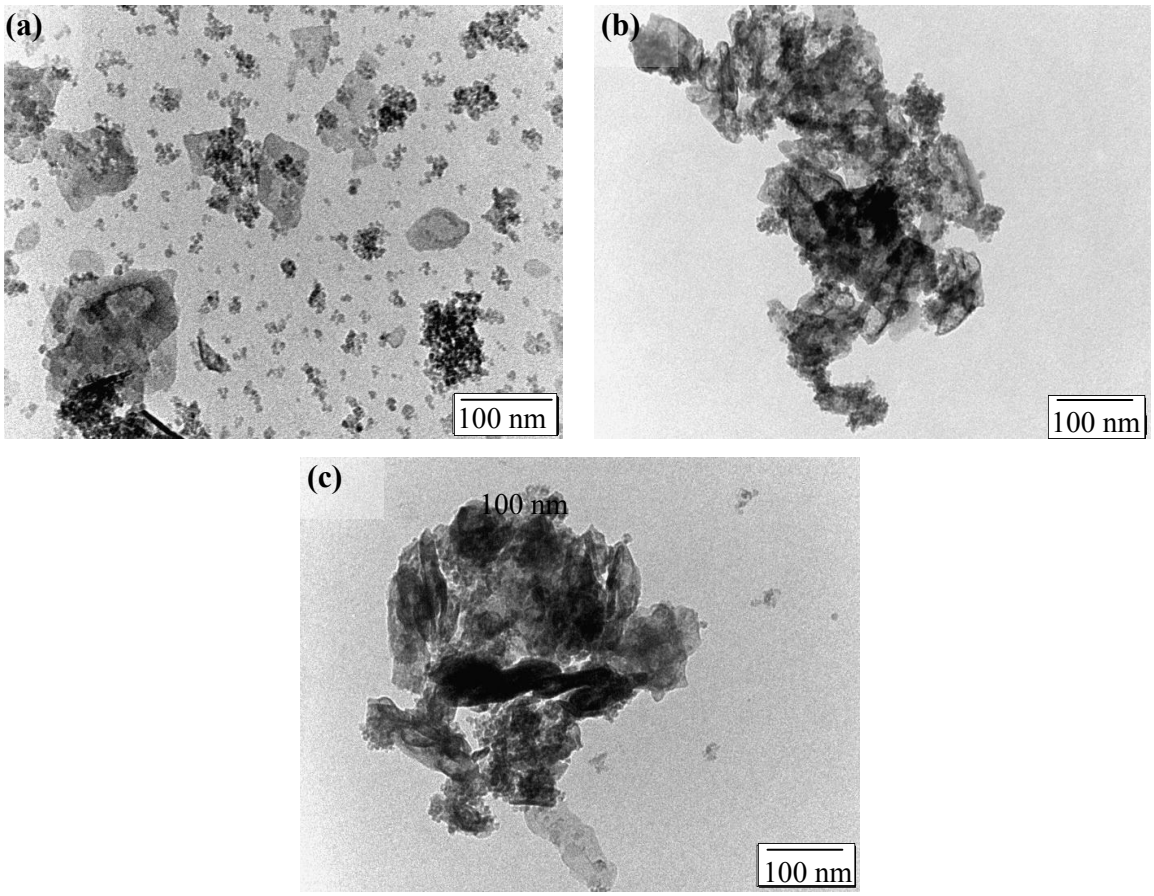

Figure 2.18 TEM images of (a) ZnFe.24 (x200k), (b) ZnFe.30 (x200k), and (c) ZnFe.32 (x200k).

2.2.2.6 SEM, SEM-EDX

The SEM images for all samples are shown in Figures 2.19-2.22. Magnesium-Al HTs, Zn-Al LDHs and Zn-Fe LDHs (excluding ZnFe.32, Figure 2.21 (c)) exhibit clusters of 3-dimensional irregular, hexagonal disk-shaped particles. The SEM images for the ZnFe.32 LDH sample, showed large 'globule-like' clusters which could be clusters of the circular particles. The SEM image of ZnAl.14 shows two unknown 'rod-like' structures with lengths of 2 μm, respectively. Mg-Fe LDH images (Figure 2.22) show large 'sheet-like' layered material. Irregular shaped smaller particles can also be seen. This layered 'sheet-like' appearance can also be seen under the 'globule-like' clusters for Zn-Fe LDHs

(Figure 2.21 (a) and (b)). This can be attributed to the irregular particles overlapping and forming larger clusters giving a layered 'sheet-like' appearance.

(a)

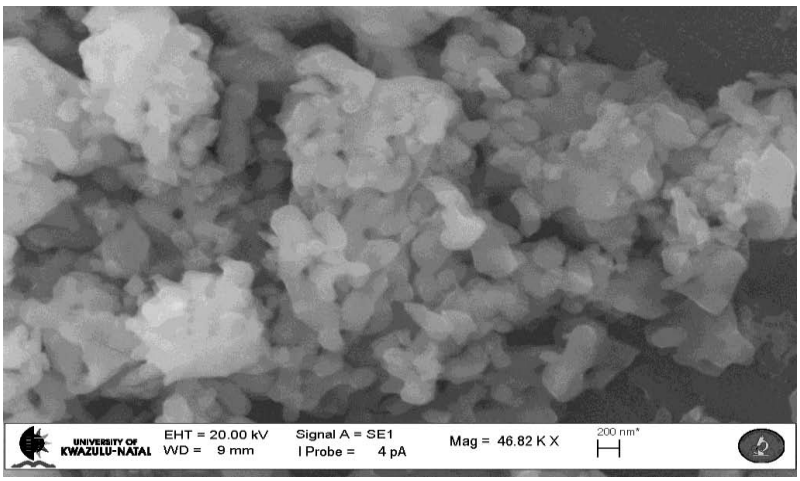

(b)

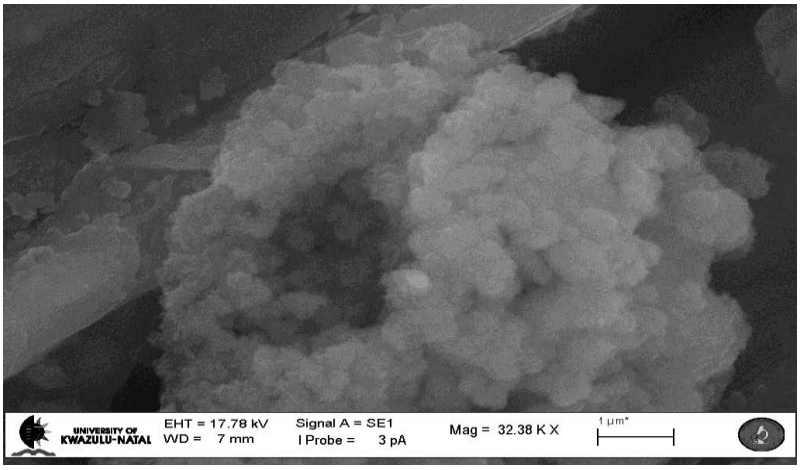

(c)

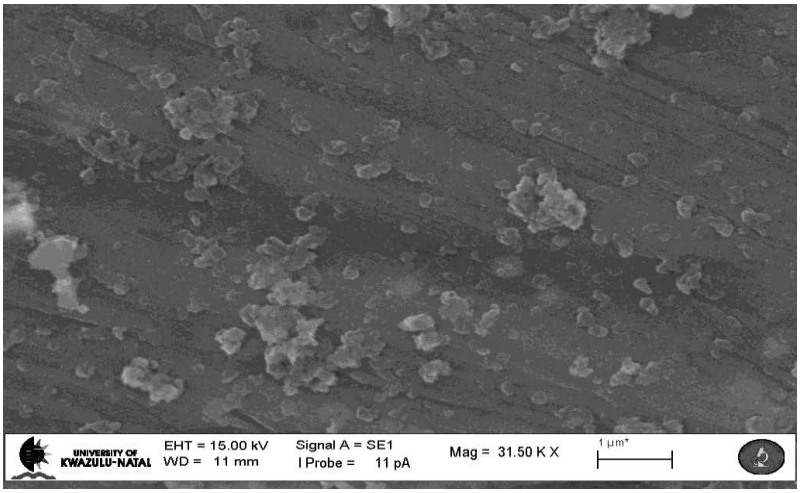

Figure 2.19 SEM images of (a) MgAl.26, (b) MgAl.31, and (c) MgAl.34.

(a)

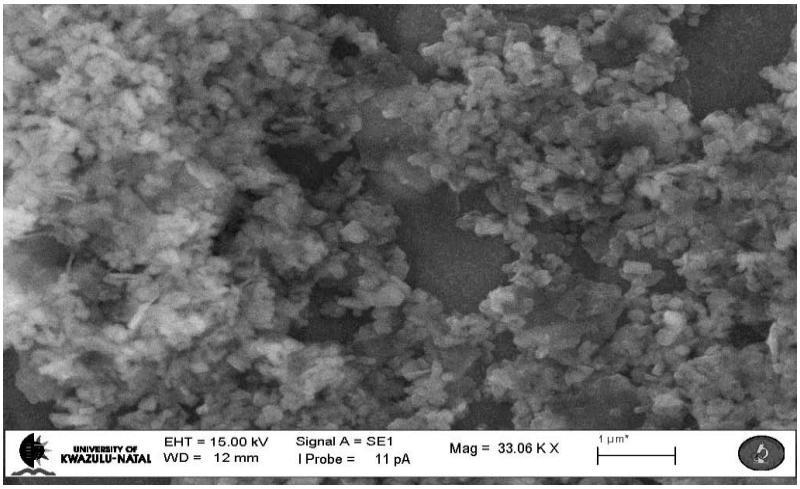

(b)

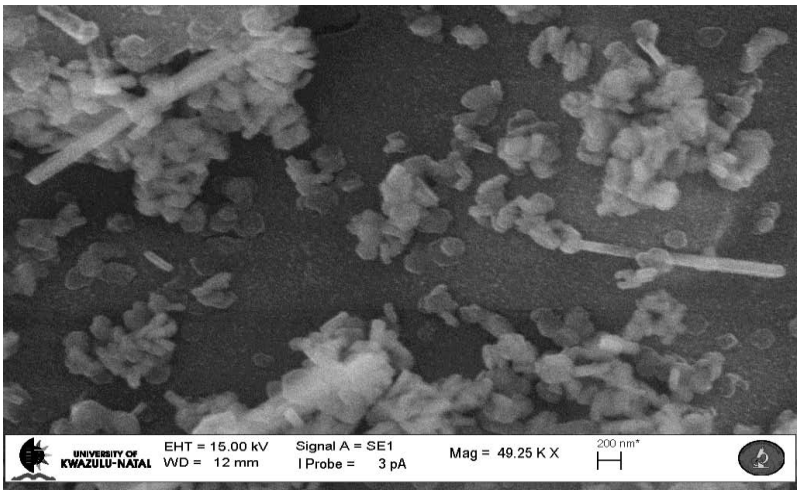

(c)

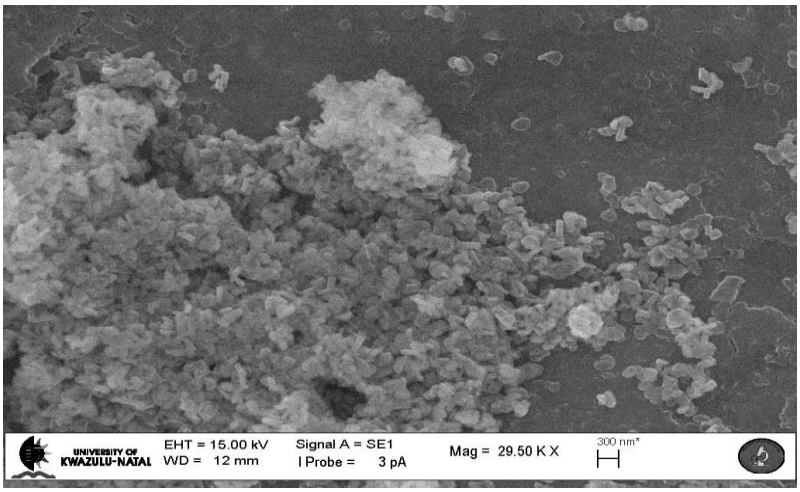

Figure 2.20 SEM images of (a) ZnAl.11, (b) ZnAl.14, and (c) ZnAl.16.

(a)

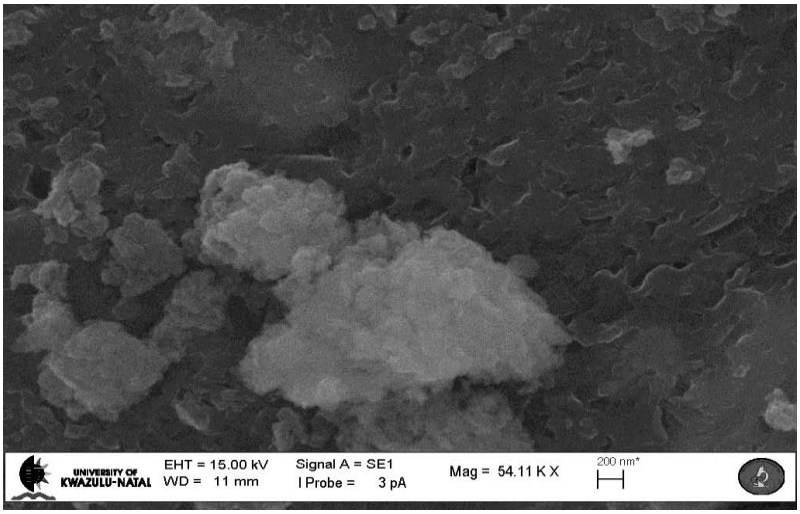

(b)

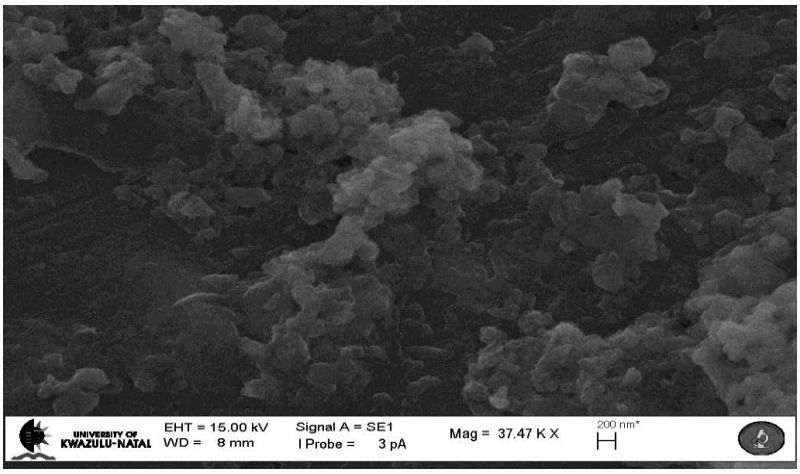

(c)

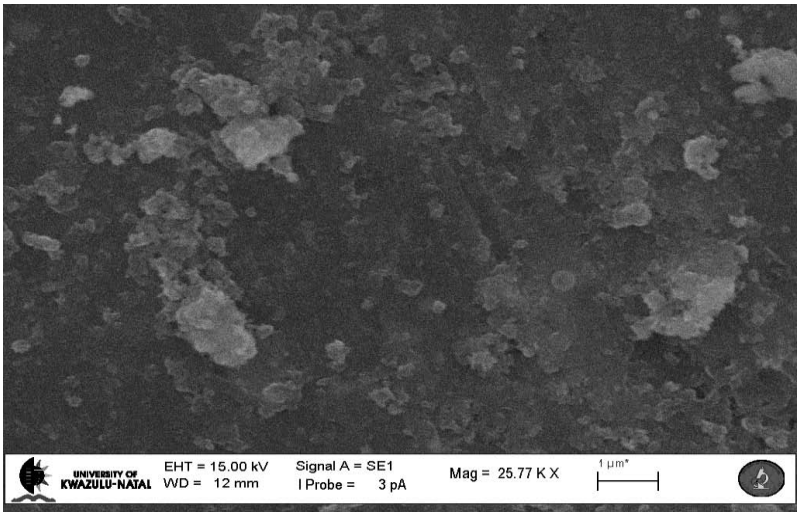

Figure 2.21 SEM images of (a) ZnFe.24, (b) ZnFe.30, and (c) ZnFe.32.

(a)

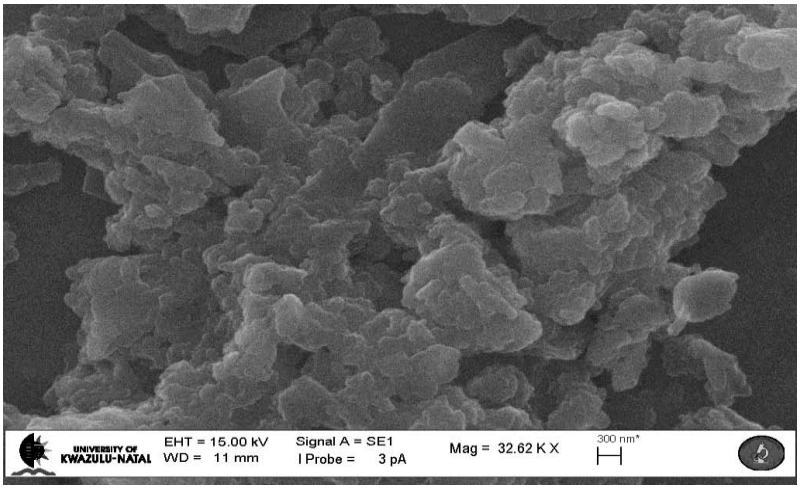

(b)

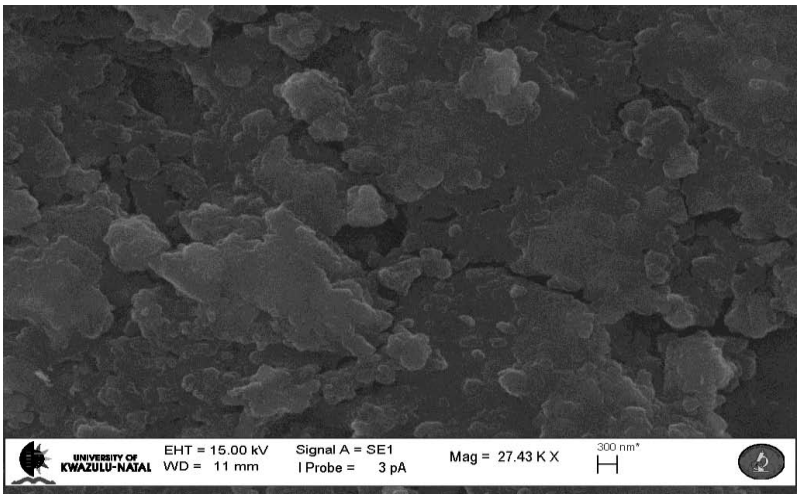

(c)

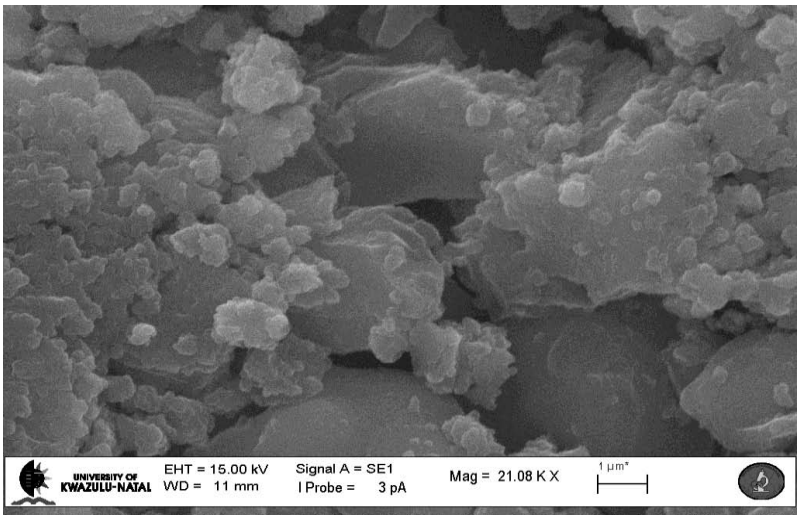

Figure 2.22 SEM images of (a) MgFe.55, (b) MgFe.58, and (c) MgFe.62.

Elemental mapping images obtained form SEM-EDX for all samples are displayed in Figures 2.23-2.26. The spectra are located in the appendix. From the elemental mapping, the distribution of M^{II} to M^{III} is fairly even with the exception of Zn-Al and Zn-Fe LDHs which both show increased amounts of surface zinc. The elemental values M^{II}:M^{III} are reported in Table 2.6.

Table 2.6 SEM-EDX elemental analysis data for each sample.

Compound	Stoichiometry (*x*)	M^{II} : M^{III}	
		Calculated	Measured
Mg-Al HT	0.31	3 :1	2.2 :1
	0.35	2.3 :1	1.8 :1
	0.4	2 :1	1.5 :1
Zn-Al LDH	0.12	3 :1	6.8 :1
	0.16	2.3 :1	5.2 : 1
	0.18	3 :1	4.7 :1
Zn-Fe LDH	0.18	3 :1	4.5 :1
	0.21	2.3 :1	3.8 :1
	0.23	2 :1	3.3 :1
Mg-Fe LDH	0.37	3 :1	1.7 :1
	0.45	2.3 :1	1.2 :1
	0.50	2 :1	1.0 :1

The measured values were fairly similar with the calculated ones for Mg-Al HTs. The values were totally different for Zn-Al, Zn-Fe and Mg-Fe LDHs as expected when compared to ICP-OES. The deviation of measured values from the calculated values can be expected from SEM-EDX analysis since this technique employs surface elemental analysis of a given compound.

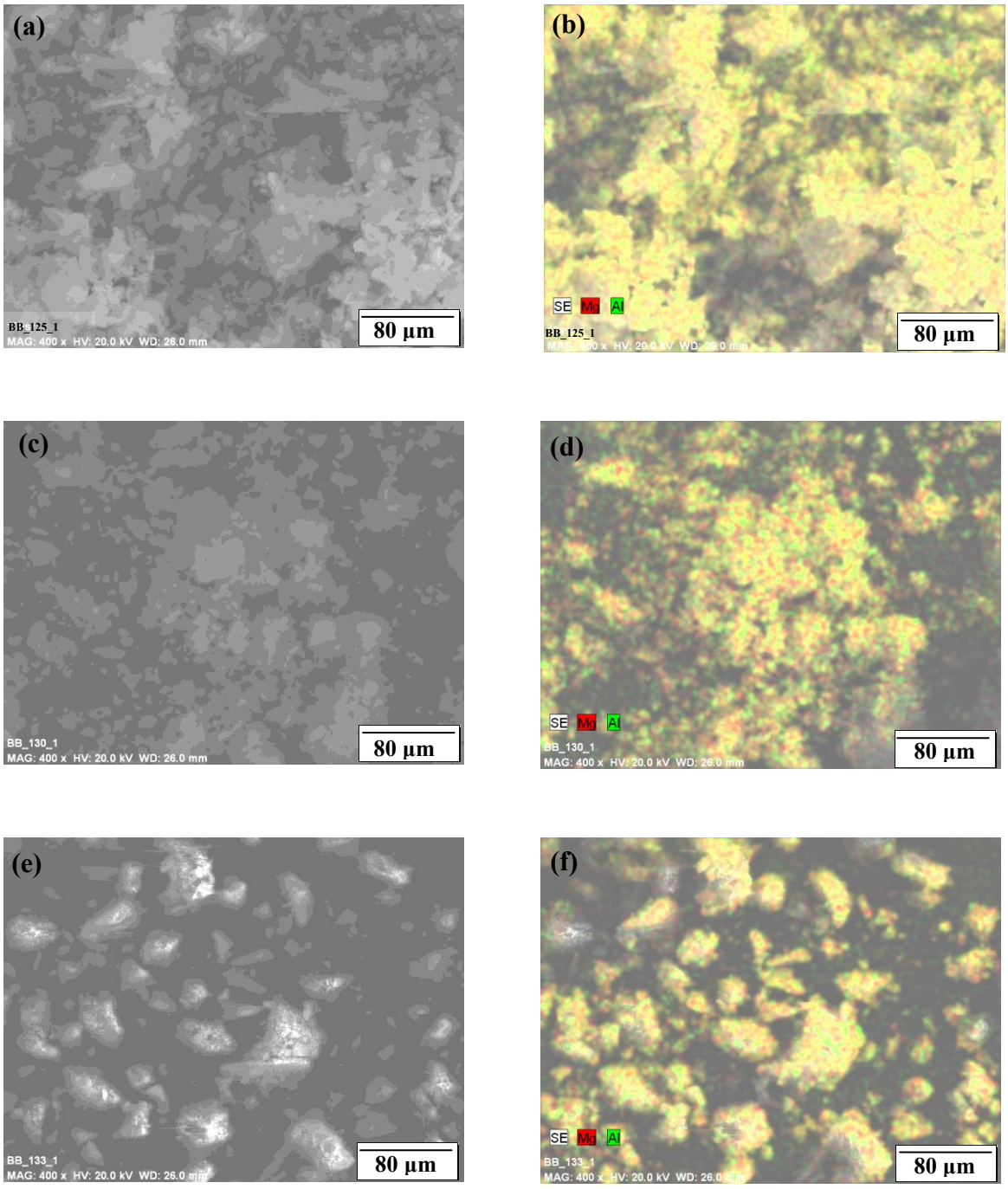

Figure 2.23 SEM-EDX mapping images of (a), (b) MgAl.26, (c), (d) MgAl.31, and (e), (f) MgAl.34.

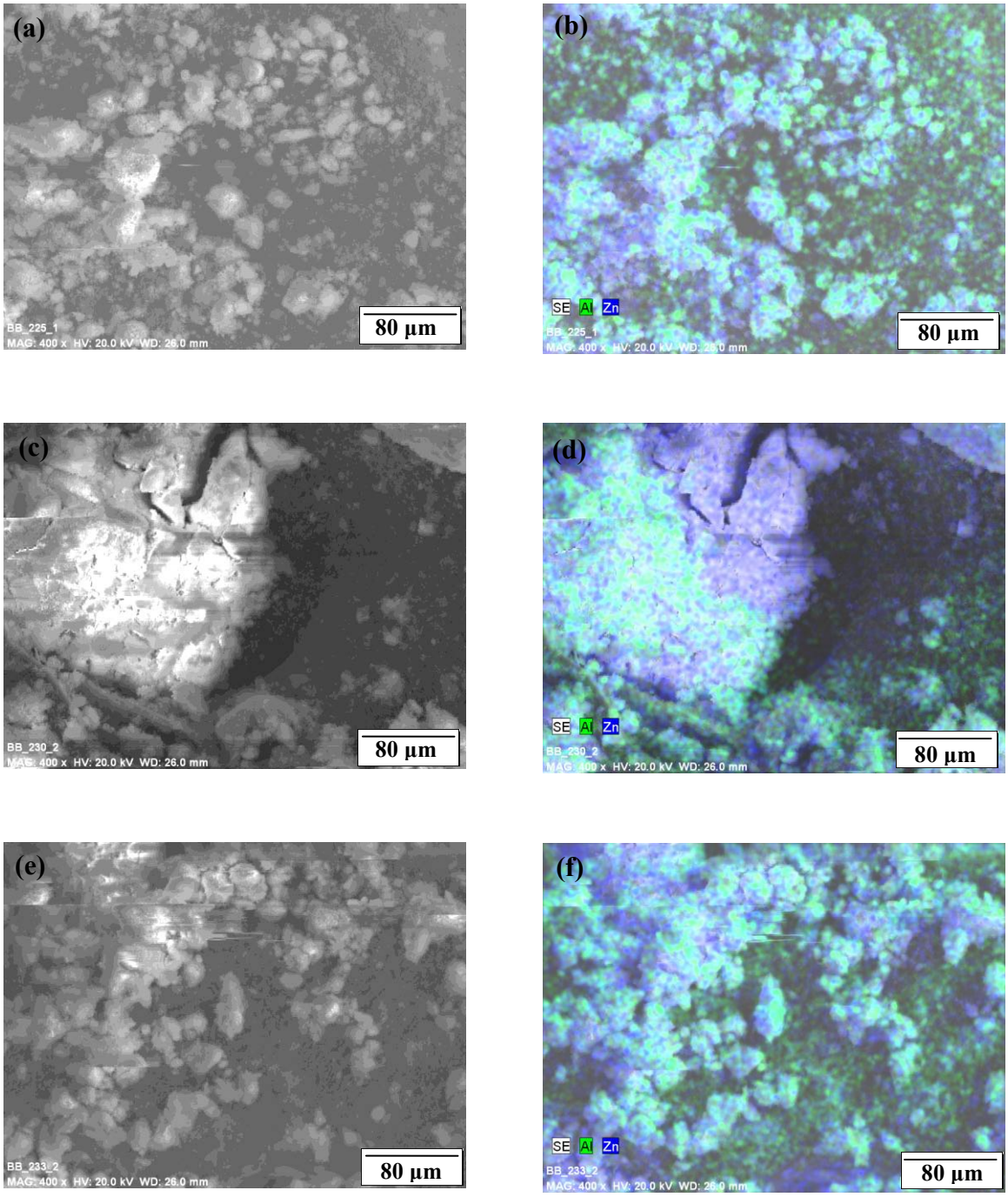

Figure 2.24 SEM-EDX mapping images of (a), (b) ZnAl.11, (c), (d) ZnAl.14, and (e), (f) ZnAl.16.

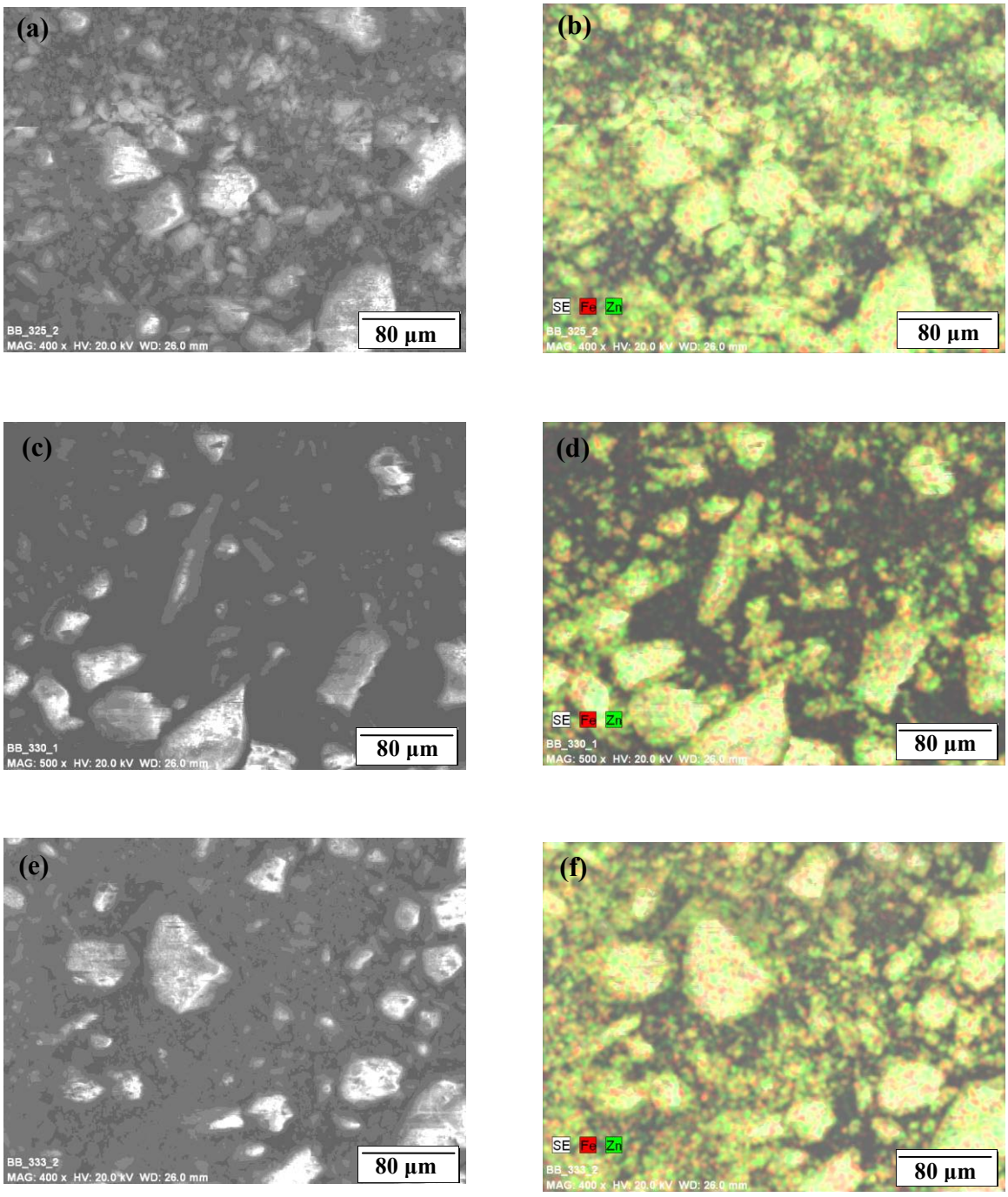

Figure 2.25 SEM-EDX mapping images of (a), (b) ZnFe.24, (c), (d) ZnFe.30, and (e), (f) ZnFe.32.

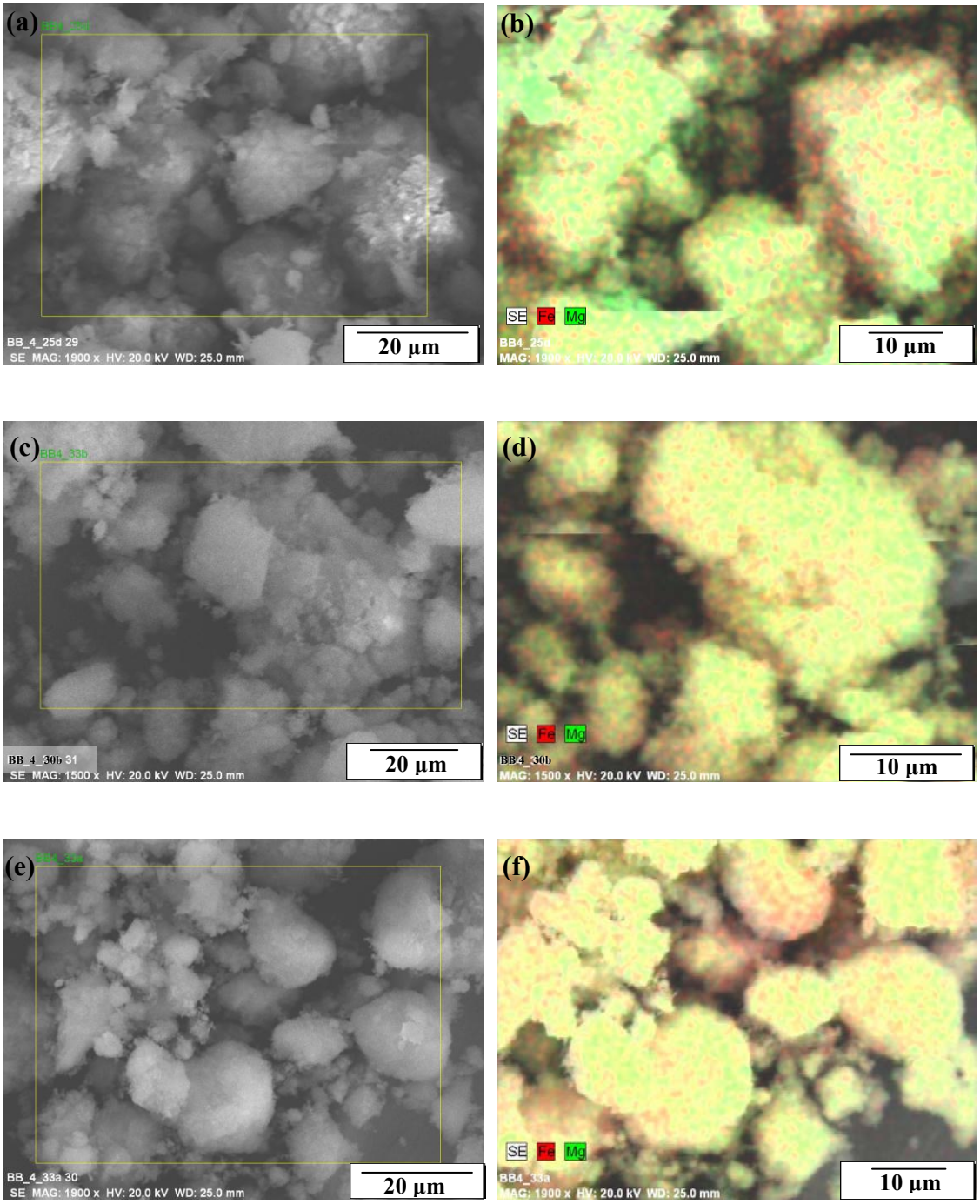

Figure 2.26 SEM-EDX mapping images of (a), (b) MgFe.55, (c), (d) MgFe.58, and (e), (f) MgFe.62.

CHAPTER THREE
DNA/NUCLEIC ACID BINDING ASSAYS, IN VITRO, CYTOTOXICITY AND TRANSFECTION ASSAYS

3.1 GEL RETARDATION ASSAY

3.1.1 Introduction

Plasmid DNA exists in three forms namely; linear, relaxed closed circular and superhelical/supercoiled. In most cases supercoiled and relaxed closed circular forms are often found with the linear form being observed less frequently. These different forms of plasmid DNA migrate at different rates during agarose gel electrophoresis. Superhelical/supercoiled DNA is a highly compacted from of the plasmid. Relaxed closed circular is found to be intact yet enzymatically relaxed, i.e. the supercoils from the superhelical form have relaxed. The linear form of a plasmid is found to have free ends, in which the DNA strands have been enzymatically cleaved in which there are physical breaks in phosphodiester bonds. Upon loading of plasmid DNA onto an agarose gel and subjecting it to electrophoresis, these different forms will migrate at different rates. Out of the three forms described, superhelical DNA, due to its compact form, migrates faster through the agarose matrix and thus will appear further down the agarose gel. It is found that the linear form of the plasmid migrates slightly slower than the superhelical and will thus migrate just before the superhelical form. Lastly the relaxed closed circular form is the slowest in migration due to the open circular ring-like form finding difficulty migrating through the agarose matrix and thus will appear closer to the point of application (agarose well).

A gel retardation assay is carried out in order to evaluate the extent of DNA binding to a specific carrier or vector. With this assay, the concentration of DNA is kept constant and the concentration of the vector is successively increased. If a known amount of the carrier and DNA are both mixed together appropriately and allowed to migrate through an agarose gel and no interaction occurs between the DNA and the vector, the DNA should migrate through the gel and the carrier will remain in the well. However if the DNA

binds to the carrier, the DNA will not migrate (i.e. retardation of migration) and hence will remain in the well bound to the carrier. Thus the successive concentration increase of vector results in less free DNA that will migrate into the agarose gel. A point will be reached where all of the DNA is vector bound and in the well - thus an optimum binding ratio of DNA:vector is determined. The DNA binding is visualized in the gel due to the incorporation of a DNA intercalating dye ethidium bromide (EtBr) which fluoresces when irradiated with UV light. Thus the appearance of orange bands against a dark background allows the exact migration of DNA to be followed under UV light. The intercalating agent can be added directly into the agarose gel preparation or the gel can be stained post-electrophoresis. The gel is then irradiated with UV light and a photographic image captured.

3.1.2 Materials and methods

3.1.2.1 DNA:HT/LDH complexes

Plasmid pCMV-GFP DNA (*The Plasmid Factory*, Germany. Concentration 1.0 mg / ml stock) was kept constant in all samples at 0.5 μg. Each HT and LDH powdered sample was made up in 18 mohm water with a final HT/LDH concentration of 10 μg / μl. Samples were prepared in 1.5 ml microcentrifuge tubes according to the following Tables 3.1-3.4.

Table 3.1 Synthesis details for DNA:Mg-Al HT complexes

Sample	Ratio DNA:HT	Volume (μl)			Total Volume (μl)
		pCMV-GFP	HT	HBS*	
MgAl.26	1:35	1.0	1.8	7.2	10.0
	1:40	1.0	2.0	7.0	10.0
	1:50	1.0	2.3	6.7	10.0
MgAl.31	1:50	1.0	2.5	6.5	10.0
	1:55	1.0	2,8	6.2	10.0
	1:60	1.0	3.0	6.0	10.0
MgAl.34	1:35	1.0	1.8	7.2	10.0
	1:40	1.0	2.0	7.0	10.0
	1:45	1.0	2.3	6.7	10.0

*Prepared Hepes buffered saline (HBS), Hepes (*Merck,* Darmstadt, Germany).

Table 3.2 Synthesis details for DNA:Zn-Al LDH complexes

Sample	Ratio DNA:LDH	Volume (µl)			Total Volume (µl)
		pCMV-GFP	LDH	HBS*	
ZnAl.11	1:60	1.0	3.0	6.0	10.0
	1:65	1.0	3.3	5.7	10.0
	1:70	1.0	3.5	5.5	10.0
ZnAl.14	1:40	1.0	2.0	7.0	10.0
	1:45	1.0	2.3	6.7	10.0
	1:50	1.0	2.5	6.5	10.0
ZnAl.16	1:40	1.0	2.0	7.0	10.0
	1:45	1.0	2.3	6.7	10.0
	1:50	1.0	2.5	6.5	10.0

*Prepared Hepes buffered saline (HBS), Hepes (*Merck,* Darmstadt, Germany).

Table 3.3 Synthesis details for DNA:Zn-Fe LDH complexes

Sample	Ratio DNA:LDH	Volume (µl)			Total Volume (µl)
		pCMV-GFP	LDH	HBS*	
ZnFe.24	1:30	1.0	1.5	7.5	10.0
	1:35	1.0	1.8	7.2	10.0
	1:40	1.0	2.0	7.0	10.0
ZnFe.30	1:30	1.0	1.5	7.5	10.0
	1:35	1.0	1.8	7.2	10.0
	1:40	1.0	2.0	7.0	10.0
ZnFe.32	1:30	1.0	1.5	7.5	10.0
	1:35	1.0	1.8	7.2	10.0
	1:40	1.0	2.0	7.0	10.0

*Prepared Hepes buffered saline (HBS), Hepes (*Merck,* Darmstadt, Germany).

Table 3.4 Synthesis details for DNA:Mg-Fe LDH complexes

Sample	Ratio DNA:LDH	Volume (µl)			Total Volume (µl)
		pCMV-GFP	LDH	HBS*	
MgFe.55	1:25	1.0	1.3	7.7	10.0
	1:30	1.0	1.5	7.5	10.0
	1:35	1.0	1.8	7.2	10.0
MgFe.58	1:45	1.0	2.3	6.7	10.0
	1:50	1.0	2.5	6.5	10.0
	1:55	1.0	2.8	6.2	10.0
MgFe.62	1:30	1.0	1.5	7.7	10.0
	1:35	1.0	1.8	7.5	10.0
	1:40	1.0	2.0	7.2	10.0

*Prepared Hepes buffered saline (HBS), Hepes (*Merck,* Darmstadt, Germany).

Samples (Mg-Al HTs, MgFe.55 and MgFe.58) were then incubated at 60^{o}C for 2 hours in a *Scientific* oven. Remaining samples (Zn-Al LDHs, Zn-Fe LDHs and MgFe.62) were incubated at 60^{o}C for 72 hours – 72 hours was determined as the required incubation time for DNA: LDH complex formation for these samples (in depth discussion on this observation indicated in results and discussion). After this incubation time the samples were then loaded onto 1% agarose gels and subjected to electrophoresis for 90 minutes at 50 V.

3.1.2.2 Agarose gel and electrophoresis

Approximately 0.2 g of agarose *(Sigma-Aldrich*, Steinheim, Germany) was dissolved with heating in 18 ml distilled water. The solution was then cooled to approximately 75^{o}C and 2 ml of 10x electrophoresis buffer (0.36 M Tris-HCl, 0.3 M NaH_2PO_4 and 0.1 M EDTA (*Merck,* Darmstadt, Germany)) was added. This was then followed by the addition of 3 µl of ethidium bromide (10 mg/ml). The solution was cooled to approximately 60-62^{o}C and poured onto a gel tray with an 8 well comb. This was allowed to set for approximately 45-60 minutes. Thereafter, the comb was removed and the tray submersed into an electrophoresis unit (*Bio-Rad Mini-Sub® Cell GT*) containing 1 x electrophoresis buffer.

To each sample, including the standard DNA marker sample, 2 µl of gel loading buffer / stop solution (40 % Sucrose, 0.05 % Bromophenol blue). Each gel contained a standard in which 10 µl of a HBS buffered solution of DNA (0.5 µg) was loaded onto the agarose gel. The incubated samples as per Tables 3.1-3.4 were loaded onto the gel alongside the standard and subjected to electrophoresis. After electrophoresis the gel was then removed and viewed under UV light using a *Syngene* G-box documentation system (*Vacutec*) and an image captured.

3.1.2.3 Characterization of DNA:HT binding

Out of the samples prepared, from gel retardation assays, MgAl.31 (1:55) was selected as an ideal representative of DNA binding due to its full retardation. The DNA:MgAl.31

(1:55) complex was then characterized using TEM, XRD, FTIR and Raman spectroscopy. The complex was prepared according to Table 3.1 for TEM analysis. For XRD, FTIR and Raman spectroscopy, the preparation of the complex was scaled up to 10:550 (mg:mg). The complexes were then incubated at 60^{o}C for 2 hours, thereafter characterization was carried out

TEM

The complex was viewed using a *Zeiss, Libra 120* TEM, employing *Zeiss* software. For sample analysis, 1 µl of the complex was placed onto a copper grid. The copper grid was then air-dried and viewed.

XRD

Both the complex and DNA-free MgAl.31 were separately analyzed directly on a *Bruker D8 Advance XRD* (CuKα radiation), using *Bruker* analysis software. Prior to sample analysis, the complex was dried in an oven at 60^{o}C for 24 hours. The entire dried powdered complex was placed onto the sample holder and gently flattened. The scan-speed was set to 0.5 seconds.

FTIR

Both the complex and 'free' DNA were separately analyzed directly on a *Perkin Elmer Spectrum Universal ATR 100 FT-IR Spectrometer*. Prior to sample analysis, the complex was dried in an oven at 60^{o}C for 24 hours. Thereafter, the intstrument crystal area was cleaned and the background collected. Approximately 0.5 g of the dried complex product was placed over the surface of the crystal and the pressure arm locked into place. The spectra were then collected.

Raman spectroscopy

Both the complex and DNA-free MgAl.31 were separately analyzed on a *DeltaNu Advantage 532* Raman Spectrometer. Each sample was placed in a clear shell vial (*VWR International*, West Chester, PA), approximately 5 mm from the base of the vial. The shell vial was then sealed and gently tapped at an angle, causing the sample to lie at an

angle sloping upwards. The shell vial was then placed into the sample holder and placed into the Raman Spectrometer. Raman analysis was performed on each sample and spectra captured using *NuSpec*^{TM} software and spectra analysis using *GRAMS/AI* spectroscopy software suite 9.00 R2.

3.1.3 Results and discussion

The synthesis of the HTs and LDHs in this study was to ascertain if these compounds have an application in gene delivery into mammalian cells in culture. Therefore the powdered product needed to be in a solution form and hence 18 mohm water was utilized. Varying degrees of solubilities were observed for all the samples (Appendix, Table A2, Figures A2 and A3). Most of the samples were not soluble in water, with the exception of MgFe.55 and MgFe.58 which remained in solution for several months.

From gel retardation assays, all HT and LDH samples showed the ability to electrostatically bind DNA at varying degrees. As discussed in chapter two, HTs and LDHs exhibit an anion interlayer that is able to undergo ion-exchange. Many authors have exploited this property giving rise to a wide variety of applications such as the removal of toxic anions and herbicides from water and the ion exchange of various pharmaceuticals and biomolecules, including the intercalation of DNA [58, 81].

In the formation of the DNA:HT/LDH complexes; ion exchange reactions were explored. Investigators using similar Mg-Al HT materials have used varying temperatures and incubation times such as; 48 hours at 60^{o}C [71], 30 minutes at 37^{o}C [115], 4 hours (involving light shaking) at 37^{o}C [27], 15 minutes (involving light shaking) at 60^{o}C [28], 12 hours at 37^{o}C [116]. All of these methods were attempted in this study; with incubation temperatures done at 37^{o}C and 60^{o}C for 15 minutes giving unsatisfactory results. However longer incubation times at 60^{o}C showed the successful formation of DNA:HT/LDH complexes that was confirmed by gel retardation. A time dependent incubation (30 minutes-72 hours) at 60^{o}C was carried out (data not shown) on all samples and it was observed that DNA had been bound by Mg-Al HTs, MgFe.55, MgFe.58 samples after 1 ½ hours incubation (<1 ½ hours, DNA was partially retarded) confirmed by gel retardation assays. Subsequent reactions were then carried out at 60^{o}C for 2 hours

for Mg-Al HTs, MgFe.55, MgFe.58 samples. All Zn-Al LDH, Zn-Fe LDH, MgAl.26 and MgFe.62 samples seemed to show a similar trend of incomplete binding of DNA while much of the DNA was seen to migrate into the gel. From the time dependent incubation it appeared that 72 hours resulted in more DNA being bound to the Zn-Al and Zn-Fe LDH samples (Figure 3.1). Subsequent reactions were then carried out at 60^{o}C for 72 hours for Zn-Al LDHs, Zn-Fe LDHs and MgFe.62 samples.

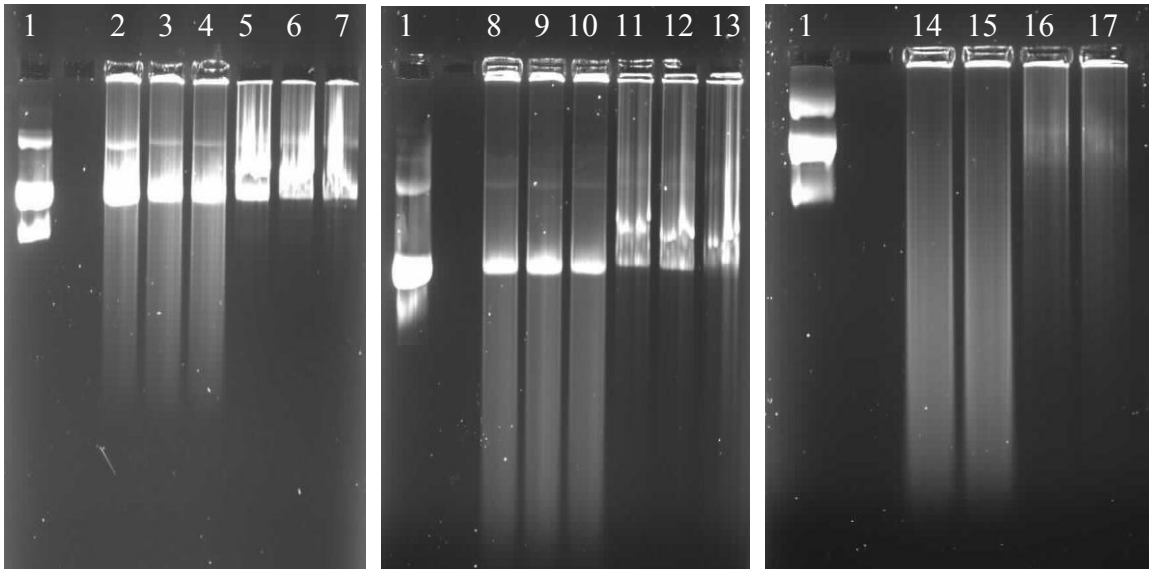

(60^{o}C, 24 hours) **(60^{o}C, 48 hours)** **(60^{o}C, 72 hours)**

Figure 3.1 Gel Retardation Assay of Zn-Al and Zn-Fe LDHs

Lane 1 = pCMV-GFP (0.5 μg)

Lane 2, 8, 14 = 1:65 ZnAl.11

Lane 3, 9, 15 = 1:45 ZnAl.14

Lane 4, 10 = 1:45 ZnAl.16

Lane 5, 11, 16 = 1:35 ZnFe.24

Lane 6, 12, 17 = 1:35 ZnFe.30

Lane 7, 13 = 1:35 ZnFe.33

DNA was kept constant at 0.5 μg.

From Figure 3.2, MgAl.26 partially retarded the DNA. i.e. the compound was able to bind some of the DNA in solution. The bound DNA remained in the well viewed as an orange band (under UV light) within the well. The unbound DNA in samples MgAl.26 is thus able to migrate as free DNA and hence resembles the standard DNA (lane one) with the appearance of orange bands (superhelical and closed circular forms visible). The ratio of DNA (μg): MgAl.26 (μg) was increased up to 1:155 so as to ascertain if more HT was required to bind the free DNA, however to no avail. MgAl.31 and MgAl.34 on the other hand, showed complete retardation at ratios 1:50 and 1:45 respectively.

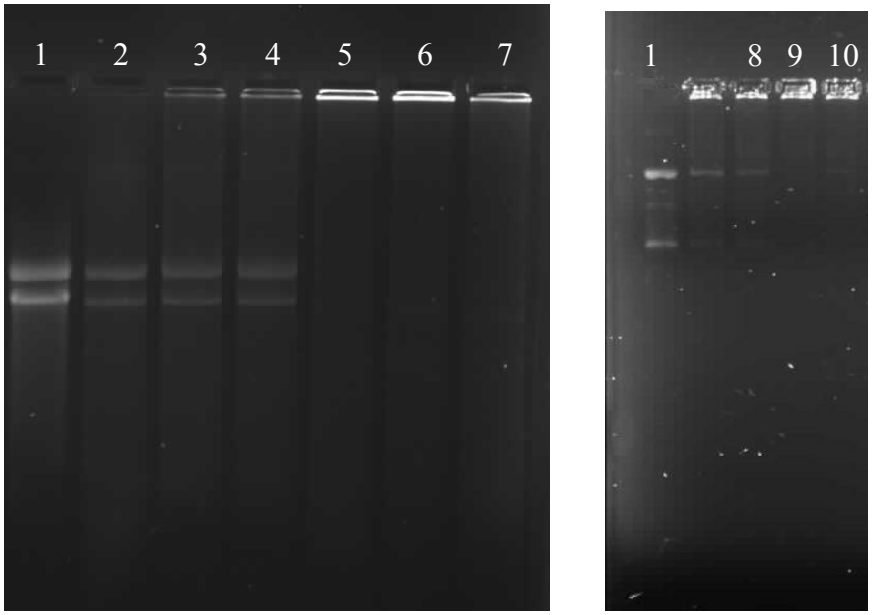

Figure 3.2 Gel Retardation Assay of Mg-Al HTs.

Lane 1 = pCMV-GFP (0.5 μg)

Lane 2 = 1:35 MgAl.26

Lane 3 = 1:40 MgAl.26

Lane 4 = 1:45 MgAl.26

Lane 5 = 1:50 MgAl.31

Lane 6 = 1:55 MgAl.31

Lane 7 = 1:60 MgAl.31

Lane 8 = 1:35 MgAl.34

Lane 9 = 1:40 MgAl.34

Lane 10 = 1:45 MgAl.34.

DNA was kept constant at 0.5 μg.

All Zn-Al LDH samples (Figure 3.3) showed very little binding ability, with more unbound DNA than bound DNA (very faint bands in well visible). Higher ratios up to 1:155 were carried are for all Zn-Al LDH samples, with no change in their retardation pattern and hence no change in their DNA binding ability. Interesting to note that the band of supercoiled DNA (i.e. the band that migrates the furthest into the gel) has been bound by the Zn-Al LDHs with the other forms of DNA remaining in solution. This is confirmed by the absence of the supercoiled band compared to the standard DNA.

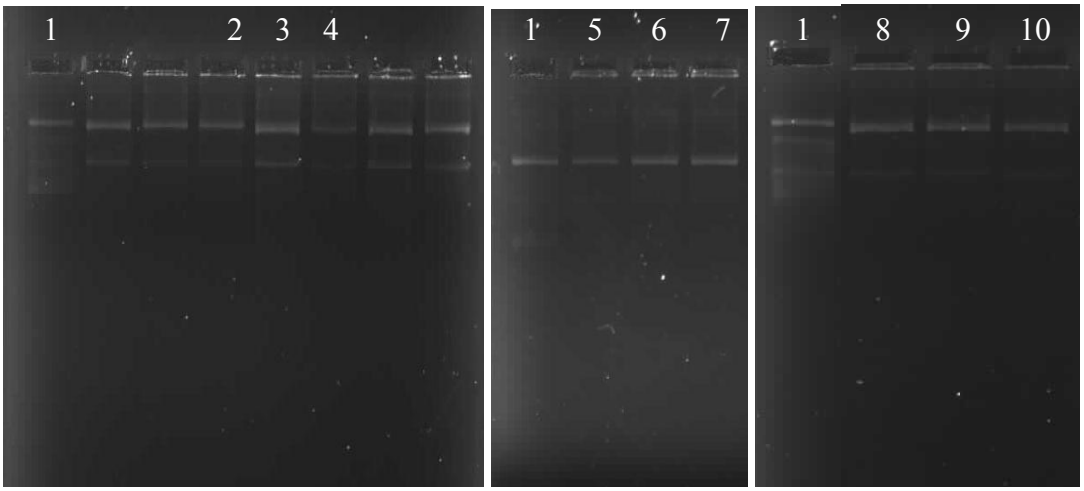

Figure 3.3 Gel Retardation Assay of Zn-Al LDHs.

Lane 1 = pCMV-GFP (0.5 μg)

Lane 2 = 1:60 ZnAl.11

Lane 3 = 1:65 ZnAl.11

Lane 4 = 1:70 ZnAl.11

Lane 5 = 1:40 ZnAl.14

Lane 6 = 1:45 ZnAl.14

Lane 7 = 1:50 ZnAl.14

Lane 8 = 1:40 ZnAl.16

Lane 9 = 1:45 ZnAl.16

Lane 10 = 1:50 ZnAl.16

DNA was kept constant at 0.5 μg.

A similar pattern was seen for Zn-Fe LDH samples (Figure 3.4), in which partial retardation was observed. Higher ratios of 1:155 were carried are for all Zn-Fe samples yet there was no change in their retardation pattern. Zn-Fe LDH samples also appeared to bind supercoiled DNA, with the exception of ZnFe.30 (Figure 3.4, lanes 5, 6, 7) in which the band of supercoiled DNA is evident. Thus both Zn-Al and Zn-Fe LDHs appear to have a selectivity for supercoiled DNA.

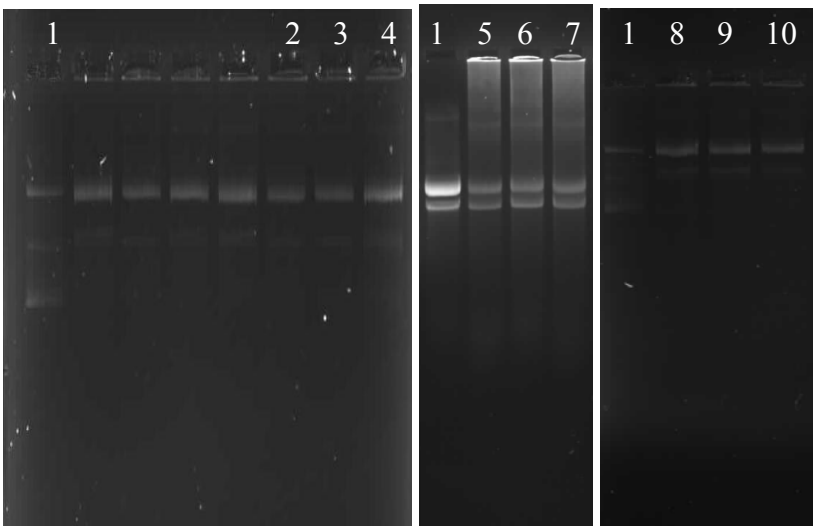

Figure 3.4 Gel Retardation Assay of Zn-Fe LDHs.

Lane 1 = pCMV-GFP (0.5 μg)

Lane 2 = 1:30 ZnFe.24

Lane 3 = 1:35 ZnFe.24

Lane 4 = 1:40 ZnFe.24

Lane 5 = 1:30 ZnFe.30

Lane 6 = 1:35 ZnFe.30

Lane 7 = 1:40 ZnFe.30

Lane 8 = 1:30 ZnFe.32

Lane 9 = 1:35 ZnFe.32

Lane 10 = 1:40 ZnFe.32

DNA was kept constant at 0.5 μg for lanes 1-4, 8-10 and 1.0 μg for lanes 5-7.

MgFe.55 and MgFe.58 (Figure 3.5) showed full retardation at about 1:30 (Lane 3) and 1:50 (Lane 5) respectively. MgFe.62 showed partial retardation, with more bound DNA seen in the well than unbound DNA. The gel retardation pattern of MgFe.62 was similar to that of Zn-Al and Zn-Fe samples. Thus the ion exchange conditions for these samples was re-evaluated and through a time dependent gel retardation the optimum incubation time was determined as 72 hours. Figure 3.1 shows improved DNA retardation, however streaking is observed right the way down the gel which is attributed to DNA degradation, this could be due to prolonged incubation at 60^{o}C or the HT / LDH itself is causing DNA degradation. Some DNA degradation was also observed for other Mg-Fe LDH samples.

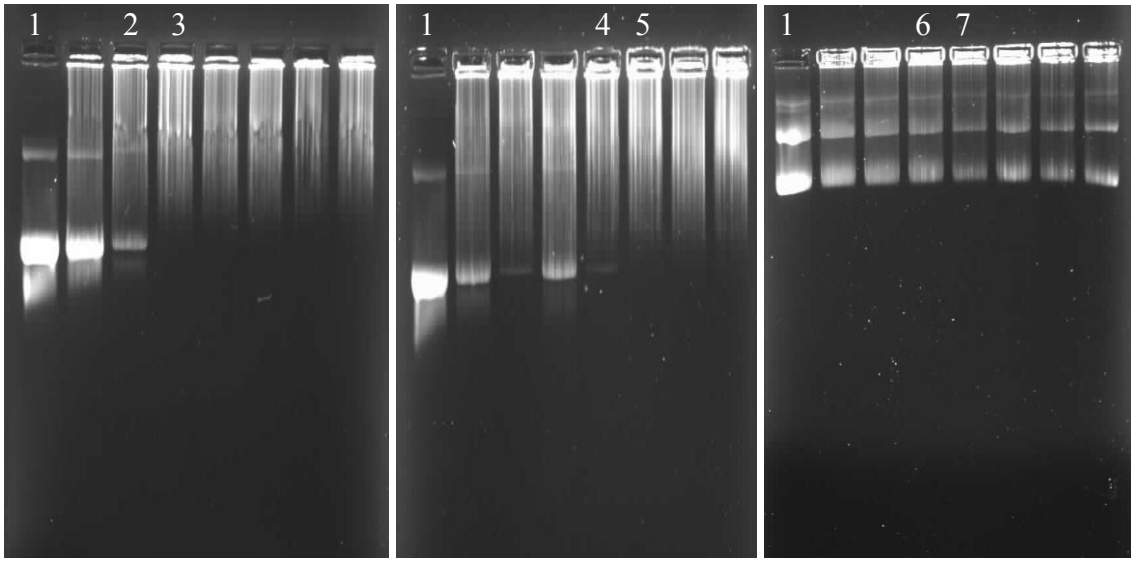

Figure 3.5 Gel Retardation Assay of Mg-Fe LDHs.

Lane 1 = pCMV-GFP (0.5 μg)

Lane 2 = 1:20 MgFe.55

Lane 3 = 1:30 MgFe.55

Lane 4 = 1:40 MgFe.58

Lane 5 = 1:50 MgFe.58

Lane 6 = 1:30 MgFe.62

Lane 7 = 1:40 MgFe.62

DNA was kept constant at 0.5 μg.

From these results, it can be seen that the HT and LDH samples showed varying degrees of DNA binding. For gene delivery studies, it is often advisable - as a rule of thumb- to take the successive ratio below and above the optimum binding ratio, since, although the optimum binding ratio is the ratio at which DNA is optimally bound, the successive ratio above or below could perhaps be more efficient in gene delivery (transfection) *in vitro* and extended to *in vivo* studies. This is due to the fact that, during complex formation of the DNA to the compound used, a successive ratio below may in fact electrostatically bind the DNA loosely due to lower amounts of the compound and may release DNA more easily than that of the optimum ratio which could perhaps bind the DNA very tightly thus decreasing the amount of DNA being released within the cell. In addition, as one is working with a biological system, the nature of the compound itself may govern the efficiency in which transfection occurs. Thus from the successive ratios used, one is then able to select the most efficient ratio in order to develop that particular ratio into *in vivo* studies. The optimum binding ratio (shown as bold) as well as the successive ratio below and above are reported below.

Table 3.5 DNA:HT/LDH ratios.

Sample	DNA:HT/LDH (µg:µg)
MgAl.26	1:35, **1:40**, 1:45
MgAl.31	1:50, **1:55**, 1:60
MgAl.34	1:35, **1:40**, 1:45
ZnAl.11	1:60, **1:65**, 1:70
ZnAl.14	1:40, **1:45**, 1:50
ZnAl.16	1:40, **1:45**, 1:50
ZnFe.24	1:30, **1:35**, 1:40
ZnFe.30	1:30, **1:35**, 1:40
ZnFe.32	1:30, **1:35**, 1:40
MgFe.55	1:25, **1:30**, 1:35
MgFe.58	1:45, **1:50**, 1:55
MgFe.62	1:30, **1:35**, 1:40

Previous studies using Mg-Al HTs in the delivery of oligonucleotides and DNA [15-17, 76, 78] indicated the mechanism of DNA binding was due to ion exchange of the interlayer anions. Thus the possible mechanism of DNA binding was evaluated in this study. XRD, FTIR, TEM and Raman spectroscopy were used in the evaluation of the binding mechanism of DNA:HT/LDH samples.

Out of the samples prepared, from gel retardation, MgAl.31 (1:55) was selected as an ideal representative of DNA binding due to its full retardation. From XRD patterns of MgAl.31 (Figure 3.6), no change in the XRD diffractogram or d-spacing values was observed (Fig. 3.6(a) versus b), in addition, if DNA was intercalated within the interlayer, a peak at about a 2-theta value of about 5-9^{o} with a value of 23.7 Å should have been observed [88], since the diameter of DNA is 23.7 Å [116]. However, from XRD software analysis, a peak showing an intensity of 1.0 % was observed at a 2-theta value of 6.305^{o} and had a d-spacing value of 14.00704 Å. This is slightly larger than half the diameter of DNA. Perhaps the DNA binds to the outside of the HT/LDH and the DNA is further compacted/sandwiched between one or more particles. If this was the case; due to the electrostatic interaction, one would observe no FTIR bonding frequencies between the HT/LDH and the DNA, therefore the FTIR spectrum should exhibit a mixture of the HT/LDH and that of 'free' DNA.

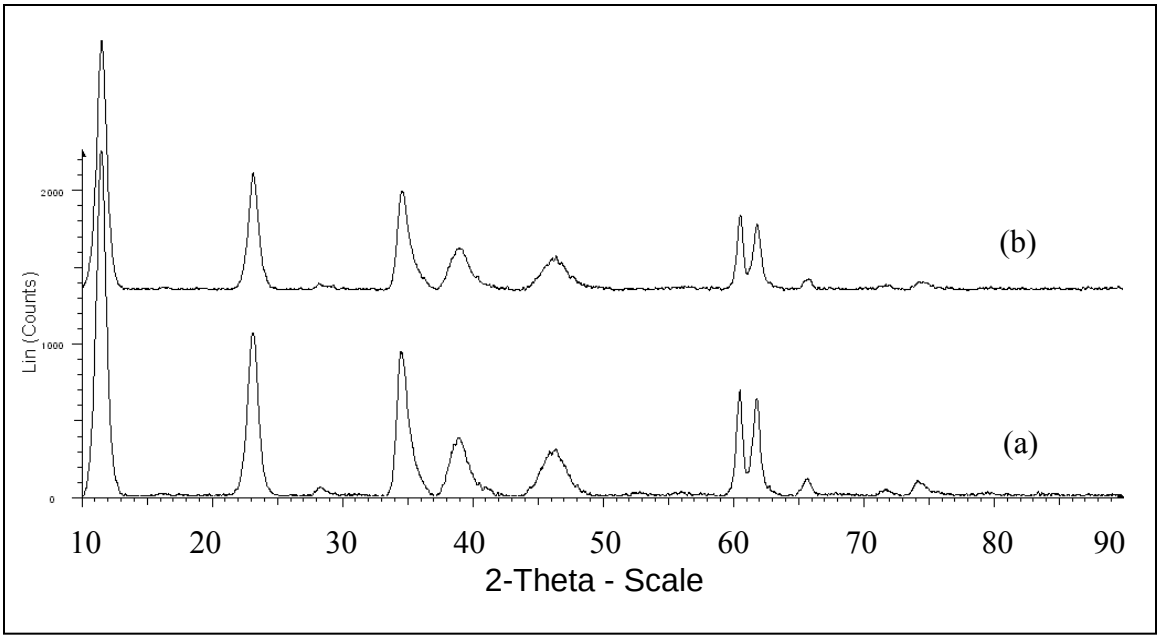

Figure 3.6 XRD pattern of (a) MgAl.31 and (b) DNA:MgAl.31.

From the FTIR spectrum (Figure 3.7), one observed that there appeared no bonding frequencies between the HT and DNA, in addition there appeared no evidence of 'free' DNA.

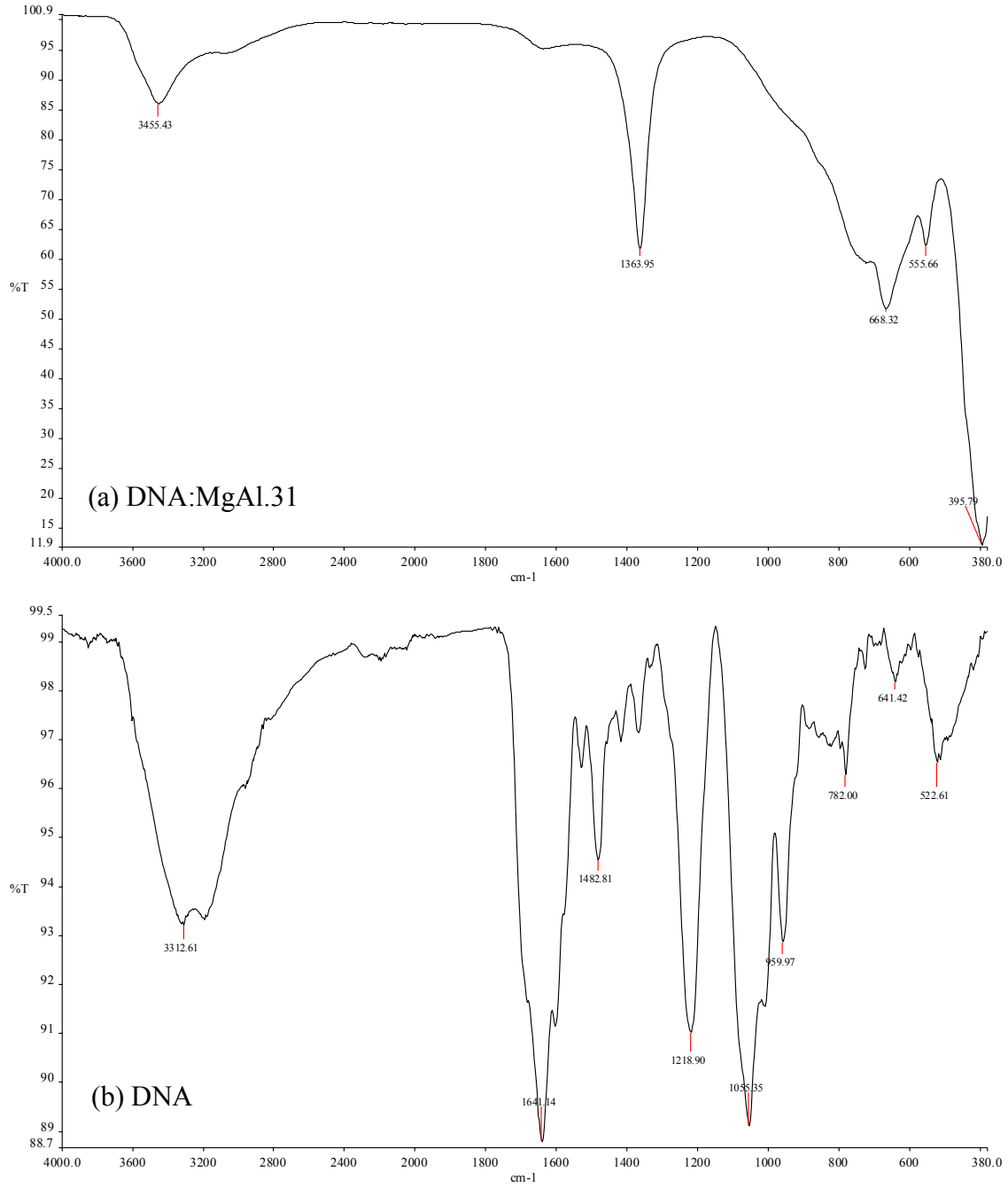

Figure 3.7 FTIR spectrum of (a) DNA:MgAl.31 and (b) DNA.

From the XRD peak at a 2-theta value of 6.305 with an intensity of 1 %, in addition the concentration ratio of 1: 55 for XRD had to be scaled-up to 10 mg: 600 mg (DNA : MgAl.31), the absence of free DNA in the FTIR spectrum could be due to the low amount of DNA in relation to the overwhelming amount of MgAl.31. Hence FTIR bonding frequencies for DNA were not visible or simply the intensity of these bonding frequencies was too low to overcome the background threshold.

TEM images of DNA:HT/LDH complexes (Figure 3.8) were captured for MgAl.26, ZnAl.11, ZnFe.24 and MgFe.58. The DNA:HT/LDH complex particles for Mg-Al HT samples showed a size range of 400-450 nm. Zn-Al LDH samples showed a size range of 200 nm- >500 nm. Zn-Fe LDH samples showed a size range of 150-300 nm and Mg-Fe LDH samples showed a size range of 200-300 nm.

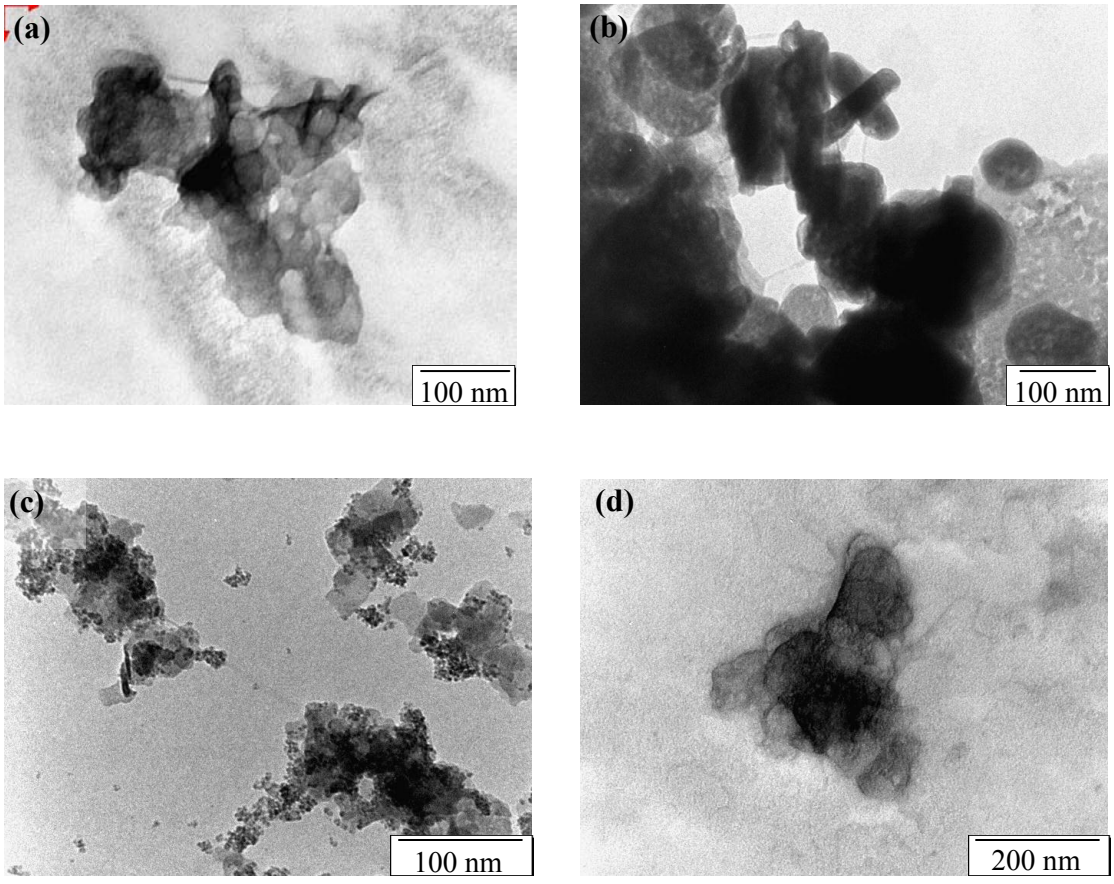

Figure 3.8 TEM images of DNA:HT/LDH complex complexes. (a) MgAl.26 (x250k), (b) ZnAl.11 (x250k), (c) ZnFe.24 (x200k), (d) MgFe.58 (x250k).

TEM images of DNA: MgAl.11 (Figure 3.9(a)-3.9(b)) show a distinct thin 'lamella-like' fissure between one/two HT particles lying side-on to the plane of view.

Figure 3.9(a) TEM image of DNA:MgAl.31 (x500k) (Image captured at Carl Zeiss SMT, NTS).

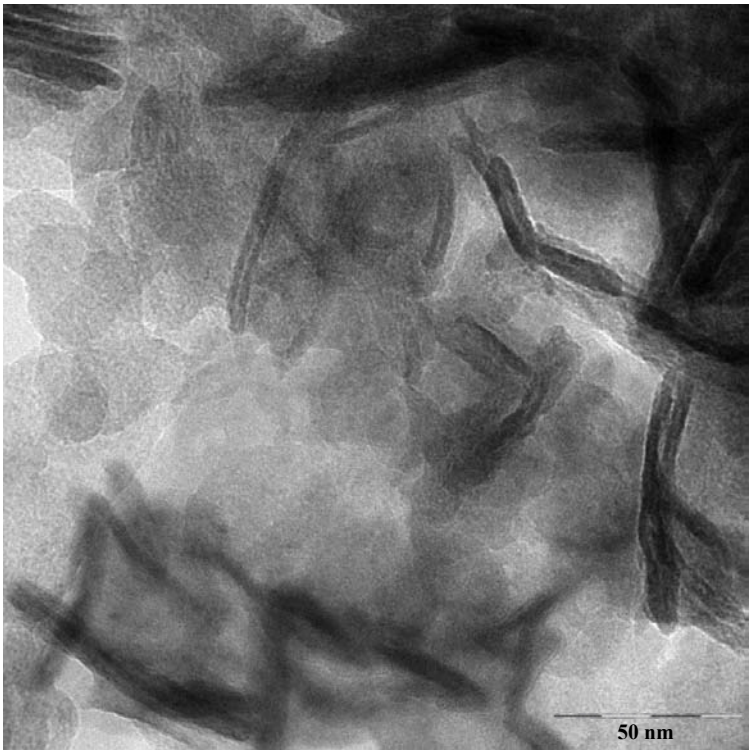

Figure 3.9(b) TEM image of DNA:MgAl.31 (x500k) (Image captured at Carl Zeiss SMT, NTS).

In relation to MgAl.31 without any DNA (Figure 3.10), TEM images indicates a visible decrease in the size of this fissure-thus complimenting the notion of DNA being sandwiched between two or more HT particles. Thus to support this notion, a nuclease digestion assay was conducted and should show increased degradation of DNA when the DNA:HT/LDH samples are subjected to nuclease enzymes-this is further discussed in section 3.2 to follow. The notion that DNA does not undergo full ion exchange with HT/LDH interlayer anions and simply binds to the external surface of one or more HT/LDH particles was also observed by Ladewig et al. [118].

Figure 3.10 TEM image of MgAl.31 (x500k) (Image captured at Carl Zeiss SMT, NTS).

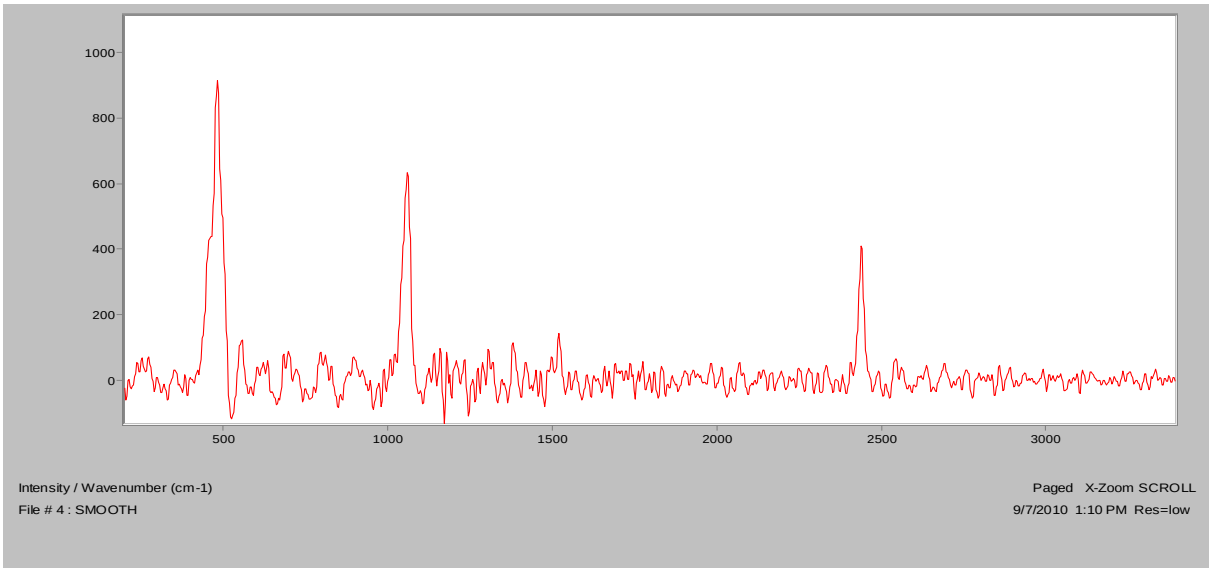

Figure 3.11 Raman spectrum of DNA:MgAl.31.

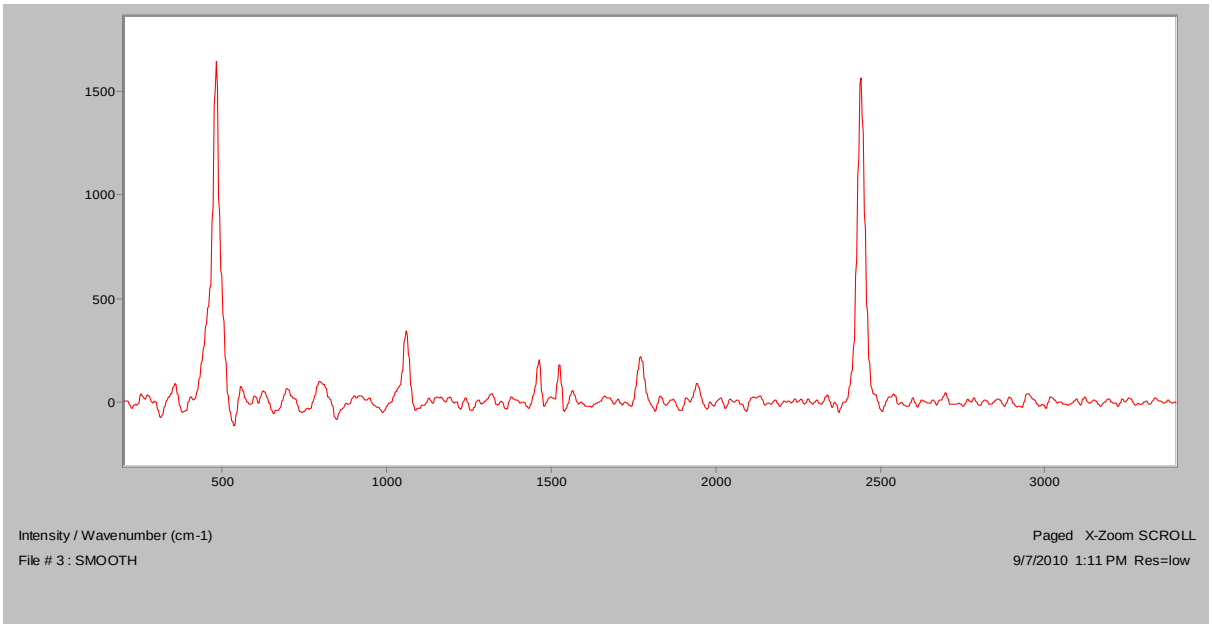

Figure 3.12 Raman spectrum of MgAl.31.

Raman spectroscopy (Figures 3.11-3.12) revealed a similar observation seen in both XRD and FTIR data showing no significant difference between that of MgAl.31 and DNA:MgAl.31, further supporting the postulation of incomplete/partial ion-exchange.

3.2 NUCLEASE DIGESTION ASSAY

3.2.1 Introduction

The ultimate fate of a carrier: DNA complex designed for gene delivery purposes, is the successful introduction of these complexes into a mammalian system and finally the subsequent release of bound DNA within the cell. All complexes whether introduced orally in a tablet / liquid form, applied to the skin or injected intravenously – must enter the blood stream where it encounters serum nucleases. Serum nuclease enzymes degrade nucleic acid molecules [119-121]. The second obstacle that these complexes need to overcome is the immune system and any undesired cytotoxic effects. This will be further discussed in cytotoxicity studies (Section 3.3). Finally, if the complex is able to enter into cells and subsequently release the bound DNA, does the DNA remain in an integral form? To address this question, a nuclease digestion assay is carried out in order to evaluate the affects of serum nuclease digestion as well as to determine if the DNA remains in an integral form once released into the cell.

In this assay, DNA:carrier (HT/LDH) complexes are prepared as determined by the gel retardation assay i.e. the optimum DNA binding ratio as well as the ratio above and below optimum DNA binding are used. These complexes are then subjected to 10 % serum which contains nucleases- thus mimicking the environment that these complexes would come into contact with in the blood stream *in vivo*. After exposure to nuclease enzymes, a chelating agent is added to bind ions used by nuclease enzymes and thus inactivating the enzyme, ceasing nuclease digestion. Thereafter these complexes are subjected to a detergent which disrupts the interaction of the DNA and the carrier, releasing the DNA into solution. This solution is then subjected to agarose gel electrophoresis and hence the extent of nuclease digestion and the integrity of the DNA are visualized. When nucleases act on DNA, the DNA is broken down into smaller fragments, which will migrate differently depending on their size. They generally appear as a smear of bands on an agarose gel. Thus the appearance of smearing of DNA is evidence that the DNA bound to the carrier:DNA complex has been degraded by nucleases. This confirms that the carrier offers little protection against nuclease digestion.

The alternate situation would be that the carrier did afford some protection and hence the absence of smeared bands and the presence of distinct bands (three bands, depending if all forms of DNA were present) is evidence that no nuclease digestion occurred. Thus the released DNA remains in an integral form and is not degraded and migrates as would 'free' DNA that has not been subjected to any form of digestion (i.e. standard control DNA). Thus for complexes that exhibit protection from nuclease digestion; one can assume that once introduced into the blood stream the bound DNA will remain integral from the time of administration up and until the complex reaches the nucleus of the cell where it is expressed.

3.2.2 Materials and methods

Reaction samples were prepared according to gel retardation complexes in the Table 3.1-4, prior to nuclease digestion. Thereafter, to each sample and control two (DNA only), 10 % $^{v}/_{v}$ FCS (*Gibco, Invitrogen*, N.Z, U.K & N.Y.) was added and the samples were incubated at 37^{o}C for 4 hours in a *Memmert* water bath. The nuclease digestion reaction was stopped by the addition of EDTA (*Merck,* Darmstadt, Germany) to the samples to a final volume of 10 mM. Thereafter 5 % ($^{v}/_{v}$) SDS ((*Merck,* Darmstadt, Germany) was added to each sample and the samples further incubated at 55^{o}C for 20 minutes. Thereafter 2 µl gel loading buffer was added into each sample and the samples were loaded onto an eight well 1 % agarose gel and run at 50 V for 120 minutes. For each agarose gel, two controls were run alongside the samples. The first (control one) being standard DNA (0.5 µg) in a buffered solution and control two, 'free' DNA (0.5 µg) subjected to nuclease digestion. After electrophoresis the gel was then removed and viewed under UV light in a *Syngene* G-box documentation system (*Vacutec*) and an image capture.

3.2.3 Results and discussion

From gel retardation assays for Mg-Al HT samples, complete retardation was observed for DNA:MgAl.31 and DNA:MgAl.34 complexes. Nuclease digestion assays performed on these complexes (Figures 3.13, 3.14 lanes 3, 4, 5 respectively) showed two distinct bands for both samples with DNA: MgAl.34 complexes showing lighter bands after addition of the detergent. Some DNA degradation was observed (smearing of bands similar to control lane two) in several of the gels. In addition, for all gels the majority of the DNA that was bound to the HT/LDH samples appeared to remain in the wells and was not sufficiently released upon addition of the detergent. The degradation for DNA bound to MgAl.31 and MgAl.34 samples, could provide further evidence that the DNA did not completely intercalate via ion exchange and hence, either bound to the peripheral of the HT exterior or in fact incomplete ion exchange occurred in which the DNA was partially intercalated leaving protruding DNA. From XRD and FTIR data the former was assumed. Thus if DNA bound to the exterior of the HT samples, little protection would have been provided to the DNA and nuclease digestion would occur. The subsequent release of DNA from the DNA:HT/LDH complexes after nuclease inactivation was carried out using an anionic detergent SDS. Although this detergent released DNA from the DNA:HT/LDH complexes, it was not totally efficient with some samples showing some DNA remaining in the well bound to HT/LDH samples. This could perhaps be due to the fact that SDS, due to its anionic nature as well as small size in relation to DNA, favoured intercalation (via ion exchange) into the DNA:HT/LDH complex thus resulting in partial release of DNA. Other methods of DNA release were attempted in place of SDS. These included the use of HCl and HNO_3 of varying concentration ranges (100 mM-1M), however these proved to give inconsistent results, in most cases inefficient release of DNA. Another method using a carbonate solution Na_2CO_3 [65] was carried out, however in all cases no DNA was released. Although not completely releasing all bound DNA, SDS appeared to be most reliable and consistent. HTs have been used as an antacid in medicine for a number of years and this is due to the fact that HT is capable of buffering the pH of the stomach at about pH 4 for extended periods of time [74]. This could explain the inefficient slow release of DNA using acid such as HCl/HNO_3. This

buffering mechanism appeared to be evident during release of DNA into cells as described in the transfection of mammalian cells in section 3.4. In addition, the slow controlled release of biomolecules and pharmaceutics from Mg-Al HTs and LDHs has been reported in literature [25-28, 67, 73, 122].

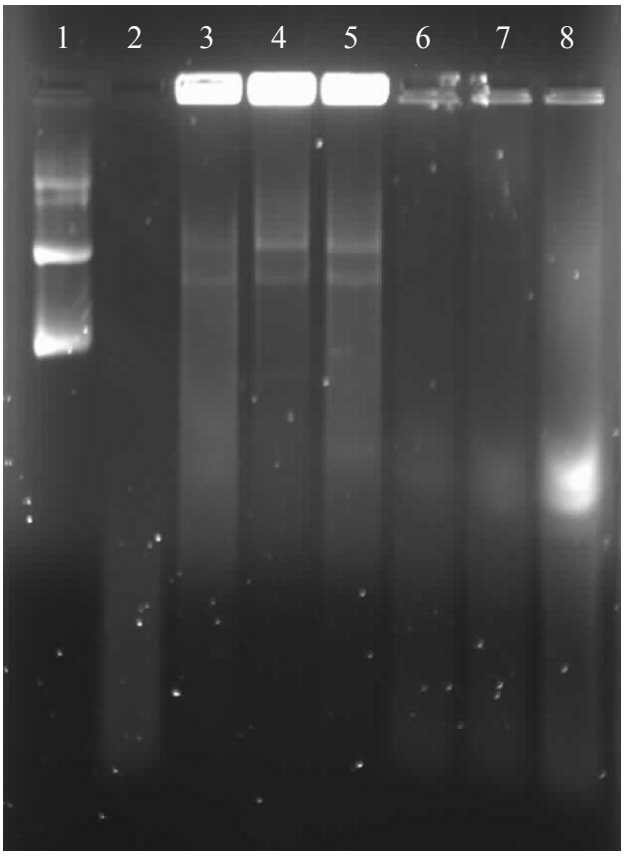

Figure 3.13 Nuclease digestion assay of MgAl.26 HT and MgFe.55 LDH.

Lane 1 = pCMV-GFP (0.5 μg)

Lane 2 = pCMV-GFP (0.5 μg) + 10% FCS

Lane 3 = 1:35 MgAl.26

Lane 4 = 1:40 MgAl.26

Lane 5 = 1:45 MgAl.26

Lane 6 = 1:25 MgFe.55

Lane 7 = 1:30 MgFe.55

Lane 8 = 1:35 MgFe.55

DNA was kept constant at 0.5 μg.

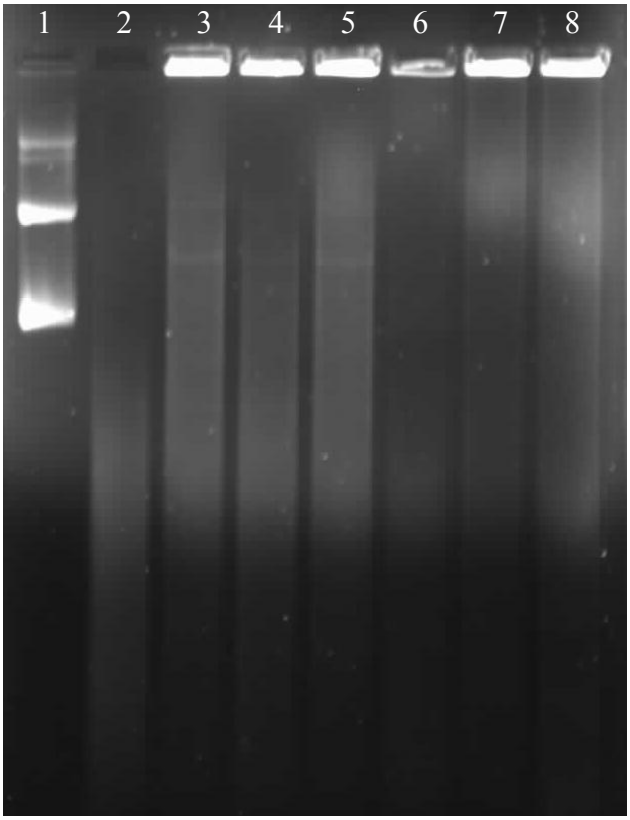

Figure 3.14 Nuclease digestion assay of MgAl.31 HT and MgFe.58 LDH.

Lane 1 = pCMV-GFP (0.5 μg)

Lane 2 = pCMV-GFP (0.5 μg) + 10% FCS

Lane 3 = 1:50 MgAl.31

Lane 4 = 1:55 MgAl.31

Lane 5 = 1:60 MgAl.31

Lane 6 = 1:45 MgFe.58

Lane 7 = 1:50 MgFe.58

Lane 8 = 1:55 MgFe.58

DNA was kept constant at 0.5 μg.

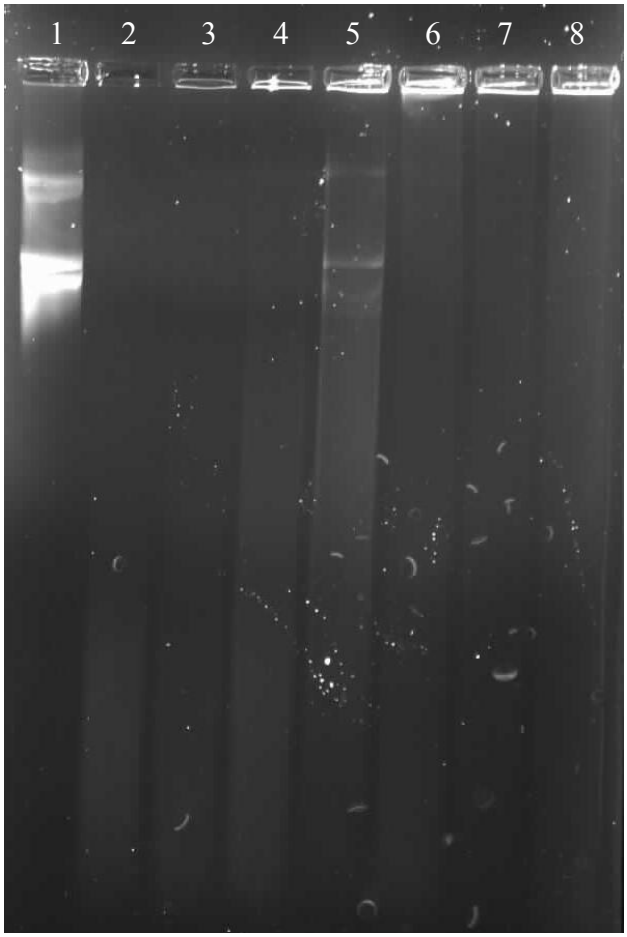

Figure 3.15 Nuclease digestion assay of MgAl.34 HT and MgFe.62 LDH.

Lane 1 = pCMV-GFP (0.5 μg)

Lane 2 = pCMV-GFP (0.5 μg) + 10% FCS

Lane 3 = 1:35 MgAl.34

Lane 4 = 1:40 MgAl.34

Lane 5 = 1:45 MgAl.34

Lane 6 = 1:30 MgFe.62

Lane 7 = 1:35 MgFe.62

Lane 8 = 1:40 MgFe.62

DNA was kept constant at 0.5 μg.

DNA degradation was also observed for MgAl.26 (Figure 3.13, lanes 3, 4, 5), however, this could be attributed to the fact that partial gel retardation was observed with unbound

DNA undergoing nuclease digestion. However, the notion of the DNA binding on the periphery of the HT samples, as described should also be taken into consideration.

All Zn-Al and Zn-Fe LDH samples showed partial retardation of DNA, with much of the DNA remaining unbound. As seen from nuclease digestion assays (Figures 3.16-18), this DNA was degraded as evident from the smearing of DNA down the gels. No distinct bands of released DNA was observed for most samples, with the exception of 1:30 ZnFe.30, 1:35 and 1:40 ZnFe.32 samples which showed released DNA.

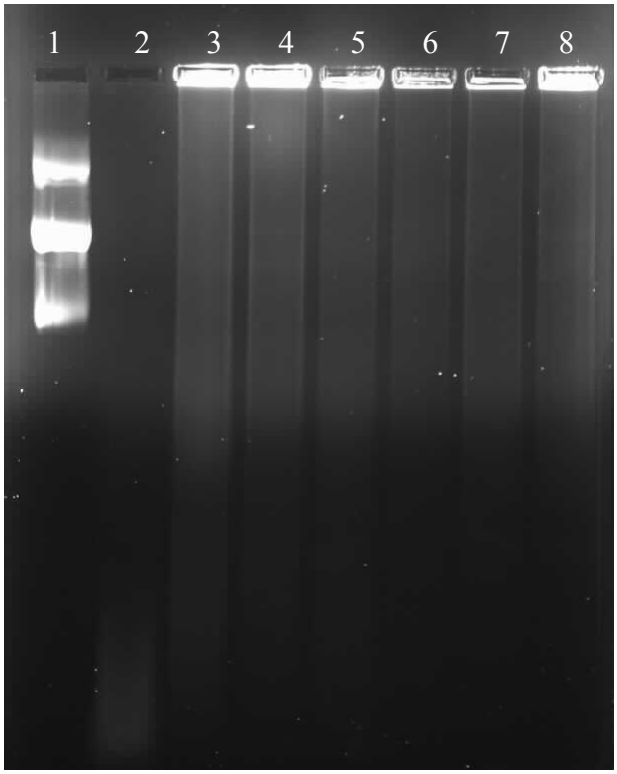

Figure 3.16 Nuclease digestion assay of ZnAl.11 LDH and ZnFe.24 LDH.

Lane 1 = pCMV-GFP (0.5 μg)

Lane 2 = pCMV-GFP (0.5 μg) + 10% FCS

Lane 3 = 1:60 ZnAl.11

Lane 4 = 1:65 ZnAl.11

Lane 5 = 1:70 ZnAl.11

Lane 6 = 1:30 ZnFe.24

Lane 7 = 1:35 ZnFe.24

Lane 8 = 1:40 ZnFe.24

DNA was kept constant at 0.5 μg.

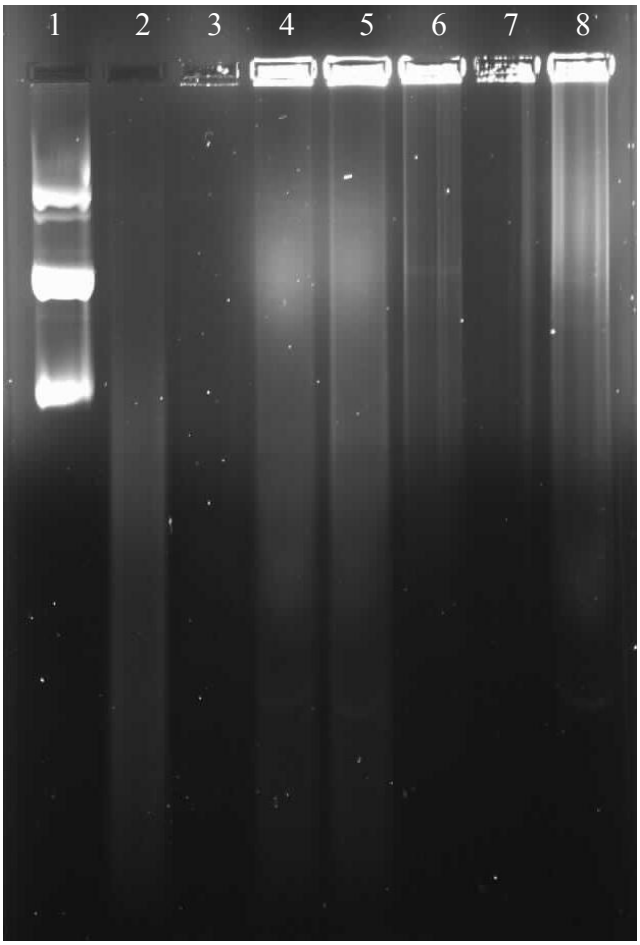

Figure 3.17 Nuclease digestion assay of ZnAl.14 LDH and ZnFe.30 LDH.

Lane 1 = pCMV-GFP (0.5 μg)

Lane 2 = pCMV-GFP (0.5 μg) + 10% FCS

Lane 3 = 1:40 ZnAl.14

Lane 4 = 1:45 ZnAl.14

Lane 5 = 1:50 ZnAl.14

Lane 6 = 1:30 ZnFe.30

Lane 7 = 1:35 ZnFe.30

Lane 8 = 1:40 ZnFe.30

DNA was kept constant at 0.5 μg.

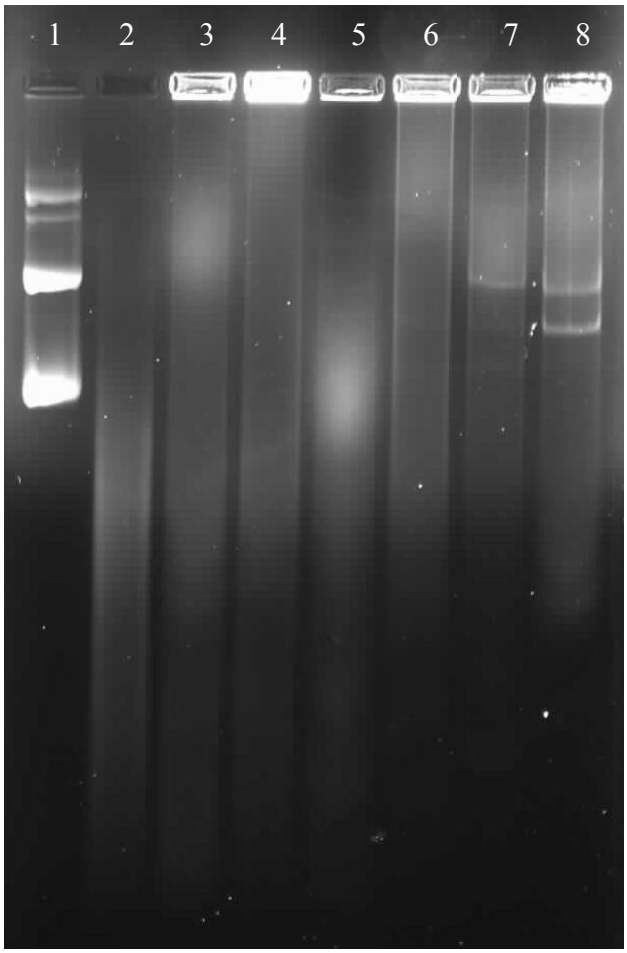

Figure 3.18 Nuclease digestion assay of ZnAl.16 LDH and ZnFe.32 LDH.

Lane 1 = pCMV-GFP (0.5 μg)

Lane 2 = pCMV-GFP (0.5 μg) + 10% FCS

Lane 3 = 1:40 ZnAl.16

Lane 4 = 1:45 ZnAl.16

Lane 5 = 1:50 ZnAl.16

Lane 6 = 1:30 ZnFe.32

Lane 7 = 1:35 ZnFe.32

Lane 8 = 1:40 ZnFe.32

DNA was kept constant at 0.5 μg.

Both MgFe.55 and MgFe.58 showed full retardation of DNA at 1:30 and 1:50 respectively. From nuclease digestion results (Figure 3.13, 3.14 lanes 6, 7, 8), DNA degradation was observed. However most of the DNA was not released as evident from

the DNA remaining within the well. MgFe.62 (Figure 3.15 lanes 6, 7, 8) showed DNA degradation; however this sample showed partial retardation with much unbound DNA remaining in solution.

Nuclease digestion gels showing bands of released DNA from respective samples (MgAl.26, MgAl.31, MgAl.34, ZnFe.32), showed that the migration of these bands did not appear to match that of the bands of free DNA (marker lane one)- this could be attributed to the fact that upon binding to the HT/LDH the released DNA underwent a conformational change appearing in one or more forms of DNA thus migrating differently, alternatively the addition of serum could have affected the released DNA's migration. Thus from nuclease digestion assays, although majority of the DNA was not released and remained bound to the HT/LDH, DNA degradation was evident. The degradation of DNA upon encountering serum can thus decrease the amount of delivered DNA into mammalian cells thus decreasing the delivery efficiency. Therefore these nuclease digestion results can be further supported in conjunction with transfection results.

According to Costantino et al. [123], the selectivity of anions within the interlayer of LDHs is as follows, $CO_2^{3-} > SO_4^{2-} >> OH^- > F^- > Cl^- > Br^- > NO_3^- > ClO_4^-$. Thus LDHs containing nitrate anions are the most suitable precursors for the uptake of biologically active species [123]. Thus the high electrostatic affinity of CO_2^{3-} potentially hinders the ion exchange of DNA into the HT/LDH interlayer region. This further supports the evidence obtained from XRD, FTIR as well as nuclease digestion assays that the DNA does not fully intercalate within the interlayer region of HTs/LDHs respectively.

3.3 CELL CULTURE AND CYTOTOXICITY STUDIES

3.3.1 Introduction

Prior to performing gene delivery experiments (transfection), the cytotoxicity of the HTs and LDHs to mammalian cells was investigated in order to determine a safe concentration range to be used.

In this study, human embryonic kidney (HEK293), hepatocellular carcinoma (HepG2) and cervical epithelial carcinoma (HeLa) mammalian cell lines where utilized in evaluating cytotoxicity. The cell viability in the presence of the various LDH materials can be determined by making use of a cell proliferation assay such as the MTS (3-(4,5-dimethylthiazol-2-yl)-5(3-carboxymethoxyphenyl)-2-(4-sulfophenyl)-2H-tetrazolium, inner salts) assay. The MTS assay is a relatively simple and quick colorimetric method used to measure dehydrogenase activity in metabolically active cells. Specifically, 3-(4,5-dimethylthiazol-2-yl)-5(3-carboxymethoxyphenyl)-2-(4-sulfophenyl)-2H-tetrazolium, inner salts (MTS) with the electron coupling reagent, phenazine methosulphate (PMS) [124], is reduced to formazan in the presence of metabolically active cells. Specifically, the reduction reaction by the enzyme dehydrogenase takes place in the mitochondria of metabolically active cells. The absorbance of the reduced formazan (soluble) is proportional to the number of viable cells in culture and hence one is able to determine the cell viability in relation to untreated control cells.

In the present study, divalent cations (M^{II}), Mg^{2+} and Zn^{2+} as well as trivalent cations (M^{III}), Al^{3+} and Fe^{3+} were selected in the preparation of hydrotalcite and LDH compounds. The choice of M^{II} and M^{III} was based upon the natural occurrence of these ions in the human body. Thus as these compounds were designed for studies on mammalian cells, the composition of these compounds was of significant importance so as to minimize toxic effects, if any; that these HT and LDH compounds could perhaps have in mammalian systems.

Magnesium (Mg) is the second most abundant intracellular cation in the human body. On average, a human adult exhibits a body content of 20-28 g of magnesium. The adult recommended daily allowance (RDA) for magnesium is 400-420 mg for men and 310 -

320 mg for women. According to Mahan and Escott-Stump [125], magnesium excesses from diet or supplementary sources are unlikely to result in toxicity; however a tolerable upper intake level is indicated at 350 mg/day for males and females.

Iron (Fe) is found throughout each cell in the body, with a total body content of about 5 g. The adult RDA for iron is 10 mg/day for men and 15 mg/day for women, although on average, men consume about 17 mg and women, 12 mg iron per day [126]. Toxicity of iron due to over dosage results when serum iron levels are greater than 180 mg/dl [125]. Wardlaw [126] states iron toxicity occurs when iron intakes exceed that of the RDA for prolonged period of times.

Zinc (Zn) is the second most abundant trace element after iron. Zinc is found to have a total body content or 2-3 g in an adult human. The RDA of zinc is 15 mg/day for men and 12 mg/day for women. On average, men consume about 15 mg and women, 9 mg zinc per day [126]. Mahan and Escott-Stump [125] indicate that the RDA for adult males is 11 mg/day and for women 8 mg /day. Zinc toxicity occurs in which zinc intake exceeds 2 g / day. However, both Wardlaw and Mahan and Escott-Stump indicate that zinc intakes over 100 mg/day results in gastrointestinal tract irritation, nausea and depression of the immune system [125, 126].

Aluminium (Al) is considered a non-essential trace element with no known biological requirement [127]. On average, adults will consume 2-5 mg/day from food and water sources. It has been shown clinically and experimentally that Al is toxic to bone, the central nervous system and the liver [127]. From clinical data involving patients being subjected to subcutaneous injections of alum-precipitated allergenic extracts for 2-4 weeks, the maximum allowance of Al was 0.85 mg/5000 protein-N units per day.

The nutritional data on the toxicity of trace elements such as, Mg, Zn, Fe and Al indicates that the amounts used in biochemical studies may not be toxic. Such amounts are in the micro-gram quantities, thus it is anticipated that DNA: HT/LDH compounds would exhibit little toxicity towards exposed HEK293, HepG2 and HeLa cells.

HEK293 cell line

HEK293 (Figure 3.19) is a human embryonic kidney derived cell line which has been widely used in cellular biology experiments due to their relative ease in propagation and transfection abilities in culture. The HEK293 cell line was originally generated in the 1970's by Frank Graham, in which normal cultures of human embryonic kidney cells were transfected with sheared adenovirus 5 DNA. It was determined that this transformation resulted in the insertion of a 4-5 kilobase fragment from the left arm of the viral genome into HEK DNA. The resultant cell line, Graham numbered as his 293rd experiment. i.e. HEK293 [105]. HEK 293 cells exhibit the following native receptor proteins; corticotrophin releasing factor type 1 receptor, sphingosine-1-phosphate receptors EDG1, EDG3, EDG5, muscarinic acetylcholine receptor M3 and transient receptors TRPC1,2,4,6 [105].

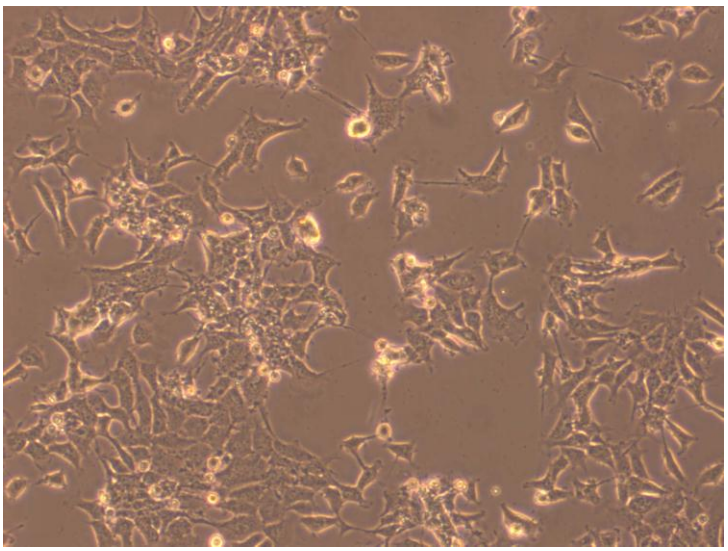

Figure 3.19 Image of HEK293 cells (x100) captured using an *Olympus* fluorescence microscope.

HepG2 cell line

HepG2 (Figure 3.20) is a human liver cell line isolated by Knowles et al. [128] from a teenage Caucasian male from Argentina with primary hepatoblastoma & hepatocellular carcinoma. It was initially derived from minces of hepatoma biopsy tissue placed on feeder layers of the mouse cell line STO [129], irradiated to the point of non-division.

Hepatoma sub-lines were selected after several months by feeder-independent *in vitro* growth in minimum essential medium (MEM) supplemented with fetal calf serum. After serial passage in MEM more than 50 times, HepG2 cells were reported to have continuing chromosome abnormalities (i.e. between 50 & 56 chromosomes) with characteristic rearrangement of chromosome one, in addition they were shown to retain the morphology and many of the biosynthetic capabilities of normal liver cells [130]. Thus as HepG2 expresses many morphological and biosynthetic capabilities of normal liver cells, for example; triglyceride and cholesterol metabolism; the HepG2 cell line is thus an ideal cell line in order for one to study fundamental functions of the liver. In addition to liver-specific metabolic functions, HepG2 also expresses many receptors; of which the asialoorosomucoid (AOM) receptor is found exclusively in the liver cells, thus making the HepG2 cell line important when undergoing studies relating to targeting of specific receptors on specific cells in gene therapy strategies.

HepG2 cells are also used in the study of the regulation of hepatic protein synthesis by cytokines (e.g. acute phase proteins) [131], as well as cancer and apoptosis studies [132].

In addition HepG2 cells are found to contain numerous amounts of mitochondria, which makes the HepG2 cell line ideal in the study of mitochondrial toxicity experiments.

HepG2 cells, when grown in culture flasks, adhere to the surface of the culture flask, forming a monolayer of cells; thus the HepG2 cells are not damaged/ lost when medium is removed/ renewed from the culture flask. A disadvantage of HepG2 cells is their unpredictability relating to their metabolism in adult human liver cells, as expression of drug-metabolizing enzymes are different to *in vivo* conditions [133].

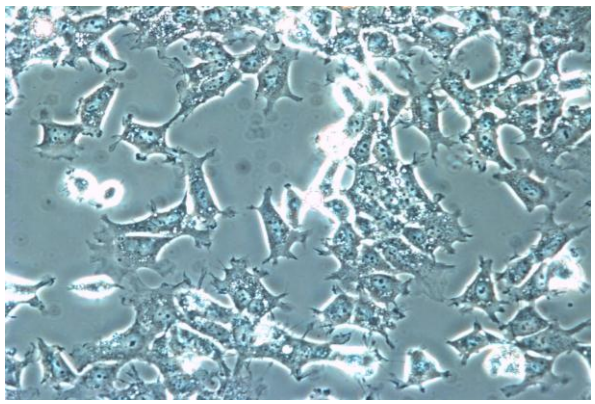

Figure 3.20 Image of HepG2 cells (x100) captured using an *Olympus* fluorescence microscope.

HeLa cell line

HeLa (Figures 3.21, 3.22) is human epithelial cell line which was derived from cervical cancer cells taken from a Ms Henrietta Lacks, who died from her cancer in 1951. HeLa cells originated from a fatal cervical carcinoma transformed by the human papillomavirus 18 (HPV18). As the HeLa cells were originally taken from a biopsy from Ms Lack's cervix in her diagnosis of her cervical carcinoma; these cells are treated as cancer cells.

HeLa cells proliferate abnormally quickly, even compared to other cancer cells. In addition, HeLa cells have an active version of the enzyme telomerase during cell division, which prevents the shortening of telomeres that is implicated in aging and eventual cell death. Thus due to the HeLa cells containing telomerase; aging and cell death is unlikely to occur; which results in the HeLa cells evading the Hayflick Limit, which is the threshold number of cell divisions that normal cells undergo before dying out in a cell culture.

The HeLa genome was formed by the horizontal gene transfer from human papillomavirus 18 (HPV18) to human cervical cells. Notably, HeLa cells have a chromosome number of 82, with four copies of chromosome 12 and three copies of chromosome 6, 8, and 17, which is different from both the contributing parent genomes.

HeLa cells; like HepG2 cells, when grown in culture flasks, adhere to the culture flask forming a monolayer of cells. In addition HeLa cells maintain contact inhibition *in vitro*; in that, as the cells multiply across the surface of the culture flask, when two adjacent cells come into contact with one another, the cells will signal to stop growing. A loss of contact inhibition is a typical sign of tumour cells (oncogenic cells). Such cells not only form a monolayer in culture but also stack up on top of one another forming clumps of cells (tumours). Generally HeLa cells are not oncogenic in animals, however; they may become oncogenic if further transformed by a viral oncogene.

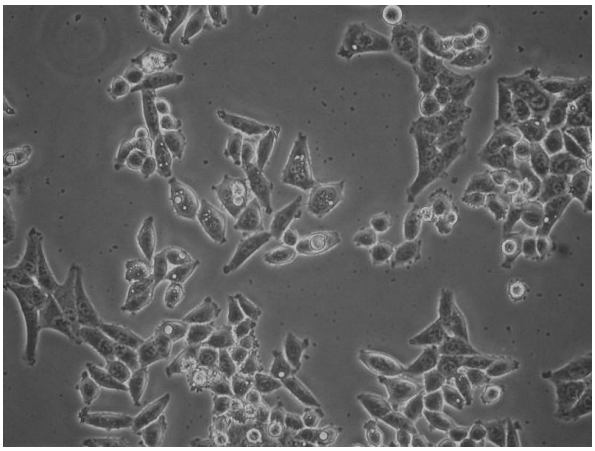

Figure 3.21 Phase contrast image of HeLa cells in culture (x100) [134]**.**

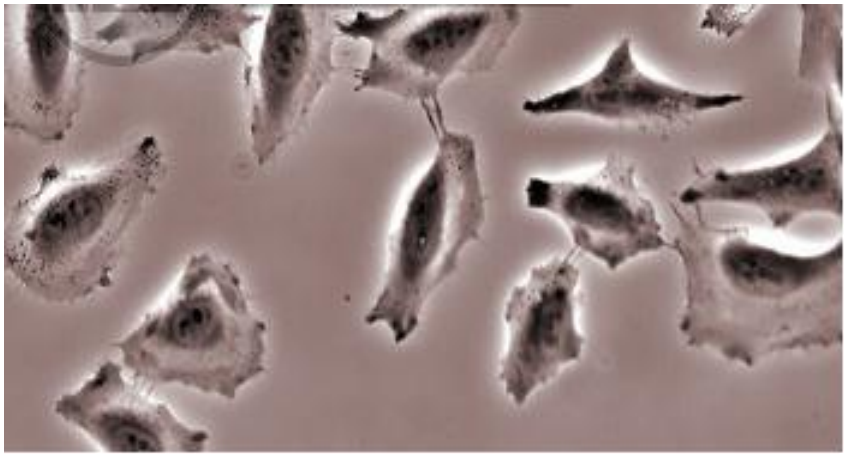

Figure 3.22 Image of HeLa Cells in culture (x200) [135]**.**

3.3.2 Materials and methods

3.3.2.1 Preparation of culture medium

One packet of minimum essential medium (MEM) + glutamine (*Gibco, Invitrogen*, N.Z, U.K & N.Y) was emptied into a sterile 2 litre glass beaker. Thereafter 900 ml of 18 Mohm water was added and mixed thoroughly using a magnetic stirrer, upon which, 10 mM $NaHCO_3$ (*Merck,* Darmstadt, Germany) was added. This was followed by the addition of 20 mM HEPES (*Merck,* Darmstadt, Germany) and 10 ml Penicillin/ streptomycin antibiotic mixture (*Gibco, Invitrogen*, N.Z, U.K & N.Y. 10 000 units penicillin/streptomycin / ml mixture). This solution was then made up to the 1 litre mark with 18 Mohm water and the pH was corrected to the optimum range of 7.3-7.4. The medium was then filtered through a 0.22 μm *Sterivex* milipore bell filter using a *Masterflex*® automatic peristaltic dispenser pump, into 5 equal 200 ml aliquots in sterile 250 ml wide-neck blue cap Schott bottles. Thereafter the medium was labeled and stored in the refrigerator at 4^{o}C. Prior to use, the medium was replenished with 10% Fetal calf serum (FCS) (*Gibco, Invitrogen*, N.Z, U.K & N.Y).

3.3.2.2 Preparation of buffers

Phosphate buffered saline (PBS) (pH = 7.3-7.4)

Approximately 140 mM NaCl, 4 mM KCl, 0.88 mM KH_2PO_4 (anhydrous) and 7.5 mM NaH_2PO_4 (anhydrous) (*Merck,* Darmstadt, Germany) were made up in 18 Mohm water to a total volume of one litre. The pH was adjusted and the solution autoclaved and stored in the refrigerator at 4^{o}C.

HEPES buffered saline (pH = 7.3-7.4)

Approximately 20 mM HEPES and 150 mM NaCl (*Merck,* Darmstadt, Germany) were made up in 18 Mohm water to a total volume of one litre. The pH was adjusted and the solution autoclaved and stored in the refrigerator at 4^{o}C.

3.3.2.3 Reconstitution of cells

Cells contained in cryovials which were previously frozen in a *NuAire -86 ^{o}C Ultralow biofreezer* were removed from the biofreezer using protective gloves and subsequently allowed to thaw in their vials in a water bath; set at 37 ^{o}C. Fetal calf serum and medium were removed from the refrigerator and placed in the 37 ^{o}C water bath. Once the cells were thawed and the FCS and medium had reached 37 ^{o}C; the vial containing the cells and the bottles containing the medium and FCS were wiped with 70% ethanol. The cells were then pelleted at 1000 rpm for 5 minutes and the tube containing the pelleted cells was opened aseptically in a class III biohazard safety cabinet. The medium (supernatant) was decanted and was reconstituted in 1 ml fresh medium, which contained 10% FCS. The cells were then transferred to a 25 cm^2 flask containing 5 ml complete medium (MEM, 10% FCS). The flask was then placed in a *Zenith* incubator set at 37 ^{o}C, and allowed to incubate overnight. The cells were allowed to attach to the flask before the medium was replenished and any cryoprotective medium or dead cells would be removed. HEK293 cells were obtained from The University of Witwatersrand, RSA. HepG2 cells and HeLa cells were obtained from *Highveld Biologicals*, Gauteng, RSA.

3.3.2.4 Trypsinization of cells

Subculturing was done when the cells were near or at confluency. The culture flask was removed from the incubator and the medium was decanted into a sterile waste bottle and the bottles neck was flamed in a class II biohazard safety cabinet. The cells in the culture flask were then washed with 5 ml PBS. Approximately 1 ml of Trypsin / Versene (*Gibco, Invitrogen*, N.Z, U.K & N.Y.) was added to cover the cells. Trypsinization was allowed to occur at room temperature for 1-5 minutes (depending on enzyme activity and type of cell line used). The culture flask was then placed on the stage of a *Nikon* TMS inverted microscope and the rounding off of the cells was observed (magnification, 10x). After this rounding off of cells, the culture flask was tapped against the palm of ones hand causing the trypsinized cells to dislodge off the flask surface. The cells were reconstituted with 2 ml of MEM containing FCS at least 10 times the volume of Trypsin / Versene in

order to inhibit the enzyme. The cells were then split (1:2) into separate 2 x 25 cm^2 flasks each containing, 5 ml MEM and 10% FCS. The cell suspension was drawn up and expelled repeatedly, using a sterile 1 ml pipette, to evenly distribute the cells before they were divided into the 25 cm^2 flasks. Cells were then incubated at 37 ^oC. Cells were subcultured every 2 - 3 days or when the cells were near or at confluency.

3.3.2.5 Cell count

Cells were successfully propagated in MEM +10 % FCS and trypsinized. After trypsinization, cells were observed on a *Nikon* TMS inverted microscope (magnification, 10x) and approximately 0.1 ml of the trypsinized cells were placed on a hemacytometer.

3.3.2.6 MTS cell proliferation assay

Cells were trypsinized and seeded into a 48 well plate at a seeding density of 3.5-4 x 10^5 cells / well and were incubated overnight in a *Zenith* incubator set at 37^oC, allowing cells to attach to the wells and grow to semi-confluency. The medium was then removed and replaced with 0.2 ml of serum free medium. Thereafter the respective compounds were added as depicted in Table 3.6. The same LDH concentration was utilized for all other LDH samples and a similar culture plate layout was employed for each compound throughout all cell lines. The details of which are shown in the appendix (Tables A17-A19).

Table 3.6 Culture plate arrangement indicating concentration (µg/10 µl) of each Mg-Al HT sample added into each well.

Well	**2**	**3**	**4**	**5**	**6**	**7**	**8**
A1 (Control) Cells	40 MgAl.26	80 MgAl.26	20 MgAl.31	60 MgAl.31	100 MgAl.31	40 MgAl.34	80 MgAl.34
B (Control) Cells	40 MgAl.26	80 MgAl.26	20 MgAl.31	60 MgAl.31	100 MgAl.31	40 MgAl.34	80 MgAl.34
C (Control) Cells	40 MgAl.26	80 MgAl.26	20 MgAl.31	60 MgAl.31	100 MgAl.31	40 MgAl.34	80 MgAl.34
D 20 µg MgAl.26	60 MgAl.26	100 MgAl.26	40 MgAl.31	80 MgAl.31	20 MgAl.34	60 MgAl.34	100 MgAl.34
E 20 µg MgAl.26	60 MgAl.26	100 MgAl.26	40 MgAl.31	80 MgAl.31	20 MgAl.34	60 MgAl.34	100 MgAl.34
F 20 µg MgAl.26	60 MgAl.26	100 MgAl.26	40 MgAl.31	80 MgAl.31	20 MgAl.34	60 MgAl.34	100 MgAl.34

The cells were then incubated at 37 ^{o}C for 4 hours, after which, the medium was then removed and replaced with 0.2 ml complete medium into each well. This was followed by further incubation of the cells at 37 ^{o}C for 48 hours. Approximately 10 minutes before the completion of the 48 hour incubation time, CellTiter 96® Aqueous One Solution Reagent (*Promega Cooperation*, Madison, USA) was thawed out for 10 minutes in a 37 ^{o}C water bath. Thereafter 40 µl of One Solution Reagent was added into each well containing 0.2 ml medium. The plate was further incubated for 4 hours at 37 ^{o}C. On completion of this incubation period, the contents of each well were read at 490 nm using a *Biomate 3* scientific spectrophotometer and absorbance values noted.

3.3.3 Results and discussion

Mg-Al HT samples showed little toxicity in all cell lines with cell viability in the range of 80-100 % for most Mg-Al samples. With exceptions of MgAl.26 (20 μg / 10 μl) exposed to HepG2 cells and MgAl.34 (20 μg / 10 μl) exposed to HeLa cells (Figures 3.24 and 3.25 respectively) which showed a cell viability slightly lower than 80 %. There does not appear to be any trend with respect to the three different Mg-Al HT samples over the concentration range in all the cell lines. There does however appear to be a similar trend in toxicity in comparison to Zn-Al LDH samples. All comparisons of trends in toxicities discussed are based upon the overall trends over the entire concentration range from 0-100 μg / 10 μl and not individually for each sample. When comparisons of individual samples are made, these comparisons are based upon samples containing the most or least amount of trivalent cation. i.e. MgAl.26 and ZnAl.11 may be compared, based upon the fact that both samples contain the highest amount of divalent cation with respect to the other samples of the same composition. Just as MgAl.34 and ZnAl.16 may be compared since both samples contain the least amount of trivalent cation.

Figures 3.23 and 3.26 over the exposed concentration range show a very similar trend with an average cell viability of 90-100 % and 80 % respectively. Figures 3.24 and 3.27 show a similar trend across the exposed concentration range with an average cell viability of 90-100 % and 80-85 % respectively. In both cases the cell viability for 20 μg / 10 μl of MgAl.26 (Figure 3.24) and ZnAl.11 (Figure 3.27) show a cell viability of 54 % which subsequently increases. ZnAl.16 (Figure 3.27) shows a slightly different trend to that of MgAl.34 (Figure 3.24). Overall, the cell viability of Mg-Al HTs and Zn-Al LDHs is very similar in the HepG2 cell line. Figures 3.25 and 3.28 show similar trends across the exposed concentration range with the exception of MgAl.31, MgAl.34 and ZnAl.14, ZnAl.16 at concentrations of 20 μg / 10 μl (Figures 3.25 and 3.28 respectively).

As Al is constant throughout all Mg-Al HT and Zn-Al LDH samples with slight changes in Mg or Zn content it is thus not unexpected that there are similar trends in toxicities. In all cell lines in the exposed concentration ranges it appears that the divalent cation is responsible for decreases in cell viabilities. However the combination of Zn and Al, in relation to Mg-Al HTs, appears to decrease the cell viability to 80 % as apposed to an

average of mostly 100% for Mg-Al HT samples. Both Mg-Al and Zn-Al samples appear to be well tolerated by all three cell lines (with exception of 20 µg / 10 µl of MgAl.26 (Figure 3.24) and ZnAl.11 (Figure 3.27) in the HepG2 cell line). The low toxicity of Mg-Al HTs is consistent with literature [25-28, 67, 89, 135, 137].

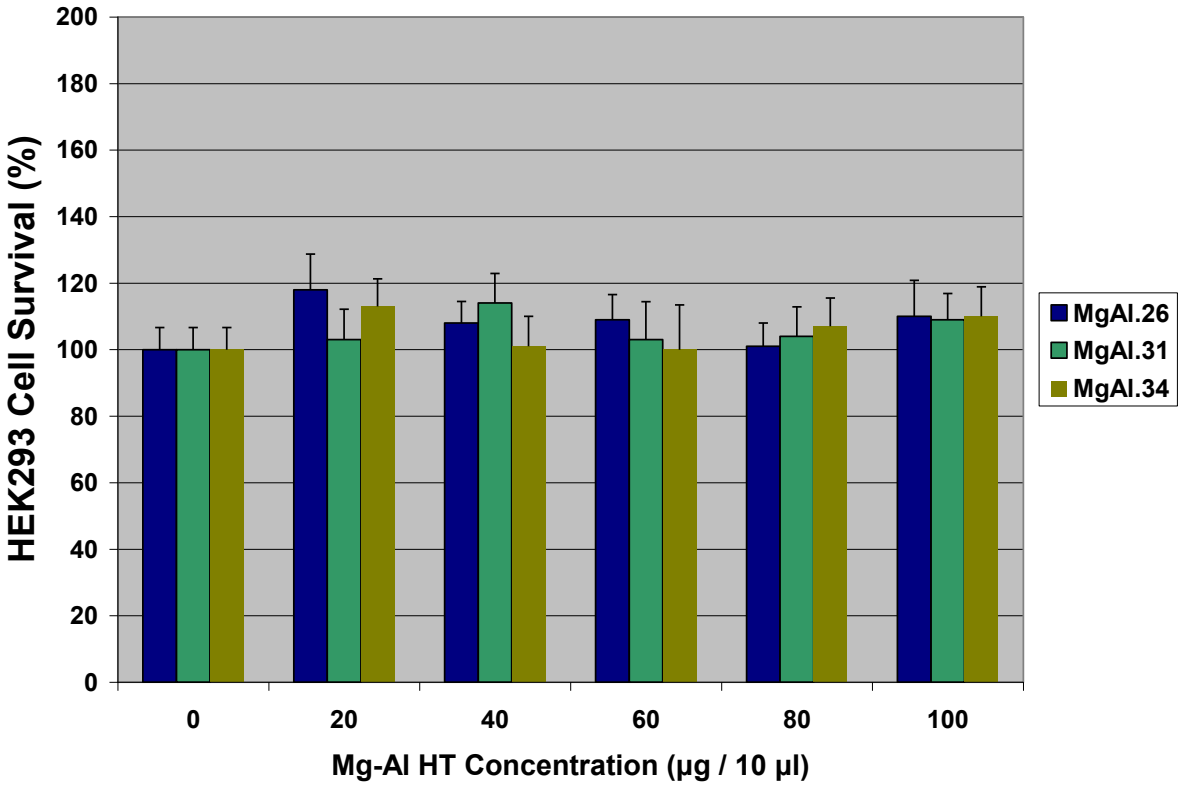

Figure 3.23 MTS cell proliferation assay of HEK293 cells exposed to Mg-Al HTs. HT concentration was varied (0, 20, 40, 60, 80, 100 µg). A control sample (0 µg HT) containing only HEK293 cells was assumed to have 100 % survival. Data are presented as means ± SD (n = 3).

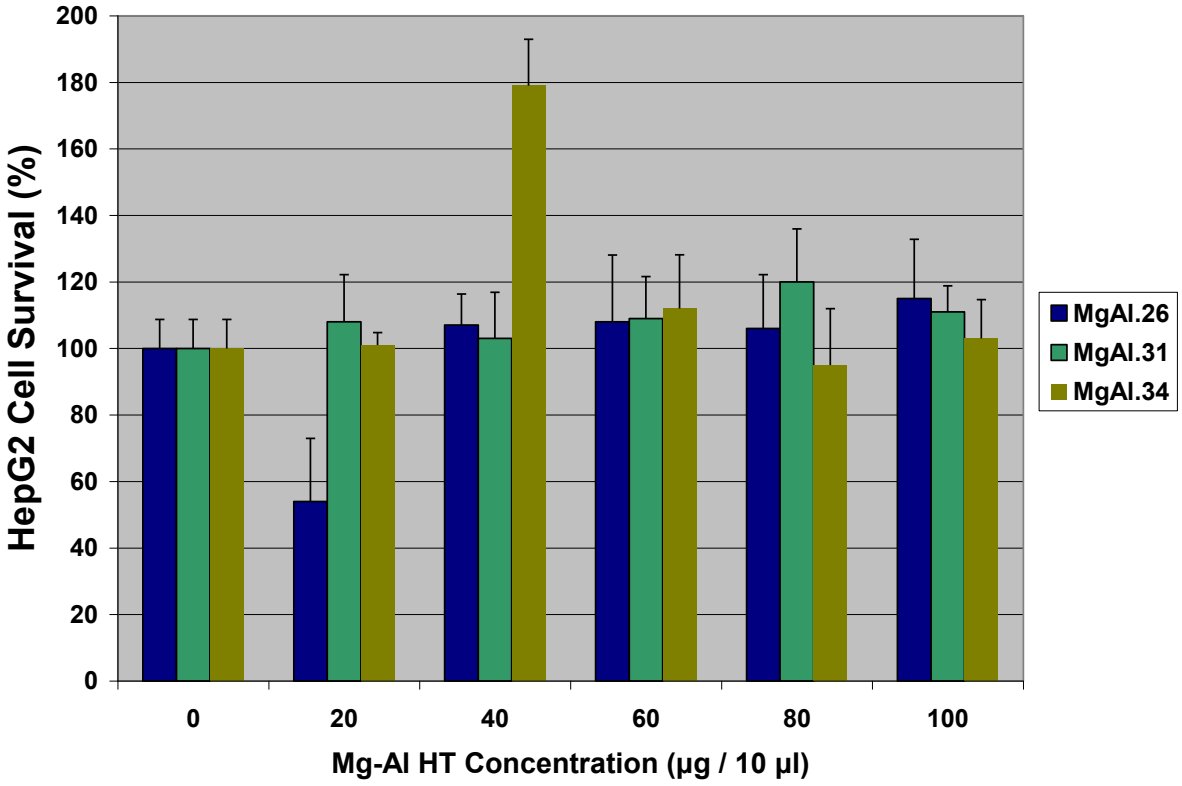

Figure 3.24 MTS cell proliferation assay of HepG2 cells exposed to Mg-Al HTs. HT concentration was varied (0, 20, 40, 60, 80, 100 µg). A control sample (0 µg HT) containing only HepG2 cells was assumed to have 100 % survival Data are presented as means ± SD (n = 3).

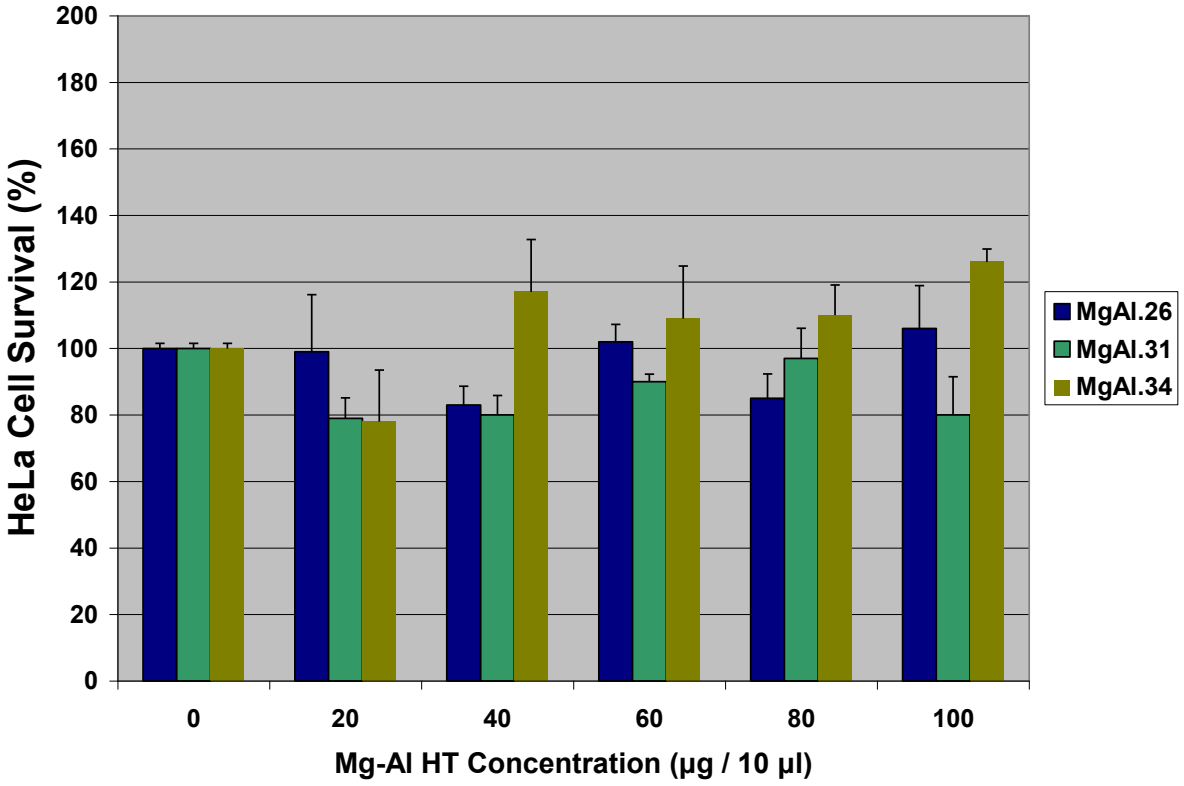

Figure 3.25 MTS cell proliferation assay of HeLa cells exposed to Mg-Al HTs. HT concentration was varied (0, 20, 40, 60, 80, 100 µg). A control sample (0 µg HT) containing only HeLa cells was assumed to have 100 % survival. Data are presented as means ± SD (n = 3).

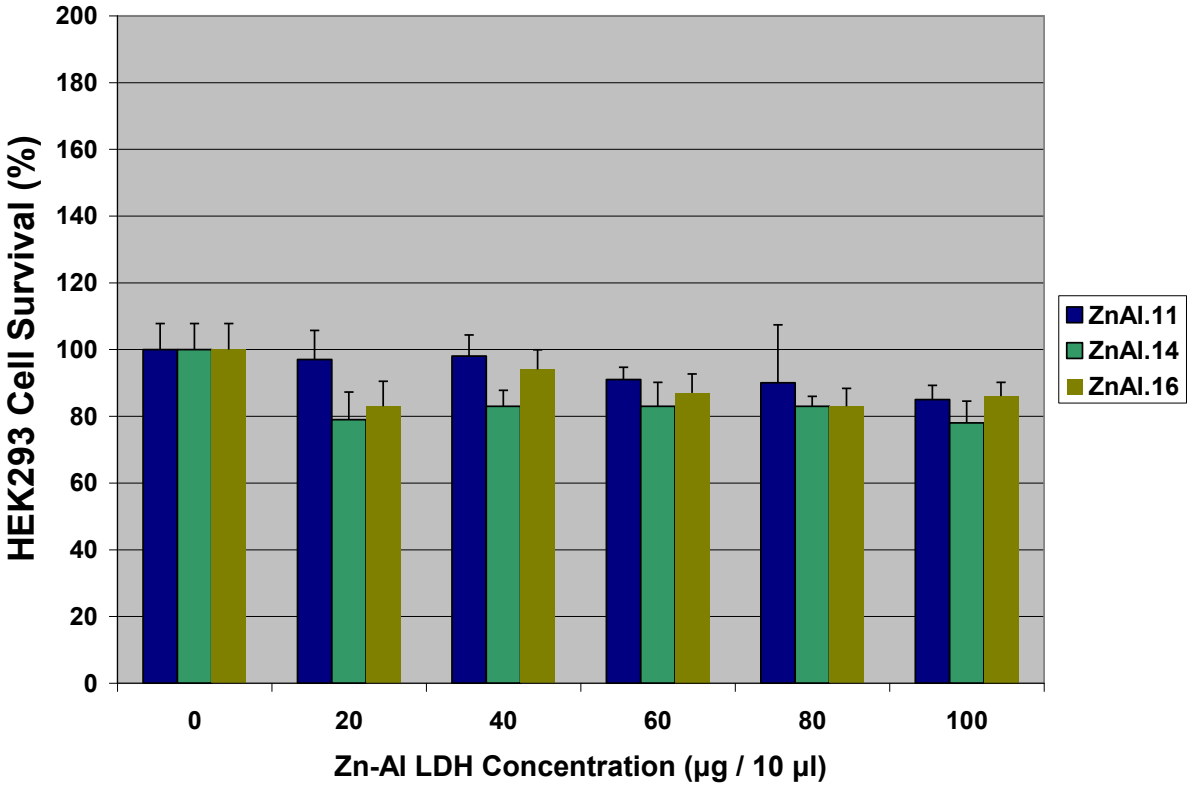

Figure 3.26 MTS cell proliferation assay of HEK293 cells exposed to Zn-Al LDHs. LDH concentration was varied (0, 20, 40, 60, 80, 100 µg). A control sample (0 µg LDH) containing only HEK293 cells was assumed to have 100 % survival. Data are presented as means ± SD (n = 3).

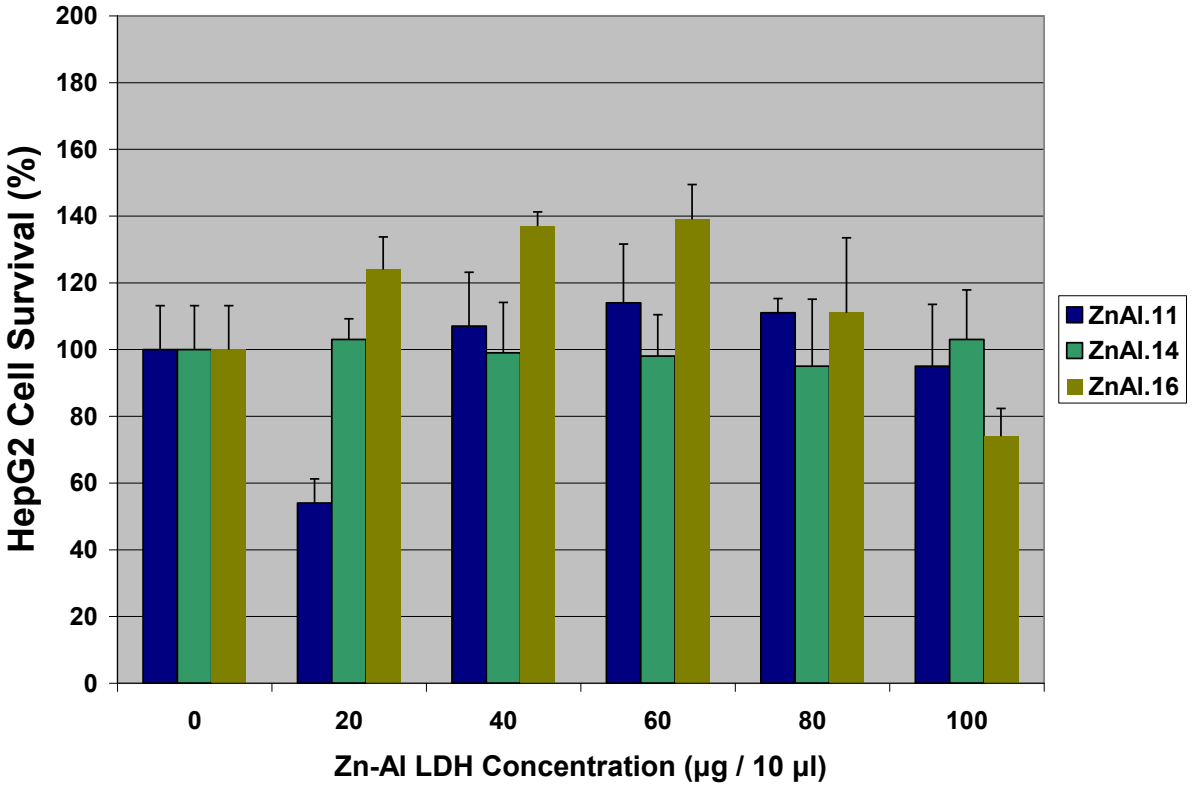

Figure 3.27 MTS cell proliferation assay of HepG2 cells exposed to Zn-Al LDHs. LDH concentration was varied (0, 20, 40, 60, 80, 100 µg). A control sample (0 µg LDH) containing only HepG2 cells was assumed to have 100 % survival. Data are presented as means ± SD (n = 3).

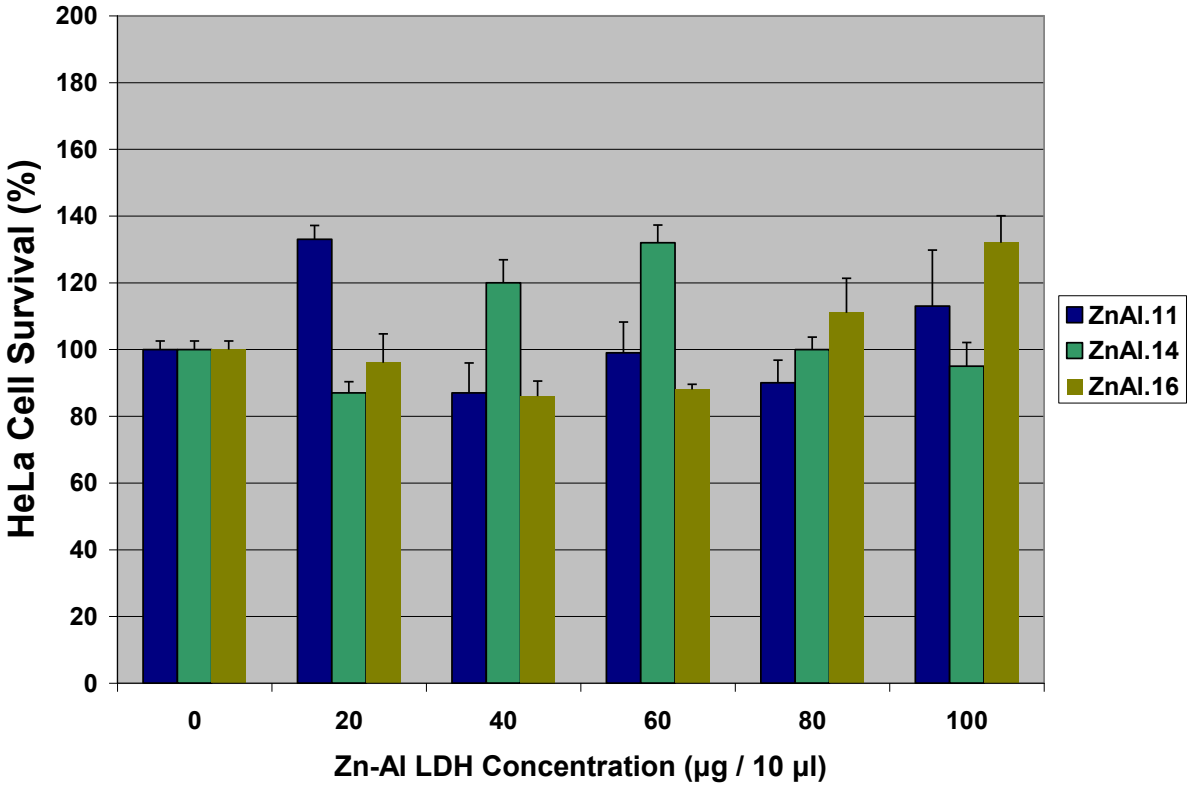

Figure 3.28 MTS cell proliferation assay of HeLa cells exposed to Zn-Al LDHs. LDH concentration was varied (0, 20, 40, 60, 80, 100 µg). A control sample (0 µg LDH) containing only HeLa cells was assumed to have 100 % survival. Data are presented as means ± SD (n = 3).

Zn-Fe LDHs showed an average cell viability of 80 % with the exception of ZnFe.24 (20-40 μg / 10 μl) and ZnFe.30 (30 μg / 10 μl) in the HepG2 cell line (Figure 3.30) which showed a cell viability of 68-70 % and 72 % respectively. Likewise with Mg-Al HT samples, there does not appear to be any trend with respect to the three different Zn-Fe LDH samples over the concentration range in all the cell lines. There does however appear to be a similar trend in toxicity in comparison to Mg-Fe LDH samples. Figures 3.29 and 3.32 show a similar trend of cell viability with an average cell viability of above 100 % for both Zn-Fe and Mg-Fe LDHs. However, Zn-Fe LDH cell viability decreases at 100 μg / 10 μl (Figure 3.29). In addition, 20 μg / 10 μl of MgFe.58 in the HEK293 cell line (Figure 3.32) shows an increased cell viability to that of 20 μg / 10 μl ZnFe.30 (Figure 3.29).

Both Zn-Fe and Mg-Fe LDH samples show a decrease in cell viability with an average cell viability of 80 % (Zn-Fe LDHs) and 80-85 % (Mg-Fe) in the HepG2 cell line (Figures 3.30 and 3.33 respectively). This is in stark contrast to both Zn-Fe (Figures 3.29 and 3.31) and Mg-Fe (Figures 3.32 and 3.39) LDH samples in the HEK293 and HeLa cell lines with an average cell viability in excess of 100 %. Zn-Fe LDH samples at 20 μg / 10 μl show a decrease in cell viability to a value of about 65-80 % (Figure 3.30). This lower cell viability for 20 μg / 10 μl is seen in Mg-Al HT and Zn-Al LDH samples in the HepG2 cell line. Mg-Fe LDHs show a higher cell viability in the HepG2 cell line. This is similar to the Zn-Fe LDHs in the same cell line.

Both Zn-Fe and Mg-Fe LDHs exhibit similar toxicity levels with an average cell viability in excess of 100 %. At 20 μg / 10 μl of MgFe.62 (Figure 3.34) shows a higher cell viability to that of ZnFe.32 (Figure 3.31) in the HeLa cell line. Overall, both Zn-Fe and Mg-Fe LDHs appear to be well tolerated within all three cell lines.

Based upon the similarities in toxicities of Zn-Fe and Mg-Fe LDHs, it appears that the LDH samples are least tolerated by the HepG2 cell line, yet cell viability remains on average above 80 %. Furthermore, out of all the samples synthesized, it appears that the presence of Fe in these LDH samples promotes cell growth with the highest cell viability values seen in the HEK293 and HeLa cell lines. The increase in cell proliferation could be due to the increased amounts of intracellular Fe which in turn increases the redox

potential and thus increases oxidative processes within the cells and hence the increase in cell viability.

Concentrations of HT and LDH samples used in gene delivery studies (transfection) are in the ranges of 35 - 40 μg / 10 μl (Mg-Al HTs), 40 - 70 μg / 10 μl (Zn-Al LDHs), 30 – 40 μg / 10 μl (Zn-Fe LDHs) and 25 – 55 μg / 10 μl (Mg-Fe LDHs). Cell viability in these ranges for each respective sample in all cell lines is on average in excess of 80%, with the exception of ZnFe.24, ZnFe.30 (20 - 40 μg / 10 μl) and MgFe.55 (40 μg / 10 μl) in the HepG2 cell line which showed cell viabilities of below 80 %. Thus the HT and LDH samples appear to be well tolerated within all cell lines. There appears to be no published data on the toxicity of Zn-Al, Zn-Fe or Mg-Fe LDHs in literature. Due to the similar structure, chemistry and binding studies that LDHs exhibit to that of HTs, it is thus not surprising that there was little toxicity associated with the synthesized LDHs.

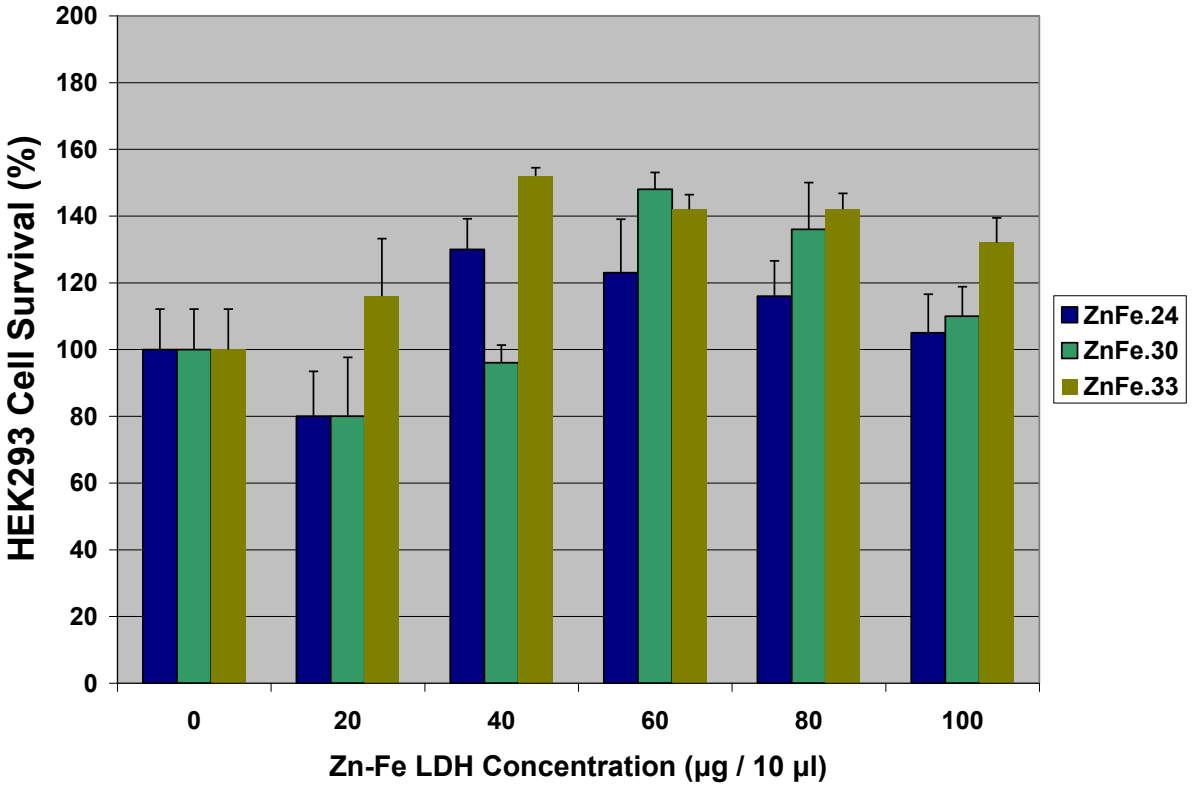

Figure 3.29 MTS cell proliferation assay of HEK293 cells exposed to Zn-Fe LDHs. LDH concentration was varied (0, 20, 40, 60, 80, 100 µg). A control sample (0 µg LDH) containing only HEK293 cells was assumed to have 100 % survival. Data are presented as means ± SD (n = 3).

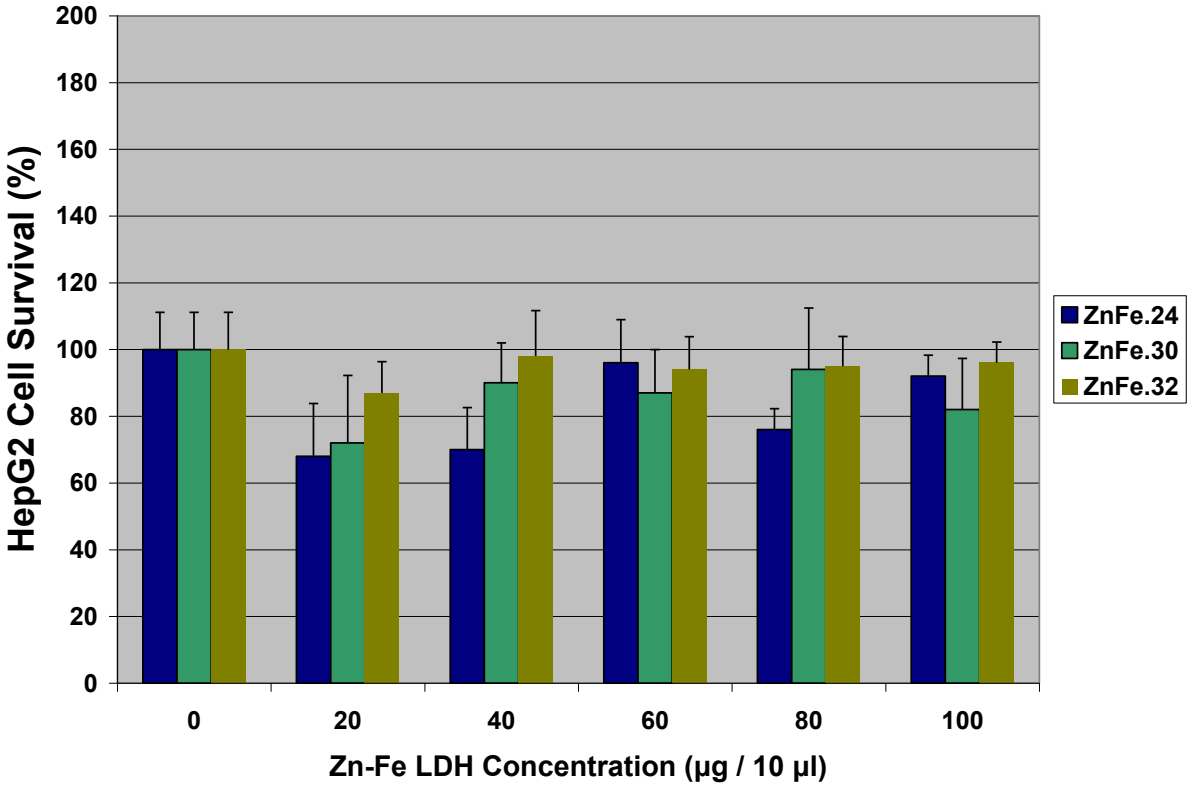

Figure 3.30 MTS cell proliferation assay of HepG2 cells exposed to Zn-Fe LDHs. LDH concentration was varied (0, 20, 40, 60, 80, 100 µg). A control sample (0 µg LDH) containing only HepG2 cells was assumed to have 100 % survival. Data are presented as means ± SD (n = 3).

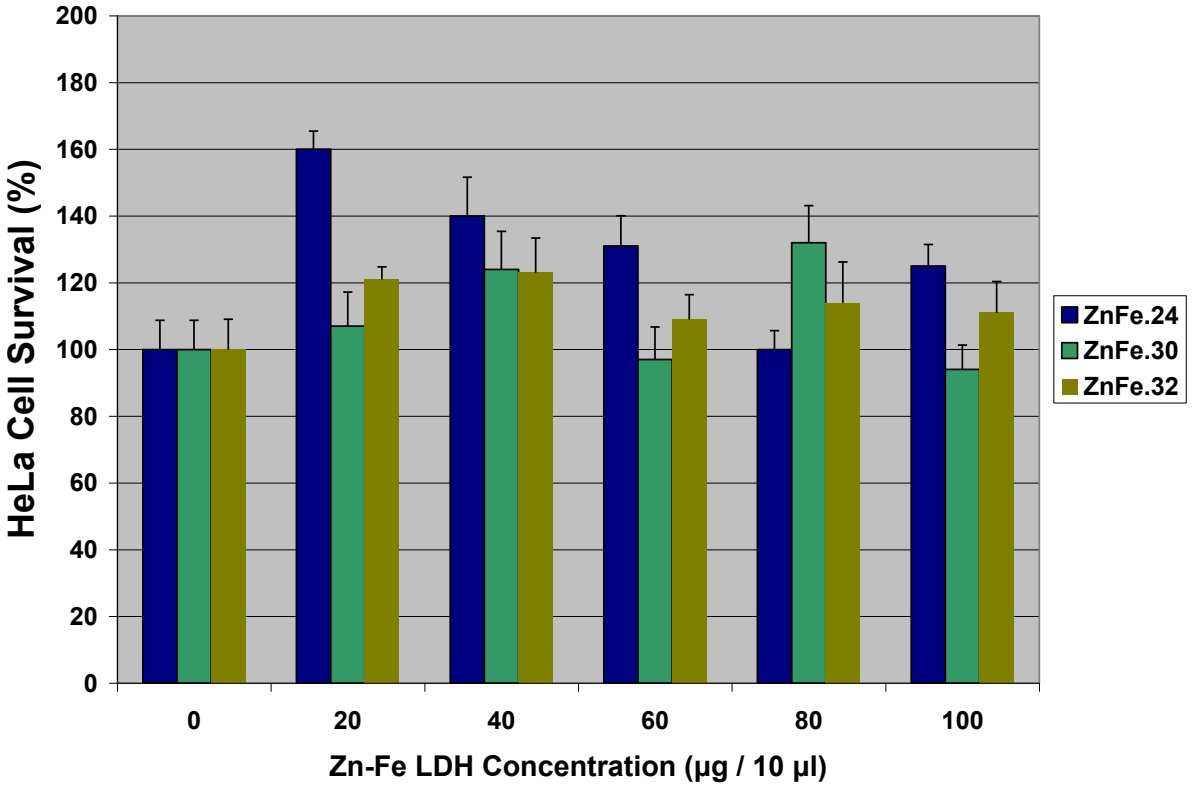

Figure 3.31 MTS cell proliferation assay of HeLa cells exposed to Zn-Fe LDHs. LDH concentration was varied (0, 20, 40, 60, 80, 100 µg). A control sample (0 µg LDH) containing only HeLa cells was assumed to have 100 % survival. Data are presented as means ± SD (n = 3).

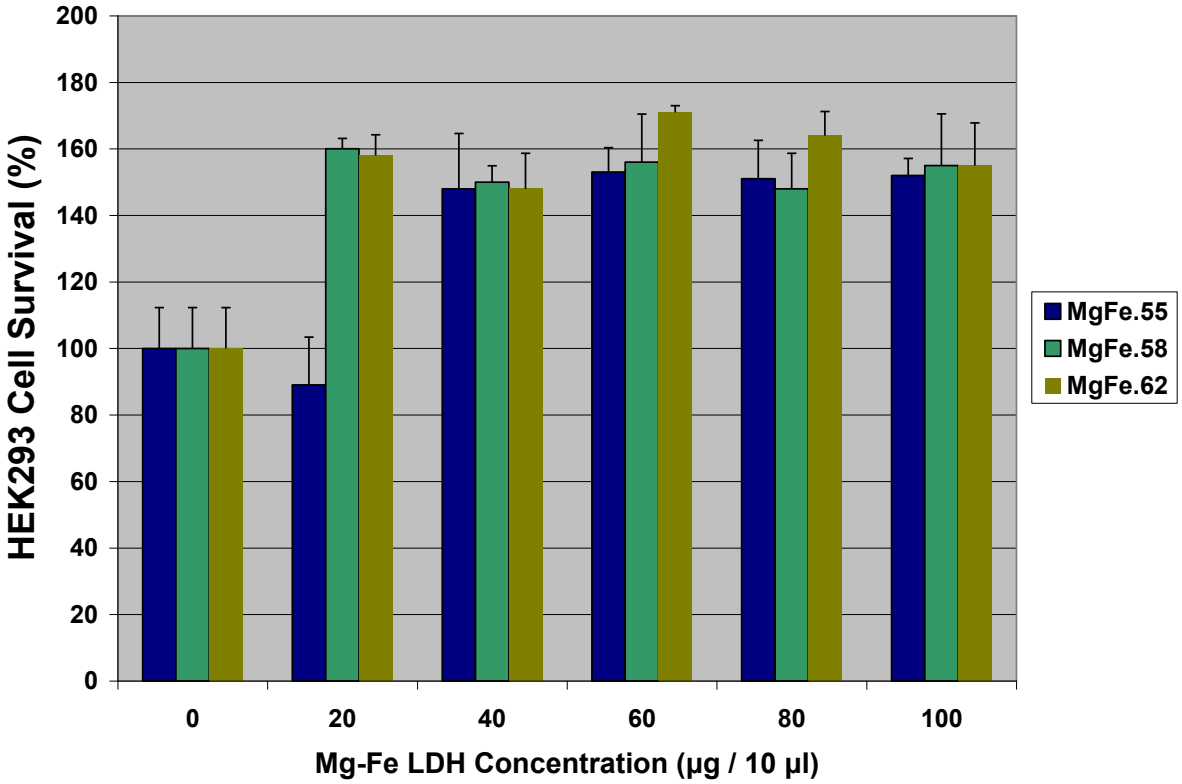

Figure 3.32 MTS cell proliferation assay of HEK293 cells exposed to Mg-Fe LDHs. LDH concentration was varied (0, 20, 40, 60, 80, 100 µg). A control sample (0 µg LDH) containing only HEK293 cells was assumed to have 100 % survival. Data are presented as means ± SD (n = 3).

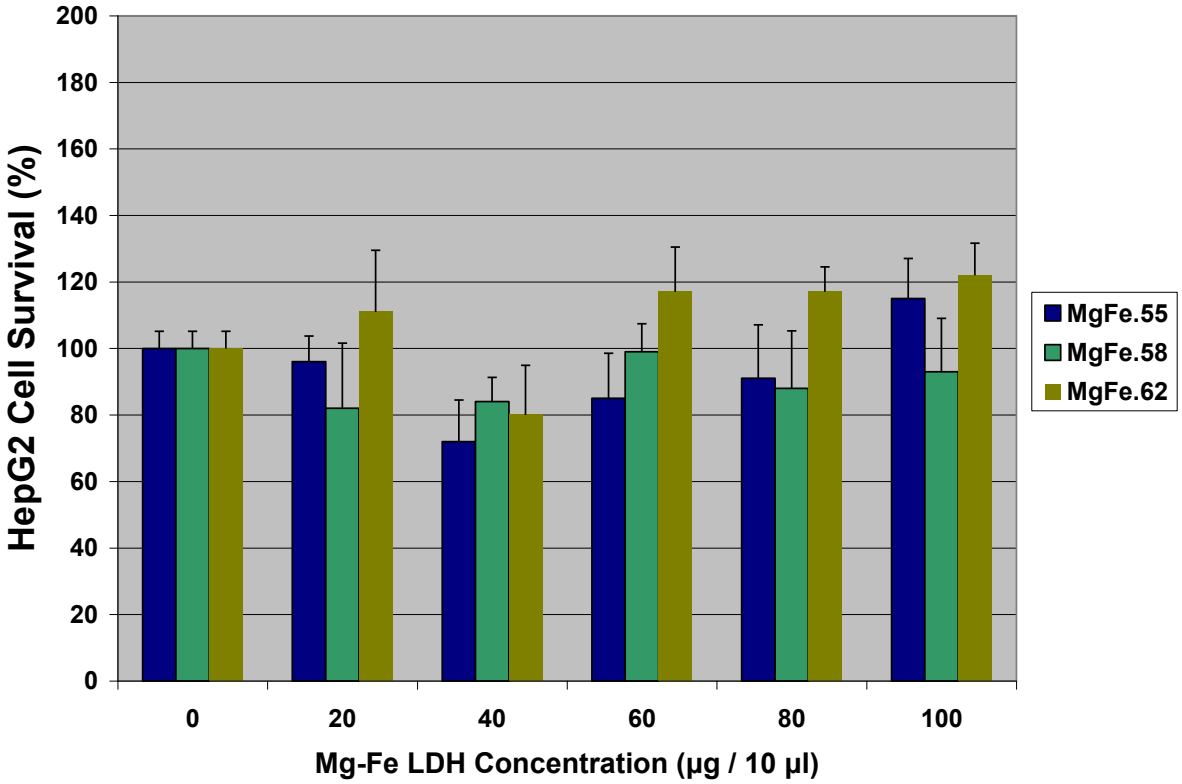

Figure 3.33 MTS cell proliferation assay of HepG2 cells exposed to Mg-Fe LDHs. LDH concentration was varied (0, 20, 40, 60, 80, 100 µg). A control sample (0 µg LDH) containing only HepG2 cells was assumed to have 100 % survival. Data are presented as means ± SD (n = 3).

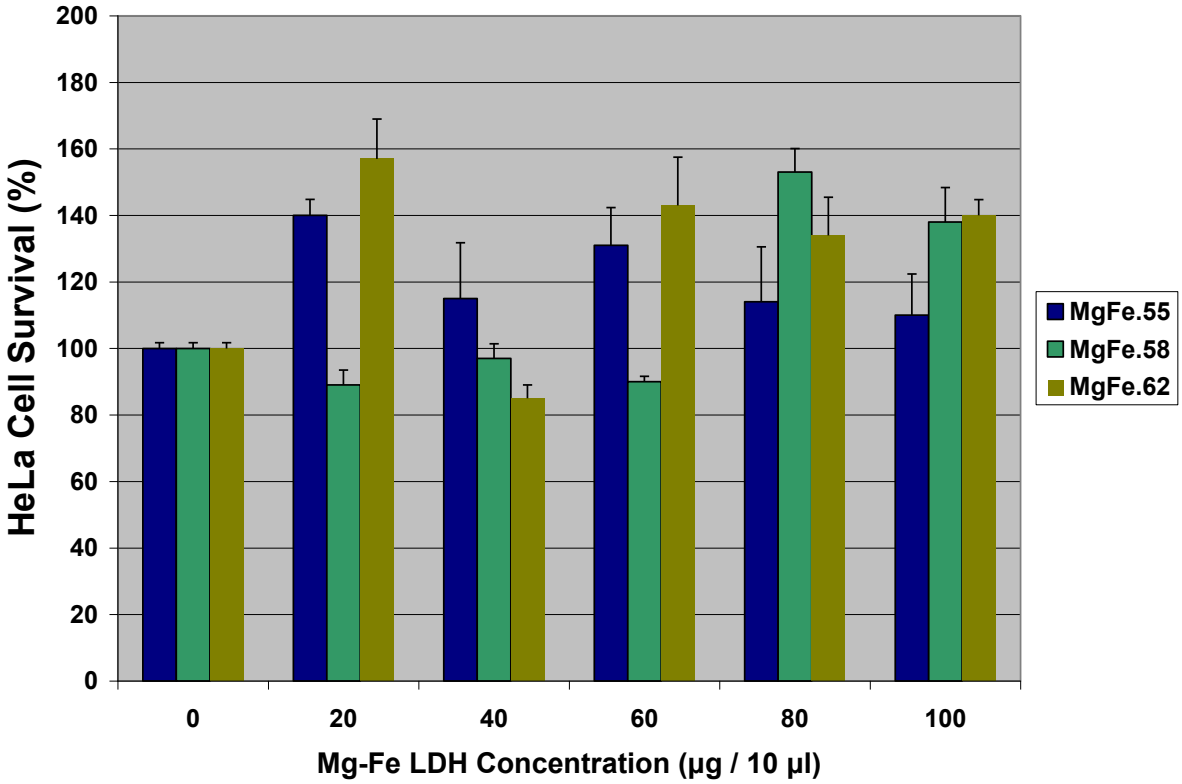

Figure 3.34 MTS cell proliferation assay of HeLa cells exposed to Mg-Fe LDHs. LDH concentration was varied (0, 20, 40, 60, 80, 100 µg). A control sample (0 µg LDH) containing only HeLa cells was assumed to have 100 % survival. Data are presented as means ± SD (n = 3).

3.4 TRANSFECTION ASSAYS

3.4.1 Introduction

In order to determine whether HT and LDH compounds have the ability to efficiently deliver DNA into mammalian cells and bring about sustained gene expression; a transfection study is conducted. Many non viral vectors have been utilized as gene delivery vehicles, but only recently have HTs and LDHs thought to have the potential as gene delivery vehicles [13, 25-28, 115, 135]. In this study, the qualitative analysis of transfection was carried out using the green fluorescent protein (GFP) assay and quantitative analysis was carried out using the luciferase reporter gene assay. GFP analysis was carried out in the HeLa cell line and the luciferase assay was done using all three cell lines. GFP has been utilized as a marker or reporter gene in transfection studies for the simple reason that once the gene encoding GFP is expressed in a cell, the GFP protein will fluoresce when irradiated with ultra violet light (UV) at a wavelength of 395 nm. Thus plasmids containing the GFP gene provide a visual analysis of gene expression within mammalian cells.

The GFP was first discovered and isolated by Osamu Shimomura in 1960, during his studies on the bioluminescence of the crystal jellyfish, *Aequorea victoria*. Shimomura determined that in order for *Aequorea Victoria*'s bioluminesce, calcium ions are released. These released calcium ions then bind to a specific protein aequorin, which releases blue light upon this calcium binding. Subsequently this blue light is absorbed by GFP which in turn presents with green light emission. The structure of GFP consists of 238 amino acids (crystal structure elucidated in 1996), which are further arranged into 11 β-strands that make up the β-barrel and an α-helix which runs through the centre of the β-barrel. The chromophore responsible for GFPs fluorescence is located in the centre of the β-barrel. The GFP structure; where R_1 and R_2 = first 64 and last 170 residues of GFP respectively, can be seen in Figure 3.35 below.

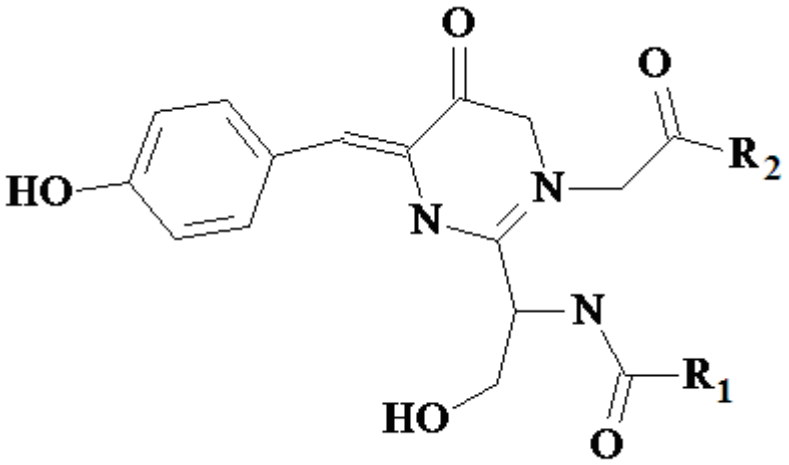

Figure 3.35 GFP structure.

In this study, the qualitative analysis of transient gene expression was carried out using plasmid pCMV-GFP encoding the GFP (Figure 3.36). This plasmid has a size of 3487 base pairs. It contains a strong promoter; the cytomegalovirus (CMV) promoter, an antibiotic resistance gene (Kanamycin), a bacterial origin of replication, the simian virus 40 polyadenylation gene (SV40 pA) and the GFP gene. The GFP transfection assay was not only used to capture a visual analysis of transfection, but in addition to determine the optimum incubation time in which transfection was at its optimum. Hence the luciferase transfection assay could be carried out at the determined optimum incubation period.

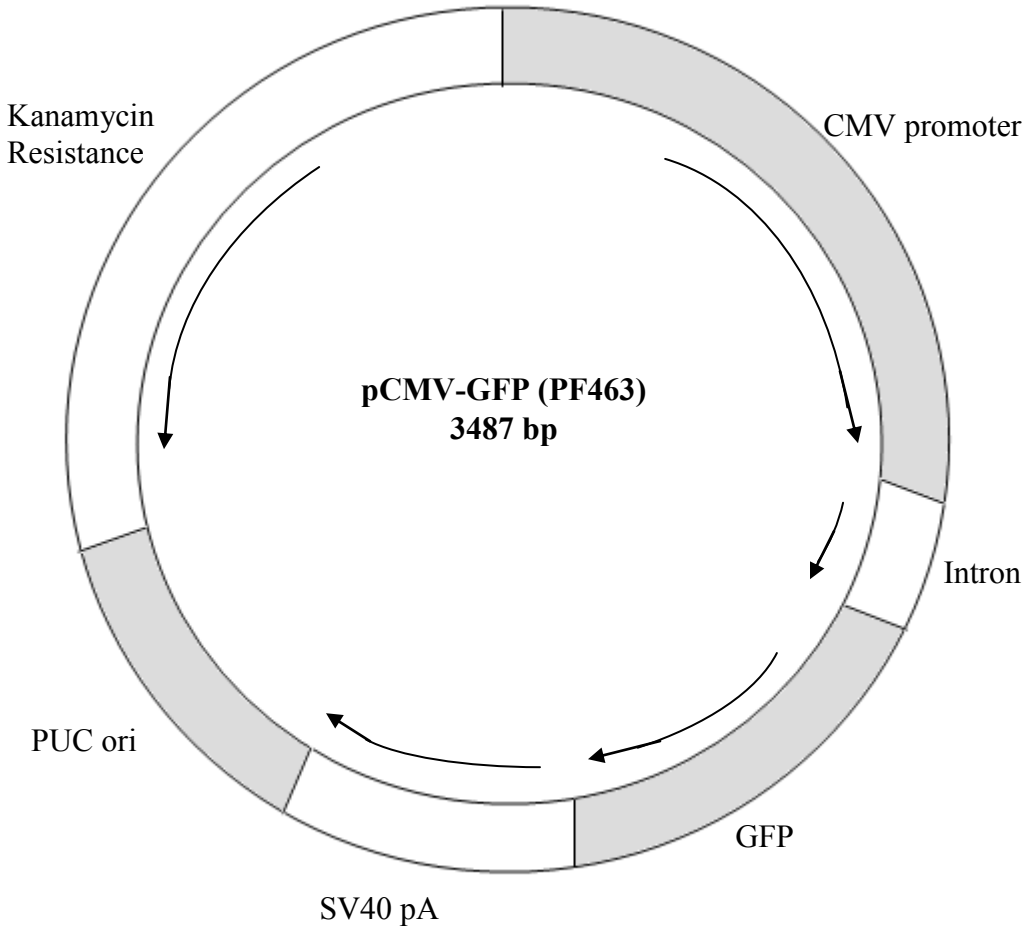

Figure 3.36 Structure of pCMV-GFP plasmid (Redrawn, *Plasmid Factory,*Germany).

In addition to the GFP assay, qualitative analysis of gene expression was carried using the luciferase reporter gene assay in all cell lines respectively.

The luciferase gene was first isolated from the North American firefly *Photinus pyralis*. This enzyme has been extensively studied in the catalysis of light production in bioluminescent organisms.

The luciferase reactions involved in the Luciferase assay are as follows;

$$\text{luciferase} + \text{luciferin} + \text{ATP} \xleftrightarrow{Mg^{2+}} \text{luciferase-luciferyl-AMP} + \text{PPi}$$

$$\text{luciferase-luciferyl-AMP} + O_2 \longleftrightarrow \text{luciferase} + \text{oxyluciferin} + \text{AMP} + CO_2 + h\nu$$

The initial reaction results in the formation of an enzyme-bound luciferyl-adenylate. The second reaction involves the oxidative decarboxylation of this luciferyl-adenylate to produce oxyluciferin, AMP, CO_2 and light (*hv*). Thus, as luciferase comes into contact with excess substrate, the reaction as depicted above; produces a flash of light measured as Relative light units (RLU) that is directly proportional to the quantity of luciferase in the reaction mixture. In this study, the plasmid pCMV-luc encoding the luciferase gene was utilized (Figure 3.37). This plasmid has a size of 6233 base pairs. It contains a strong promoter; the simian virus (SV40) promoter, SV40 enhancer, SV40 late polyadenylation site, an antibiotic resistance gene (Ampicillin), bacterial origin of replication and the luciferase gene (luc). Thus upon the entry of the plasmid into eukaryotic cells, the luciferase gene is expressed, and upon the addition of substrates, luciferin, ATP and oxygen; results in light production that is measured in a luminometer. The luciferase gene is composed of seven exons separated by six extremely short introns ranging from 48-58 bases long (Figure 3.38).

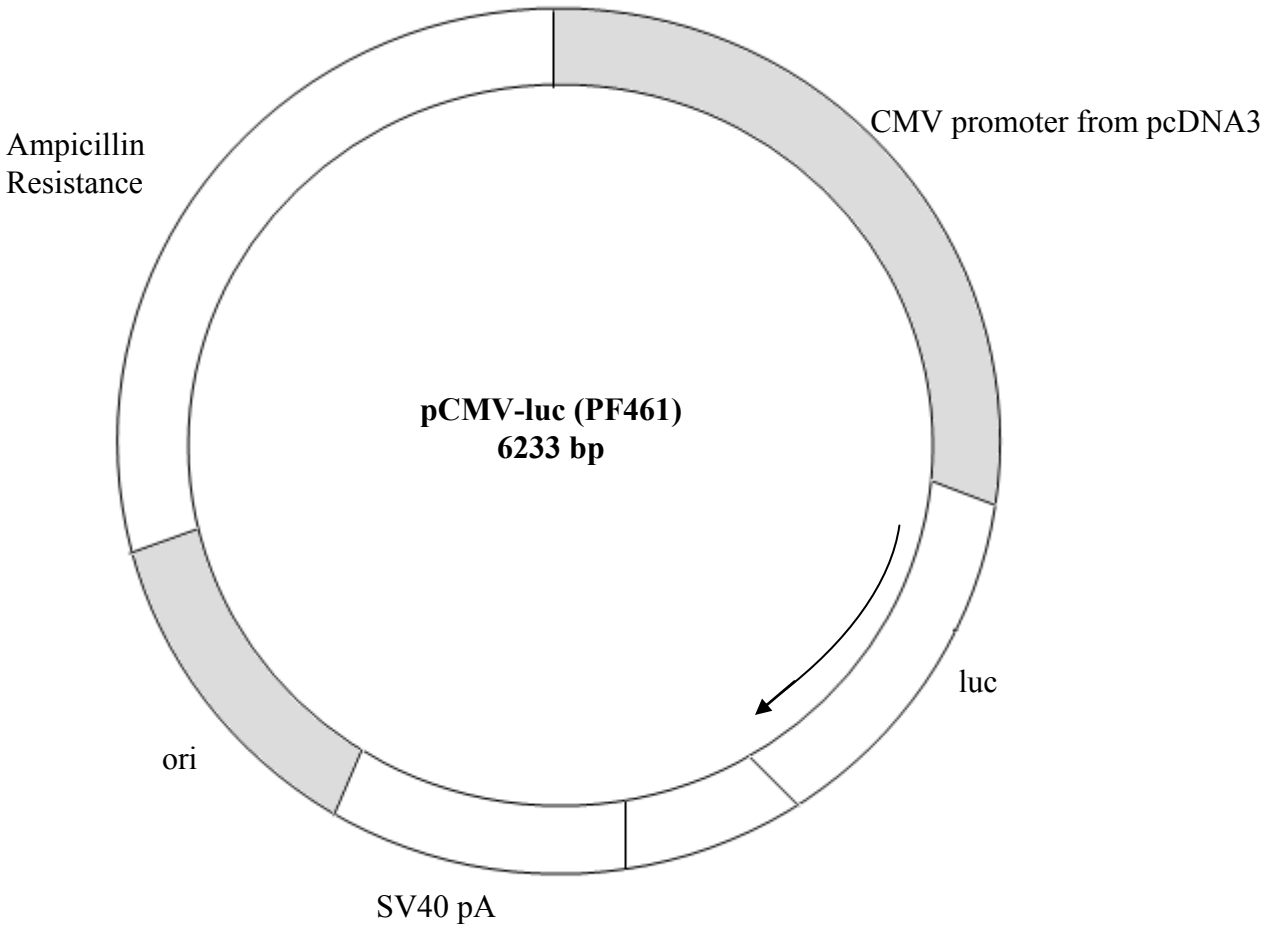

Figure 3.37 Structure of pCMV-luc plasmid (Redrawn, *Plasmid Factory,*Germany).

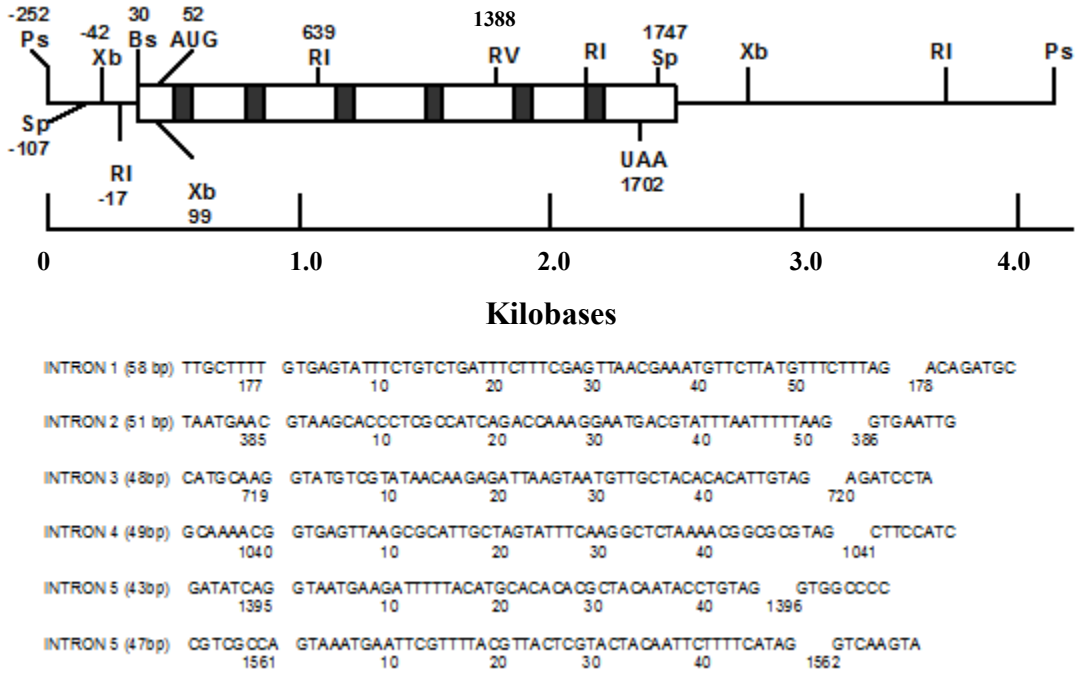

Figure 3.38 Structure of the *P.pyralis* luciferase gene. Introns are depicted as shaded boxes, with Exons depicted by non-shaded boxes. In addition; indicated are intron sequences 1-5. Furthermore, Restriction sites abbreviations as follows; *Ps = Pst 1, Sp = Ssp 1, Xb = Xba 1, R1=EcoR 1, Bs=Bsm 1,* and *RV=EcoR V.*

Upon completion of the determination of luciferase activity (RLU), the amount of protein in the respective cell lysates used were determined using the Bicinchoninic Acid (BCA) Assay. The principle of the BCA Assay is alike the Lowry procedure, in that both rely on the development of a Cu^{2+} - protein complex under alkaline conditions, followed by the reduction of Cu^{2+} to Cu^{1+}. The amount of reduction is proportional to the protein present. It has been observed that cystine, cysteine, tyrosine, tryptophan and peptide bonds are able to reduce Cu^{2+} to Cu^{1+}. BCA forms a purple-blue complex with Cu^{1+} in alkaline environments, thus providing the basis to monitor the reduction of alkaline Cu^{2+} by proteins at an absorbance maximum of 562 nm. The BCA is much more applicable and sensitive than the Lowry or Biuret methods and less variable than the Bradford assay. The BCA assay has advantages such as lower susceptibility to detergents, the formed colour complex is stable, and is applicable over a wide range of protein concentrations.

Sample protein concentrations are hence determined with the use of a standard protein curve.

In this study, the qualitative analysis of transfection was carried out using the green fluorescent protein (GFP) assay and quantitative analysis was carried out using the luciferase reporter gene assay.

3.4.2 Green fluorescent protein transfection assay

3.4.2.1 Materials and methods

HeLa cells were first trypsinized (as per section 3.3.2.4) and seeded into a 48 well plate at a cell density of 3.5-4 x 10^5 cells / well and incubated at 37^{o}C overnight. Reaction complexes were prepared (Tables 3.1-3.4) prior to GFP assay. Thereafter the growth medium was removed and replaced with 0.5 ml of complete medium into each well. Thereafter the optimum binding ratio (Table 3.5) for DNA:HT (MgAl.26), DNA:LDH (ZnAl.11, ZnFe.24 and MgFe.55) complexes were added as shown in Table 3.7. The plate was then incubated at 37^{o}C for 84 hours. After 24, 27, 48, 72 and 84 hours incubation, each well was observed for GFP fluorescence using an *Olympus* fluorescence microscope and images captured using a dedicated fluorescence camera.

Table 3.7 Culture plate indicating DNA: LDH complexes of each sample added into each well.

Well	**2**	**3**	**4**	**5**	**6**	**7**
A1 (Control) Cells	1:40 DNA : MgAl.26	Empty well	1:35 DNA : ZnFe.24	Empty well	Empty well	Empty well
B (Control) Cells	1:40 DNA : MgAl.26	Empty well	1:35 DNA : ZnFe.24	Empty well	Empty well	Empty well
C (Control) Cells	1:40 DNA : MgAl.26	Empty well	1:35 DNA : ZnFe.24	Empty well	Empty well	Empty well
D 1 µg pCMV-GFP	1:65 DNA : ZnAl.11	Empty well	1:30 DNA : MgFe.55	Empty well	Empty well	Empty well
E 1 µg pCMV-GFP	1:65 DNA : ZnAl.11	Empty well	1:30 DNA : MgFe.55	Empty well	Empty well	Empty well
F 1 µg pCMV-GFP	1:65 DNA : ZnAl.11	Empty well	1:30 DNA : MgFe.55	Empty well	Empty well	Empty well

3.4.2.2 Results and discussion

The assay for GFP was utilized in order to determine the optimum incubation period to obtain maximum GFP expression, in addition to obtaining a visual account of transfection. Thus one sample (containing the highest amount of divalent cation) was chosen from each composition group. i.e., MgAl.26, ZnAl.11, ZnFe.24 and MgFe.55. Based upon the similar chemistry that the HTs and LDHs exhibit, it was thus concluded that other samples not utilized in GFP analysis would yield similar results.

The expression of GFP as seen by fluorescence measurements, confirms that the HeLa cells were successfully transfected. Upon addition of the DNA:HT/LDH material into the wells resulted in the complexes gravitating to the bottom of the well shrouding the cells (BF images). The sedimentation of theses complexes is ideal in transfecting adherent cell lines. Non-adherent cell lines have been used in transfection studies using Mg-Al HTs in which the results thus far have proven to be unsuccessful [118].

The first sign of GFP expression was noted after 27 hours for DNA: MgAl.26 (Figure 3.39), with DNA:Zn-Al/Zn-Fe and Mg-Fe LDH complexes showing no fluorescence. After 48 hours incubation GFP fluorescence was observed in all wells (Figure 3.40). Intensity of fluorescence was found to be the same for all samples. Zn-Fe and Mg-Fe LDH samples that showed increased cell proliferation in the cytotoxicity assays correlated with the visual appearance of GFP fluorescence due to the high number of transfected cells (Figures 3.40 (f), (h), 3.47 (f), (h)). From comparisons of BF images against GFP fluorescent images, an average of 80 % of cells were transfected.

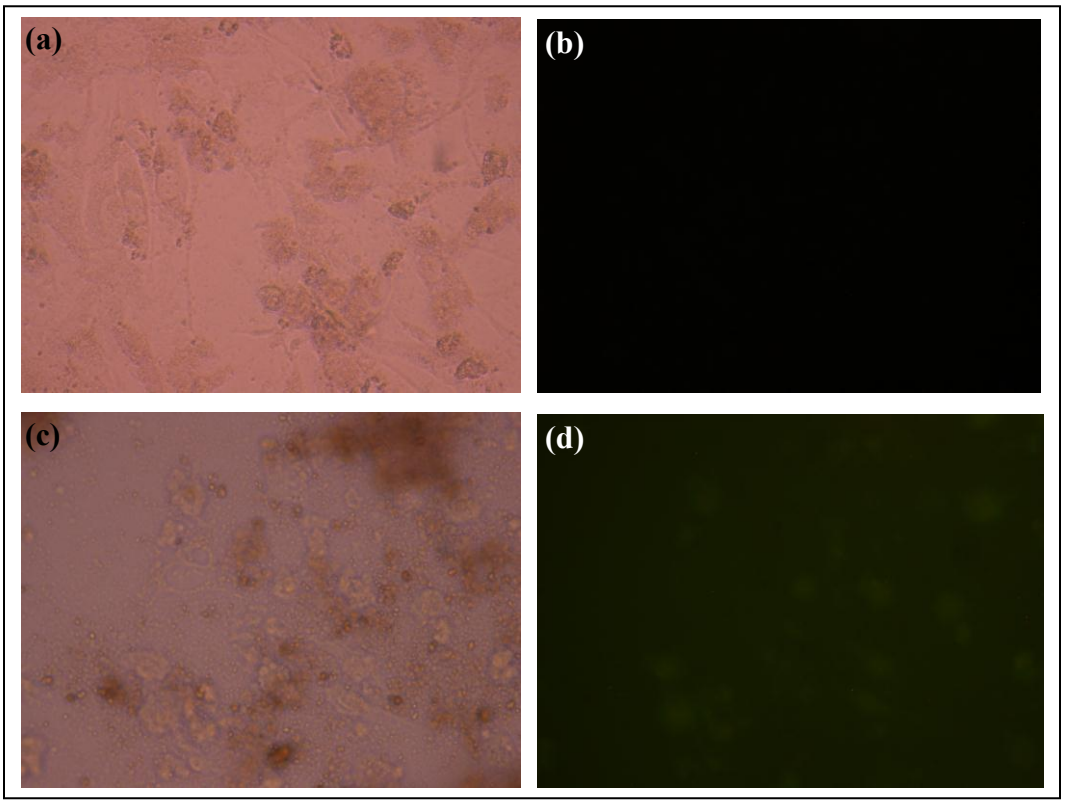

Figure 3.39 GFP fluorescence images (x200) of **(a)** Cells only (Control) Bight field (BF), **(b)** Control cells UV **(c)** DNA : MgAl.26 (1: 40) BF , **(d)** DNA : MgAl.26 (1: 40) UV, after 27 hours incubation.

The intensity of GFP fluorescence appeared to remain constant from 48 hours up until 72 hours (Figure 3.41) but faded at 96 hours. In addition, cell detachment was observed. As the culture medium was not changed over the entire incubation period, the observed cell detachment can thus be explained. The decrease in fluorescence could be due to the lack of fresh medium and hence an increase in cell apoptosis. In addition, the DNA:HT/LDH complexes were observed to shroud the cells, as seen in BF images of GFP expression as well as from figure 3.42.

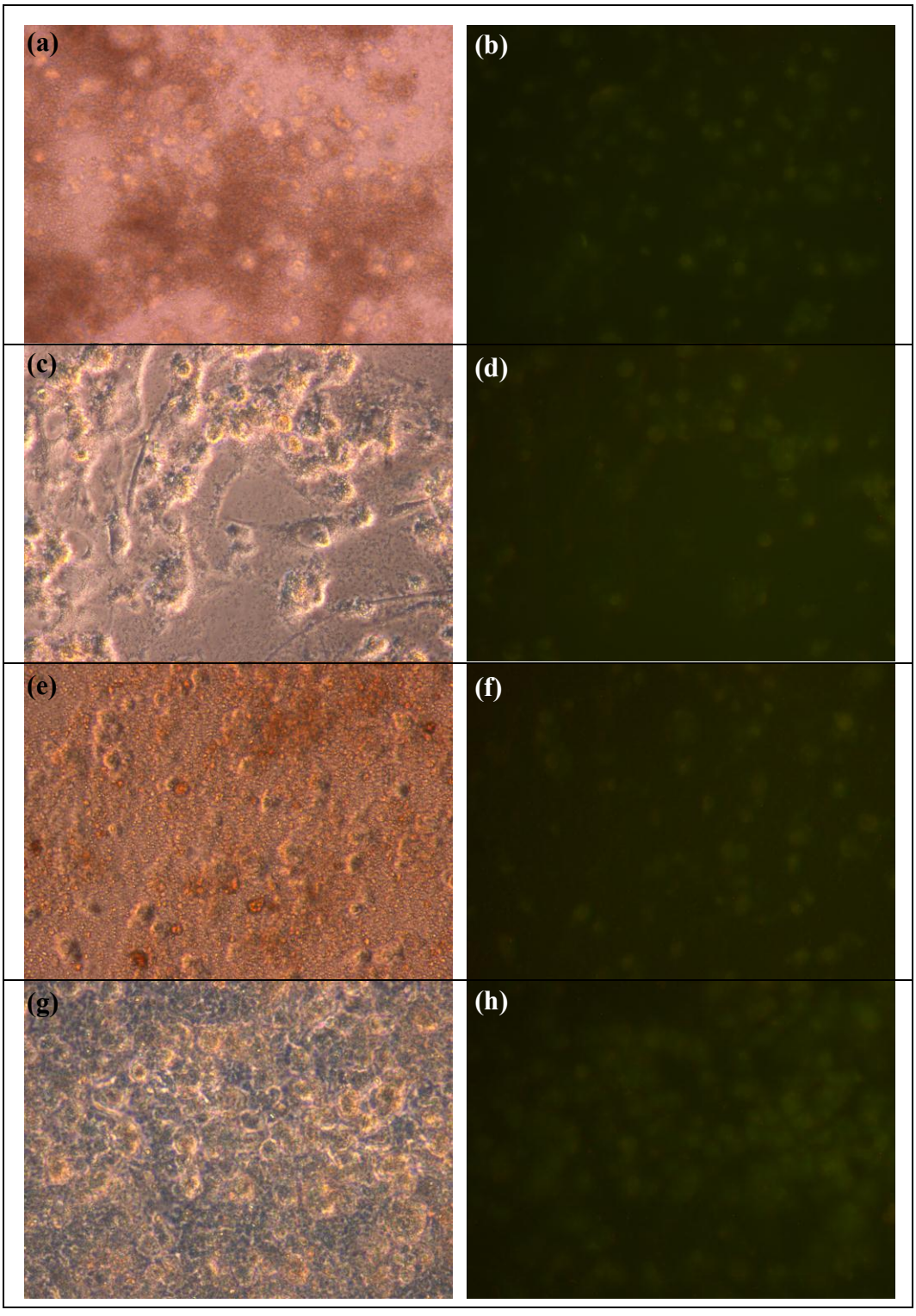

Figure 3.40 GFP fluorescence images (x200) of **(a)** DNA: MgAl.26 (1:40) (BF), **(b)** DNA: MgAl.26 UV **(c)** DNA: ZnAl.11 (1: 65) BF, **(d)** DNA: ZnAl.11 (1: 65) UV **(e)** DNA: ZnFe.24 (1: 35) BF, **(f)** DNA: ZnFe.24 (1: 35) UV **(g)** DNA: MgFe.55 (1: 30) BF, **(h)** DNA: MgFe.55 (1: 30) UV, after 48 hours incubation.

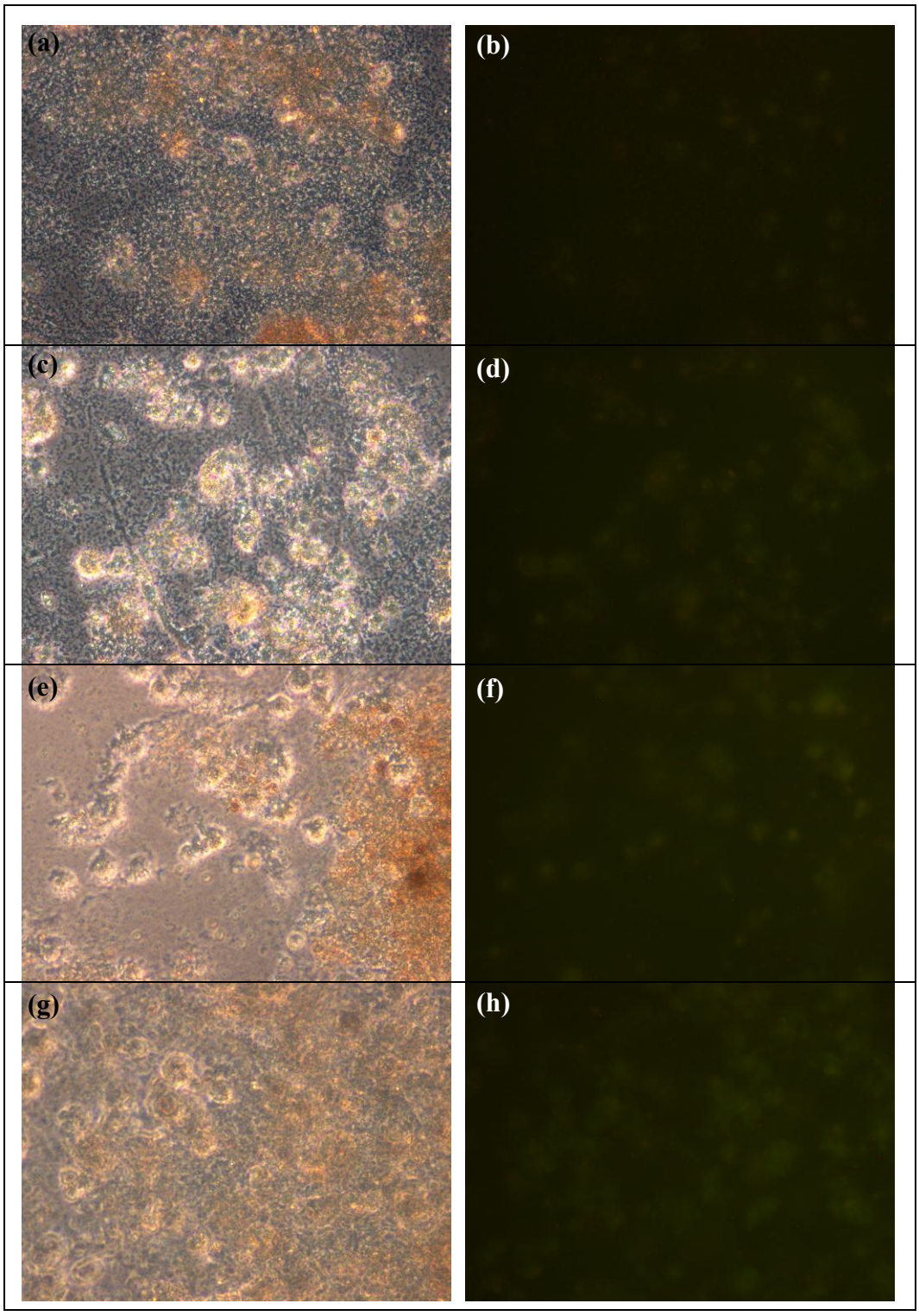

Figure 3.41 GFP fluorescence images (x200) of **(a)** DNA: MgAl.26 (1:40) (BF), **(b)** DNA: MgAl.26 UV **(c)** DNA: ZnAl.11 (1: 65) BF, **(d)** DNA: ZnAl.11 (1: 65) UV **(e)** DNA: ZnFe.24 (1: 35) BF, **(f)** DNA: ZnFe.24 (1: 35) UV **(g)** DNA: MgFe.55 (1: 30) BF, **(h)** DNA: MgFe.55 (1: 30) UV, after 72 hours incubation.

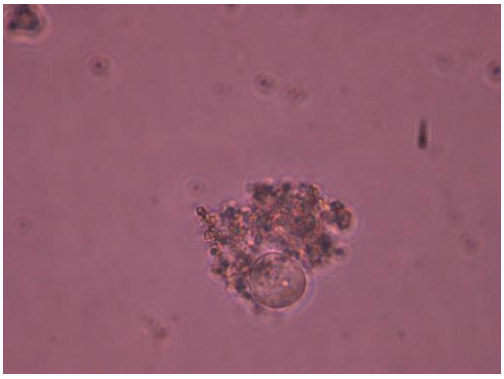

Figure 3.42 Detached HeLa cell showing HT (MgAl.26) surrounding cell (x200).

The GFP expression over the 96 hour incubation period was shown to be gradual over the first 24 hours (prominent in Mg-Al HT sample). HTs have shown a prolonged controlled release of pharmaceutics and biomolecules *in vitro* [25-28, 67, 73, 122]. From nuclease digestion observations and DNA release behavior in this study, all HTs and LDHs have shown a prolonged release of DNA. This is further supported by the visual analysis of GFP expression over the 96 hour incubation period, thus confirming that all the samples in this study exhibit a prolonged controlled release of pCMV-DNA *in vitro*. The prolonged release of DNA can be attributed to the buffering capability that HT and LDH exhibit once membrane bound within lysosomes.

Nuclease digestion studies revealed that MgAl.26, MgAl.31, MgAl.34 and ZnFe.32 were able to adequately release pCMV-GFP however the released DNA did not match the migration of the marker DNA. It was suggested that perhaps the pCMV-GFP was modified by HT/LDH binding. However if the DNA was modified to such an extent that the GFP gene was damaged in some way, the transcription and translation of the GFP gene would thus have been affected which would result in an absence or limited amount of GFP. This certainly would have been observed in the GFP assay. Thus as GFP expression was not inhibited due to damage or a conformational change in the pCMV-GFP during release, this suggests that the release mechanism involving SDS is different to that of the prolonged acid and enzymatic digestion which occurs within the lysosome. Nuclease digestion studies also indicate degradation of DNA; however this degradation does not appear to be significant in relation to transfection activity.

Since the optimum GFP expression occurred within 48 hours to 72 hours, the latter was utilized as the maximum incubation period for quantitative analysis of gene expression using the luciferase reporter gene assay.

3.4.3 Luciferase transfection assay

3.4.3.1 Materials and methods

All cells were first trypsinized (as per section 3.3.2.4) and seeded into a 48 well plate at a cell density of 3.5-4 x 10^5 cells / well and incubated at 37^{o}C overnight. Reaction complexes were prepared as in tables 3.1-3.4, with 1 μg / μl pCMV-luc DNA (*The Plasmid Factory*, Germany). After overnight incubation, the growth medium was removed and replaced with 0.5 ml of complete medium into each well. Thereafter the reaction complexes for each sample were added to the culture plate as shown in Table 3.8 overleaf. A similar culture plate layout was employed for each HT/LDH compound according to respective optimum binding ratios, including the ratio above and below (Tables 3.1-3.4). The same layout was employed throughout all cell lines. The details of which are shown in the appendix (Tables 20-22).

Table 3.8 Culture plate indicating DNA: Mg-Al HT complexes of each sample added into each well.

Well	**2**	**3**	**4**	**5**	**6**	**7**
A1 (Control) Cells	1 : 35 DNA : MgAl.26	1 : 45 DNA : MgAl.26	1 : 55 DNA : MgAl.31	1 : 35 DNA : MgAl.34	1 : 45 DNA : MgAl.34	Empty well
B (Control) Cells	1 : 35 DNA : MgAl.26	1 : 45 DNA : MgAl.26	1 : 55 DNA : MgAl.31	1 : 35 DNA : MgAl.34	1 : 45 DNA : MgAl.34	Empty well
C (Control) Cells	1 : 35 DNA : MgAl.26	1 : 45 DNA : MgAl.26	1 : 55 DNA : MgAl.31	1 : 35 DNA : MgAl.34	1 : 45 DNA : MgAl.34	Empty well
D 1 µg pCMV-luc	1 : 40 DNA : MgAl.26	1 : 50 DNA : MgAl.31	1 : 60 DNA : MgAl.31	1 : 40 DNA : MgAl.34	Empty well	Empty well
E 1 µg pCMV-luc	1 : 40 DNA : MgAl.26	1 : 50 DNA : MgAl.31	1 : 60 DNA : MgAl.31	1 : 40 DNA : MgAl.34	Empty well	Empty well
F 1 µg pCMV-luc	1 : 40 DNA : MgAl.26	1 : 50 DNA : MgAl.31	1 : 60 DNA : MgAl.31	1 : 40 DNA : MgAl.34	Empty well	Empty well

The cells were then incubated at 37 ^{o}C for 72 hours. After 72 hours the growth medium was removed and cells were washed with PBS. Approximately 60 µl of 1x cell culture lysis reagent (*Promega Corporation*, Madison, USA) was added into each well. The plate was then placed on a *Stuart Scientific STR 6* platform shaker for 15 minutes at 30 rev / minute. The cells were removed by gentle scrapping of the well with a pasteur pipette and each cell lysate was from each well was transferred to respective microcentrifuge tubes. The samples were centrifuged briefly (5 seconds) at 12 000 x g to pellet out the cell debris. Approximately 20 µl of each cell free extract was mixed with 100 µl luciferase

assay reagent (*Promega Cooperation*, Madison, USA) and placed in a *Lumac Biocounter 1500* luminometer and luminescence recorded.

The residual cell free extract was used in the BCA Assay. A set of standard bovine serum albumin (BSA) solutions were prepared in order to construct a standard BSA curve. BSA concentrations of 5, 10, 15, 20, 25, 30 ug / 100 µl were prepared from a 1 mg BSA / ml in 0.15 M NaCl containing 0.05 % sodium azide stock solution (*Sigma-Aldrich*, Steinheim, Germany). In addition a BCA working reagent was prepared, which consisted of 50 parts of Bicinchoninic Acid to 1 part of copper (II) sulphate. Thereafter 50 µl of each BSA standard solution was mixed with 1 ml of BCA working reagent. Each BSA standard solution was then mixed and incubated at 37 ^{o}C for 30 minutes. Following incubation, the absorbance of each BSA standard solution was determined at a wavelength of 562 nm using a *Biomate 3* scientific spectrophotometer. The cell free extract was analyzed in a similar way. Approximately 50 µl of each cell free extract was added to 1 ml of BCA working reagent, this solution was mixed and subsequently incubated at 37 ^{o}C for 30 minutes. This was then followed by the absorbance readings of each cell free extract at 562 nm. The concentration of each cell free extract was then determined from the BSA standard curve.

3.4.3.2 Results and discussion

The incubation time for the luciferase assays was based upon GFP assay observations. However shorter incubation times (24 hours and 48 hours) were attempted (data not shown) for the luciferase assays all of which showed very low luciferase activities. This supports the evidence from the GFP assay as well as the notion that these HT and LDH compounds exhibit controlled prolonged release of pCMV-luc intracellularly.

Highest luciferase activity was observed in the HEK293 cell line with a maximum RLU / mg protein value of 16.4 x 10^6 produced from DNA: MgFe.55 (1:30) (Figure 3.46). The luciferase activities in the HepG2 and HeLa cell lines showed similar maxima RLU / mg protein values of 0.15-0.4 x 10^6.

All DNA: HT / LDH complexes produced higher luciferase activities than the controls in the HEK293 cell line. There appeared to be no significant trend in relation to different ratios within a HT / LDH composition group or between different composition groups. For some samples there were significant standard deviations. These were due to drastic jumps in the RLU obtained between each triplicate in a ratio. The MTS assay indicated cell proliferation for some samples (Fe containing) in addition the GFP assay showed increased transfection for Fe containing samples. However this observed cell proliferation did not translate into higher luciferase activities nor did it exhibit similar trends seen in the cytotoxicity assays.

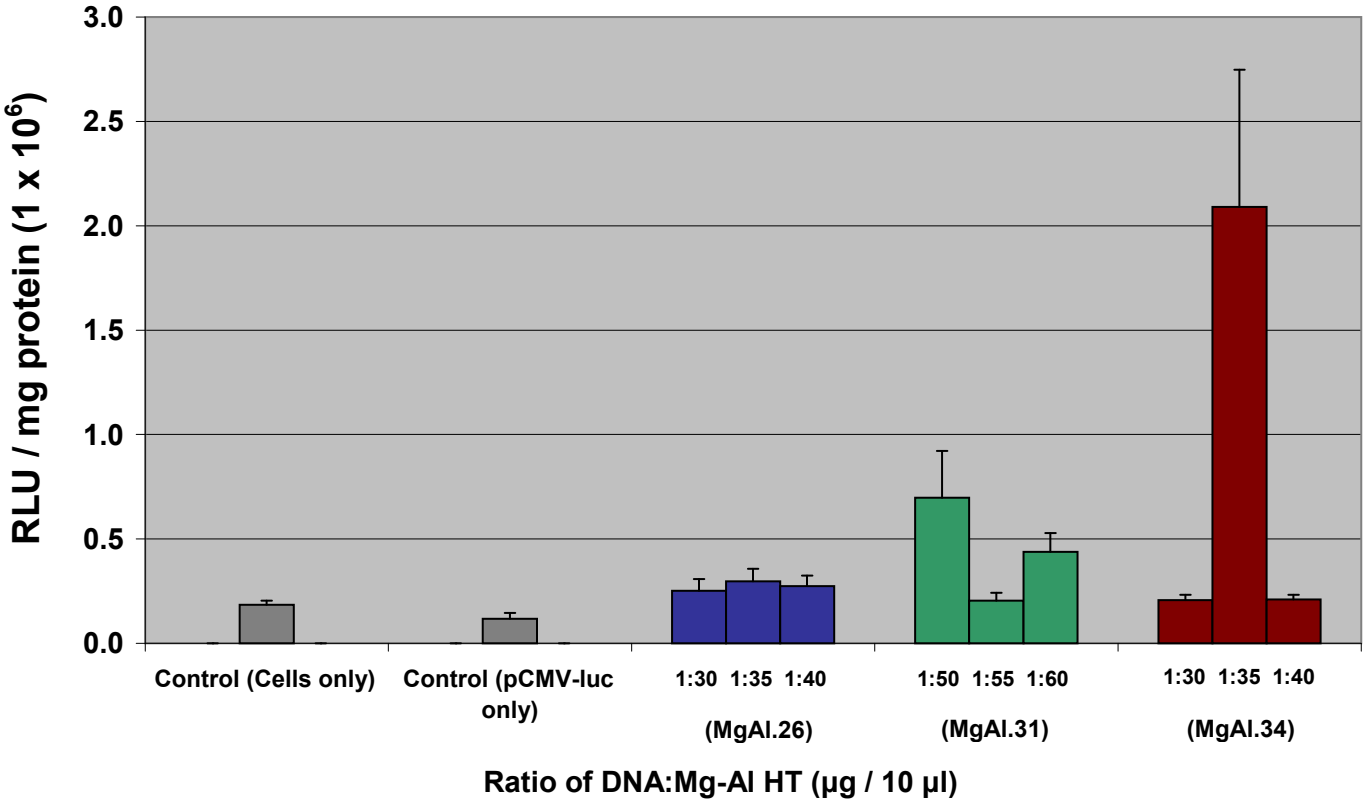

Figure 3.43 Luciferase Assay using Mg-Al HT in HEK293 cells. DNA : Mg-Al HT ratios were varied (1:30-1:60). pCMV-luc DNA used was kept constant at 1.0 µg. Two controls were used, one containing only HEK293 cells and a second control sample containing cells and pCMV-luc DNA (1.0 µg). Data are presented as means ± SD (n = 3).

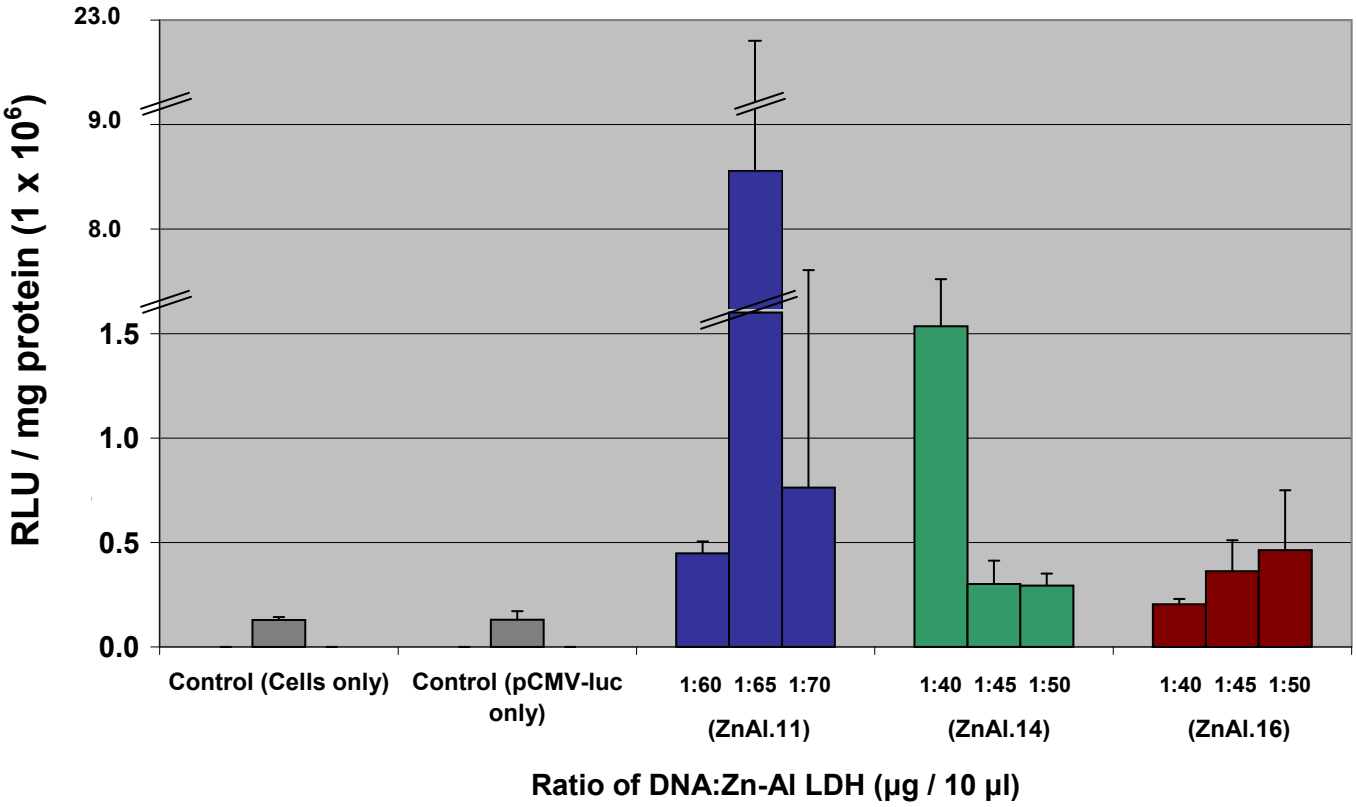

Figure 3.44 Luciferase Assay using Zn-Al LDH in HEK293 cells. DNA : Zn-Al LDH ratios were varied (1:40-1:70). pCMV-luc DNA used was kept constant at 1.0 µg. Two controls were used, one containing only HEK293 cells and a second control sample containing cells and pCMV-luc DNA (1.0 µg). Data are presented as means ± SD (n = 3).

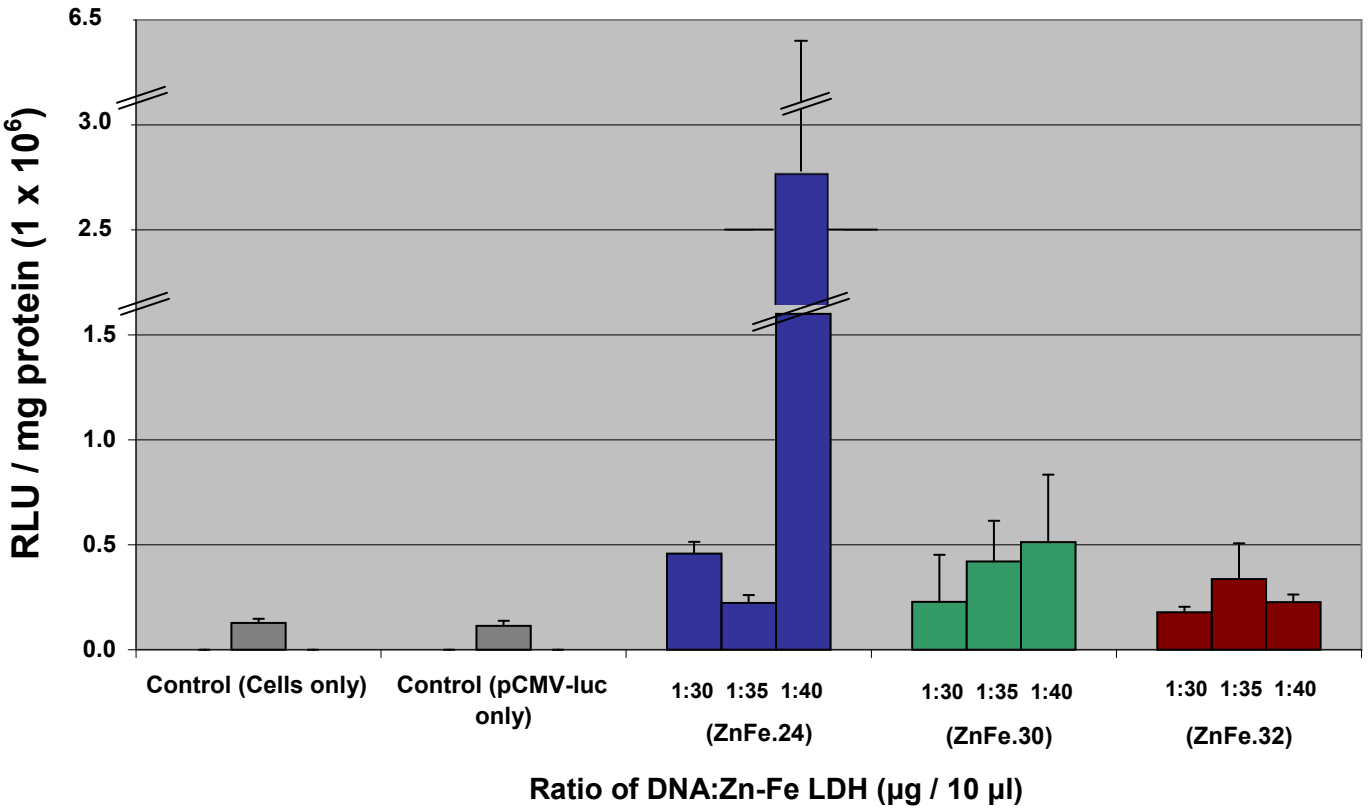

Figure 3.45 Luciferase Assay using Zn-Fe LDH in HEK293 cells. DNA : Zn-Fe LDH ratios were varied (1:30-1:40). pCMV-luc DNA used was kept constant at 1.0 µg. Two controls were used, one containing only HEK293 cells and a second control sample containing cells and pCMV-luc DNA (1.0 µg). Data are presented as means ± SD (n = 3).

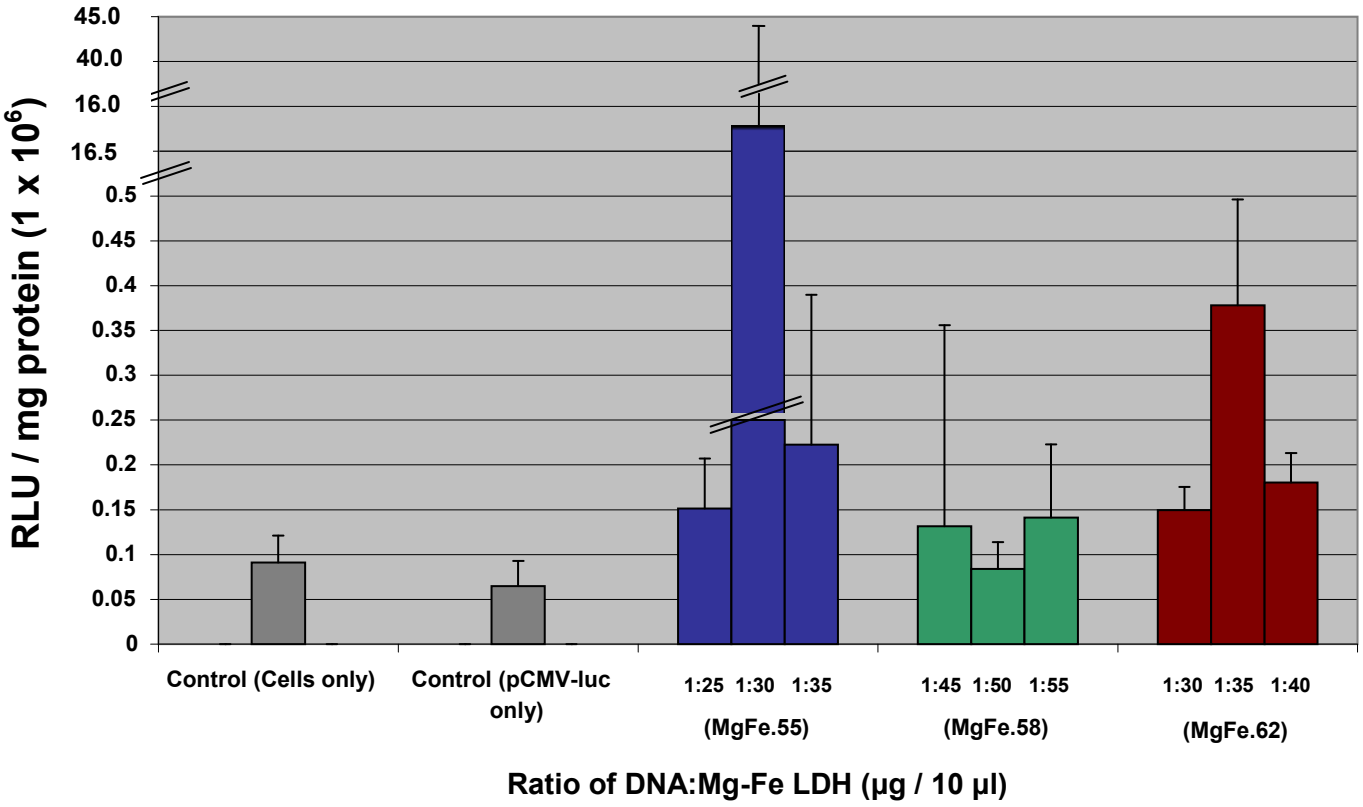

Figure 3.46 Luciferase Assay using Mg-Fe LDH in HEK293 cells. DNA : Mg-Fe LDH ratios were varied (1:25-1:55). pCMV-luc DNA used was kept constant at 1.0 µg. Two controls were used, one containing only HEK293 cells and a second control sample containing cells and pCMV-luc DNA (1.0 µg). Data are presented as means ± SD (n = 3).

Luciferase activities for DNA:HT/LDH complexes in HepG2 cells were much lower than that of HEK293 cells. Interestingly, majority of DNA: Zn-Al and Zn-Fe LDHs (Figures 3.48, 3.49) showed luciferase activities lower than control cells, thus indicating that very little pCMV-luc DNA entered into the cells or the DNA itself was degraded and hence very little activity seen. From binding assay results, majority of Zn-Al and Zn-Fe samples were unable to completely bind all available DNA with more DNA remaining in solution. Thus this could explain the lower luciferase activities. Although majority of DNA: Zn-Al samples showed lower luciferase activities than the controls, with the maximum luciferase activity in HepG2 cells produced by DNA: ZnAl.14 (1:40) (Figure 3.48). The lowest luciferase activities in HepG2 cells were produced by DNA: Zn-Fe samples (Figure 3.49).

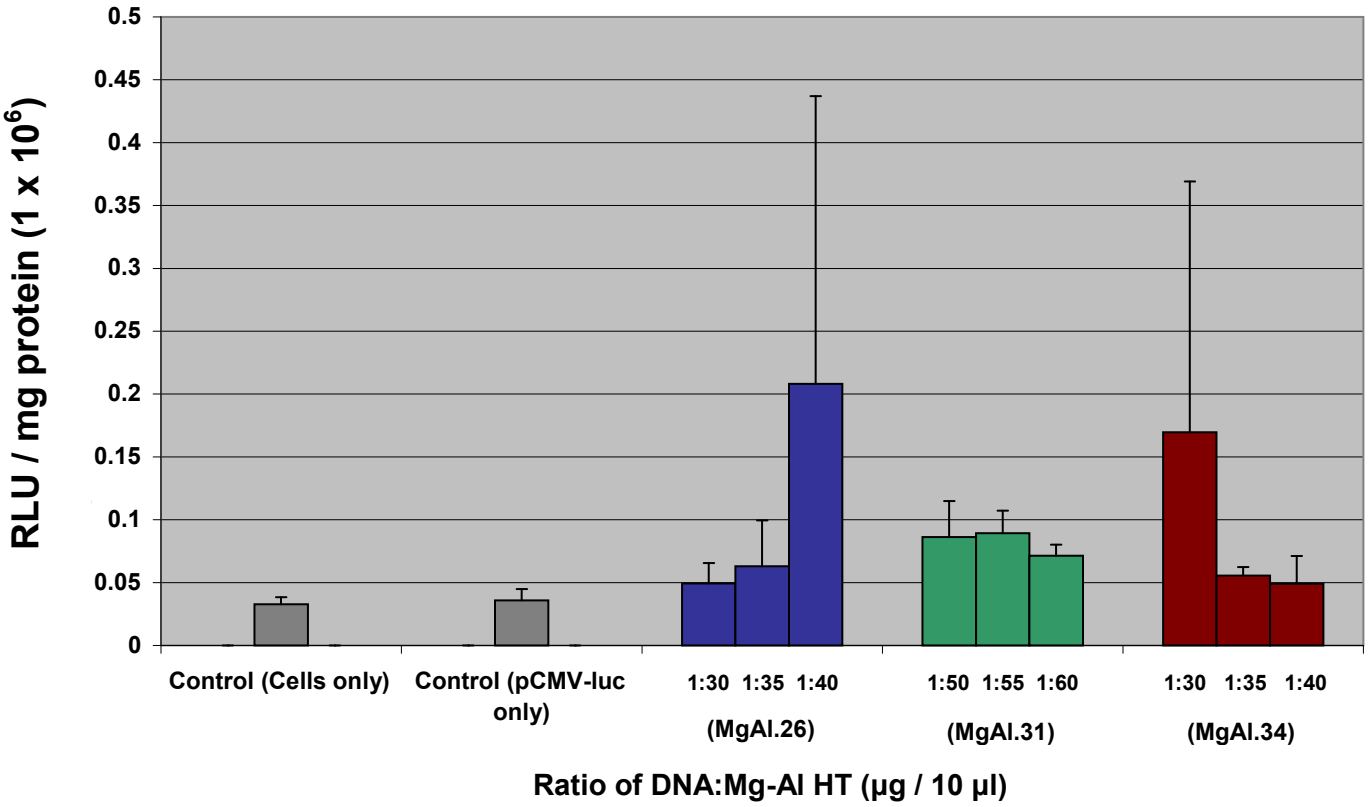

Figure 3.47 Luciferase Assay using Mg-Al HT in HepG2 cells. DNA : Mg-Al HT ratios were varied (1:30-1:60). pCMV-luc DNA used was kept constant at 1.0 µg. Two controls were used, one containing only HepG2 cells and a second control sample containing cells and pCMV-luc DNA (1.0 µg). Data are presented as means ± SD (n = 3).

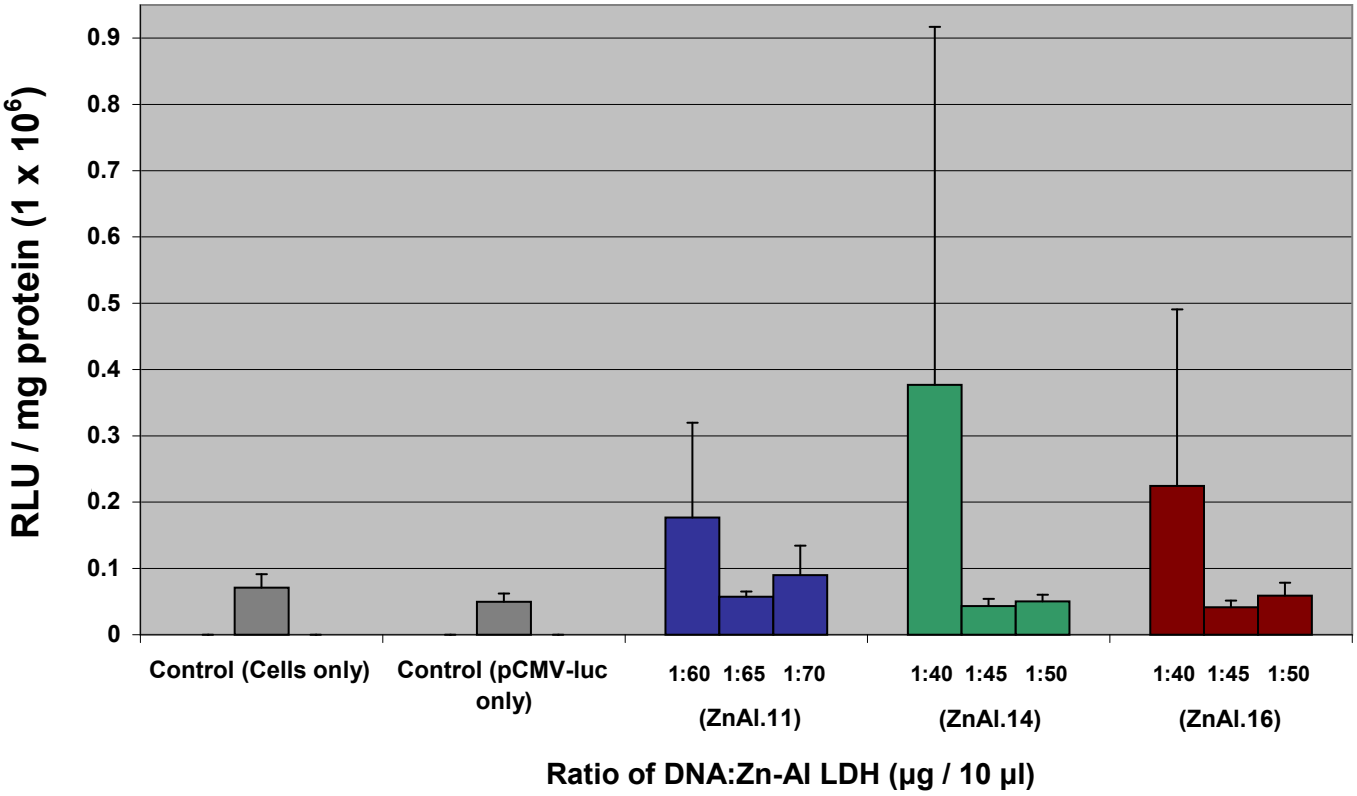

Figure 3.48 Luciferase Assay using Zn-Al LDH in HepG2 cells. DNA : Zn-Al LDH ratios were varied (1:40-1:70). pCMV-luc DNA used was kept constant at 1.0 µg. Two controls were used, one containing only HepG2 cells and a second control sample containing cells and pCMV-luc DNA (1.0 µg). Data are presented as means ± SD (n = 3).

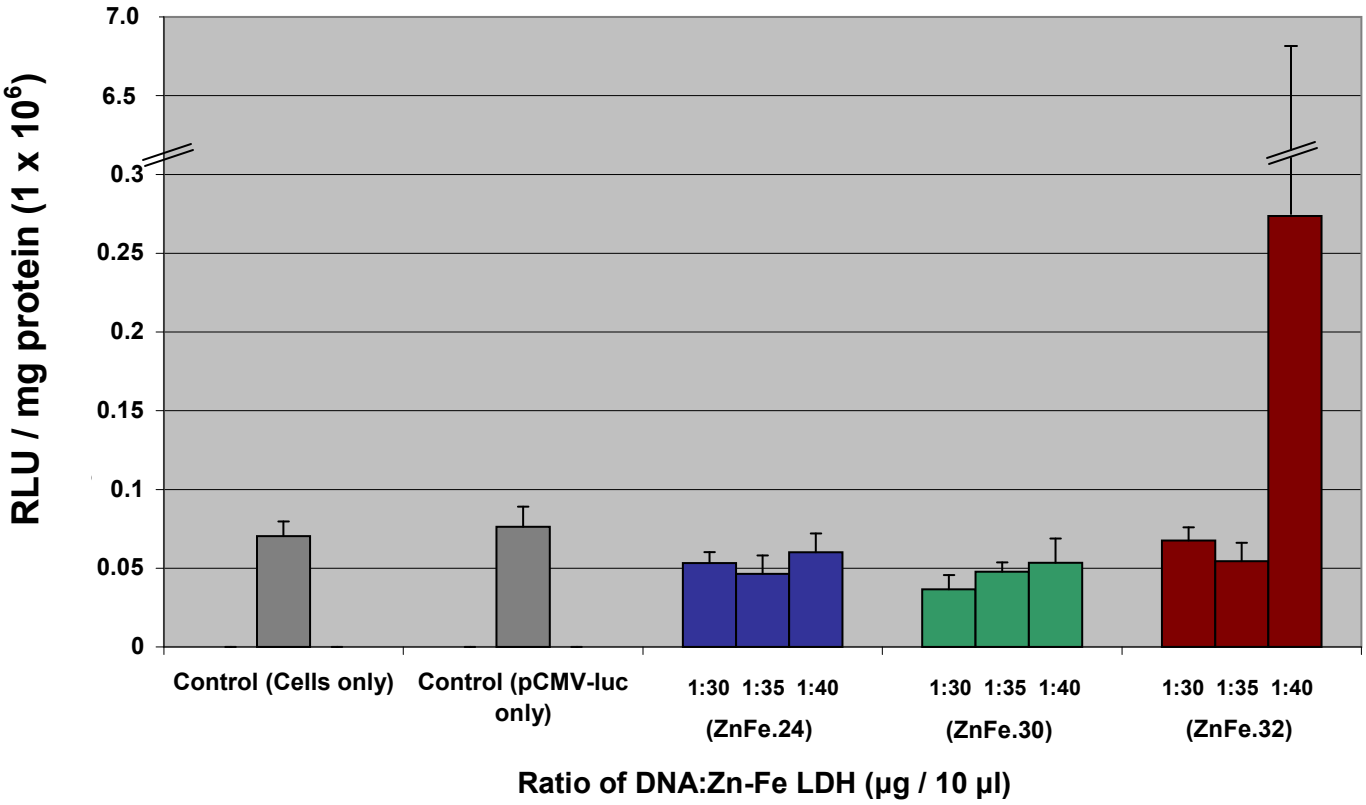

Figure 3.49 Luciferase Assay using Zn-Fe LDH in HepG2 cells. DNA : Zn-Fe LDH ratios were varied (1:30-1:40). pCMV-luc DNA used was kept constant at 1.0 µg. Two controls were used, one containing only HepG2 cells and a second control sample containing cells and pCMV-luc DNA (1.0 µg). Data are presented as means ± SD (n = 3).

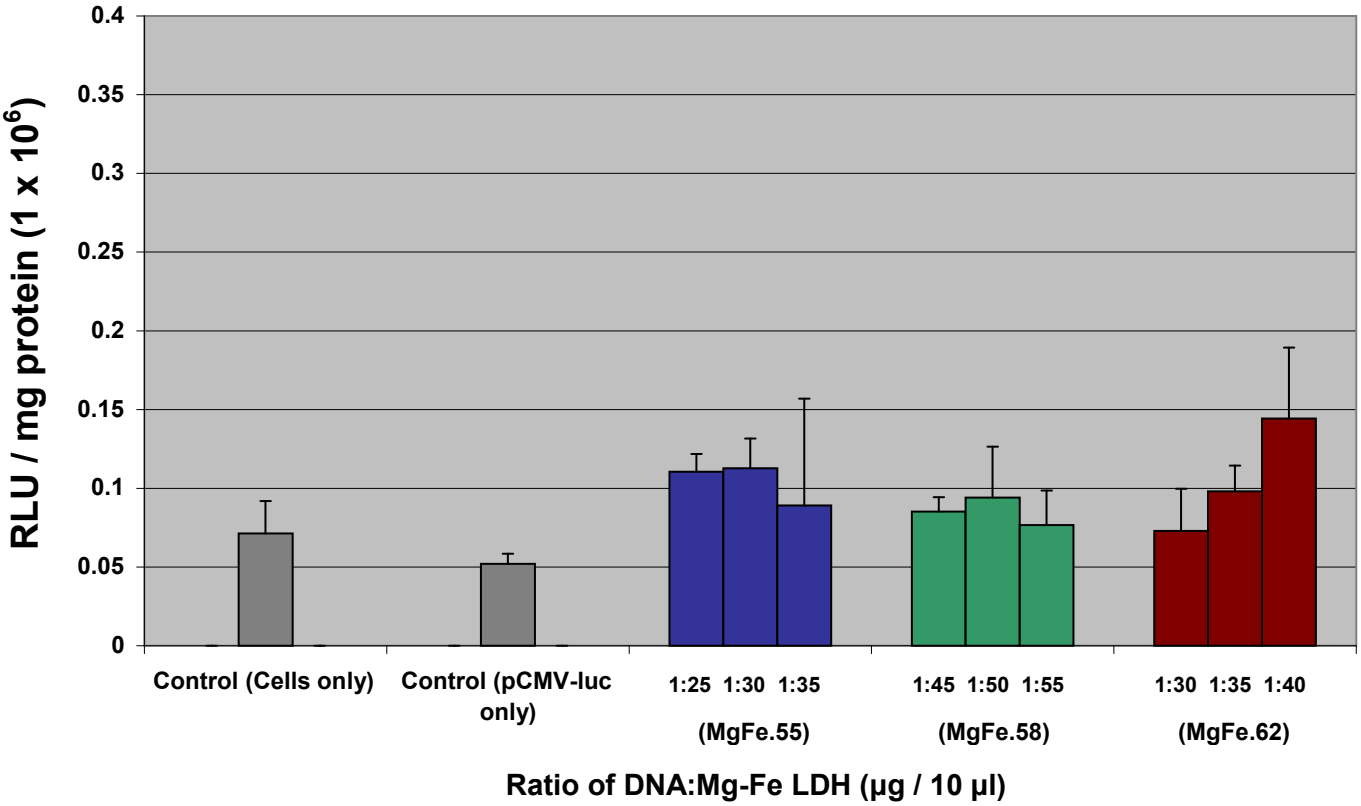

Figure 3.50 Luciferase Assay using Mg-Fe LDH in HepG2 cells. DNA : Mg-Fe LDH ratios were varied (1:25-1:55). pCMV-luc DNA used was kept constant at 1.0 µg. Two controls were used, one containing only HepG2 cells and a second control sample containing cells and pCMV-luc DNA (1.0 µg). Data are presented as means ± SD (n = 3).

Luciferase activities in HeLa cells showed varied results, with some DNA: Zn-Al, Zn-Fe and Mg-Fe LDH complexes showing lower activities than control cells. However, efficient transfection of HeLa cells with all HT and LDH samples used was observed by the GFP assay. The highest luciferase activities in the HeLa cell line were produced from DNA: Mg-Al HT complexes (Highest for MgAl.31, 1:60, Figure 3.51). The HeLa cells also showed no specific trend for the DNA:HT and LDH complexes. Slight changes in the value of x ($M^{III}/M^{II}+M^{III}$) seem to lead to dramatic changes in luciferase values and hence the observed dramatic increases and decreases in RLU between samples.

The luciferase activities in the three cell lines produced using DNA:HT/LDH samples, on average was fairly active. In the HepG2 and HeLa cell lines, majority of DNA: Zn-Al and Zn-Fe complexes exhibit poor luciferase activity. When comparing all cell lines, DNA:Mg-Al HTs appear to be the most efficient, followed by DNA:Mg-Fe LDHs and lastly DNA:Zn-Al/Zn-Fe samples. In terms of specific cell lines, DNA:Mg-Fe LDHs exhibit the highest luciferase activity in the HEK293 cell line. DNA:Zn-Fe LDHs exhibit the highest luciferase activity in the HepG2 cell line and DNA:Mg-Al LDHs in the HeLa cell line. Thus, from the results of the luciferase transfection assay it can be seen that HTs and LDHs have the ability to efficiently deliver DNA into mammalian cells in culture.

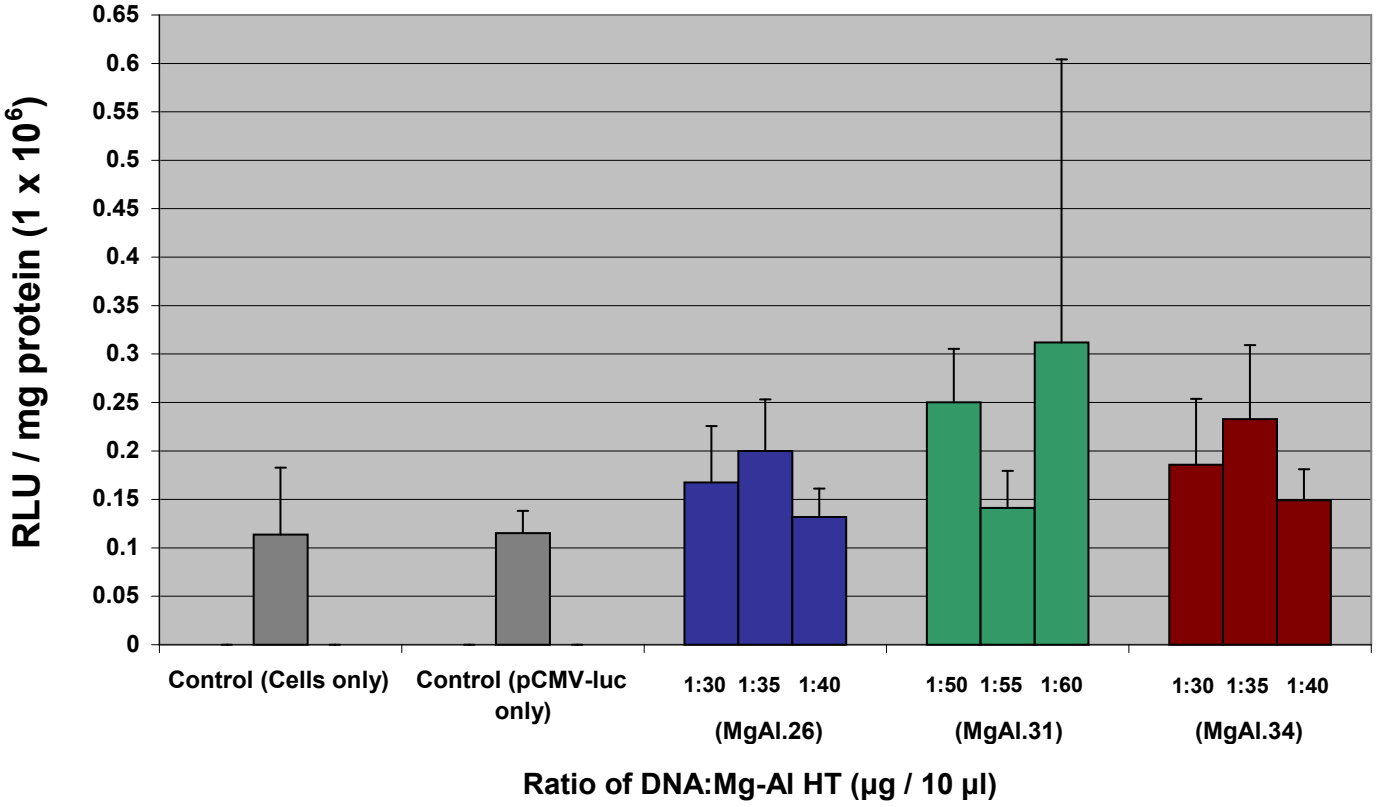

Figure 3.51 Luciferase Assay using Mg-Al HT in HeLa cells. DNA : Mg-Al HT ratios were varied (1:30-1:60). pCMV-luc DNA used was kept constant at 1.0 µg. Two controls were used, one containing only HeLa cells and a second control sample containing cells and pCMV-luc DNA (1.0 µg). Data are presented as means ± SD (n = 3).

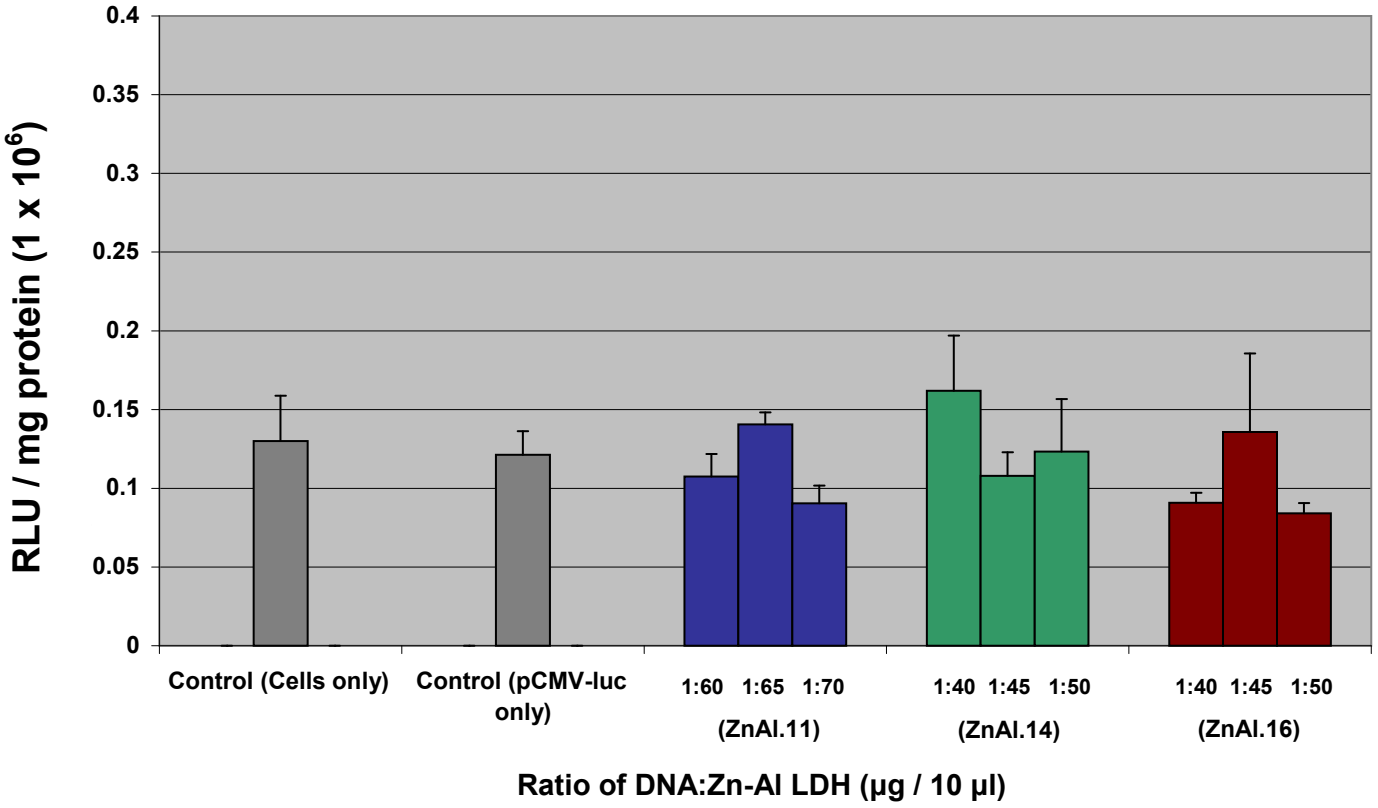

Figure 3.52 Luciferase Assay using Zn-Al LDH in HeLa cells. DNA : Zn-Al LDH ratios were varied (1:40-1:70). pCMV-luc DNA used was kept constant at 1.0 µg. Two controls were used, one containing only HeLa cells and a second control sample containing cells and pCMV-luc DNA (1.0 µg). Data are presented as means ± SD (n = 3).

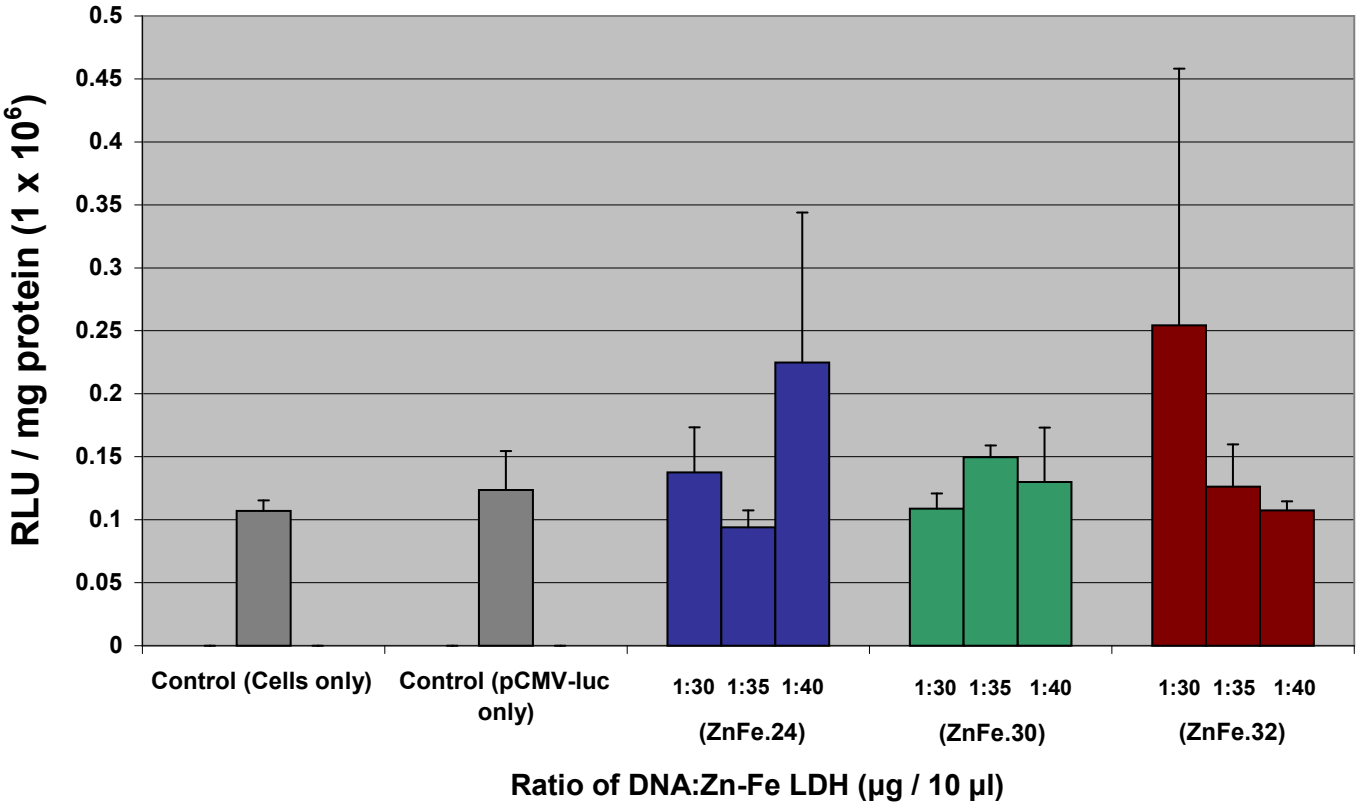

Figure 3.53 Luciferase Assay using Zn-Fe LDH in HeLa cells. DNA : Zn-Fe LDH ratios were varied (1:30-1:40). pCMV-luc DNA used was kept constant at 1.0 µg. Two controls were used, one containing only HeLa cells and a second control sample containing cells and pCMV-luc DNA (1.0 µg). Data are presented as means ± SD (n = 3).

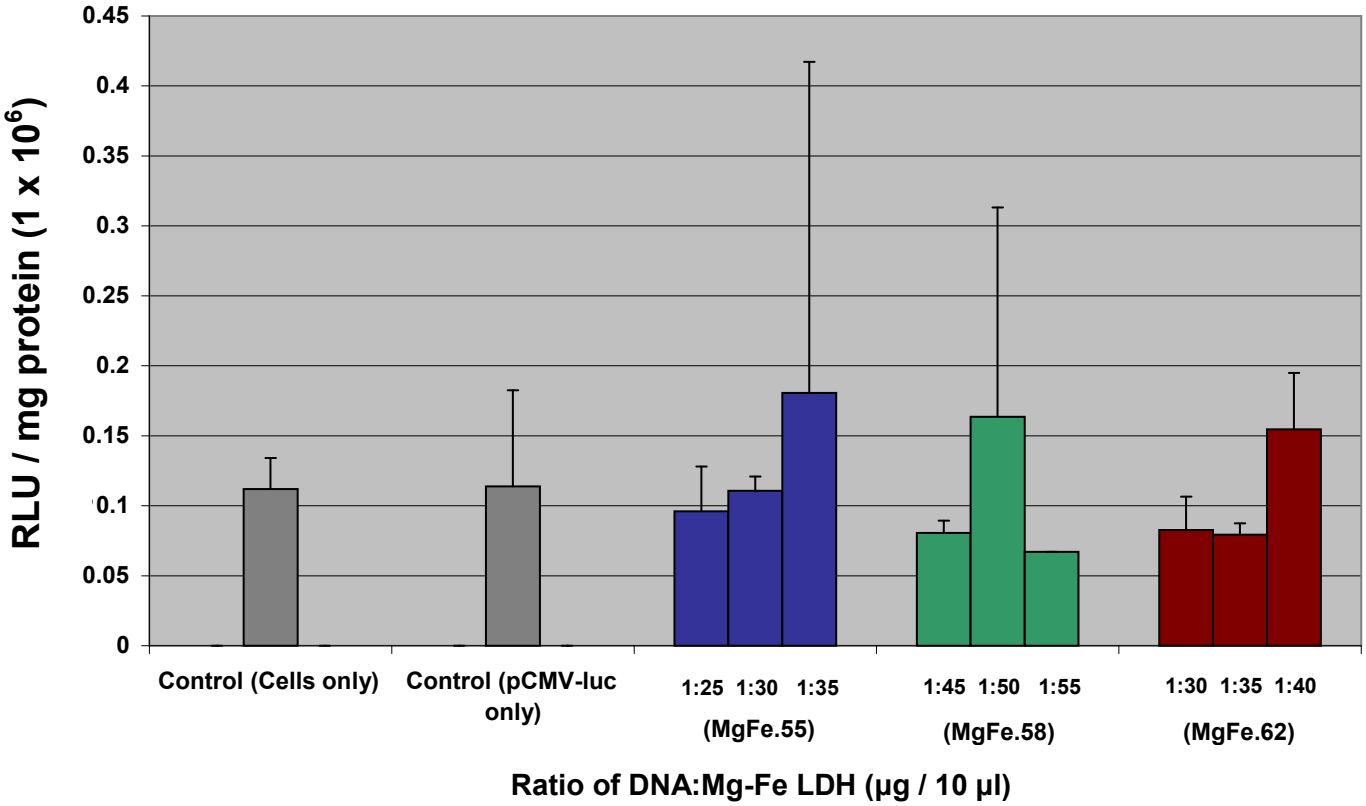

Figure 3.54 Luciferase Assay using Mg-Fe LDH in HeLa cells. DNA : Mg-Fe LDH ratios were varied (1:25-1:55). pCMV-luc DNA used was kept constant at 1.0 µg. Two controls were used, one containing only HeLa cells and a second control sample containing cells and pCMV-luc DNA (1.0 µg). Data are presented as means ± SD (n = 3).

CHAPTER FOUR
CONCLUSION

All HT (Mg-Al) and LDH (Zn-Al, Zn-Fe and Mg-Fe) compounds were successfully synthesized using co-precipitation. Hydrotalcites and LDHs containing these cations have been previously mentioned in literature, however to our knowledge the values of *x* for Zn-Al and Mg-Fe LDHs reported in the current study have not been evaluated prior to this. Significantly, values of *x* as low as 0.11-0.16 for Zn-Al LDHs were recorded. Elemental analysis confirmed higher amounts of zinc in these compounds. It was concluded that the higher amounts of zinc was attributed to electrostatic repulsion between trivalent metals. This is a result of substitutions of Zn^{2+} by Al^{3+} within the brucite-like layer, however the accumulation of Al^{3+} ions increases electrostatic repulsion between neighbouring Al^{3+} ions. The repulsion of trivalent Al, results in more positions within the brucite-layer being left vacant for Zn^{2+} to fill. Rojas Delgado et al. [135] observed similar findings in their studies of Zn-Al LDHs. Mg-Fe LDHs exhibited higher values of *x* ranging from 0.55-0.62. Elemental analysis revealed a fairly even distribution of Mg and Fe which could be attributed to the fact that these cations have very similar ionic radii. All Mg-Al HT, Zn-Al and Mg-Fe LDH XRD data and diffractograms were consistent with literature findings with the exception of Zn-Fe LDHs. The XRD data for Zn-Fe LDHs indicated the presence of $ZnFe_20_4$ and Fe_2O_3 species confirmed form JCPDS data. (22-1012 $ZnFe_20_4$ and 24-72 (Fe_2O_3)10R Hematite). X-ray diffractograms for Mg-Al HTs and Zn-Al and Mg-Fe LDHs exhibited intense symmetric lines at low 2θ values and less intense asymmetric lines at higher 2θ values, including the distinctive doublet peak at a 2θ value of 60^o indicative of a layered material which is distinctive of a hydrotalcite-like structure. The vibrational structure and characteristic functional moieties of the compounds were confirmed through FTIR and Raman spectroscopy. Electron microscopy revealed particles exhibiting classical morphologies typical of HT and LDH compounds and had an average lateral size of 200-300 nm. Significantly, sonication of inorganic compounds in ethanol for 30 minutes prior to viewing ensures adequate particle distribution and prevents compound aggregation.

Currently, Mg-Al HTs have been reported in literature having applications in gene delivery. To our knowledge Zn-Al, Zn-Fe and Mg-Fe LDHs being utilized in gene delivery is novel to the field of inorganic compound based gene delivery.

All of the HT and LDH compounds were studied in their ability to bind DNA and effectively deliver DNA to mammalian cells in culture was explored. All of the HT and LDH compounds exhibited the ability to bind DNA to varying degrees through a gel retardation assay or band shift assay. The mechanism of DNA binding to HT was examined through XRD, FTIR, Raman spectroscopy and electron microscopy. Two plausible mechanisms were proposed. The first being partial ion exchange of DNA for the HT anion interlayer, with the remainder of DNA protruding into the reaction solution. The protruding DNA is then able to partially intercalate, via ion exchange into the interlayer of a second HT particle forming aggregates of DNA: HT complexes. The alternative mechanism to the former, is one in which DNA bound to the peripheral surface of a HT particle with no ion exchange occurring. Therefore once DNA had bound to the exterior of one particle, a second or third HT particle would thus bind to the exposed DNA and thus sandwich the DNA within an aggregation of two or more HT particles. Previous studies using HTs (Mg-Al) in gene delivery have indicated complete ion exchange mechanism.

Nuclease digestion assays were carried out in order to evaluate the ability of these compounds protect the bound DNA in the presence of serum. It was observed that all compounds had the ability to protect most of the bound DNA. The cytotoxicity of the compounds was evaluated in the HEK293, HepG2 and HeLa mammalian cell lines using the MTS assay. Most of the compounds exhibited cell viabilities in excess of 80 %. Significantly, there appears to be no published data on the toxicity of Zn-Al, Zn-Fe or Mg-Fe LDHs in literature. Finally, transfection studies were carried out utilizing green fluorescent protein (GFP) analysis and luciferase gene expression in the above mammalian cells in culture. It was noted that all HTs and LDHs were able to release DNA in a controlled prolonged manner over a period of three days. Gene expression (GFP) commenced after 27 hours and reached a maximum at 72 hours. Efficient gene expression was observed with luciferase activities for DNA: HTs ranging from 0.05 x 10^6

- 2.0 x 10^6 RLU / mg protein and DNA: LDHs ranging from 0.05 x 10^6 - 16.7 x 10^6 RLU/ mg protein. Highest luciferase activity was recorded as 16.7 x 10^6 RLU / mg protein.

From this study, it can be demonstrated that HTs and LDHs compounds have immense promise in gene delivery strategies. A number of significant findings relating to the chemistry and biochemistry of HT and LDHs compounds in this study have not been described in literature prior to this. These findings are indeed a positive and invaluable contribution to the understanding and capacity development of HTs and LDHs for their application in gene delivery to mammalian cells in culture.

References

[1] F. Cavani, F. Trifiro, A. Vaccari, *Hydrotalcite-type anionic clays: preparation, properties and applications*, Catal. Today, **11**(2)(1991) 175-301.

[2] F. J. Bröcker, L. Kainer, German Patent, 2024282, 1970. UK Patent, 1342020, 1971.

[3] J. H. Choy, S. Y, Kwak, Y. J. Jeong, J. S. Park, *Inorganic layered double hydroxides as non-viral vectors*, Angew.Chem. Int. Ed., **39**(22)(2000) 4042-4045.

[4] G. D. Evans, T. C. R. Slade, *Structural aspects of layered double hydroxides. Layered Double Hydroxides*, *Structure and Bonding*, Springer-Verlag., **119**(2006) 1-87.

[5] S. Miyata, *Physico-chemical properties of synthetic hydrotalcites in relation to composition*, Clays and Clay Miner., **28**(1)(1980) 50-56.

[6] S. Miyata, *The synthesis of hydrotalcite-like compounds and their structures and physico-chemical properties – I: The systems* Mg^{2+}-Al^{3+}-NO_3^- *and* Mg^{2+}-Al^{3+}-Cl^-, Mg^{2+}-Al^{3+}-ClO_4^-, Ni^{2+}-Al^{3+}-Cl^- *and* Zn^{2+}-Al^{3+}-Cl^-, Clays and Clay Miner., **23**(1975) 369-375.

[7] S. Miyata, A. Okada, *Synthesis of hydrotalcite-like compounds and their physico chemical properties - The systems* Mg^{2+}-Al^{3+}-SO_4^{2-} *and* Mg^{2+}-Al^{3+}-CrO_4^{2-}, Clays and Clay Miner., **25**(1977) 14-18.

[8] F. Annabi-Bergaya, *Layered clay minerals. Basic research and innovative composite applications*, Microporous and Mesoporous Mater., **107**(2008) 141-148.

[9] D. Zhang, C. H. Zhou, C. X. Lin, D. S. Tong, W. H. Yu, *Synthesis of clay Minerals*, Appl. Clay Sci., Article in Press (2010)doi:10.1016/j.clay.2010.06.019

[10] P. Boulet, H. C. Greenwell, S. Stackhouse, P. V. Coveney, *Recent advances in understanding the structure and reactivity of clays using electronic structure calculations*, J. of Mol. Str: THEOCHEM., **762**(2006) 33-48.

[11] A Vaccari, *Preparation and catalytic properties of cationic and anionic clays*, Catal. Today, **41**(1998) 53-71.

[12] A. Vaccari, *Clays and catalysis: a promising future*, Appl. Clay Sci., **14** (1999) 161-198.

[13] B. Li, J. He, D. G. Evans, X. Duan, *Inorganic layered double hydroxides as a drug delivery system intercalation and in vitro release of fenbufen*, Appl. Clay Sci., **27**(2004) 199-207.

[14] J. R. Ruiz, C. Jiménez-anchidrián, M. Mora, *Palladium supported on hydrotalcite as a catalyst for the Suzuki cross-coupling reaction*, Tetrahedron., **62**(2006) 2922-2926.

[15] J. He, M. Wei, B. Li, Y. Kang, G. D. Evans, X. Duan, *Structural aspects of layered double hydroxides. Layered Double Hydroxides*, *Structure and Bonding*, Springer-Verlag., **119**(2006) 89-119.

[16] M. Trikeriotis, D. F. Ghanotakis, *Intercalation of hydrophilic and hydrophobic antibiotics in layered double hydroxides*, Int. J. Pharmaceutics., **332**(2007) 176-184.

[17] M. Islam, R. Patel, *Organic-inorganic hybrid ion-exchangers and layered double hydroxides*, Lambert Academic Publishing AG & Co. KG, USA (2009).

[18] G. Evans, X. Duan, *Preparation of layered double hydroxides and their applications as additives in polymers*, *as precursors to magnetic materials and in biology and medicine*, The Royal Society of Chemistry., (2006) 485-496.

[19] R. C. Evans, *An introduction to crystal chemistry*, *Second Edition*, Cambridge University Press. Cambridge, London (1964).

[20] P. J Durrant, B. Durrant, *Introduction to advanced Inorganic Chemistry*, *Second Edition*, Longman Group LTD, London (1970).

[21] W. G. Brindley, S. Kikkawa, *Thermal behavior of hydrotalcite and of anion exchanged forms of hydrotalcite*, Clays and Clay Miner., **28**(2)(1980) 87-91.

[22] M. Vucelic, W. Jones, D. G. Moggridge, *Cation ordering in synthetic layered double hydroxides*, Clays and Clay Miner., **45**(6)(1997) 803-813.

[23] H-J. Wolk, S. Muller, Patent application, *Process for the preparation of nanocrystalline hydrotalcite compounds*, IPC8 Class: AB32B516FI, USPC Class: 428402, (2009).

[24] N. Du, W. G. Hou, S. E. Song, *A novel composite: layered double hydroxides encapsulated in vesicles*, J. of Phys. Chem. B., **111**(2007) 13909-13913.

[25] Z. P. Xu, G. Q (Max). Lu, *Layered double hydroxide nanomaterials as potential cellular drug delivery agents*, Pure Appl. Chem., **78**(9)(2006) 1771-1779.

[26] Z. P. Xu, Q. H. Zeng, G. Q. Lu, A. B. Yu, *Inorganic nanoparticles as carriers for efficient cellular delivery*, Chem. Eng. Sci., **61**(2006) 1027-1040.

[27] Z. P. Xu, T. L. Walker, K. L. Liu, H. M. Cooper, G. Q. H. Lu, P. F. Bartlett, *Layered double hydroxide nanoparticles as cellular delivery vectors of supercoiled plasmid DNA*, Int. J. of Nanomed., **2**(2) (2007) 163-174.

[28] Z. P. Xu, M. Niebert, K. Porazik, T. L. Walker, H. M. Cooper, A. P. J. Middelberg, P. P. Gray, P. P. Bartlett, G. Q. H. Lu, *Subcellular compartment targeting of layered double hydroxide nanoparticles*, J. Control. Release, **130**(2008) 86-94.

[29] I. Rousselot, C. Taviot-guého, J. P. Besse, *Synthesis and characterization of Ga/Al containing layered double hydroxides: study of their basic properties through the Knoevenagel condensation of benzaldehyde and ethyl cyanoacetate, and comparison to other LDHs*, Int. J. Inorg. Mater., **1**(1999) 165-174.

[30] N. N. Das, J. Konar, M. K. Mohanta, A. K. Upadhaya, *Synthesis,characterization and adsorptive properties of hydrotalcite-like compounds derived from titanium rich bauxite*, Reac. Kin. Mech. Cat., **99**(2010) 167-176.

[31] O. Saber, *Preparation and characterization of a new nano-structural material, Co-Sn LDH*, Journal of Physics: Conference Series, **61**(2007) 825-830.

[32] M. Intissar, S. Holler, F. Malherbe, J. P. Besse, F. Leroux, *Incorporation of* Ti^{4+} *into layered double hydroxide sheets? The response by x-ray diffraction and absorption study*, Journal of Physics and Chemistry of Solids, **65**(2004) 453-457.

[33] C. J. Serna, J. L. Rendon, J. E. Iglesias, *Crystal-chemical study of layered* $[Al_2Li(OH)_6]^+X^-.nH_20$, Clays and Clay Miner., **30**(3)(1982) 180-184.

[34] W. G. Brindley, S. Kikkawa, *A crystal-chemical study of Mg,Al and Ni,Al hydroxyl-perchlorates and hydroxyl-carbonates*, Am. Miner., **64**(1979) 836-843.

[35] F. Millange, R. I. Walton, D. O'Hare, *Time resolved in situ x-ray diffraction study of the liquid-phase reconstruction of Mg-Al-carbonate hydrotalcite-like compounds*, J. Mater. Chem., **10**(2000) 1713-1720.

[36] G. J. Ross, H. Kodama, *Properties of a synthetic magnesium-aluminum carbonate hydroxide and its relationship to magnesium-aluminum double hydroxide*, *manasseite and hydrotalcite*, Am. Miner., **52** (1967) 1036-1047.

[37] E. López-Salinas, M. García-Sánchez, J. A. Montoya, D. R. Acosta, J. A. Abasolo, I. Schifter, *Structural characterization of synthetic hydrotalcite-like* $[Mg_{1x}Ga_x(OH)_2](CO_3)_{x/2}.mH_2O$, Langmuir, **13**(1997) 4748-4753.

[38] M. Bellotto, B. Rebours, O. Clause, J. Lynch, D. Bazin, E. Elkaïm, *Hydrotalcite decomposition mechanism: A clue to the structure and reactivity of spinel-like mixed oxides*, J. Phys. Chem., **100**(1996) 8535-8542.

[39] G. Mascolo, *Synthesis of anionic clays by hydrothermal crystallization of amorphous precursors*, Appl. Clay Sci., **10**(2005) 21-30.

[40] G. Mao, M. Tsuji, Y. Tamaura, *Synthesis and* CO_2 *adsorption features of a hydrotalcite-like compound of the* Mg^{2+}-Al^{3+}-$Fe(CN)_6^{4-}$ *system with high layer charge*, Clays and Clay Miner., **41**(6)(1993) 731-737.

[41] F. Thevenot, R. Szymanski, P. Chaumette, *Preparation and characterization of Al-rich Zn-Al hydrotalcite-like compounds*, Clays and Clay Miner., **37**(5)(1989) 396-402.

[42] L. Legrand, G. Sagon, S. Lecomte, A. Chausse, R. Messina, *A Raman and infrared study of a new carbonate green rust obtained by electrochemical way*, Corrosion Science, **43**(2001) 1739-1749.

[43] C. Misra, A. J. Perrotta, *Composition and properties of synthetic hydrotalcites*, Clays and Clay Miner., **40**(2)(1992) 145-150.

[44] E. Suzuki, S. Idemura, Y. Ono, *Properties of hexacyanocobaltate (III)-exchanged hydrotalcite-like minerals*, Clays and Clay Miner., **37**(2)(1989) 173-178.

[45] Z. Janakieva, C. Nachev, D. Yanakieva, *Pyroaurite*, *hydrotalcite and manasseite from Krumovo deposit- new materials for Bulgaria*, Geosciences, (2007) 68-69.

[46] M. L. Kantam, S. Roy, M. Roy, B. Sreedhar, B. M. Choudary, R. L. De, *Layered double hydroxides supported rhodium(0): An efficient and reusable catalyst for Heck*, *Suzuki*, *and Stille reactions of haloarenes*, J. Mol. Catal., **273**(2007) 26-31.

[47] D. G. Cantrell, L. J. Gillie, A. F. Lee, K. Wilson, *Structure-reactivity correlations in MgAl hydrotalcite catalysts for biodiesel synthesis*, Appl. Catal. A: Gen., **287**(2005) 183-190.

[48] C. T. Chang, B. J. Liaw, C. T. Huang, Y. Z. Chen, *Preparation of Au/Mg_xAlO hydrotalcite catalysts for CO oxidation*, Appl. Catal. A: Gen., **332**(2007) 216-224.

[49] Á.Mastalir, Z. Király, *Pd nanoparticles in hydrotalcite: mild and highly selective catalysts for alkyne semihydrogenation*, J. Catal., **220**(2003) 372-381.

[50] J. S. Valente, J. Hernandez-Cortez, M. S. Cantu, G. Ferrat, E. López-Salinas, *Calcined layered double hydroxides Mg–Me–Al (Me: Cu*, *Fe*, *Ni*, *Zn) as bifunctional catalysts*, Catal. Today, **150**(2010) 340-345.

[51] D. Kim, C. Huang, H. Lee, I. Han, S. Kang, S. Kwon, J. Lee, Y. Hane, H. Kime, *Hydrotalcite-type catalysts for narrow-range oxyethylation of 1-dodecanol using ethyleneoxide*, Appl. Catal. A: Gen., 249(2003) 229-240.

[52] R. Zăvoianu, R. Bîrjega, O. D. Pavel, A. Cruceanu, M. Alifanti, *Hydrotalcite like compounds with low Mo-loading active catalysts for selective oxidation of cyclohexene with hydrogen peroxide*, Appl. Catal. A: Gen., **286**(2005) 211-220.

[53] S. K. Jana, Y. Kubota, T. Tatsumi, *High activity of Mn-MgAl hydrotalcite in heterogeneously catalyzed liquid-phase selective oxidation of alkylaromatics to benzylic ketones with 1 atm of molecular oxygen*, J. Catal., **247** (2007) 214-222.

[54] D. Kishore, A. E. Rodrigues, *Catalytic oxidation of isophorone to ketoisophorone over ruthenium supported MgAl-hydrotalcite*, Catal Comm., **8** (2007) 1156-1160.

[55] A. H. Padmasri, A. Venugopal, J. Krishnamurthy, K. S. Rama Rao, P. Kanta Rao, *Novel calcined Mg-Cr hydrotalcite supported Pd catalysts for the hydrogenolysis of* CCl_2F_2, J. Mol. Catal., **181**(2002) 73-80.

[56] A. F. Lucrédioa, J. D. A. Bellidob, E. M. Assafa, *Effects of adding La and Ce to hydrotalcite-type Ni/Mg/Al catalyst precursors on ethanol steam reforming reactions*, Appl. Catal. A: Gen., Article in Press doi:10.1016/j.apcata.2010.08.026

[57] G. R. Williams, T. G. Dunbar, A. J. Beer, A. M. Fogg, D. O'Hare, *Intercalation chemistry of the novel layered double hydroxides* $[MAl_4(OH)_{12}](NO_3)_2.yH_2O$ *(M = Zn*, *Cu*, *Ni and Co). 2: Selective intercalation chemistry*, J. Mater. Chem., **16**(2006) 1231-1237.

[58] S. J. Palmer, R. L. Frost, *Use of hydrotalcites for the removal of toxic anions from aqueous solutions*, Ind. Eng. Chem. Res., Article in press.10.1021/ie101104r.

[59] K-H. Goha, T. T. Lim, Z. Dong, *Application of layered double hydroxides for removal of oxyanions: A review*, Water Research, **42**(2008) 1343-1368.

[60] T. Bujdosó, Á. Patzkó, Z. Galbács, I. Dékány, *Structural characterization of arsenate ion exchanged MgAl-layered double hydroxide*, Appl. Clay Sci., **44**(2009) 75-82.

[61] R. Anbarasan, R. Anandhakrishnan, G. Vivek, *Synthesis and characterizations of poly(α-naphthylamine)-nanocomposites*, Polymer Composites, (2008) 949-953.

[62] S. Gago, M. Pillinger, T. M. Santos, I. S. Gonçalves, *Zn-Al layered double hydroxide pillared by different dicarboxylate anions*, Ceramics-Silikáty, **48**(4) (2004) 155-158.

[63] V. Ambrogi, L. Perioli, V. Ciarnelli, M. Nochetti, C. Rossi, *Effect of gliclazide immobilization into layered double hydroxide in drug release*, Eur. J. Pharm. Biopharm., **73**(2009) 285-291.

[64] G. Zi, B. E. Rolfe, Z. P. Xu, A. C. Thomas, J. H. Campbell, G. Q. M. Lu, *Enhance effects of low molecular weight heparin intercalated with layered double hydroxides nanoparticles on rat vascular smooth muscle cells*, Biomaterials, Article in Press. Accepted 19 March 2010.

[65] S. Aisawa N. Higashiyama S. Takahashi, H. Hirahara, D. Ikematsu, H. Kondo, H. Nakayama, E. Narita, *Intercalation behaviour of L-ascorbic acid into layered double hydroxides*, Appl. Clay Sci., **35**(2007) 146-154.

[66] M. Del Arco, A. Fernández, C. Martín, V. Rives, *Intercalation of mefenamic and meclofenamic acid anions in hydrotalcite-like matrixes*, Appl. Clay Sci., **36**(2007) 133-140.

[67] L. Qin, M. Xue, W. Wang, R. Zhu, S. Wang, J. Sun, R. Zhang, X. Sun, *The in vitro and in vivo anti-tumor effect of layered double hydroxides nanoparticles as delivery for podophyllotoxin*, Int. J. Pharmaceutics., Article in Press. (2010). doi:10.1016/j.ijpharm.2009.12.044.

[68] S. Aisawa, S. Sasaki, S. Takahashi, H. Hirahara, H. Nakayama, E. Narita, *Intercalation of amino acids and oligopeptides into Zn-Al layered double hydroxide by coprecipitation reaction*, J Phys. and Chem. Sol., **67**(2006) 920-925.

[69] Á. Fudala, I. Pálinkó, I. Kiricsi, *Preparation and characterization of hybrid organic inorganic composite materials using the amphoteric property of amino acids: Amino acid intercalated layered double hydroxide and montmorillonite*, Inorg. Chem., **38**(1999) 4653-4658.

[70] J-C. Dupin, H. Martinez, C. Guimon, E. Dumitriu, I. Fechete, *Intercalation compounds of Mg-Al layered double hydroxides with dichlophenac: different methods of preparation and physico-chemical characterization.*, Appl. Clay Sci., **27**(2004) 95-106.

[71] J. H. Choy, S. Y, Kwak, Y. J. Jeong, J. S. Park, Inorganic layered double hydroxides as non-viral vectors, Angew.Chem. Int. Ed., **39**(22)(2000) 4042-4045.

[72] I. PálinkÓ, *Organic-inorganic nanohybrids of biologically important biomolecules and layered double hydroxides*, Nanopages, **1**(3)(2006) 295-314.

[73] H. Nakayama, A. Hatekeyama, M. Tsuhako, *Encapsulation of nucleotides and DNA into Mg-Al layered double hydroxide*, Int. J. Pharm., Article in Press. Accepted 12 April 2010.

[74] N. Bejoy, *Hydrotalcite the clay that cures*, Resonance, (2001) 57-61.

[75] S. P. Newman, W. Jones, P. O'Connor, D. M. Stamires, *Synthesis of 3R2 polytype of a hydrotalcite-like* mineral, J. Mater. Chem., **12**(2002) 153-155.

[76] M. Badreddine, M. Khaldi, A. Legrouri, A. Barroug, M. Chaouch, A. De Roy, J. P. Besse, *Chloride-hydrogenophosphate ion exchange into zinc-aluminum chloride layered double* hydroxide, Mater. Chem. Phys., **52**(1998) 235-239.

[77] M. Drezdzon, *Synthesis of isopolymetelate-pillered hydrotalcite via organic anion-pillered precursors.* Inorg. Chem., **27**(1988) 4628-4632.

[78] S. Sharma, K. Kushwaha, V. K. Srivastava, S. D. Bhatt, R. V. Jasra, *Effect of hydrothermal conditions on structural and textural properties of synthetic hydrotalcites of varying Mg / Al ratio*, Ind. Eng. Chem. Res., **46**(2007) 4856-4865.

[79] S. P. Newman, W. Jones, *Comparative study of some layered hydroxide salts containing exchangeable interlayer anions*, J. Solid State Chem., **148**(1999) 26- 40.

[80] A. Legrouri, M. Lakraimi, A. Barroug, A. De Roy, J. P. Besse, *Removal of herbicide 2,4-dichlorophenoxyacetate from water to zinc-aluminium-chloride layered double hydroxides*, Water Research, **39**(2005) 3441-3448.

[81] N. Morel-desrosiers, J. Pisson, Y. Israël, C. Taviot-guého, J. P. Besse, J-P. Morel, *Intercalation of dicarboxylate anions into Zn-Al-Cl layered double hydroxide: microcalorimetric determination of the enthalpies of anion exchange*, J. Mater. Chem., **13**(2003) 2582-2585.

[82] F. M. Vichi, O. L. Alves, *Preparation of Cd/Al layered double hydroxides and their intercalation reactions with phoshonic acids*, J. Mater. Chem., **7**(8) (1997) 1631-1634.

[83] R. Roto, F. Nindiyasari, I. Tahir, *Removal of hexacyanoferrate(II) using Zn-Al OAc hydrotalcite as an anion exchanger*, J. Phys. Sci., **20**(2) (2009) 73-84.

[84] F. R. Costa, A. Leuteritz, U. Wagenknecht, D. Jehnichen, L. Häuбler, G. Heinrich, *Intercalation of Mg-Al layered double hydroxide by anionic surfactants: Preparation and characterization*, Appl. Clay Sci., **38**(2008) 153-164.

[85] M. Meyn, C. Beneke, G. Lagaly, *Anion-exchange reactions of hydroxyl double salts*, Inorg. Chem., **32**(1993) 1209-1215.

[86] R. Trujillano, M. J. Holgado, F. Pigazo, V. Rives, *Preparation*, *physicochemical characterization and magnetic properties of Cu-Al layered double hydroxides with CO_3^{2-} and anionic surfactants with different alkyl chains in the interlayer*, Physica A., **373**(2006) 267-273.

[87] S. Carlino, M. J. Hudson, S. W. Husain, J. A. Knowles, *The reaction of molten phenylphosphonic acid with layered double hydroxide and its calcined oxide*, Solid State Ionics, **84**(1996) 117-129.

[88] K. Ladewig, M. Niebert, Z. P. Xu, P. P. Gray, G. Q. M, *Efficient siRNA delivery to mammalian cells using layered double hydroxide nanoparticles*, Biomaterials, **31**(2010) 1821-1829.

[89] Y. Wong, K. Markham, Z. P. Xu, M. Chen, G. Q. M. Lu, P. F. Bartlett, H. M. Cooper, *Efficient delivery of siRNA to cortical neurons using layered double hydroxide nanoparticles*, Biomaterials, (2010)doi:10.1016/j.biomaterials. 2010.07.077.

[90] J. F. Crow, *Anecdotal*, *historical and critical commentaries on genetics*, Genetics, **131**(1992) 761-768.

[91] O. T. Avery, C. M. MacLoed, M. McCarty, *Studies on the chemical nature of the substance inducing transformation of pneumococcal types*, J. of Exp. Med., **19**(1994) 137-158.

[92] A. Vaheri, J. S. Pagano, *Infectious poliovirus RNA: A sensitive method of assay.* Virology, **27**(1965) 434-436.

[93] F. L. Graham, A. J. Van Der Eb, *A new technique for the assay of infectivity of human adenovirus 5 DNA*, Virology, **52**(1973) 456-467.

[94] F. S. Collins, *The language of life: DNA and the revolution in personalized medicine*, Harper Collins Publishers. USA (2010).

[95] S. A. Rosenberg, P. Aebersold K. Cornetta, A. Kasid, R. A. Morgan, R. Moen, E. M. Karson, M. T. Lotze, J. C. Yang, S. L. Topalian, *Gene transfer into humans: Immunotherapy of patients with advanced melanoma using tumor infiltrating lymphocytes modified by retroviral gene transduction*, New Engl. J. Med., **323**(1990) 570-578.

[96] L. Huang, M-C. Hung, E. Wagner, *Nonviral vectors for gene therapy*, Academic Press. USA (1999).

[97] G. Renaudin, M. Francois, O. Evrard, *Order and disorder in the lamellar hydrated tetracalcium monocarboaluminate compound*, Cement and Concrete Research, **29**(1999) 63–69.

[98] M. R. Kang, H. M. Lim, S. C. Lee, S. H. Lee, K. J. Kim, *Layered double hydroxide and its anion exchange capacity*, Journal of Materials Online, **1**(2005) 1-13.

[99] S. P. Newman, W. Jones, *Synthesis*, *characterization and applications of layered double hydroxides containing organic guests*, New J. Chem., **22**(1998) 105-115.

[100] M. Meyn, C. Beneke, G. Lagaly, *Anion-exchange reactions of layered double hydroxides*, Inorg. Chem., **29**(1990) 5201-5207.

[101] E. L. Crepaldi, P.C Pavan, J. B. Valim, *Chemical*, *structural*, *and thermal properties of Zn(II)–Cr(III) layered double hydroxides intercalated with sulfated and sulfonated surfactants*, J. Coll. Inter. Sci., **248**(2002) 429-442.

[102] D. A. Skoog, D. M. West, F. J. Holler, S. R. Crouch, *Fundamentals of Analytical Chemistry*, *8th Edition*, (2004) Brooks/Cole, Canada. Pages 744-781.

[103] R. E. Dinnebier, S. J. L. Billinge, *Powder Diffraction*, *Theory and Practice*, (2008) RSC Publishing. Cambridge, UK.

[104] P. Atkins, J. De Paula, *Atkins' Physical Chemistry*, (2006). Oxford University Press, Oxford, UK. Page 277.

[105] http://en.wikipedia.org/wiki/HEK_cell. (11/2010)

[106] H. A. Szymanski, *Raman Spectroscopy*, *Theory and Practice*, (1967) Plenum Press, New York.

[107] E. Smith, G. Dent, *Modern Raman Spectroscopy-A Practical Approach*, (2005), John Wiley & Sons LTD, England.

[108] R. Rojas Delgado, C. P. De Pauli, C. Barriga Carrasco, M. J. Avena, *Influence of M^{II}/M^{III} ratio in surface-charging behavior of Zn–Al layered double Hydroxides*, Appl. Clay Sci., **40**(2008) 27-37.

[109] H. Zhang, X. Wen, Y. Wang, *Synthesis and characterization of sulfate and dodecylbenzenesulfonate intercalated zinc-iron layered double hydroxides by one-step coprecipitation route*, J. Solid State Chem., **180**(2007) 1636-1647.

[110] H. S. Panda, R. Srivastava, D. Bahadur, *Stacking of lamella in Mg / Al hydrotalcites: Effects of metal ion concentrations on morphology*, Mater. Res. Bull., **43**(2008) 1448-1455.

[111] J. T. Kloprogge, L. Hickey, R. L. Frost, *Heating stage Raman and infrared emission spectroscopic study of the dehydroxylation of synthetic Mg-hydrotalcite*, Appl. Clay Sci., **18**(2001) 37-49.

[112] X. Xie, X. Ren, J. Li, X. Hu, Z. Wang, *Preparation of small particle sized ZnAl hydrotalcite-like compounds by ultrasonic crystallization*, Journal of Natural Gas Chemistry., **15**(2006) 100-104.

[113] T. Montanari, M. Sisani, M. Nocchetti, R. Vivani, M. C. H. Delgado, G. Ramis, G. Busca, U. Costantino, *Zinc-aluminum hydrotalcites as precursors of basic catalysts: Preparation*, *characterization and study of the activation of Methanol*, Catal. Today, Article in Press. (2009) doi:10.1016/j.cattod.2009.09.012

[114] R. L. Frost, S. J. Palmer, H. J. Spratt. Synthesis and Raman spectroscopic study of Mg/Al, Fe hydrotalcites with variable cationic ratios. J. Raman Spect., **40**(9)(2009) 1138-1143.

[115] L. Desigaux, M. B. Belkacem, P. Richard, J. Cellier, P. Léone, L. Cario, F. Leroux, C. Taviot-Guého, B. Pitard, *Self assembly and characterization of layered double hydroxides DNA hybrids*, Am. Chem. Soc., NANOLetters. **6**(2)(2006)199-204.

[116] J. M. Berg, J. L. Tymoczko, L. Stryer. Biochemistry, Sixth Edition. (2006) W. H. Freeman and Company, New York. pp 787.

[117] J. M. Oh, S. J. Choi, G. E Lee, J. E. Kim, J. Choy, *Inorganic metal hydroxide nanoparticles for targeted cellular uptake through clathrin mediated endocytosis*, Asian J. Chem., **4**(2009) 67-73.

[118] K. Ladewig, M. Niebert, Z. P. Xu, P. G. Gray, G. Q. M. Lu, *Controlled preparation of layered double hydroxide nanoparticles and their application as gene delivery vehicles*, Appl. Clay Sci., **48**(2010) 280-289.

[119] R. Piva, E. Lambertini, L. Penolazzi, M. C. Facciolo, A. Lodi, G. Aguiari, C. Nastruzzi and L. del Senno. *In vitro stability of polymerase chain reaction-generated DNA fragments in serum and cell extracts*, Biochemical Pharmacology, **56**(1998) 703–708.

[120] I. R. C. Hill, M. C. Garnett, F. Bignotti, S. S. Davis. *Determination of protection from serum nuclease activity by DNA-polyelectrolyte complexes using an electrophoretic method.* Anal. Biochem., **291**(2001) 62–68.

[121] D.M. Tidd, H.M. Warenius. *Partial protection of oncogene, anti-sense oligodeoxynucleotides against serum nuclease degradation using terminal methylphosphonate groups.* Br. J. Cancer, **60**(1989) 343-350.

[122] K. M. Tyner, M. S. Roberson, K. A. Berghorn, L. Lib, R. F. Gilmour Jr., C. A. Batt, E. P. Giannelis, *Intercalation*, *delivery*, *and expression of the gene encoding green fluorescence protein utilizing nanobiohybrids*, J. Control. Release, **100**(2004) 399–409

[123] U. Costantino, V. Ambrogi, M. Nocchetti, L. Perioli, *Hydrotalcite-like compounds: Versatile layered hosts of molecular anions with biological activity*, Microporous and Mesoporous Materials, **107**(2008) 149-160.

[124] Promega CellTitre 96® Aqueous One Solution Cell Proliferation Assay Catalogue. 2008-2009.

[125] K. L. Mahan, S. Escott-Stump, *Krause's food*, *nutrition*, *& diet therapy. Eleventh Edition*, Chapter Five, (2004) Saunders. USA

[126] G. Wardlaw, *Perspectives in nutrition*, *Fourth Edition,* Chapter Fourteen, (1999) WCB/Mc Graw-Hill Company. USA.

[127] G. L. Klein, *Nutritional aspects of aluminium toxicity*, Nutrition Research Reviews, **3**(1990) 117- 141.

[128] D. P Aden, A. Fogel, S. Damjanov, B. Plotkin, B. B. Knowles, *Controlled synthesis of HBsAg in a differentiated human liver carcinoma-derived cell line*, Nature, **282** (1979) 615-616.

[129] G. R. Martin, M. J. Evans, *Embryonic stem cells: the mouse source-vehicle for mammalian genetics and beyond*, Cell, **6**(1975) 467-474.

[130] B. B. Knowles, C. C. Howe, D. P. Aden, *Human hepatocellular carcinoma cell lines secrete the major plasma proteins and hepatitis B surface antigen*, Science, **209**(1980) 497-499.

[131] I. Stonans, *HepG2 human hepatoma cells express multiple cytokine genes*, Cytokine, **11**(2)(1999) 151-156.

[132] Horst Ibelgaufts' COPE: Cytokines & Cells Online Pathfinder Encyclopaedia.

[133] http://www.dharmacon.com; siRNA Transfection Protocol Dharma*FECT* 1 or 4 HepG2. (10/2010)

[134] http://commons.wikimedia.org/wiki/Image:HeLa_cells.jpg. (10/2010)

[135] http://www.shutterstock.com/pic-112754.html. (10/2010)

[136] A. Li, L. Qin, W. Wang, R. Zhu, Y. Yu, H. Liu, S. Wang, *The use of layered double hydroxides as DNA vaccine delivery vector for enhancement of anti-melanoma immune response*, Biomaterials, (2010)doi:10.1016/j.biomaterials.2010.08.107.

[137] Z. Gu, B. E. Rolfe, Z. P. Xu, A. C. Thomas, J. H. Campbell, G. Q.M. Lu, *Enhanced effects of low molecular weight heparin intercalated with layered double hydroxide nanoparticles on rat vascular smooth muscle cells*, Biomaterials, (2010)doi:10.1016/j.biomaterials.2010.03.050.

Appendix

Synthesis of HTs and LDHs

Calculations of required amounts of precursors for the synthesis of HTs and LDHs:

A typical calculation for the preparation of $Mg_6Al_2(OH)_{16}(CO_3)^{2-}.4H_20$ HT.
For $x = 0.25$, i.e. Mg: Al = 3: 1

$Mg(NO_3)_2.6H_20$ (0.15 M)
Mass of $Mg(NO_3)_2.6H_20$ required = 0.15 mol x 256 g. mol^{-1}
= 38.4 g

$Al(NO_3)_2.9H_20$ (0.05 M)
Mass of $Al(NO_3)_2.6H_20$ required = 0.05 mol x 375 g. mol^{-1}
= 18.75 g

NaOH (1.0 M)
Mass of NaOH required = 1.0 mol. dm^{-3} x 0.4 dm^{-3} x 40 g. mol^{-1}
= 16 g
for 400 ml of solution.

Na_2CO_3 (1.0 M)
Mass of Na_2CO_3 required = 1.0 mol. dm^{-3} x 0.25 dm^{-3} x 106 g. mol^{-1}
= 26.5 g

Table A1 Details for the synthesis of HT and LDH materials

Compound	*x*	Mass (g)			
		M^{II}	M^{III}	NaOH	Na_2CO_3
MgAl.25	0.26	38.4	18.75	16	26.5
MgAl.31	0.31	29.44	18.75	16	26.5
MgAl.34	0.34	51.2	37.5	16	26.5
ZnAl.11	0.11	44.5	18.75	16	26.5
ZnAl.14	0.14	34.155	18.75	16	26.5
ZnAl.16	0.16	59.4	37.5	16	26.5
ZnFe.24	0.24	44.5	14.35	16	26.5
ZnFe.30	0.30	34.155	14.35	16	26.5
ZnFe.32	0.32	59.4	28.7	16	26.5
MgFe.55	0.55	38.4	14.35	16	26.5
MgFe.58	0.58	29.44	14.35	16	26.5
MgFe.62	0.62	51.2	28.7	16	26.5

HT and LDH Physical Properties

Table A2 Physical appearance and properties of HT and LDH products.

Sample	Physical properties		
	Colour	**Appearance**	**Solubility in water**
MgAl.26	White	Fine powder, Pliable.	Not soluble, remains as a sediment / pellet.
MgAl.31	White	Fine powder, Pliable.	Not soluble, remains as a sediment / pellet.
MgAl.34	White	Fine powder, Pliable.	Not soluble, remains as a sediment / pellet.
ZnAl.11	White	Fine powder, Pliable, greasy feel.	Not soluble, remains as a sediment / pellet.
ZnAl.14	White	Fine powder, Pliable, greasy feel.	Not soluble, remains as a sediment / pellet.
ZnAl.16	White	Fine powder, Pliable, greasy feel.	Not soluble, remains as a sediment / pellet.
ZnFe.24	Red-orange	Fine powder, Pliable feel.	Not soluble, remains as a sediment / pellet.
ZnFe.30	Red-orange	Fine powder, Pliable feel.	Not soluble, remains as a sediment / pellet.
ZnFe.32	Red-orange	Fine powder, Pliable feel.	Not soluble, remains as a sediment / pellet.
MgFe.55	White	Fine powder, Pliable feel, satiny/slight shimmer.	Slightly soluble, remains in suspension for several months.
MgFe.58	White, orange undertones	Fine powder, Pliable feel, satiny/slight shimmer.	Slightly soluble, remains in suspension for several months.
MgFe.62	Red-orange	Fine powder, Pliable feel.	Not soluble, remains as a sediment / pellet.

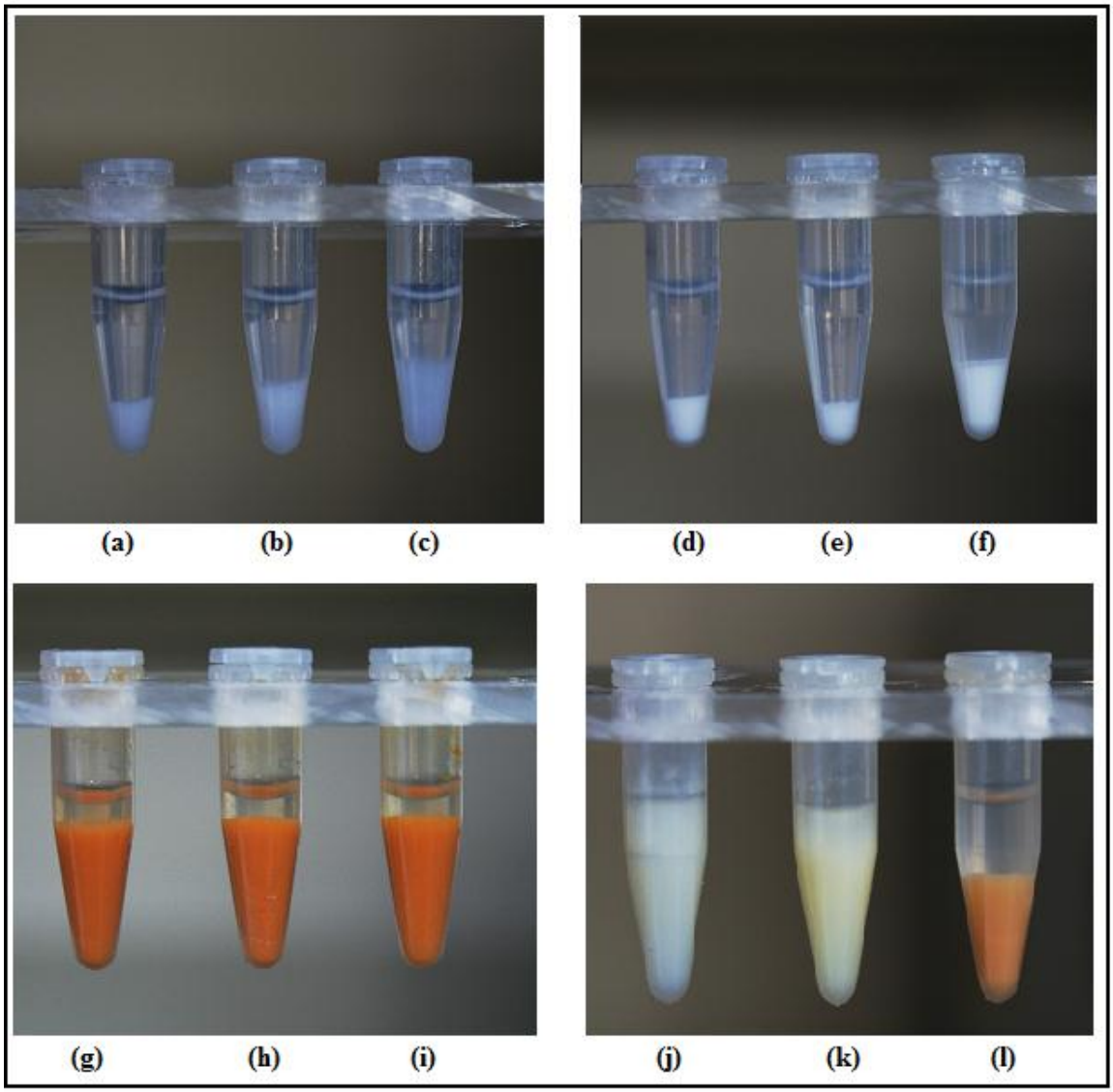

Figure A1 Solubility of HTs and LDHs in 18 mohm water, HT / LDH concentration = 10 µg / µl. Total volume in tube, approximately 0.8 ml. (a) MgAl.26 (b) MgAl.31 (c) MgAl.34 (d) ZnAl.11 (e) ZnAl.14 (f) ZnAl.16 (g) ZnFe.24 (h) ZnFe.30 (i) ZnFe.32 (j) MgFe.55 (k) MgFe.58 (l) MgFe.62.

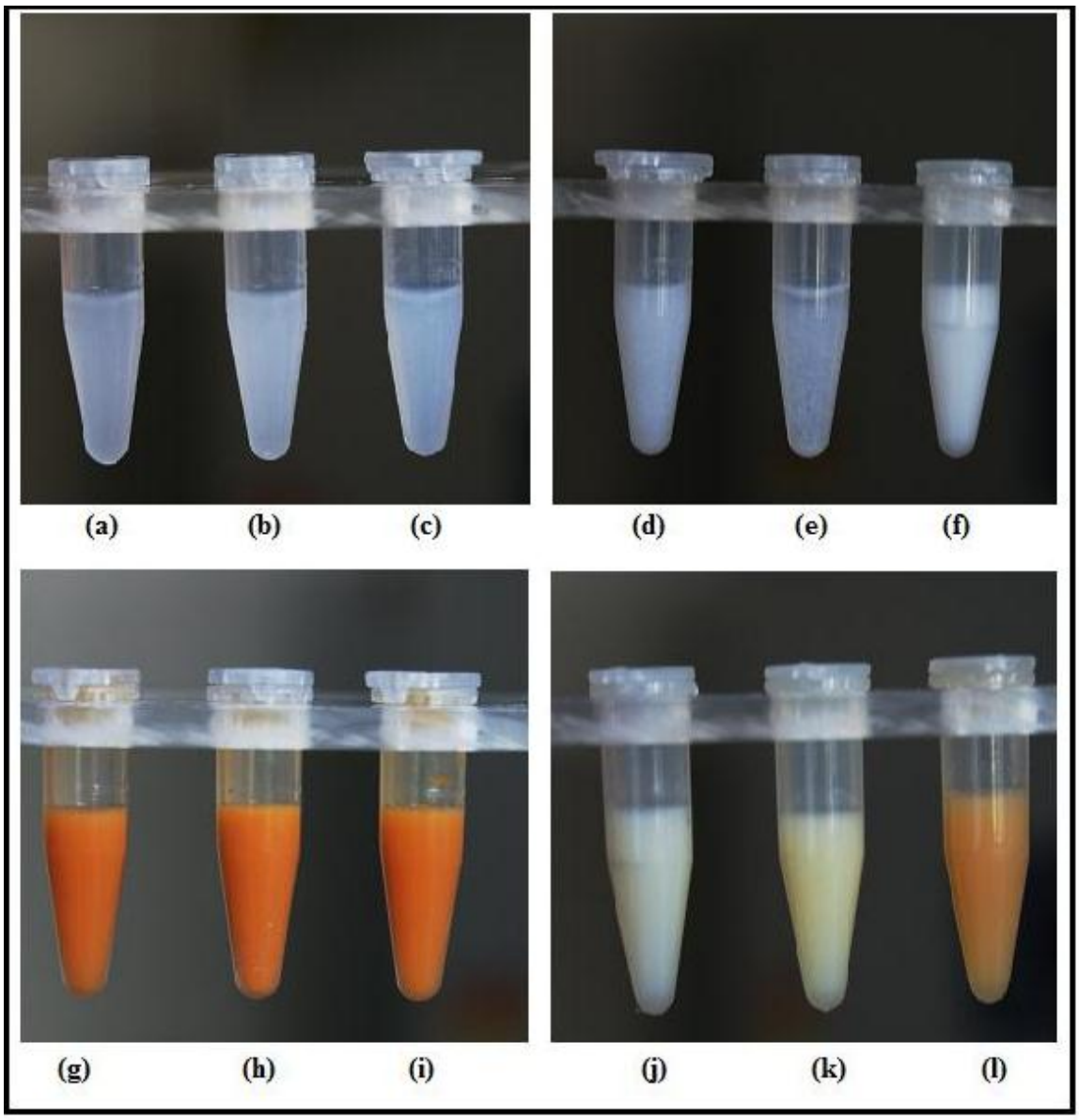

Figure A2 Solubility of HTs and LDHs in 18 mohm water, 30 minutes after 20 minutes sonication. HT / LDH concentration = 10 μg / μl. Total volume in tube, approximately 0.8 ml. (a) MgAl.26 (b) MgAl.31 (c) MgAl.34 (d) ZnAl.11 (e) ZnAl.14 (f) ZnAl.16 (g) ZnFe.24 (h) ZnFe.30 (i) ZnFe.32 (j) MgFe.55 (k) MgFe.58 (l) MgFe.62.

Table A3 d-basal spacing values for Mg-Al HTs, Zn-Al, Zn-Fe and Mg-Fe LDHs.

Compound	$M^{II} : M^{III}$	Basal spacing / Å						
		d_{003}	d_{006}	d_{012}	d_{015}	d_{018}	d_{110}	d_{113}
MgAl.25	0.25	7.90	3.92	2.60	2.32	1.97	1.53	1.50
MgAl.31	0.30	7.77	3.85	2.59	2.31	1.96	1.53	1.50
MgAl.34	0.33	7.69	3.82	2.57	2.29	1.94	1.52	1.49
ZnAl.11	0.11	7.69	3.81	2.60	2.30	1.94	1.54	1.50
ZnAl.14	0.14	7.71	3.82	2.60	2.30	1.95	1.54	1.50
ZnAl.16	0.16	7.69	3.81	2.60	2.30	1.94	1.53	1.50
ZnFe.24	0.25	6.87	3.70	2.58	2.32	1.96	1.58	1.59
ZnFe.30	0.30	6.87	3.70	2.58	2.32	1.96	1.58	1.59
ZnFe.32	0.33	6.89	3.70	2.58	2.32	1.96	1.58	1.59
MgFe.55	0.55	7.85	3.90	2.63	2.33	1.99	1.55	1.52
MgFe.58	0.58	7.84	3.89	2.63	2.35	1.99	1.55	1.52
MgFe.62	0.62	7.83	3.89	2.63	2.35	2.01	1.55	1.52

Table A4 FWHM and respective 2θ-values for Mg-Al HTs, Zn-Al, Zn-Fe and Mg-Fe LDHs.

Compound	$M^{II}:M^{III}$	2θ-value	FWHM*
MgAl.25	0.25	11.179	0.84
MgAl.31	0.30	11.374	0.833
MgAl.34	0.33	11.495	0.549
ZnAl.11	0.11	11.496	0.256
ZnAl.14	0.14	11.459	0.267
ZnAl.16	0.16	11.494	0.261
ZnFe.24	0.25	12.833	0.814
ZnFe.30	0.30	12.833	0.83
ZnFe.32	0.33	12.828	0.829
MgFe.55	0.55	11.251	0.627
MgFe.58	0.58	11.274	0.771
MgFe.62	0.62	11.278	0.675

*FWHM=Full width at half maximum of peak ($d_{(003)}$) corresponding to 100 % intensity

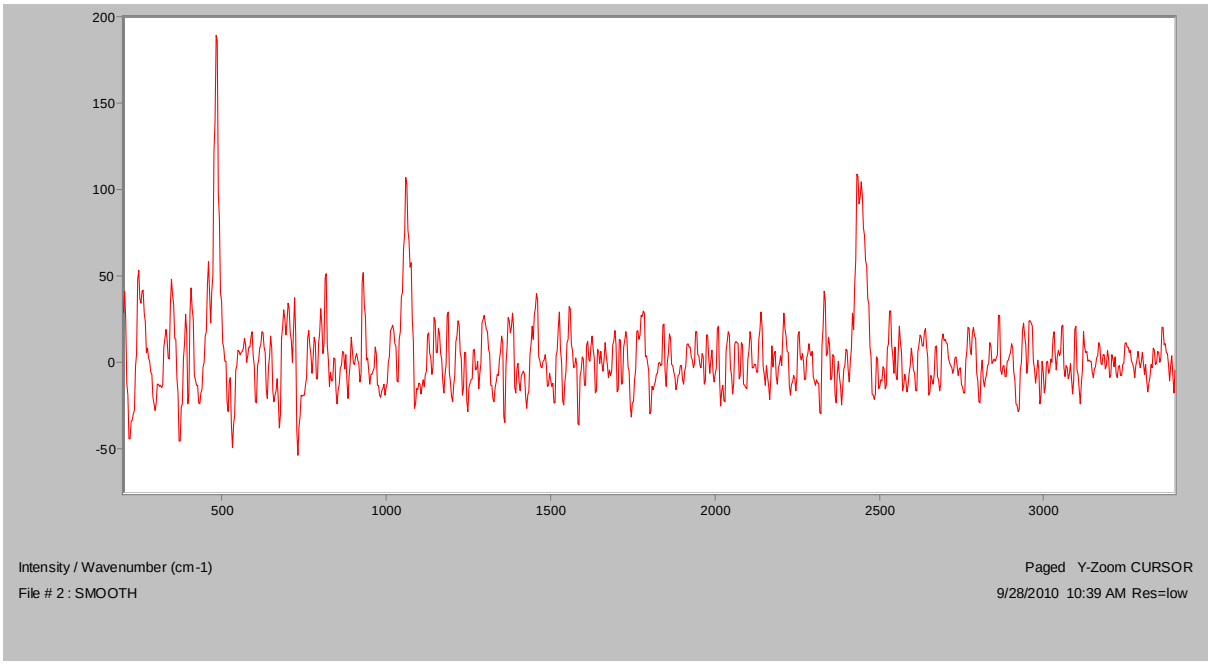

Figure A3 Raman spectrum of MgAl.31.

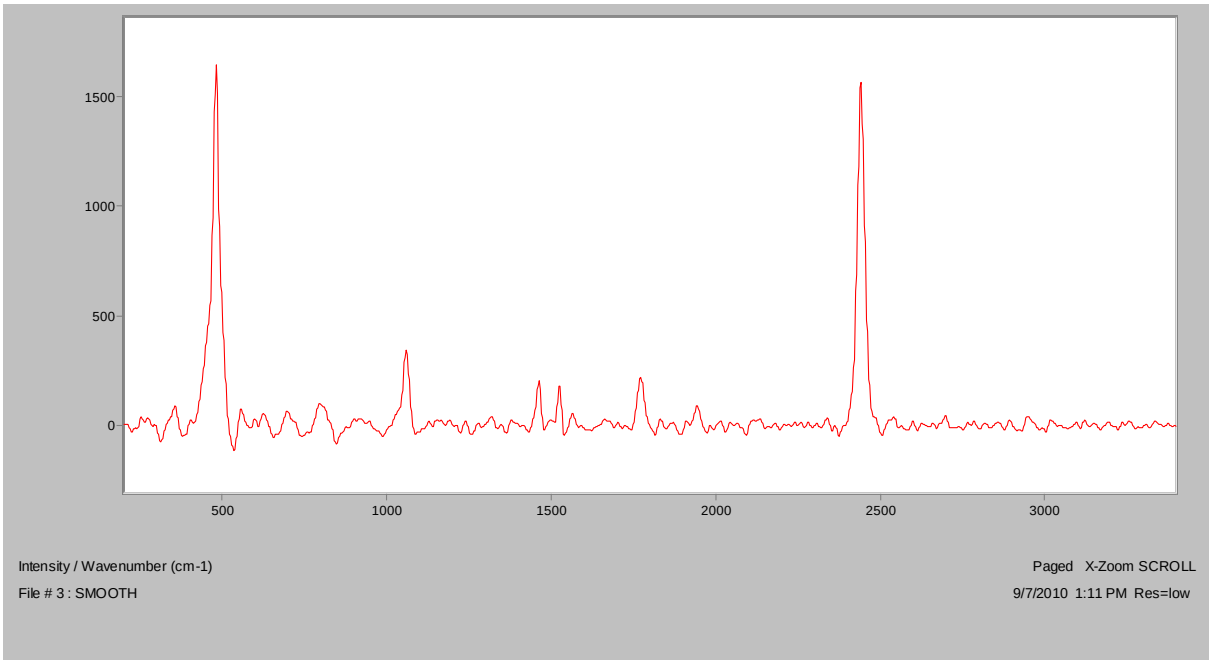

Figure A4 Raman spectrum of MgAl.34.

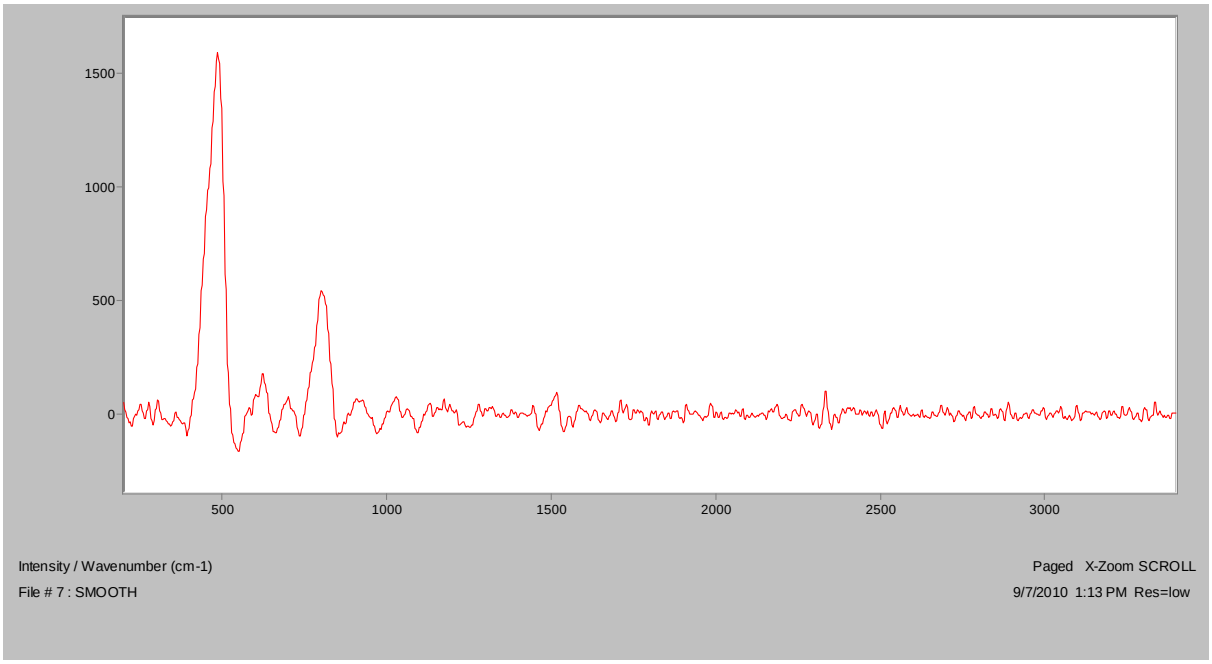

Figure A5 Raman spectrum of ZnAl.14.

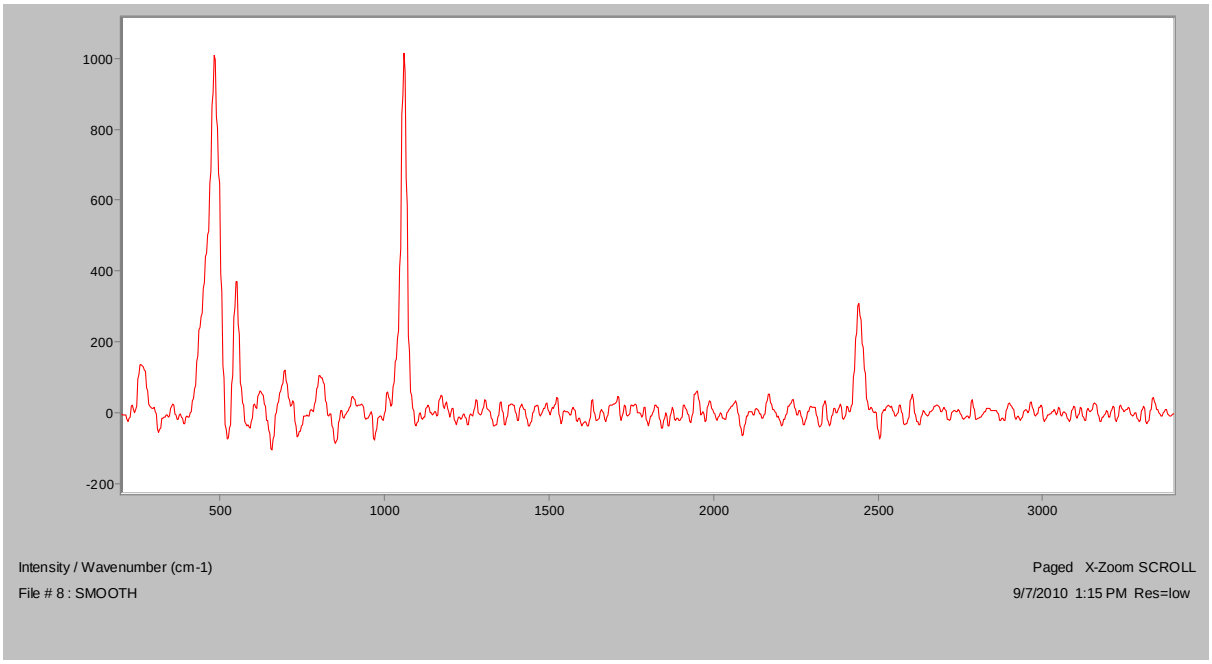

Figure A6 Raman spectrum of ZnAl.16.

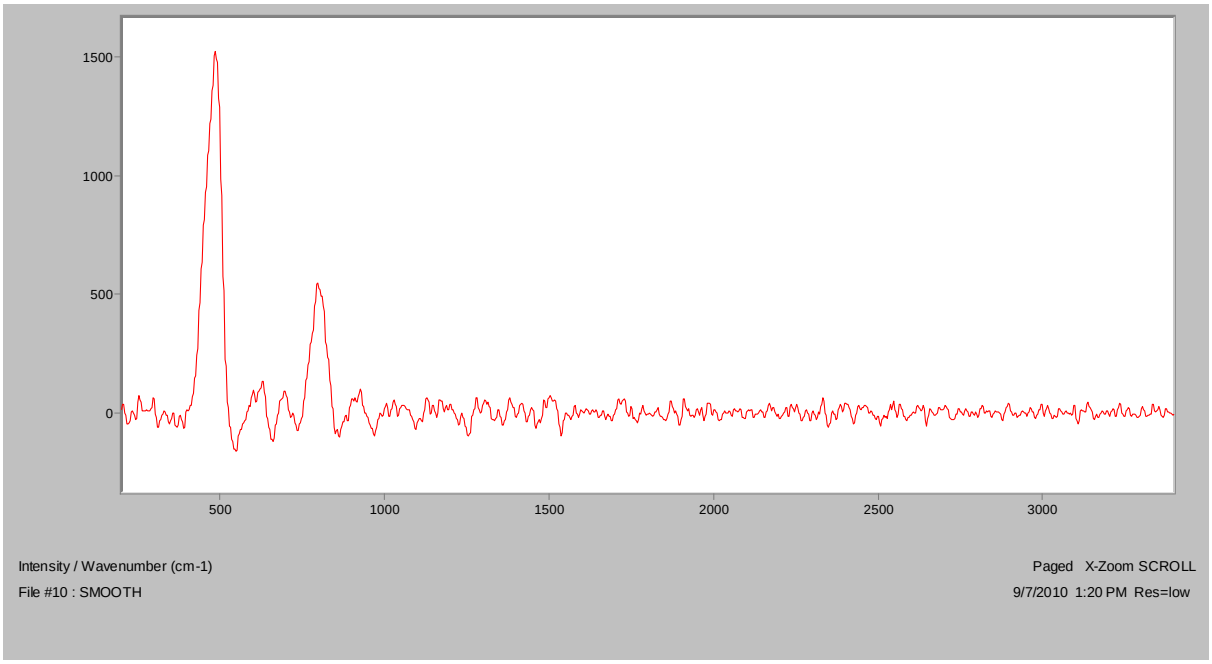

Figure A7 Raman spectrum of ZnFe.30.

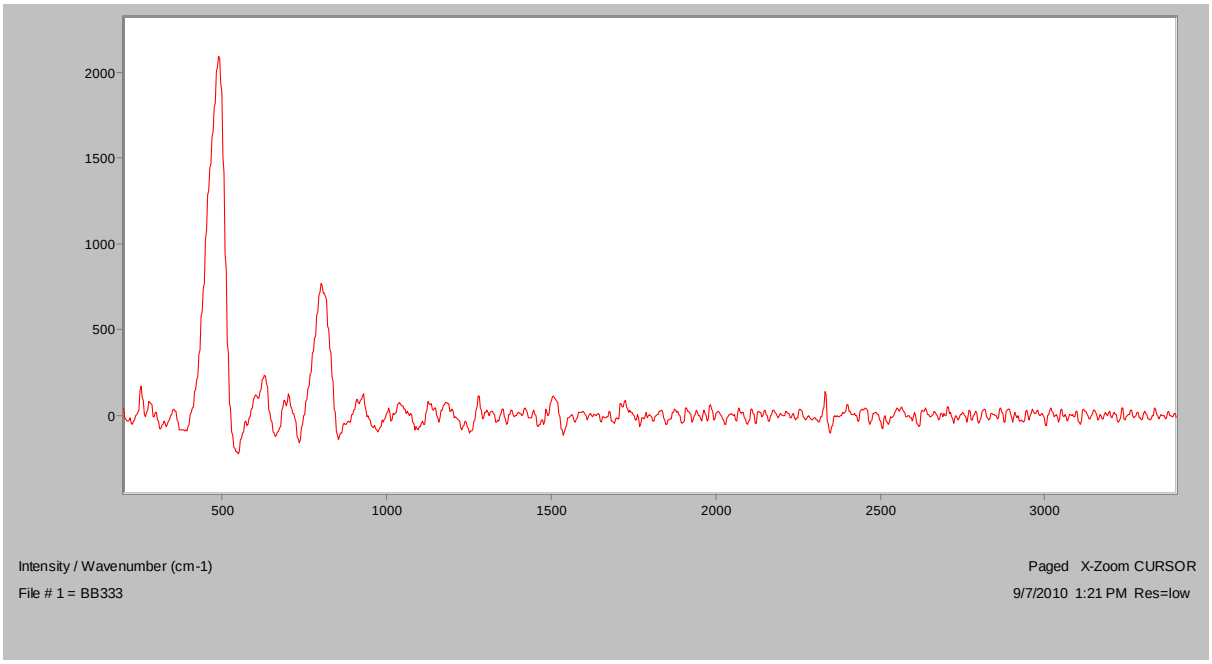

Figure A8 Raman spectrum of ZnFe.32.

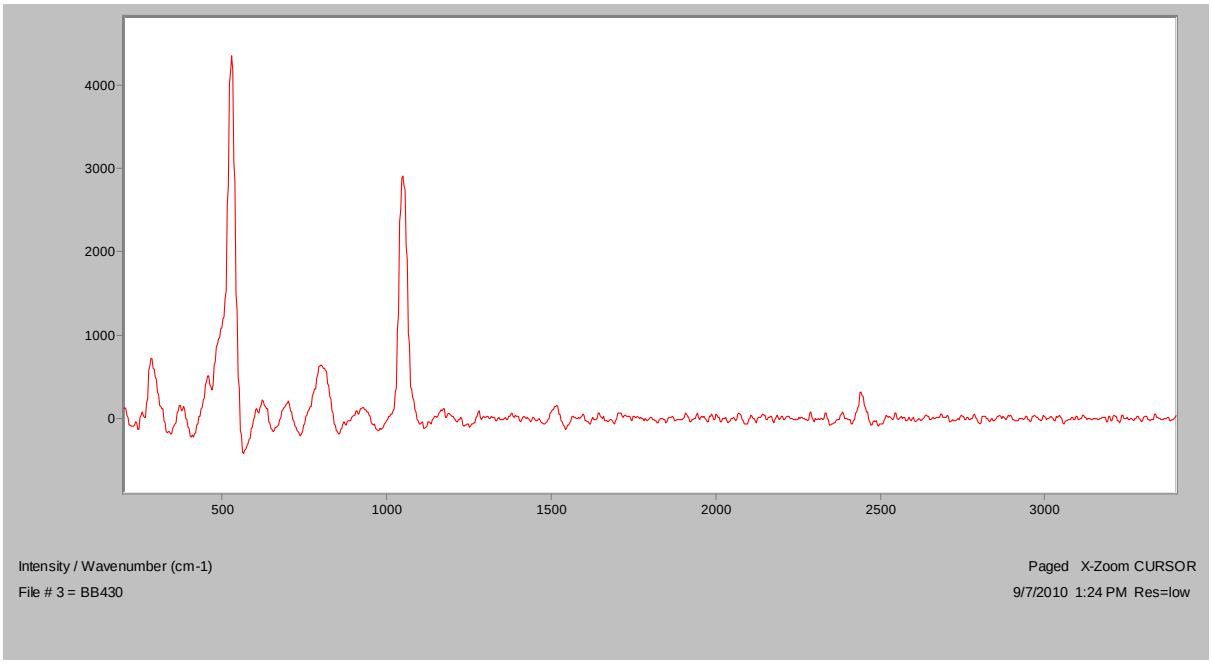

Figure A9 Raman spectrum of MgFe.58.

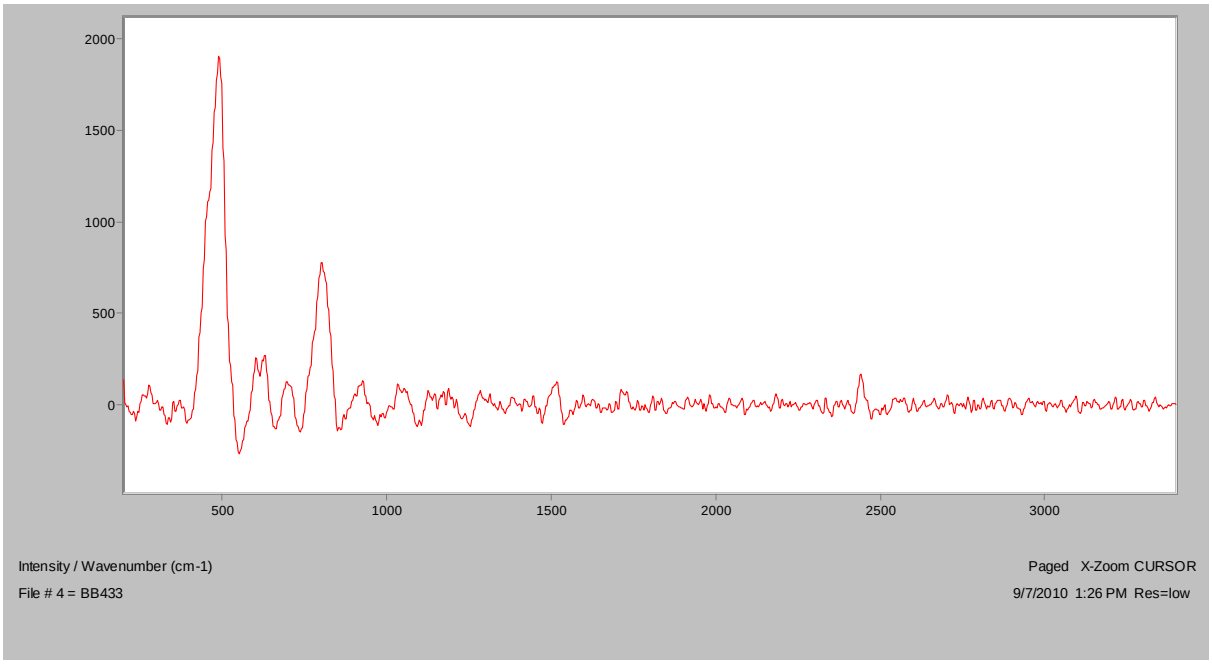

Figure A10 Raman spectrum of MgFe.62.

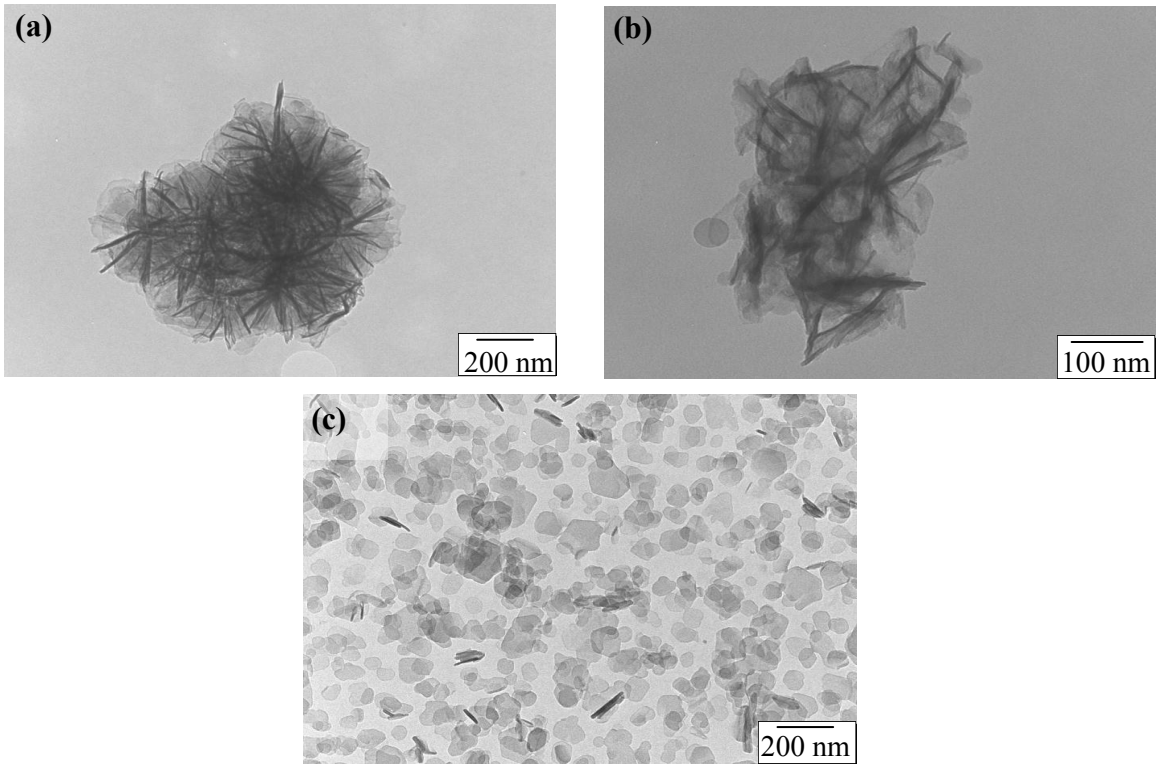

Figure A11 TEM images of (a) MgAl.26 (x75k), (b) MgAl.31 (x200k), and (c) MgAl.34 (x75k).

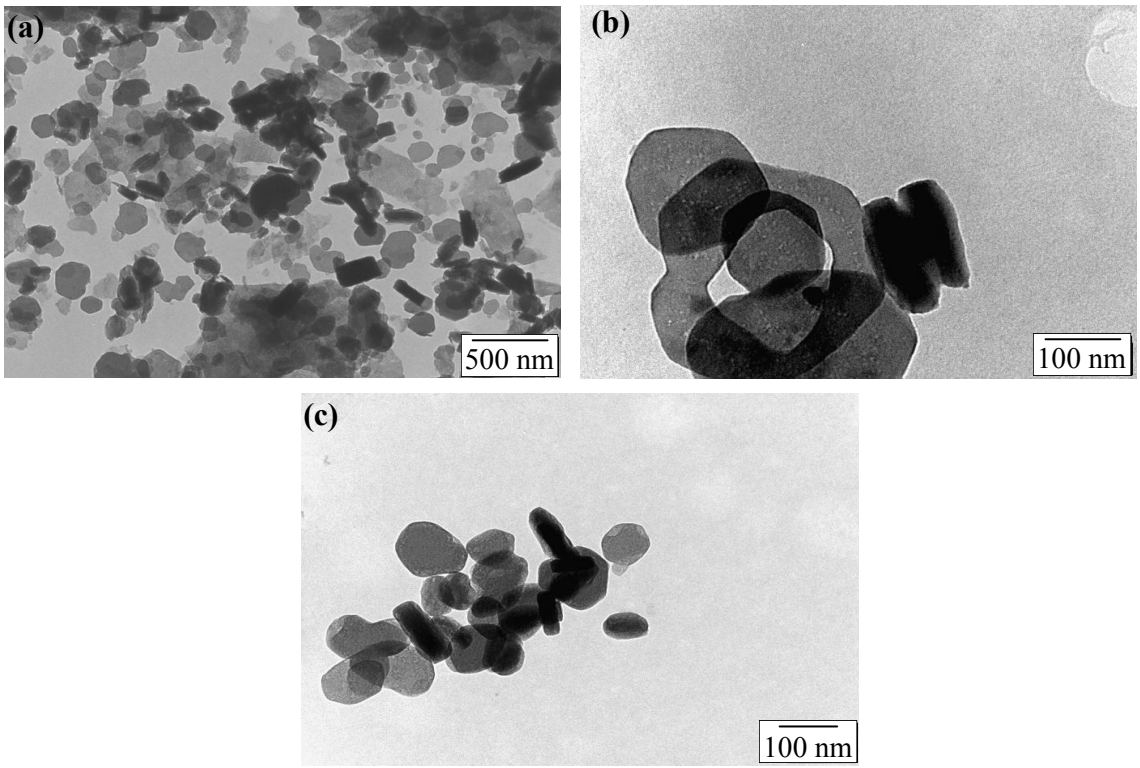

Figure A12 TEM images of (a) ZnAl.11 (x40k), (b) ZnAl.14 (x200k), and (c) ZnAl.16 (x75k).

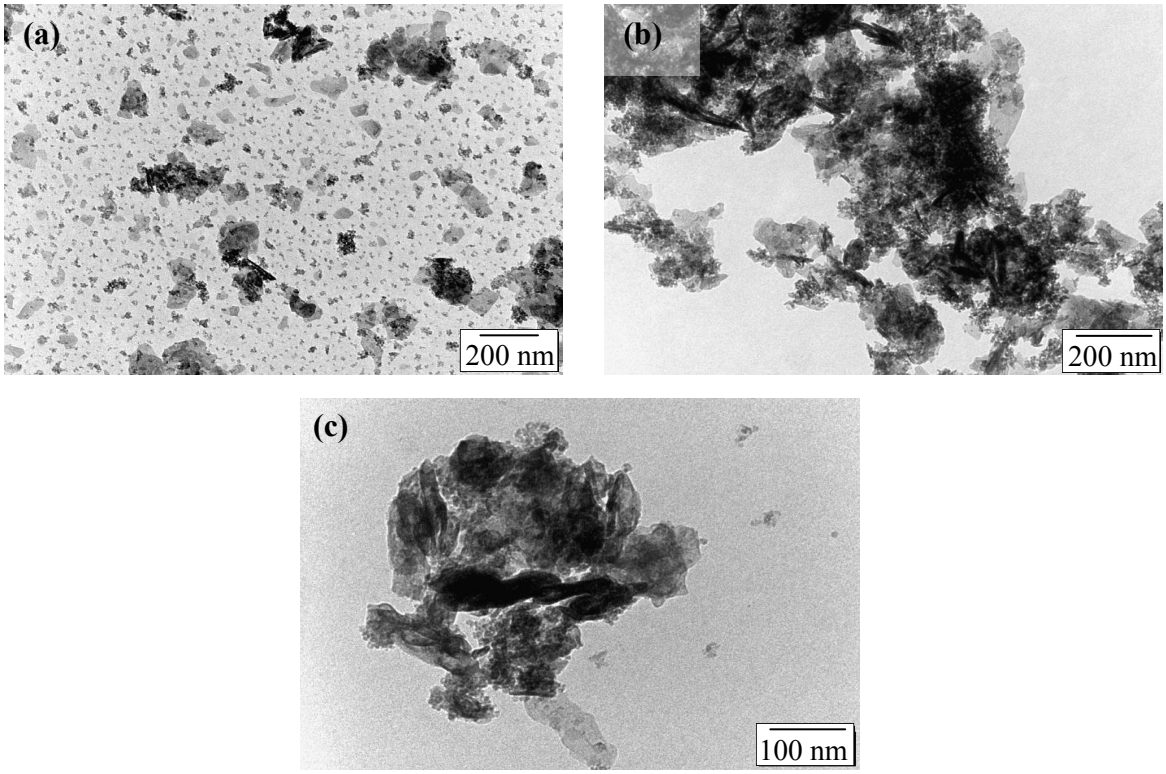

Figure A13 TEM images of (a) ZnFe.24 (x75k), (b) ZnFe.30 (x100k), and (c) ZnFe.32 (x100k).

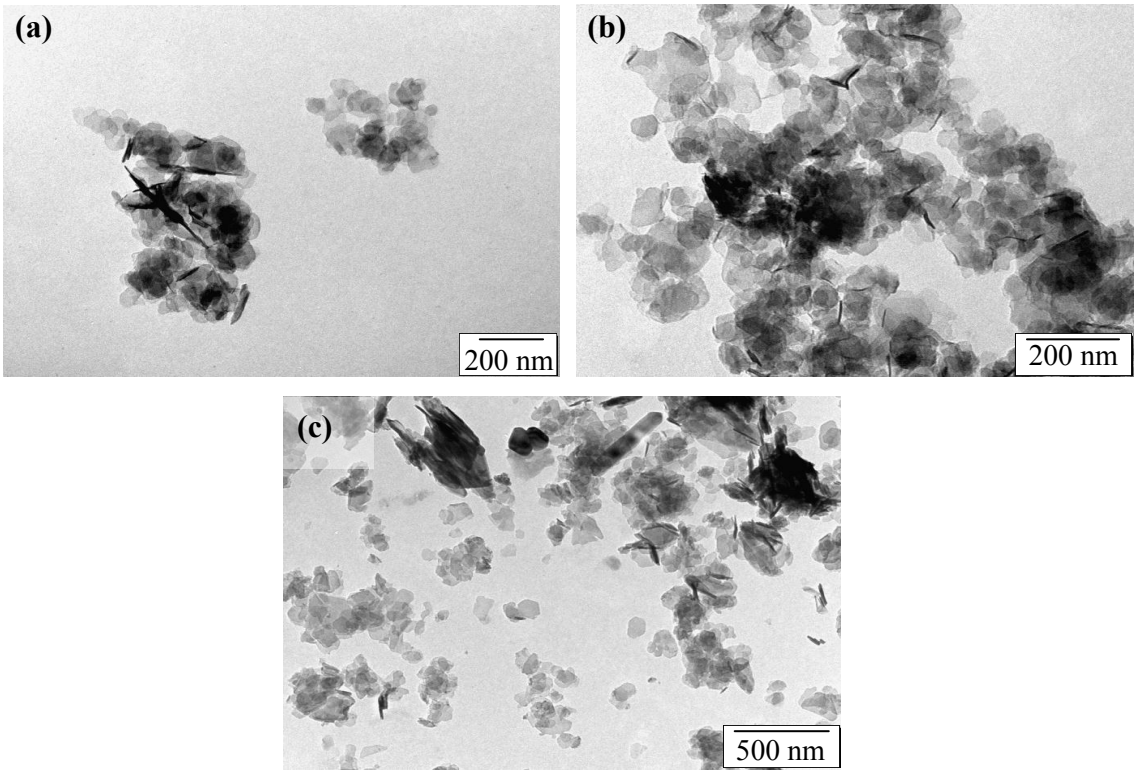

Figure A14 TEM images of (a) MgFe.55 (x100k), (b) MgFe.58 (x150k), and (c) MgFe.62 (x60k).

SEM-EDX Data

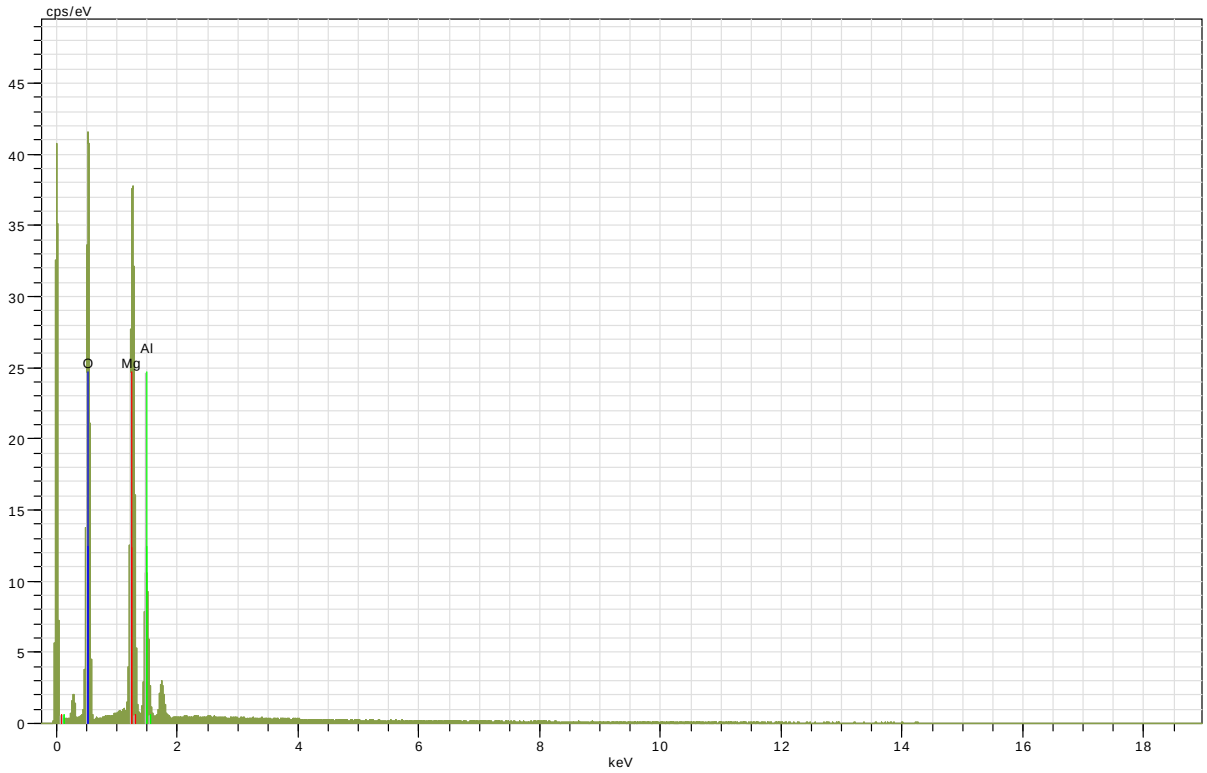

Figure A15 SEM-EDX spectrum for MgAl.26.

Table A5 SEM-EDX elemental data for MgAl.26.

El	AN	Series	unn. C [wt.%]	norm. C [wt.%]	Atom. C [at.%]	Compound	Comp. C [wt.%]	norm. Comp. C [wt.%]	Error [wt.%]
O	8	K-series	18.85	42.24	53.41		0.00	0.00	1.4
Mg	12	K-series	17.65	39.55	32.93	MgO	65.59	29.27	1.0
Al	13	K-series	8.13	18.21	13.66	Al2O3	34.41	15.36	0.4
		Total:	44.63	100.00	100.00				

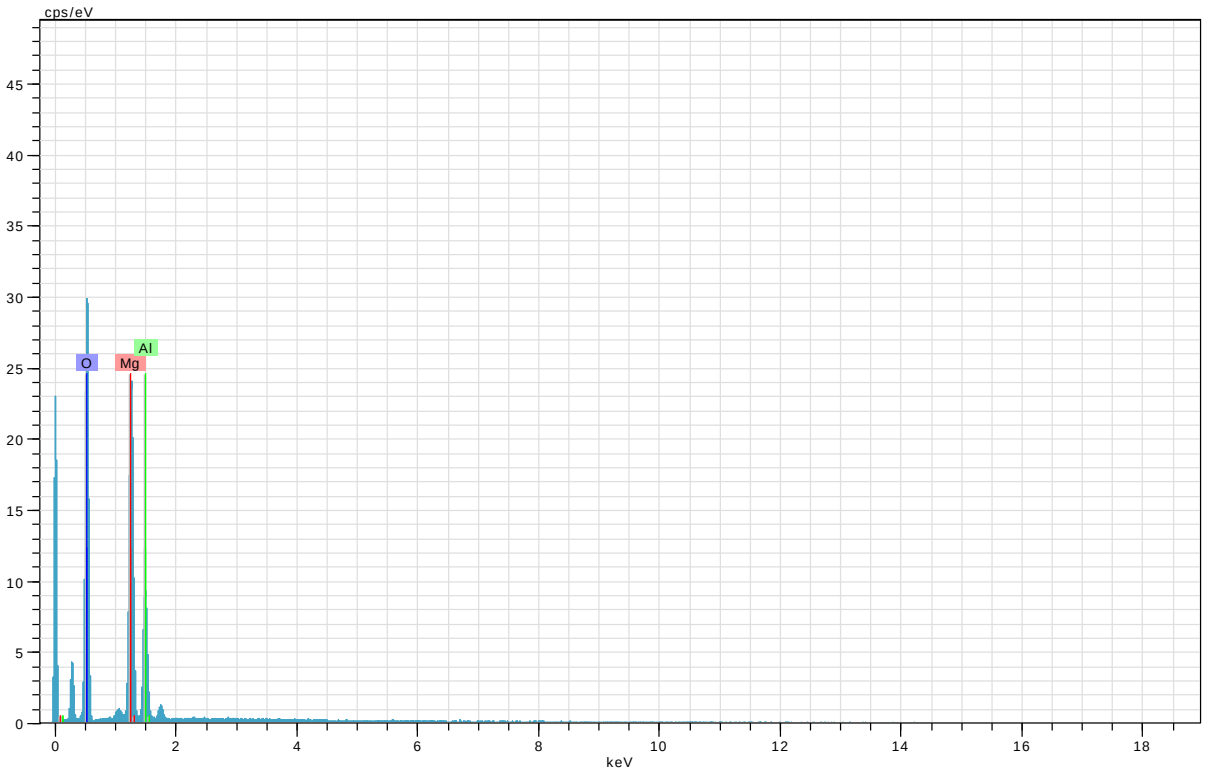

Figure A16 SEM-EDX spectrum for MgAl.31.

Table A6 SEM-EDX elemental data for MgAl.31.

El	AN	Series	unn. C [wt.%]	norm. C [wt.%]	Atom. C [at.%]	Compound	Comp. C [wt.%]	norm. Comp. C [wt.%]	Error [wt.%]
O	8	K-series	21.62	42.57	53.87		0.00	0.00	1.6
Mg	12	K-series	18.68	36.79	30.65	MgO	61.01	30.98	1.1
Al	13	K-series	10.48	20.64	15.48	Al2O3	38.99	19.80	0.5
		Total:	50.78	100.00	100.00				

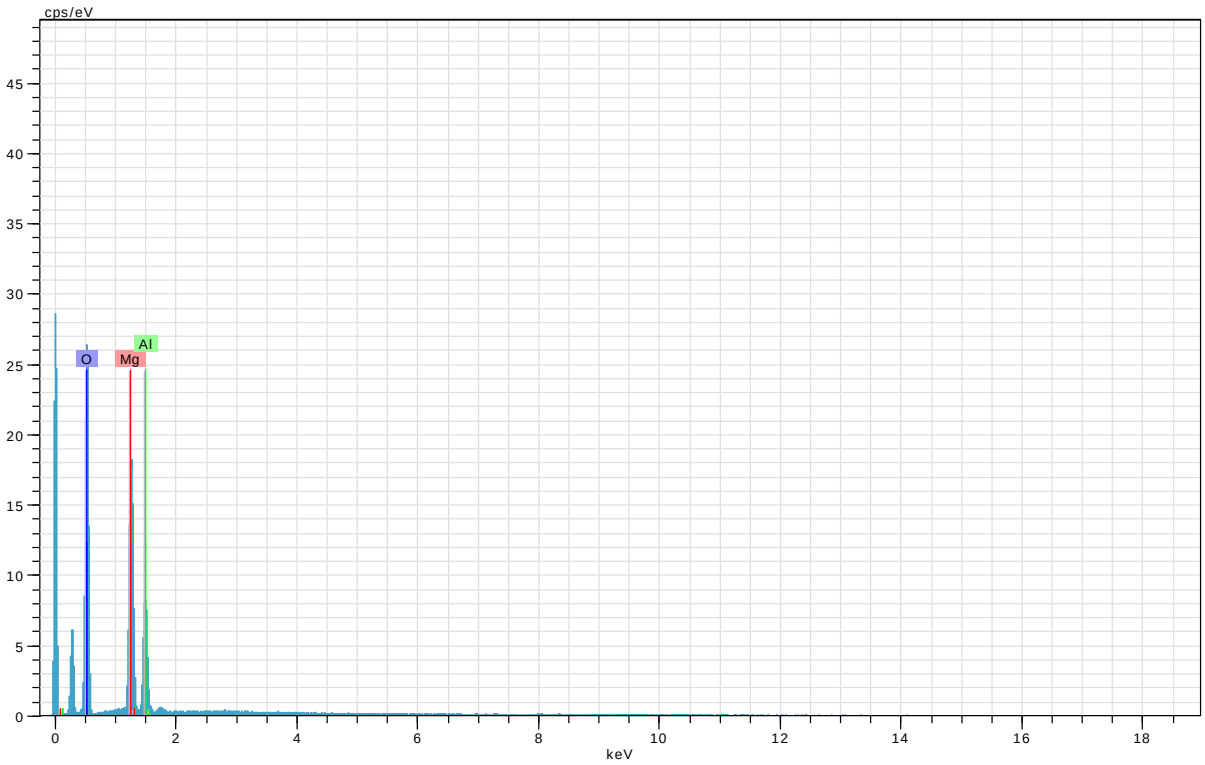

Figure A17 SEM-EDX spectrum for MgAl.34.

Table A7 SEM-EDX elemental data for MgAl.34.

El	AN	Series	unn. C [wt.%]	norm. C [wt.%]	Atom. C [at.%]	Compound	Comp. C [wt.%]	norm. Comp. C [wt.%]	Error [wt.%]
O	8	K-series	17.29	42.87	54.28		0.00	0.00	1.3
Mg	12	K-series	13.85	34.34	28.62	MgO	56.95	22.97	0.8
Al	13	K-series	9.19	22.78	17.10	Al2O3	43.05	17.37	0.5
		Total:	40.34	100.00	100.00				

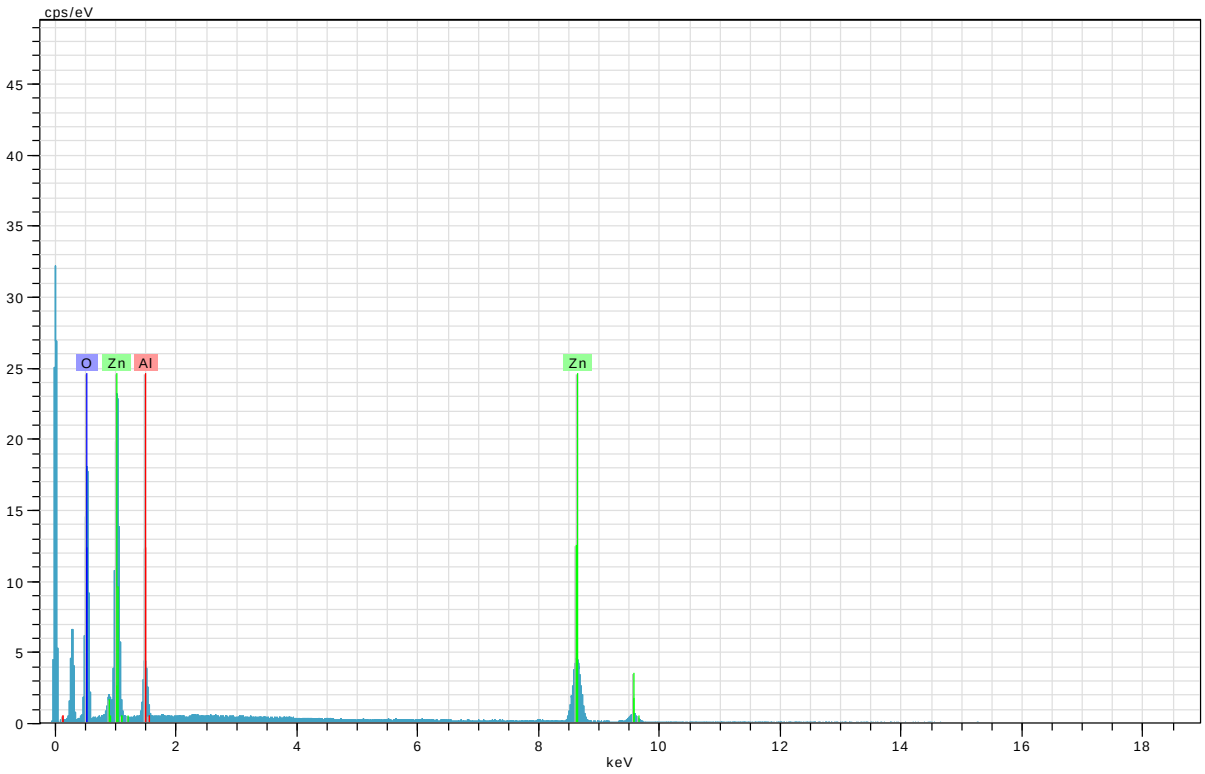

Figure A18 SEM-EDX spectrum for ZnAl.11.

Table A8 SEM-EDX elemental data for ZnAl.11.

El	AN	Series	unn. C [wt.%]	norm. C [wt.%]	Atom. C [at.%]	Compound	Comp. C [wt.%]	norm. Comp. C [wt.%]	Error [wt.%]
O	8	K-series	17.33	24.69	53.09		0.00	0.00	1.0
Al	13	K-series	6.81	9.71	12.38	Al2O3	18.34	12.87	0.4
Zn	30	K-series	46.05	65.61	34.53	ZnO	81.66	57.32	1.3
		Total:	70.19	100.00	100.00				

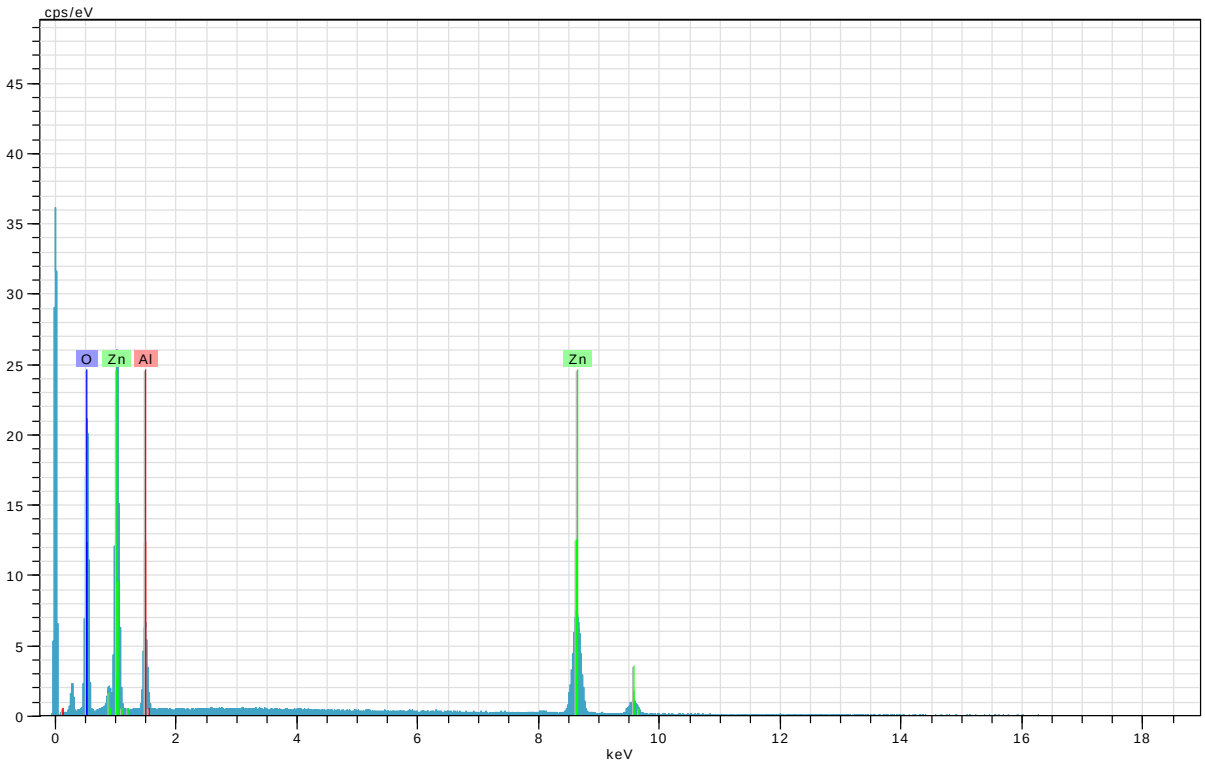

Figure A19 SEM-EDX spectrum for ZnAl.14.

Table A9 SEM-EDX elemental data for ZnAl.14.

El	AN	Series	unn. C [wt.%]	norm. C [wt.%]	Atom. C [at.%]	Compound	Comp. C [wt.%]	norm. Comp. C [wt.%]	Error [wt.%]
O	8	K-series	21.98	25.84	53.67		0.00	0.00	1.3
Al	13	K-series	10.15	11.93	14.69	Al2O3	22.54	19.17	0.5
Zn	30	K-series	52.94	62.24	31.63	ZnO	77.46	65.90	1.5

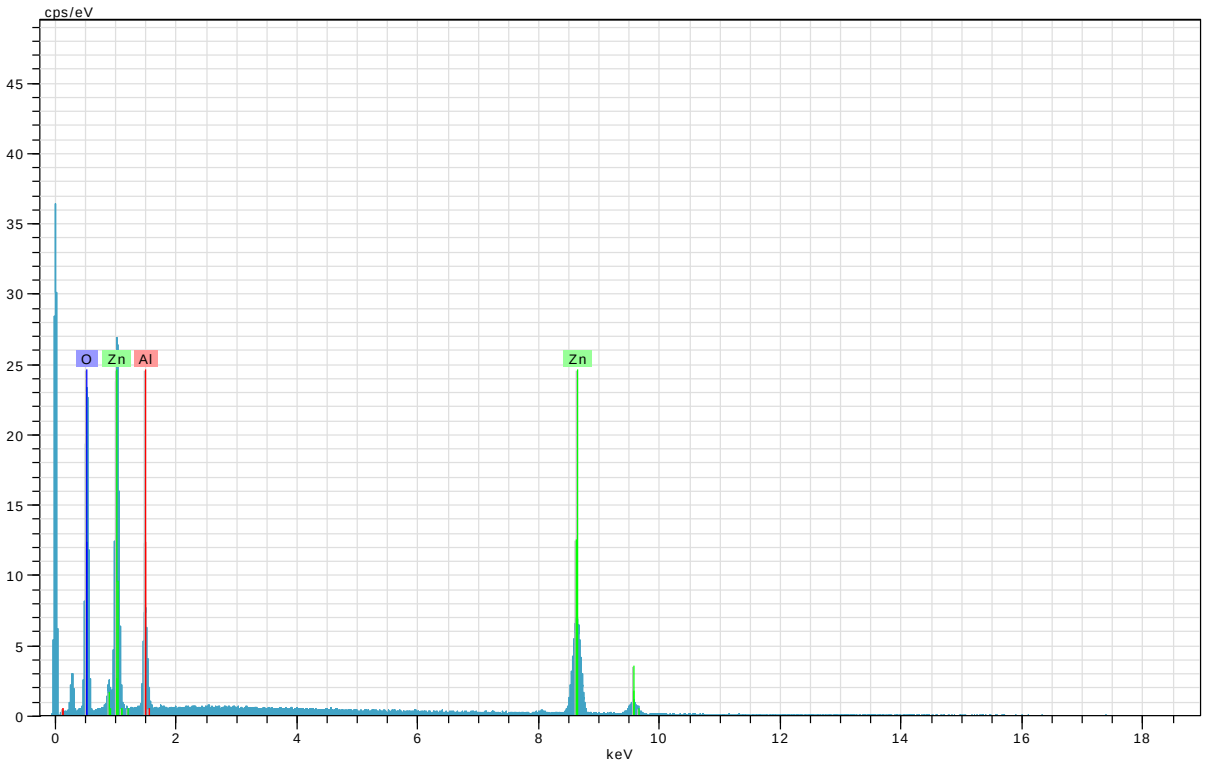

Figure A20 SEM-EDX spectrum for ZnAl.16.

Table A10 SEM-EDX elemental data for ZnAl.16.

El	AN	Series	unn. C [wt.%]	norm. C [wt.%]	Atom. C [at.%]	Compound	Comp. C [wt.%]	norm. Comp. C [wt.%]	Error [wt.%]
O	8	K-series	19.44	26.33	53.91		0.00	0.00	1.1
Al	13	K-series	9.51	12.87	15.63	Al2O3	24.33	17.96	0.5
Zn	30	K-series	44.90	60.80	30.46	ZnO	75.67	55.88	1.3
		Total:	73.84	100.00	100.00				

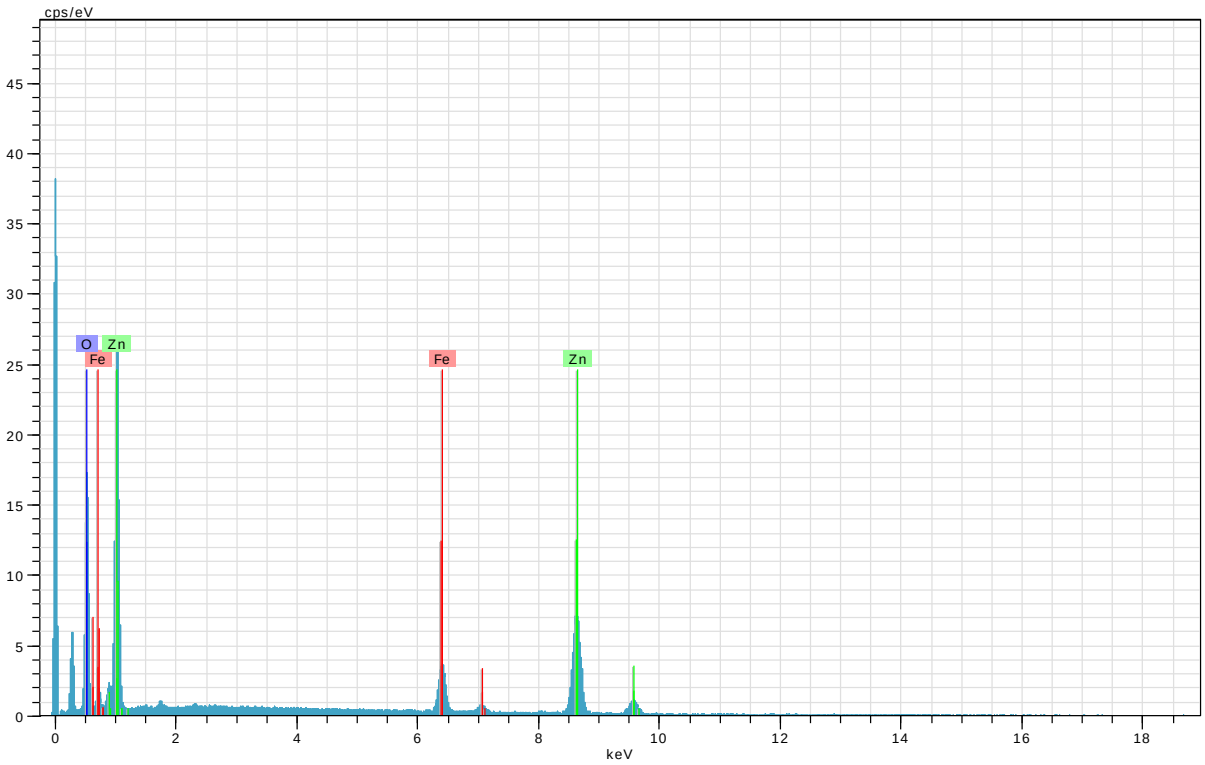

Figure A21 SEM-EDX spectrum for ZnFe.24.

Table A11 SEM-EDX elemental data for ZnFe.24.

El	AN	Series	unn. C [wt.%]	norm. C [wt.%]	Atom. C [at.%]	Compound	Comp. C [wt.%]	norm. Comp. C [wt.%]	Error [wt.%]
O	8	K-series	14.75	21.78	52.47		0.00	0.00	0.6
Fe	26	K-series	9.68	14.30	9.87	Fe2O3	20.45	13.85	0.3
Zn	30	K-series	43.29	63.92	37.67	ZnO	79.55	53.88	1.2
		Total:	67.72	100.00	100.00				

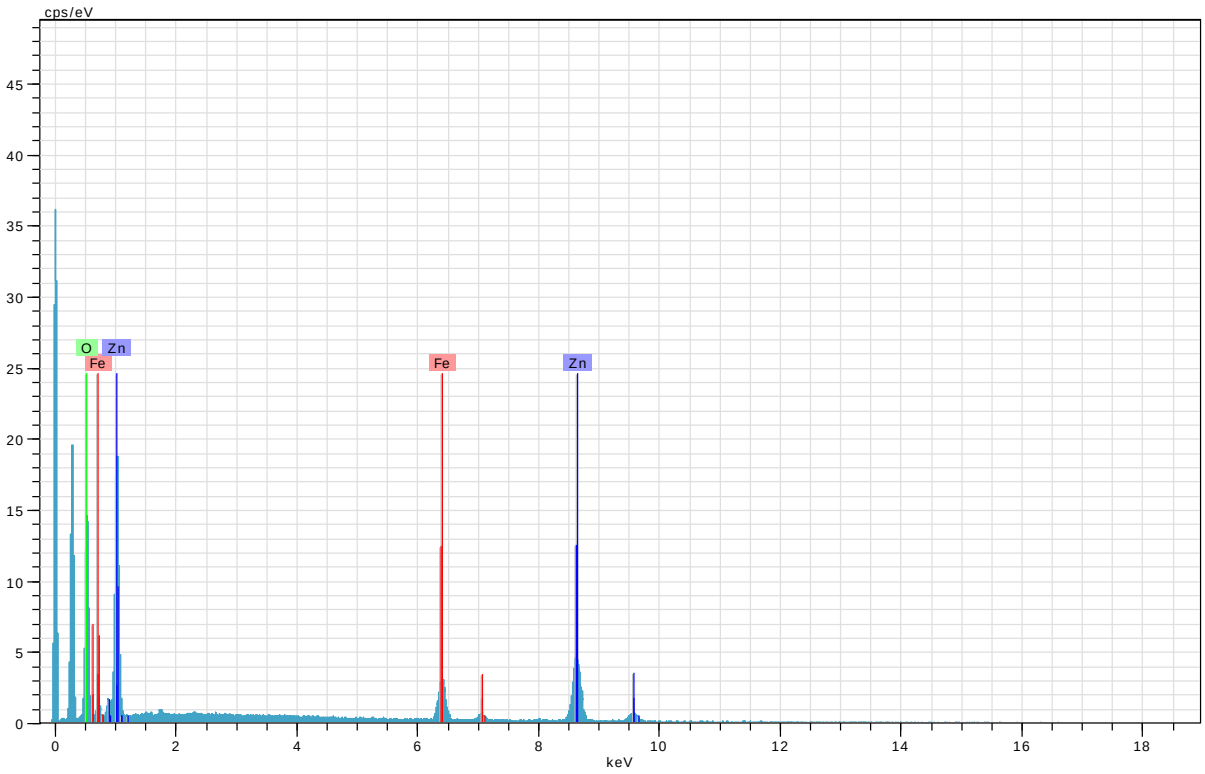

Figure A22 SEM-EDX spectrum for ZnFe.30.

Table A12 SEM-EDX elemental data for ZnFe.30.

El	AN	Series	unn. C [wt.%]	norm. C [wt.%]	Atom. C [at.%]	Compound	Comp. C [wt.%]	norm. Comp. C [wt.%]	Error [wt.%]
O	8	K-series	14.01	22.06	52.77		0.00	0.00	0.6
Fe	26	K-series	10.26	16.15	11.07	Fe2O3	23.10	14.66	0.3
Zn	30	K-series	39.23	61.79	36.16	ZnO	76.90	48.83	1.1
		Total:	63.49	100.00	100.00				

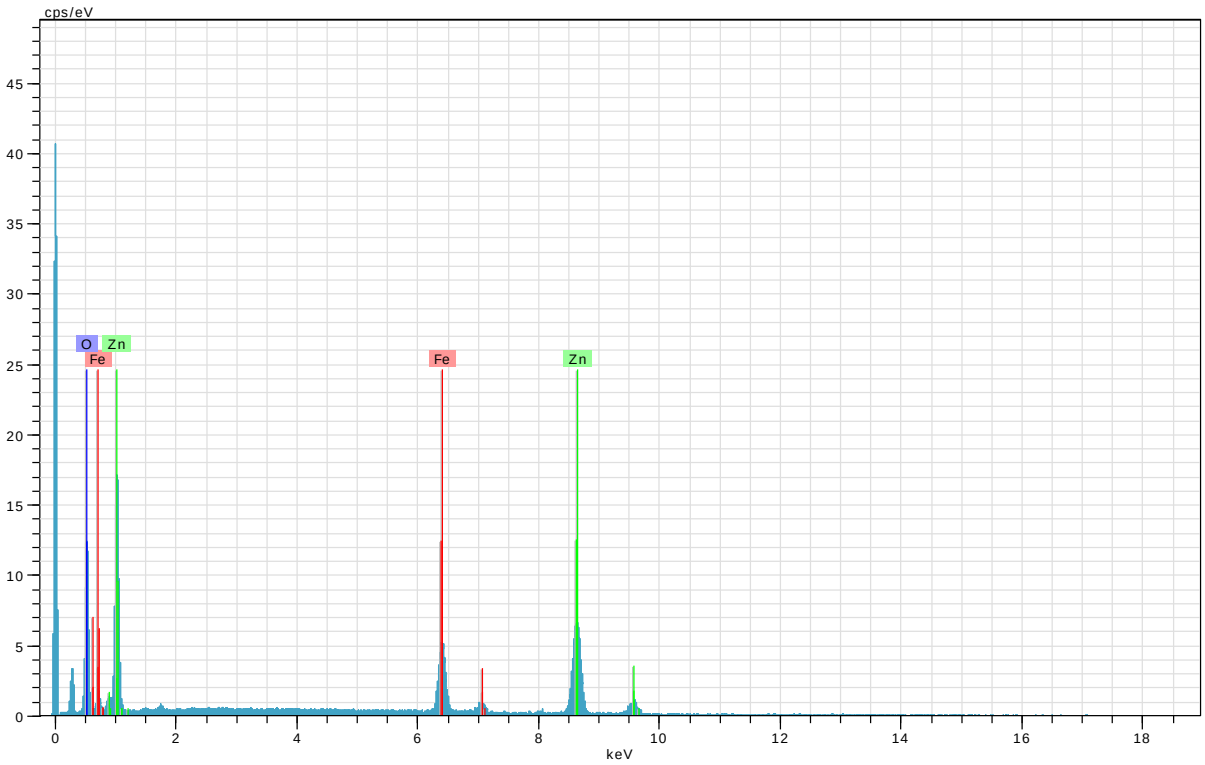

Figure A23 SEM-EDX spectrum for ZnFe.32.

Table A13 SEM-EDX elemental data for ZnFe.32.

El	AN	Series	unn. C [wt.%]	norm. C [wt.%]	Atom. C [at.%]	Compound	Comp. C [wt.%]	norm. Comp. C [wt.%]	Error [wt.%]
O	8	K-series	17.41	22.31	53.03		0.00	0.00	0.7
Fe	26	K-series	13.90	17.81	12.13	Fe2O3	25.46	19.87	0.4
Zn	30	K-series	46.73	59.88	34.84	ZnO	74.54	58.16	1.3
		Total:	78.03	100.00	100.00				

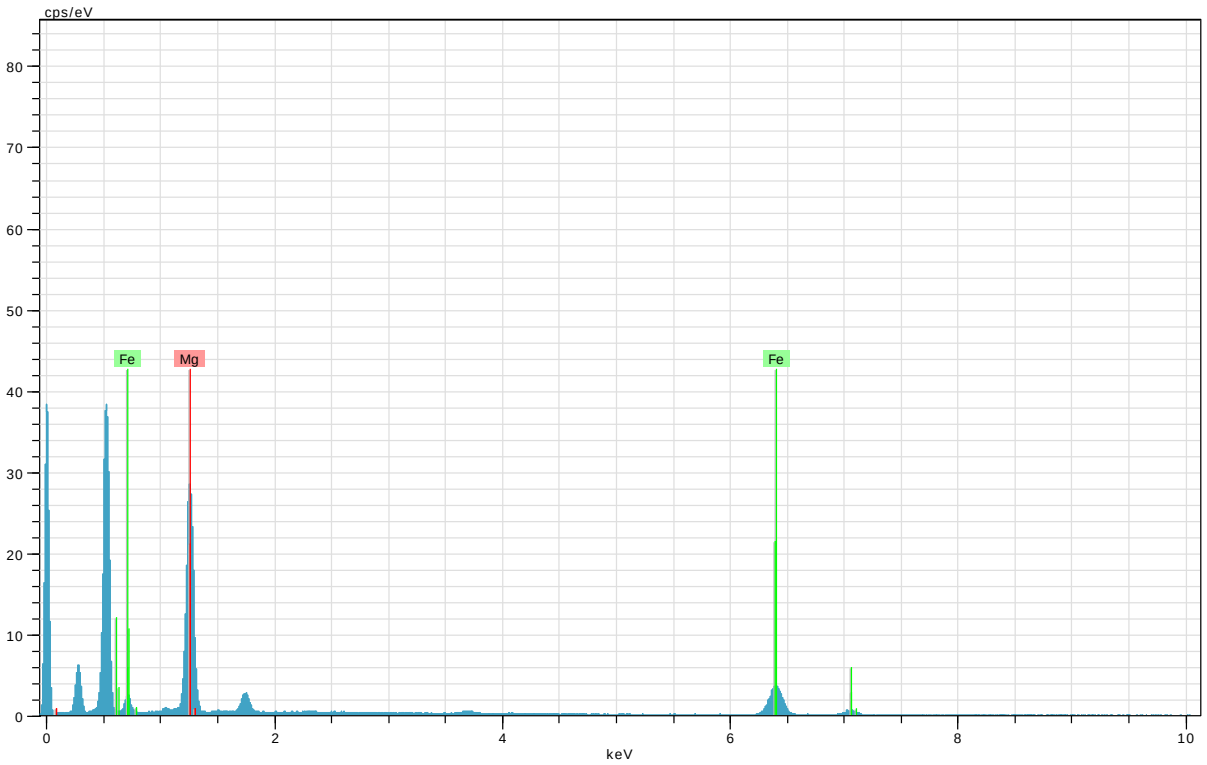

Figure A24 SEM-EDX spectrum for MgFe.55.

Table A14 SEM-EDX elemental data for MgFe.55.

Element	Series	unn. C [wt.%]	norm. C [wt.%]	Atom. C [at.%]	Compound	Comp. C [wt.%]	norm. Comp. C [wt.%]	Error [wt.%]
Magnesium	K-series	24.42	39.66	37.64	MgO	65.76	40.50	1.4
Iron	K-series	14.75	23.95	9.89	Fe2O3	34.24	21.09	0.4
Oxygen	K-series	22.42	36.40	52.47		0.00	0.00	1.4
	Total:	61.59	100.00	100.00				

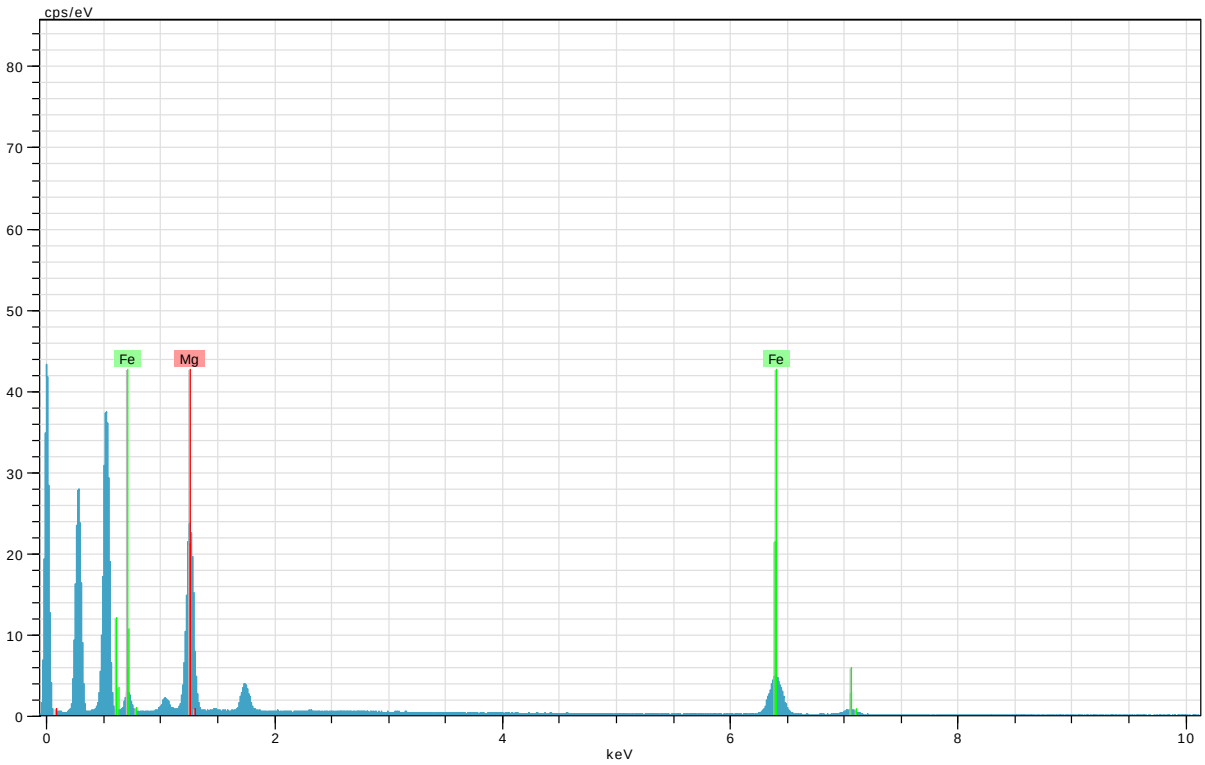

Figure A25 SEM-EDX spectrum for MgFe.58.

Table A15 SEM-EDX elemental data for MgFe.58.

Element	Series	unn. C [wt.%]	norm. C [wt.%]	Atom. C [at.%]	Compound	Comp. C [wt.%]	norm. Comp. C [wt.%]	Error [wt.%]
Magnesium	K-series	18.58	35.08	34.39	MgO	58.17	30.81	1.0
Iron	K-series	15.50	29.26	12.48	Fe2O3	41.83	22.16	0.4
Oxygen	K-series	18.89	35.66	53.12		0.00	0.00	1.2
	Total:	52.97	100.00	100.00				

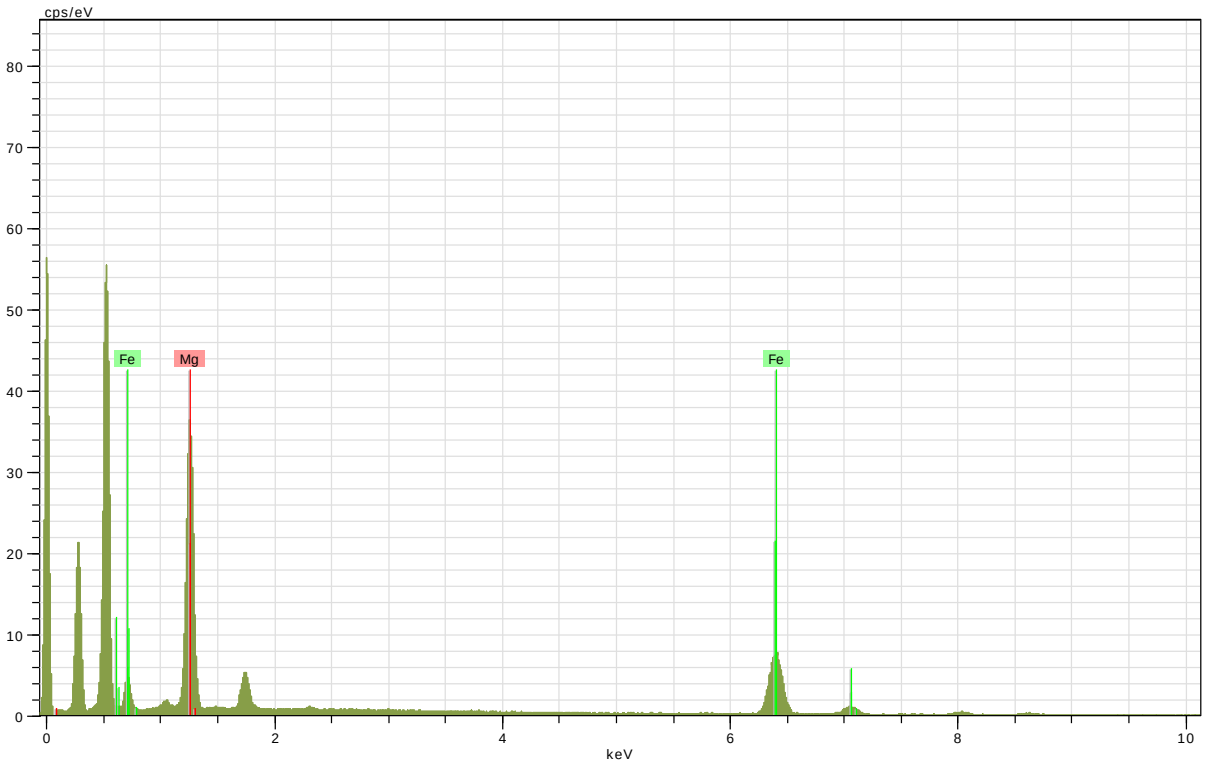

Figure A26 SEM-EDX spectrum for MgFe.62.

Table A16 SEM-EDX elemental data for MgFe.62.

Element	Series	unn. C [wt.%]	norm. C [wt.%]	Atom. C [at.%]	Compound	Comp. C [wt.%]	norm. Comp. C [wt.%]	Error [wt.%]
Magnesium	K-series	20.76	33.10	32.93	MgO	54.89	34.43	1.2
Iron	K-series	19.79	31.55	13.66	Fe2O3	45.11	28.29	0.6
Oxygen	K-series	22.17	35.35	53.41		0.00	0.00	1.4
	Total:	62.72	100.00	100.00				

Cell Culture and Cytotoxicity Studies

Cytotoxicity Studies

Table A17 Culture plate arrangement indicating concentration (μg/10 μl) of each Zn-Al LDH sample added into each well.

Well	**2**	**3**	**4**	**5**	**6**	**7**	**8**
A1 (Control) Cells	40 ZnAl.11	80 ZnAl.11	20 ZnAl.14	60 ZnAl.14	100 ZnAl.14	40 ZnAl.16	80 ZnAl.16
B (Control) Cells	40 ZnAl.11	80 ZnAl.11	20 ZnAl.14	60 ZnAl.14	100 ZnAl.14	40 ZnAl.16	80 ZnAl.16
C (Control) Cells	40 ZnAl.11	80 ZnAl.11	20 ZnAl.14	60 ZnAl.14	100 ZnAl.14	40 ZnAl.16	80 ZnAl.16
D 20 μg ZnAl.11	60 ZnAl.11	100 ZnAl.11	40 ZnAl.14	80 ZnAl.14	20 ZnAl.16	60 ZnAl.16	100 ZnAl.16
E 20 μg ZnAl.11	60 ZnAl.11	100 ZnAl.11	40 ZnAl.14	80 ZnAl.14	20 ZnAl.16	60 ZnAl.16	100 ZnAl.16
F 20 μg ZnAl.11	60 ZnAl.11	100 ZnAl.11	40 ZnAl.14	80 ZnAl.14	20 ZnAl.16	60 ZnAl.16	100 ZnAl.16

Table A18 Culture plate arrangement indicating concentration (μg/10 μl) of each Zn-Fe LDH sample added into each well.

Well	**2**	**3**	**4**	**5**	**6**	**7**	**8**
A1 (Control) Cells	40 ZnFe.24	80 ZnFe.24	20 ZnFe.30	60 ZnFe.30	100 ZnFe.30	40 ZnFe.32	80 ZnFe.32
B (Control) Cells	40 ZnFe.24	80 ZnFe.24	20 ZnFe.30	60 ZnFe.30	100 ZnFe.30	40 ZnFe.32	80 ZnFe.32
C (Control) Cells	40 ZnFe.24	80 ZnFe.24	20 ZnFe.30	60 ZnFe.30	100 ZnFe.30	40 ZnFe.32	80 ZnFe.32
D 20 μg ZnFe.24	60 ZnFe.24	100 ZnFe.24	40 ZnFe.30	80 ZnFe.30	20 ZnFe.32	60 ZnFe.32	100 ZnFe.32
E 20 μg ZnFe.24	60 ZnFe.24	100 ZnFe.24	40 ZnFe.30	80 ZnFe.30	20 ZnFe.32	60 ZnFe.32	100 ZnFe.32
F 20 μg ZnFe.24	60 ZnFe.24	100 ZnFe.24	40 ZnFe.30	80 ZnFe.30	20 ZnFe.32	60 ZnFe.32	100 ZnFe.32

Table A19 Culture plate arrangement indicating concentration (μg/10 μl) of each Mg-Fe LDH sample added into each well.

Well	**2**	**3**	**4**	**5**	**6**	**7**	**8**
A1 (Control) Cells	40 MgFe.55	80 MgFe.55	20 MgFe.58	60 MgFe.58	100 MgFe.58	40 MgFe.62	80 MgFe.62
B (Control) Cells	40 MgFe.55	80 MgFe.55	20 MgFe.58	60 MgFe.58	100 MgFe.58	40 MgFe.62	80 MgFe.62
C (Control) Cells	40 MgFe.55	80 MgFe.55	20 MgFe.58	60 MgFe.58	100 MgFe.58	40 MgFe.62	80 MgFe.62
D 20 μg MgFe.55	60 MgFe.55	100 MgFe.55	40 MgFe.58	80 MgFe.58	20 MgFe.62	60 MgFe.62	100 MgFe.62
E 20 μg MgFe.55	60 MgFe.55	100 MgFe.55	40 MgFe.58	80 MgFe.58	20 MgFe.62	60 MgFe.62	100 MgFe.62
F 20 μg MgFe.55	60 MgFe.55	100 MgFe.55	40 MgFe.58	80 MgFe.58	20 MgFe.62	60 MgFe.62	100 MgFe.62

Transfection Studies

Table A20 Culture plate indicating DNA: Zn-Al LDH complexes of each sample added into each well.

Well	**2**	**3**	**4**	**5**	**6**	**7**
A1 (Control) Cells	1:60 DNA : ZnAl.11	1:70 DNA : ZnAl.11	1:45 DNA : ZnAl.14	1:40 DNA : ZnAl.16	1:50 DNA : ZnAl.16	Empty well
B (Control) Cells	1:60 DNA : ZnAl.11	1:70 DNA : ZnAl.11	1:45 DNA : ZnAl.14	1:40 DNA : ZnAl.16	1:50 DNA : ZnAl.16	Empty well
C (Control) Cells	1:60 DNA : ZnAl.11	1:70 DNA : ZnAl.11	1:45 DNA : ZnAl.14	1:40 DNA : ZnAl.16	1:50 DNA : ZnAl.16	Empty well
D 1 µg pCMV-luc	1:65 DNA : ZnAl.11	1:40 DNA : ZnAl.14	1:50 DNA : ZnAl.14	1:45 DNA : ZnAl.16	Empty well	Empty well
E 1 µg pCMV-luc	1:65 DNA : ZnAl.11	1:40 DNA : ZnAl.14	1:50 DNA : ZnAl.14	1:45 DNA : ZnAl.16	Empty well	Empty well
F 1 µg pCMV-luc	1:65 DNA : ZnAl.11	1:40 DNA : ZnAl.14	1:50 DNA : ZnAl.14	1:45 DNA : ZnAl.16	Empty well	Empty well

Table A21 Culture plate indicating DNA: Zn-Fe LDH complexes of each sample added into each well.

Well	**2**	**3**	**4**	**5**	**6**	**7**
A1 (Control) Cells	1:30 DNA : ZnFe.24	1:40 DNA : ZnFe.24	1:35 DNA : ZnFe.30	1:30 DNA : ZnFe.32	1:35 DNA : ZnFe.32	Empty well
B (Control) Cells	1:30 DNA : ZnFe.24	1:40 DNA : ZnFe.24	1:35 DNA : ZnFe.30	1:30 DNA : ZnFe.32	1:35 DNA : ZnFe.32	Empty well
C (Control) Cells	1:30 DNA : ZnFe.24	1:40 DNA : ZnFe.24	1:35 DNA : ZnFe.30	1:30 DNA : ZnFe.32	1:35 DNA : ZnFe.32	Empty well
D 1 µg pCMV-luc	1:35 DNA : ZnFe.24	1:30 DNA : ZnFe.30	1:40 DNA : ZnFe.30	1:35 DNA : ZnFe.32	Empty well	Empty well
E 1 µg pCMV-luc	1:35 DNA : ZnFe.24	1:30 DNA : ZnFe.30	1:40 DNA : ZnFe.30	1:35 DNA : ZnFe.32	Empty well	Empty well
F 1 µg pCMV-luc	1:35 DNA : ZnFe.24	1:30 DNA : ZnFe.30	1:40 DNA : ZnFe.30	1:35 DNA : ZnFe.32	Empty well	Empty well

Table A22 Culture plate indicating DNA: Mg-Fe LDH complexes of each sample added into each well.

Well	**2**	**3**	**4**	**5**	**6**	**7**
A1 (Control) Cells	1:25 DNA : MgFe.55	1:35 DNA : MgFe.55	1:50 DNA : MgFe.58	1:30 DNA : MgFe.62	1:40 DNA : MgFe.62	Empty well
B (Control) Cells	1:25 DNA : MgFe.55	1:35 DNA : MgFe.55	1:50 DNA : MgFe.58	1:30 DNA : MgFe.62	1:40 DNA : MgFe.62	Empty well
C (Control) Cells	1:25 DNA : MgFe.55	1:35 DNA : MgFe.55	1:50 DNA : MgFe.58	1:30 DNA : MgFe.62	1:40 DNA : MgFe.62	Empty well
D 1 μg pCMV-luc	1:30 DNA : MgFe.55	1:45 DNA : MgFe.58	1:55 DNA : MgFe.58	1:35 DNA : MgFe.62	Empty well	Empty well
E 1 μg pCMV-luc	1:30 DNA : MgFe.55	1:45 DNA : MgFe.58	1:55 DNA : MgFe.58	1:35 DNA : MgFe.62	Empty well	Empty well
F 1 μg pCMV-luc	1:30 DNA : MgFe.55	1:45 DNA : MgFe.58	1:55 DNA : MgFe.58	1:35 DNA : MgFe.62	Empty well	Empty well